

University of Reading

A Design and Synthesis of Model Membrane Systems for Probing
Lipid-Polyphenol Interactions

Ryan T. Coones

Thesis submitted in partial fulfilment of the requirements
for the degree of Doctor of Philosophy

Department of Pharmacy
School of Chemistry, Food, and Pharmacy
March 2023

Declaration

I confirm that this is my own work and the use of all material from other sources has been properly and fully acknowledged.

Ryan T. Coones

Abstract

Modelling cellular membranes is crucial to understand how their structure affects function. Further, to investigate membrane-target interactions, accurate biological membrane models are essential. Understanding membrane interactions in this way has applications for *in vivo* processes, pharmaceuticals and medicine, nutrition, and agriculture among others. This thesis presents research findings for two particular kinds of model membranes, bacterial and epithelial, and their interactions with a series of polyphenolic compounds. A distinction is made within about the nature of the “models”, where some models referred to are physical in nature, and others are computational or mathematical models. The epithelial model becomes focused on the human gastrointestinal epithelium. Here the lipid composition of this novel model epithelial membrane presented is the most complex and accurate model published to date.

This work emphasises the importance of developing more complex model membranes for biological studies. This research aims to bridge the gap between their study and the ability to use surface sensitive techniques to measure membranes and their interactions. Similarly, the benefits of polyphenolic compounds are identified, and some polyphenols whose mechanism of action is relatively poorly understood are investigated in order to move towards developing structure-activity relationships.

Analysis of model membranes through development and interaction with polyphenolic compounds is achieved through complementary surface sensitive techniques that allow lipid bilayer formation and interaction with polyphenols to be measured. Development of the lipid composition of the model bacterial and epithelial membranes takes place through analysis of single lipid components and investigates the effects of mixing lipids within model membranes through calorimetric and surface pressure measurements. Determination of polyphenol presence at a membrane interface, real-time measurement of mass changes for membrane formation and polyphenol interaction, and most crucially structural resolution of interactions in the nanometer regime are achieved using state of the art supported and floating lipid membranes.

Mechanisms by which interaction of polyphenols with model biological lipid membranes is explored, with a comparison between bacterial and epithelial membranes highlighted to show variation in polyphenol interaction with membranes of differing phospholipid composition. The effects of lipid composition of membranes is studied using epithelial membranes of iteratively more complex and accurate composition, with membrane composition

informed by a thorough meta-analysis of epithelial membrane lipid headgroup composition. We are able to show two different modes of action of polyphenols within membranes depending on the type and lipid composition of the membrane where nuances of polyphenol interaction are rationalised in terms of the molecular properties of the polyphenol under investigation.

Bacterial model membranes, both physically and computationally, show strong and persistent interactions under flow with (-)-epigallocatechin gallate and Tellimagrandin-II, when characterised by neutron reflectometry. In the case of Tellimagrandin-II, apparent membrane lysis is observed with multilamellar membrane stacking occurring in the sample cell. By contrast, the epithelial membrane shows binding to the surface of, and intercalation into the tail region, of the membrane. The differences between these two modes of interaction have important implications where the dietary, pharmaceutical, and antimicrobial properties of these compounds is concerned.

Acknowledgements

I would like to extend my deepest gratitude to my supervisors Professor Becky Green and Professor Richard Frazier, who provided invaluable guidance, expertise, wisdom, and support. Without them, realisation of this project would have not been possible. I am forever grateful to them and will endeavour to apply the lessons they have taught me over the years. I would also like to thank Dr. Luke Clifton for his insight and skill in planning and carrying, as well as regular access to the facility, throughout all the neutron experiments and data analysis. Without his help I would likely still be inside a beamline cabin to this day.

I would like to thank the University of Reading for funding and supporting this project, As in any facet of of life, it is exceedingly difficult to go a journey alone. Particular thanks go to Professor Kenneth Shankland who provided endless advice and direction in my teaching career in the department. I also remain indebted to Oliver Hancox for endless conversation, both research and otherwise, and most importantly for selflessly enabling my (our?) caffeine dependency. I would also like to thank Peter, Emma, and Sam over the years for providing the balance to compliment my work, and for helping to maintain my sanity.

To my parents I am thankful for their unconditional support and encouragement over the years as well as the spirit to follow my intellectual aspiration. Finally to Nicole, thank you for your patience, support and care during my Ph.D. Without your help I might not have had the determination to complete this thesis.

Contents

1	Introduction	22
1.1	Lipids and Membrane Architecture	24
1.1.1	Biological Membrane Structure and Function	25
1.2	Variation in Membranes	28
1.3	Reviewing Current Membrane Modelling Techniques	29
1.4	Polyphenols and their Membrane Interactions	34
1.5	Aims and Objectives	36
2	Instrumentation and Experimental Procedures	47
2.1	Membrane Preparation Methods	49
2.2	Addition of Polyphenols to Membranes	49
2.2.1	Vesicle Preparation	49
2.3	Surface Pressure Measurements	50
2.3.1	Langmuir-Blodgett Monolayers & Instrument Setup	50
2.3.2	Pressure-Area Isotherms	50
2.3.3	Compressibility Modulus	52
2.4	Differential Scanning Calorimetry	52
2.4.1	Lipid Phases	52
2.4.2	Instrument Setup	53
2.5	Fourier Transform Infrared Spectroscopy	53
2.5.1	Instrument Setup	53
2.5.2	Applications for FTIR in Membrane Studies	54
2.6	Quartz Crystal Microbalance	55
2.6.1	The Piezoelectric Effect	55
2.6.2	The Sauerbrey Relationship	55
2.6.3	Instrument Setup	56
2.7	Neutron Reflection and Scattering Experiments	58
2.7.1	Theory	58
2.7.2	Instruments and Setup	59
2.7.3	Modelling Methods	59
3	Design & Synthesis of a Bacterial Membrane Model	64
3.1	Bacterial Membrane Composition	66
3.1.1	Lipid Compositional Justification	66
3.2	Results & Discussion	67
3.2.1	Fundamental Bacterial Membrane Models	67
3.2.2	Calorimetric Behaviour of Bacterial Model Membranes	68
3.3	Model Membrane Characterisation with Supported Lipid Bilayers	71

3.3.1	Structural Evaluation of Model Bacterial Membrane using Neutron Reflectometry	74
3.3.2	Discussion	76
3.4	Summary	80
4	Investigating the Interactions of Polyphenolic Compounds with a Bacterial Membrane Model	85
4.1	Lipid-Polyphenol interactions at the air water interface	87
4.2	Increasing Complexity: Interactions with Vesicles	89
4.2.1	Ideal versus Non-ideal Lipid Interactions in Bacterial Model Membranes	92
4.2.2	Bacterial Model Membranes' Interactions with Tellimagrandins I and II	95
4.3	Characterising Interactions with Supported Lipid Bilayers	101
4.3.1	Interactions of EGCg with a Model Bacterial Membrane	103
4.3.2	Interactions of Tellimagrandin II with a Model Bacterial Membrane	107
4.3.3	Interactions of Tellimagrandin I with a Model Bacterial Membrane	110
4.4	Floating Model Bacterial Membrane Interactions with EGCg using Neutron Reflectometry	115
4.4.1	Interactions with EGCg from the Bulk Solution	116
4.5	Analysis of Model Bacterial Membranes Containing Pre-Mixed EGCg	119
4.6	Floating Model Bacterial Membrane Interactions with Tellimagrandin-II using Neutron Reflectometry	122
4.7	Summary	126
5	Systematically Reviewing Lipid Head Group Composition within Biological Membranes	133
5.1	Motivation for Understanding Lipid Headgroup Composition of Membranes	136
5.2	Methodology	136
5.2.1	Systematically Reviewing Epithelial Cell Composition	136
5.2.2	Search Terms and Selection Criteria	137
5.3	Bacterial and Erythrocyte Membrane Search	141
5.3.1	Bacterial Outer Membrane Composition	141
5.3.2	Human Erythrocyte Membrane Composition	141
5.4	Publication Rate for 'Lipid Composition' Studies	142
5.5	Epithelial Membrane Compositional	143
5.6	Bacterial Outer Membrane Composition	147
5.7	Human Erythrocyte Membrane Composition	148
5.8	Membrane Composition Comparison	149
5.9	Outlier Search	151
5.10	Open Questions and Further Work	154
5.11	Summary	155

6	Model Epithelial Membranes and Interactions with Polyphenols	165
6.1	Epithelial Membrane Architecture	167
6.1.1	Motivation for Epithelial Membrane Modelling	167
6.2	Results	168
6.2.1	Developing the Complexity of the Model Lipid Membrane	168
6.2.2	Determination of Model Epithelial Membrane Interactions Using Supported Lipid Bilayers	169
6.2.3	Characterising Model Epithelial Membrane Interactions with Neutron Reflectometry	172
6.2.4	Refining the Model Membrane Composition	181
6.3	Summary	187
7	Epilogue	191
7.1	Concluding Remarks	191
7.2	Recommendations for Further Work	196
A	Appendix1	199
A.1	Fitting Parameters for Model Bacterial Membrane + EGCg . . .	199
A.1.1	Interaction from Solution	199
A.1.2	Interaction from Doped Bilayer	200
A.2	Fitting Parameters for Model Bacterial Membrane + Tel-II . . .	201
A.3	Fitting Parameters for Model Epithelial Membrane + Tel-II . . .	203
A.4	Fitting Parameters for Model Epithelial Membrane + Tel-I . . .	204
A.5	Fitting Parameters for Optimised Model Epithelial Membrane + Tel-II	205
A	Appendix2	207

List of Figures

1.1	Depiction of lipid classes, along with categorical examples of each class and a simplified schematic representation.	25
1.2	Structures of some common membrane lipids. Head groups are shown in blue and are phosphate bound. The glycerol-derivative backbone is also shown along with the positions of the R-groups that can vary in length and saturation.	26
1.3	Schematics of some typical methods for physical membrane modelling systems and for observing their interactions; Top left – micelles, typical of surfactants and other hydrophobic molecules when introduced to an aqueous environment. Top right – monolayers, very common set-up for Langmuir–Blodgett type experiments for measuring lipid surface pressure and tension. Bottom left – vesicles, these can adopt a large size regime and are frequently used to mimic simple bilayer interactions when formed with lipids. Bottom right – asymmetric bilayers, complex layer formation is taking centre stage in many surface sensitive techniques as they become more accurate and complex.	30
1.4	Lipid phases within a bilayer, with a schematic representation of how tail chains and headgroups are oriented as the sample passes through the transition temperature.	32
1.5	A map of the thesis showing the outline of each chapter, and some of the main points to be covered in each section of research. These points can be related to the three research questions set out above.	39
2.1	A pressure-area isotherm of DPPG (0.5 mg/mL, 20 μ L, subphase = NaCl (100 mM)) demonstrating the three phases of compression; the gaseous (G) phase shows no interaction between lipid molecules, the liquid expanded (LE) phase shows some minimal ordering between molecules, and the condensed (C) phase where the molecules at the surface are tightly packed together. The compressibility modulus shows changes in the lipid phase, for example the minimum at 8 mN.m ⁻¹ shows the G-LE transition.	51
2.2	Schematic illustration of the ATR-FTIR setup. The IR beam is shown to be internally reflected by the Si substrate and hits the membrane sample at multiple points along the path to the detector.	54
2.3	A simple schematic of the QCM-D setup.	56

2.4	A typical example of changes to frequency and dissipation during the deposition of a supported lipid bilayer at the Si-water interface. Here a single overtone is shown for both Δf (frequency) and ΔD (dissipation) with the important times labelled: (1) lipid vesicle injections, (2) vesicle adsorption and spontaneous rupture (3) SLB formation, (4) osmotic shock with pure D_2O , and (5) buffer wash.	58
2.5	Schematic depicting the layers assumed to be present and used for all initial neutron reflectometry fits showing the under layers, SAM (purple), floating lipid bilayer (yellow), and bulk solution.	61
3.1	Skeletal lipid structures for (a) DPPC, (b) DPPG, (c) DPPE, (d) DOPC, and (e) DOPG.	67
3.2	(Left) Pressure-area isotherms of the individual lipid components used in the process for forming a bacterial membrane model. DPPC (blue) and DPPG (orange) show 3 distinct phases, while DOPC (purple) and DOPG (green) show condensed phases at relatively large APM compared to their longer, more saturated, chain counterparts. DPPE (yellow) also shows only two phases. (Right) Compressibility moduli for each lipid are given, depicting the elasticity of the monolayer. Colours of the compressibility moduli are matched to the pressure-area isotherms, and have been vertically offset for clarity.	69
3.3	DSC thermograms for the single lipids and the bacterial mixtures to demonstrate the phase transition temperatures of the individual and mixed components.	70
3.4	ATR-FTIR spectrum for DOPC/DOPG (7:3) supported at the Si-water interface cropped to show the (a) aliphatic C-H vibrational modes for the lipid hydrocarbon tails and the ester stretching mode. The full spectrum is shown in panel (b) with areas of interest highlighted in coloured boxes. Features for O-D and O-H are coloured in yellow, aliphatic C-H features are in red and the ester C=O in green. Peak assignments are given in table 3.2.	73
3.5	Example of changes to frequency and dissipation during the deposition of a DOPC/DOPG (7:3) SLB at the Si-water interface. Critical changes to the system are indicated in the in-figure annotations highlighting vesicle adsorption, rupture, and buffer wash to remove any loosely bound unruptured vesicles.	74
3.6	Panels (A-D) showing neutron reflectivity profiles for data (points) and model fits (lines) for a COOH-SAM/Gold/Permalloy coated silicon substrate (blue) with DOPC/DOPG (7:3) model membrane (red) in various contract solutions. (E) Neutron SLD profiles showing the Si-Py-SAM-COOH underlayers (blue) with DOPC/DOPG (7:3) bilayer (red) interaction in H_2O , gold and silicon matched water, and D_2O contrasts. The SLD profile (E) has been cropped to show membrane regions more clearly, leaving out the underlayers.	75

3.7	Neutron SLD profile for a DOPC/DOPG (7:3) model membrane system showing the Si-Py-SAM-COOH underlayers (blue) with DOPC/DOPG (7:3) bilayer (red) interaction in H ₂ O, gold and silicon matched water, and D ₂ O contrasts. The underlaid cartoon shows the functionalised gold surface and the attached SAM, the water gap between the underlayers and the model membrane, and the two leaflets of the membrane itself.	77
4.1	Chemical structure of 1,2,3,4,6-penta-O-galloyl d-glucose (PGG).	87
4.2	Compression isotherms of DPPG where the fraction of PGG in the sample increases from pure DPPG (blue), DPPG:PGG = 10:1 (orange), DPPG:PGG = 5:1 (yellow), DPPG:PGG = 3:1 (purple), DPPG:PGG = 2:1 (green). Compressibility moduli of the isotherms are shown above the compression isotherms.	88
4.3	Mean molecular area versus composition of PGG for DPPG/PGG monolayers at the air-water interface at the fixed surface pressure values. The data were fit to a parabolic polynomial to demonstrate their non-linearity using Matlab's <i>polyfit</i> function.	89
4.4	DSC thermograms for non-ideal DPPE/DPPG (3:2, blue) with the addition of 1,2,3,4,6-pentagalloylglucose (PGG) at lipid:PGG ratios of 10:1 (orange), 5:1 (black), and 2:1 (purple).	91
4.5	(a) Structure of (-)-epigallocatechin gallate (EGCg). (b) DSC thermograms for ideally mixed DPPE/DPPG (3:2, blue) vesicles. Lipid:EGCg ratios increase from 10:1 (orange), 5:1 (yellow), and to 2:1 (purple) showing that increasing the EGCg concentration induced demixing of the lipid membrane components.	93
4.6	DSC thermograms for non-ideal DPPE/DPPG (3:2, blue) with interactions with (-)-epigallocatechin gallate (EGCg) at lipid:EGCg ratios of 10:1 (orange) and 5:1 (black).	94
4.7	Exploring the effects of induced mixing with an ideally mixed DPPE/DPPG (3:2) + EGCg at a lipid:EGCg ratio of 2:1. Scans of the same sample were taken at t = 2 (blue), 4 (orange), 8 (yellow), 24 (purple), and 26h (green) to measure the evolution of the lipid layer due to the addition of EGCg.	96
4.8	(a) Structure of Tellimagrandin II. (b) DSC thermograms for ideally mixed DPPE/DPPG (3:2, blue) vesicles. Lipid:Tel-II ratios increase from 10:1 (orange), 5:1 (yellow), and to 2:1 (purple) showing that increasing the Tel-II concentration results in induced mixing of the lipid membrane components.	98
4.9	(a) Structure of Tellimagrandin I. (b) DSC thermograms for ideally mixed DPPE/DPPG (3:2, blue) vesicles. Lipid:Tel-I ratios increase from 10:1 (orange), 5:1 (yellow), and to 2:1 (purple) showing that increasing Tel-I concentration results in induced mixing of the lipid membrane components.	99

4.10	Schematic representation of a polyphenol interacting electrostatically at the lipid bilayer surface. The anionic DPPG headgroup is shown here to offer a lone electron pair from one of the glycerol oxygen atoms that protrudes at the bilayer surface for hydrogen bond donation from the polyphenol. The polyphenol example given here is Tellimagrandin II and the bilayer depicted represents the DOPC/DOPG (7:3) bilayer used in SLB and neutron experiments.	101
4.11	FTIR spectrum for a DOPC/DOPG (7:3) SLB before (blue) and after (orange) addition of EGCg (100 μM), showing relevant sections to highlight the asymmetric (2920 cm^{-1}) and symmetric (2840 cm^{-1}) C–H stretching modes as well as the C=O stretching mode (1724 cm^{-1}). After the addition of EGCg (100 μM) a peak can be seen having appeared (1603 cm^{-1}) as a result of the presence of EGCg at the interface, as well as an increase in the area under the peak at 1724 cm^{-1}	104
4.12	Kinetics of interaction of EGCg (100 μM) with the bacterial model DOPC/DOPG (7:3) membrane. The top panel (red) shows the small increases in the area under the peak at 1724 cm^{-1} corresponding the ester groups in the lipid tails. The EGCg ester groups are thought to cause the increased peak area. For the feature that appears at 1603 cm^{-1} (blue) the aromatic C=C, C–H and C–OH are likely responsible.	105
4.13	QCM-D plots showing changes to both frequency and dissipation (ΔF , ΔD respectively) in the 3rd (red, green) 5th (orange, teal), 7th (yellow, purple), and 9th (grey, grey) overtones for formation of a DOPC/DOPG (7:3) SLB followed by interaction with EGCg (100 μM). Bilayer formation was ensured through osmotic shock after vesicle adsorption. The change in ΔF shows that the interaction at the bilayer surface was strong enough such that the EGCg remained bound at the membrane surface under constant flow of buffer solution.	106
4.14	FTIR spectrum for a DOPC/DOPG (7:3) SLB before (blue) and after (orange) addition of Tel-II (100 μM), showing relevant sections to highlight the asymmetric (2920 cm^{-1}) and symmetric (2840 cm^{-1}) C–H stretching modes as well as the C=O stretching mode (1724 cm^{-1}). With the addition of Tel-II (100 μM) a peak appears at 1595 cm^{-1} along with an increase in the area under the peak at 1724 cm^{-1}	108

4.15	Figure showing changes to FTIR peak areas for Tel-II (100 μM) with the bacterial model DOPC/DOPG (7:3) membrane. The top panel (red) in each shows increases in the area under the peak at 1724 cm^{-1} corresponding the the ester groups in the lipid tails. The ester linkages in the polyphenol are likely the cause of the increased peak area. For the feature that appears at 1595 cm^{-1} (blue) the aromatic C=C, C-H and C-OH are likely responsible. The changes to the peak area was measured in 3 parts with (a) the initial changes as the Tel-II was injected across the membrane, (b) longer timescale increases as measured overnight, and (c) reaction termination after excess Tel-II was rinsed away from the surface. (d) shows all three sets of changes overlaid.	109
4.16	QCM-D plots showing changes to both frequency and dissipation (ΔF , ΔD respectively) in the 3rd (red, green) 5th (orange, teal), 7th (yellow, purple), and 9th (grey, grey) overtones for formation of a DOPC/DOPG (7:3) SLB followed by interaction with Tellimagrandin II (100 μM). Bilayer formation was ensured through osmotic shock after vesicle adsorption. The change in ΔF shows that the interaction at the bilayer surface was strong enough such that the Tel-II remained bound at the membrane surface under constant flow of buffer solution.	111
4.17	FTIR spectrum for a DOPC/DOPG (7:3) SLB before (blue) and after (orange) addition of Tel-I (100 μM), showing relevant sections to highlight the asymmetric (2920 cm^{-1}) and symmetric (2840 cm^{-1}) C-H stretching modes as well as the C=O stretching mode (1726 cm^{-1}). With the addition of Tel-I (100 μM) a peak appears at 1577 cm^{-1} along with an increase in the area under the peak at 1726 cm^{-1}	112
4.18	Plots to show the kinetics of interaction of Tel-I (100 μM) with the bacterial model DOPC/DOPG (7:3) membrane. The top panel (red) shows the small increases in the area under the peak at 1726 cm^{-1} corresponding the the ester groups in the lipid tails. The EGCg ester groups are thought to cause the increased peak area. For the feature that appears at 1577 cm^{-1} (blue) the aromatic C=C, C-H and C-OH are likely responsible.	113
4.19	QCM-D plots showing changes to both frequency and dissipation (ΔF , ΔD respectively) in the 3rd (red, green) 5th (orange, teal), 7th (yellow, purple), and 9th (grey, grey) overtones for formation of a DOPC/DOPG (7:3) SLB followed by interaction with Tellimagrandin I (100 μM). Bilayer formation was ensured through osmotic shock after vesicle adsorption. The change in ΔF shows that the interaction at the bilayer surface was strong enough such that the Tel-I remained bound at the membrane surface under constant flow of buffer solution.	114

4.20	Panels (A-D) showing neutron reflectivity profiles for data (points) and model fits (lines) for a COOH-SAM/Gold/Permalloy coated silicon substrate (green) with DOPC/DOPG (7:3) model membrane before (blue) and after (red) interaction with (-)-EGCg (100 μ M) in various contrasts. (E) Neutron SLD profiles showing the Si-Py-SAM-COOH underlayers (green) with DOPC/DOPG (7:3) bilayer both before (blue) and after (red) interaction with (-)-EGCg (100 μ M) solution in H ₂ O, gold and silicon matched water, and D ₂ O contrasts. The SLD profile (E) has been cropped to show membrane regions more clearly, leaving out the underlayers.	117
4.21	SLD plot for the DOPC/DOPG (7:3) model membrane system overlaid with a schematic illustration of the underlayers, SAM, and bilayer with EGCg interactions included. The amount of EGCg in the external layers reduces as the distance away from the membrane increases, leaving a less EGCg-dense, and more hydrated layer to match the tapering of the SLD profile into the bulk solution.	119
4.22	Panels (A-D) showing neutron reflectivity profiles for data (points) and model fits (lines) for a COOH-SAM/Gold/Permalloy coated silicon substrate (blue) with DOPC/DOPG (7:3) pre-mixed (doped) with (-)-EGCg (100 μ M) model membrane (red) in various contrasts. (E) Neutron SLD profiles showing the Si-Py-SAM-COOH underlayers (green) with DOPC/DOPG (7:3) bilayer both before (blue) and after (red) interaction with (-)-EGCg (100 μ M) solution in H ₂ O, gold and silicon matched water, and D ₂ O contrasts. The SLD profile (E) has been cropped to show membrane regions more clearly, leaving out the underlayers.	120
4.23	SLD plot for the DOPC/DOPG (7:3) model membrane system doped with EGCg (100 μ M) overlaid over a schematic illustration of the underlayers, SAM, and bilayer with intercalated EGCg. The inclusion of EGCg in the tail region corresponds to a thicker tail group compared to the either the lipid only bilayer or the bilayer after interaction with EGCg from solution.	122
4.24	Panels (A-C) showing neutron reflectivity profiles for data (points) and model fits (lines) for a COOH-SAM/Gold/Chromium coated silicon substrate (green) with DOPC/DOPG (7:3) model membrane before (blue) and after (red) interaction with Tel-II (100 μ M) in various contrast solutions. (D) Neutron SLD profiles showing the Si-Cr-Au-SAM-COOH underlayers (green) with DOPC/DOPG (7:3) bilayer both before (blue) and after (red) interaction with Tel-II (100 μ M) solution in H ₂ O, gold and silicon matched water, and D ₂ O contrasts. The SLD profile has been cropped to show membrane regions more clearly, leaving out the underlayers.	124

4.25	Neutron SLD profile overlaid on a diagrammatic representation of the 4 membrane regions of decreasing coverage. Tel-II is depicted both in the membrane regions and in the solution layers moving towards and in the bulk solution. Consecutive membranes show decreasing bilayer coverage moving away from the Si interface. Values output from the fitting are shown in table 4.10. SLD profile has been cropped to the membrane region of interest leaving out the underlayers.	126
5.1	(a) Flow diagram that summarising the method for the selection of relevant articles to be included in the data set collected for lipid headgroup composition of epithelial membranes. (b) Schematic showing how search terms were combined between lists using both AND and OR Boolean operators.	139
5.2	Chart displaying the number of lipids reported per publication as a percentage.	140
5.3	Stacked bar plot representing the number of publications for a given year as a result of the search term ‘lipid composition’. Colouring within the bars represents the total number of publications in a given filter term used to refine the overall ‘lipid composition’ search. The smaller coloured bars are included within the total count and form part of the blue bars. The date range for the publication rate spans from the earliest date allowed by the search engine, 1970, until writing of the manuscript started in Feb 2020. It is likely that publications after Feb 2020 would have contributed to a larger value for that particular bar.	142
5.4	Values of overall mean lipid content taken from the studies found as a result of the initial literature search in Web of Science (n = 54). These percentages represent the proportion of lipids present in all membranes irrespective of origin or type. Numerical values for the mean are presented along with their standard deviation. Numerical values for the results shown here can be found in 5.1.	143
5.5	Plot displaying mean compositional data for intestinal studies obtained from the systematic review search for articles that pertained to intestinal tissues (n = 18), epithelial samples (n = 22), and samples that related to the human GIT epithelium (n = 10). Values are presented as relative means \pm SEM and can be found numerically in table 5.2.	145
5.6	Figure showing the mean relative percentage lipid compositions of the human GIT epithelium (blue, n=10), the human erythrocyte membrane (orange, n=9), and a bacterial outer membrane (green, n=21). The GIT and erythrocyte membranes are compared according to the common lipid species that are contained within the respective membrane, while all the lipid species taken from the bacterial membrane search are shown. Numerical values for the data presented here can be found in tables 5.2, 5.3 and 5.4.	147

5.7	Grouped bar chart showing mean lipid composition that varies by sample environment as well as species. Lipid environments are compared according to common lipid types. It should be noted that the animal GIT value for PG has no error bar because there is only value reported. Values are given as mean relative percentage with their associated SEM values.	150
5.8	Box and whisker plots displaying the spread of data for each lipid available from the results of the literature search. The red line represents the median value with the edges of the box showing the 25th and 75th percentiles. Data points that are outliers are represented using the red '+' marker.	151
5.9	Scatter plot showing year of publication for lipid data relating to PC headgroup containing lipids. Mean value (black line), 1 and 1.5 x standard deviation (solid red and dashed red lines respectively) are shown for data points taken from the systematic literature search.	152
5.10	Scatter plots showing the spread of the relative percentages of lipid head groups taken from the systematic literature search. Mean value (black line), 1 and 1.5 x standard deviation (solid red and dashed red lines respectively) are shown and data points are grouped by their year of publication. The colour scheme for this figure is the same as for figure 5.9.	153
5.11	Scatter plot showing the relative percentages of cholesterol and sphingomyelin to understand if the presence of one membrane component can be used as a predictor of the other. A simple linear regression ($R^2=-0.023$) shows that cholesterol content cannot be used as a predictor of sphingomyelin amount within a membrane.	154
6.1	Skeletal structure of egg sphingomyelin as used for the epithelial model membrane samples.	168
6.2	FTIR spectrum for a DOPC/DOPE/SM (6:3:1) SLB before (blue) and after (orange) addition of (-)-EGCg (100 μM), showing regions of interest highlighting the asymmetric (2920 cm^{-1}) and symmetric (<i>ca.</i> 2840 cm^{-1}) C-H stretching modes as well as the C=O stretching mode (<i>ca.</i> 1720 cm^{-1}), as well as a peak assigned to the amide moiety from the sphingomyelin headgroup at 1620 cm^{-1} . With the addition of (-)-EGCg there is an increase in the area under the broad feature between 1550 at 1740 cm^{-1} showing the interaction with the model membrane is persistent under solution flow.	170

6.3	FTIR spectrum for a DOPC/DOPS/Chol/SM (5:2:2:1) SLB before (blue) and after (orange) addition of (-)-EGCg (100 μM), showing regions of interest highlighting the asymmetric (2930 cm^{-1}) and symmetric (<i>ca.</i> 2850 cm^{-1}) C–H stretching modes as well as the C=O stretching mode (<i>ca.</i> 1720 cm^{-1}), as well as a peak assigned to the amide moiety from the sphingomyelin headgroup at 1610 cm^{-1} . With the addition of (-)-EGCg there is an increase in the area under the broad feature between 1550 at 1730 cm^{-1} showing the interaction with the model membrane is persistent after substantial washing of the membrane surface.	171
6.4	QCM-D plots showing changes to both frequency and dissipation (ΔF , Δd respectively) in the 3rd (red, green) 5th (orange, teal), 7th (yellow, purple), and 9th (grey, grey) overtones for formation of a DOPC/DOPS/Chol/SM (5:2:2:1) SLB followed by interaction with (-)-EGCg (100 μM). Bilayer formation was ensured through osmotic shock after vesicle adsorption (stage 2). The change in ΔF shows that the interaction at the bilayer surface was strong enough such that the (-)-EGCg remained bound at the membrane surface under constant flow of buffer solution (stage 4).	172
6.5	Panels (A-C) showing neutron reflectivity profiles for data (points) and model fits (lines) for a COOH-SAM/Gold/Chromium coated silicon substrate (green) with DOPC/DOPS/Chol/SM (5:2:2:1) model membrane before (blue) and after (red) interaction with Tel-II (100 μM) in various solution contrasts. (D) Neutron SLD profiles showing the Si-Cr-Au-SAM-COOH underlayers (green) with DOPC/DOPS/Chol/SM (5:2:2:1) bilayer both before (blue) and after (red) interaction with Tel-II (100 μM) solution in H_2O , gold matched water (AuMW), and D_2O contrasts. The SLD profile has been cropped to show membrane regions more clearly, leaving out the underlayers.	174
6.6	Neutron SLD profile overlaid on a cartoon of the model epithelial membrane composed of DOPC/DOPS/Chol/SM (5:2:2:1). The schematic shows the variable regions of Tel-II thickness external to the bilayer along with the large amount of intercalation within the membrane. Values output from the fitting are shown in table 6.1. SLD profile has been cropped to the membrane region of interest leaving out the underlayers.	176
6.7	Panels (A-C) showing neutron reflectivity profiles for data (points) and model fits (lines) for a COOH-SAM/Gold/Chromium coated silicon substrate (green) with DOPC/DOPS/Chol/SM (5:2:2:1) model membrane before (blue) and after (red) interaction with Tel-I (100 μM) in various solution contrasts. (D) Neutron SLD profiles showing the Si-Cr-Au-SAM-COOH underlayers (green) with DOPC/DOPS/Chol/SM (5:2:2:1) bilayer both before (blue) and after (red) interaction with Tel-I (100 μM) solution in H_2O , gold matched water (AuMW), and D_2O contrasts. The SLD profile has been cropped to show membrane regions more clearly, leaving out the underlayers.	177

6.8	Neutron SLD profile overlaid on a cartoon of the model epithelial membrane composed of DOPC/DOPS/Chol/SM (5:2:2:1). The schematic shows the variable regions of Tel-I thickness moving from the outside of the membrane towards the bulk solution. Values output from the fitting are shown in table 6.2. SLD profile has been cropped to the membrane region of interest leaving out the underlayers.	179
6.9	ATR-FTIR spectrum for model DOPC/DOPS/Chol/SM (5:1:2:2) membrane before (blue) and after (orange) interaction with (-)-EGCg (100 μ M). Symmetric and asymmetric C–H stretching modes, at 2850 and 2930 cm^{-1} respectively, remain unchanged after the interaction. Area under the features at 1580-1620 cm^{-1} increase in intensity after the interaction due to the presence of aromatic C–O and C–C stretching at the interface.	182
6.10	ATR-FTIR spectrum for model DOPC/DOPS/Chol/SM (5:1:2:2) membrane before (blue) and after (orange) interaction with Tel-II (100 μ M). Symmetric and asymmetric C–H stretching modes, at 2825 and 2910 cm^{-1} respectively are unaffected by the addition of Tel-II. Area under the features at 1560-1650 cm^{-1} increase in intensity after the interaction due to the presence of aromatic C–O and C–C stretching at the membrane surface.	183
6.11	Panels (A-C) showing neutron reflectivity profiles for data (points) and model fits (lines) for a COOH-SAM/Gold/Chromium coated silicon substrate (green) with DOPC/DOPS/Chol/SM (5:1:2:2) model membrane before (blue) and after (red) interaction with Tel-II (100 μ M) in various solution contrasts. (D) Neutron SLD profiles showing the Si-Cr-Au-SAM-COOH underlayers (green) with DOPC/DOPS/Chol/SM (5:1:2:2) bilayer both before (blue) and after (red) interaction with Tel-II (100 μ M) solution in H ₂ O, gold matched water (AuMW), and D ₂ O contrasts. The SLD profile has been cropped to show membrane regions more clearly, leaving out the underlayers.	184
6.12	Neutron SLD profile overlaid on a cartoon of the model epithelial membrane composed of DOPC/DOPS/Chol/SM (5:1:2:2). The schematic shows the variable regions of Tel-II thickness moving from the outer leaflet of the membrane towards the bulk solution. Values output from the fitting are shown in table 6.2. SLD profile has been cropped to the membrane region of interest leaving out the underlayers.	186

List of Tables

3.1	Mean transition temperatures for the individual lipids and ideal plus non-ideal lipid mixtures along with associated standard deviation (S.D.) and standard error (S.E.) values.	71
3.2	FTIR peak assignments for aliphatic lipid regions as well as H ₂ O and D ₂ O from the buffer. <i>ss</i> - symmetric stretch; <i>as</i> - asymmetric stretch	72
3.3	Parameter values and error bounds (upper bound, lower bound) for key parameters from the fitting and error estimation routines for a DOPC/DOPG (7:3) model bacterial floating membrane. . .	76
4.1	Summary of changes to DSC thermograms upon polyphenol addition, along with associated causes for temperature shifts in lipid samples.	90
4.2	Transition temperatures for non-ideal DPPE/DPPG (3:2) + PGG. Associated standard deviation values and standard error of the mean values are also given.	91
4.3	Transition temperatures for ideal DPPE/DPPG (3:2) + EGCg. Associated standard deviation values and standard error of the mean values are also provided.	92
4.4	Transition temperatures for non-ideal DPPE/DPPG (3:2) + EGCg. Associated standard deviation values and standard error of the mean values are also provided.	94
4.5	Transition temperatures for non-ideal DPPE/DPPG (3:2) + Tellimagrandin II. Associated standard deviation values and standard errors of the mean are also given.	97
4.6	Transition temperatures for DSC thermograms of non-ideal DPPE/DPPG (3:2) + Tellimagrandin I interactions. Associated standard deviation values and standard errors of the mean are also given.	97
4.7	Table of values for logP, DSC transition temperature shift for each lipid component, number of free galloyl groups and molecular area of each of the polyphenols investigated for lipid interactions with DSC calorimetry. ^a taken from the highest lipid:polyphenol concentration sample. ^b Molecular area estimated using the Chemdraw Professional (v20.0.0.41) molecular area tool.	100

4.8	Parameter values and error bounds (upper bound, lower bound) for key parameters from the fitting and error estimation routines for the DOPC/DOPG (7:3) model bacterial membrane before and after interaction with EGCg (100 μ M). Parameters with no associated error bounds have been derived from the appropriate SLD profiles.	118
4.9	Parameter values and error bounds (upper bound, lower bound) for key parameters from the fitting and error estimation routines for the DOPC/DOPG (7:3) model bacterial membrane before and after interaction with EGCg (100 μ M) and a pre-mixed with EGCg (100 μ M). Parameters with no associated error bounds have been derived from the appropriate SLD profiles. The values from table 3.3 have been repeated here for convenience.	121
4.10	Values and error bounds (upper bound, lower bound) for key parameters from the fitting and error estimation routines for the DOPC/DOPG (7:3) model bacterial membrane before and after interaction with Tel-II (100 μ M) and a pre-mixed with EGCg (100 μ M). Parameters with no associated error bounds have been derived from the appropriate SLD profiles.	125
5.1	Values that accompany the plot shown in figure 5.4 for the overall mean lipid headgroup composition as averaged from all 54 articles that were output from the systematic search. Values are given as rel% and quoted alongside are the SEM and standard deviations of the mean.	144
5.2	Comparison of the lipid compositions of samples taken from the literature study conducted as outlined above. Data below is from the total 54 articles found, and divided into subsets related to intestinal (n = 18), epithelial (n = 22), and human GIT epithelial samples (n = 10) to accompany the plots show in figure5.5. Values are given as rel% and quoted alongside are the SEM and standard deviations of the mean.	146
5.3	Lipid composition of the bacterial outer membrane (n=21), as shown in figure 5.6 to highlight how individual lipid abundance compares to both the human GIT epithelium and human erythrocyte membrane. Values are given as mean relative % \pm SEM, and shown with the standard deviations.	148
5.4	Lipid composition of the human erythrocyte membrane (n=9), as shown in figure 5.6 to highlight how individual lipid abundance compares to both the human GIT epithelium and human erythrocyte membrane. Values are given as mean relative % \pm SEM, and shown with the standard deviations.	149
6.1	Table of values for some key parameters from fits for DOPC/DOPS/Chol/SM (5:2:2:1) model membrane before and after interaction with Tel-II. Errors are taken from Bayesian error estimation routines as an output of the fitting of the experimental data. Parameters with no associated error bounds have been derived from the appropriate SLD profiles.	175

6.2	Table of values for some key parameters from fits for DOPC/DOPS/Chol/SM (5:2:2:1) model membrane before and after interaction with Tel-I. Error values are from Bayesian error estimation routines as an output of the fitting of the experimental data. Parameters with no associated error bounds have been derived from the appropriate SLD profiles.	178
6.3	Values for some key structural properties for Tel-I and Tel-II. These values are linked to their membrane interaction results from NR and SLB data. ^a Molecular area estimated using the Chemdraw Professional (v20.0.0.41) molecular area tool; ^b Interaction with DOPC/DOPS/Chol/SM (5:2:2:1) model; ^c Interaction with DOPC/DOPS/Chol/SM (5:1:2:2) model	180
6.4	Table of values and error bounds (lower bound, upper bound) for some key parameters from fits for DOPC/DOPS/Chol/SM (5:1:2:2) model membrane before and after interaction with Tel-II. Error values are from Bayesian error estimation routines as an output of the fitting of the experimental data. Parameters with no associated error bounds have been derived from the appropriate SLD profiles.	185
A.1	Full list of parameters for the fitting of the DOPC/DOPG (7:3) model bacterial membrane with addition of EGCg (100 μ M) as shown in figure 4.21. Values are given with their associated limits beyond which the model was not permitted to step when finding best fits parameters.	199
A.2	Full list of parameters for the fitting of the DOPC/DOPG (7:3) model bacterial membrane with addition of EGCg (100 μ M) as shown in figure 4.23. Values are given with their associated limits beyond which the model was not permitted to step when finding best fits parameters.	200
A.3	Full list of parameters for the fitting of the DOPC/DOPS/Chol/SM (5:2:2:1) model epithelial membrane with addition of Tel-II (100 μ M) as shown in figure 4.25. Values are given with their associated limits beyond which the model was not permitted to step when finding best fits parameters.	201
A.4	Full list of parameters for the fitting of the DOPC/DOPS/Chol/SM (5:2:2:1) model epithelial membrane with addition of Tel-II (100 μ M) as shown in figure 6.6. Values are given with their associated limits beyond which the model was not permitted to step when finding best fits parameters.	203
A.5	Full list of parameters for the fitting of the DOPC/DOPS/Chol/SM (5:2:2:1) model epithelial membrane with addition of Tel-II (100 μ M) as shown in figure 6.8. Values are given with their associated limits beyond which the model was not permitted to step when finding best fits parameters.	204

A.6	Full list of parameters for the fitting of the DOPC/DOPS/Chol/SM (5:1:2:2) model epithelial membrane with addition of Tel-II (100 μ M) as shown in figure 6.12. Values are given with their associated limits beyond which the model was not permitted to step when finding best fits parameters. . . .	205
A.1	Table summarising experimental conditions for some bacterial membrane interaction studies that showed non-optimal conditions or results, and that ultimately were deemed not suitable for neutron reflectometry samples.	208
A.2	Table summarising experimental conditions for some epithelial membranes and interaction studies that showed non-optimal conditions or results, and that ultimately were deemed not suitable for neutron reflectometry samples.	209

—*The low entropy of the past
renders the notion of cause an
effective one.*

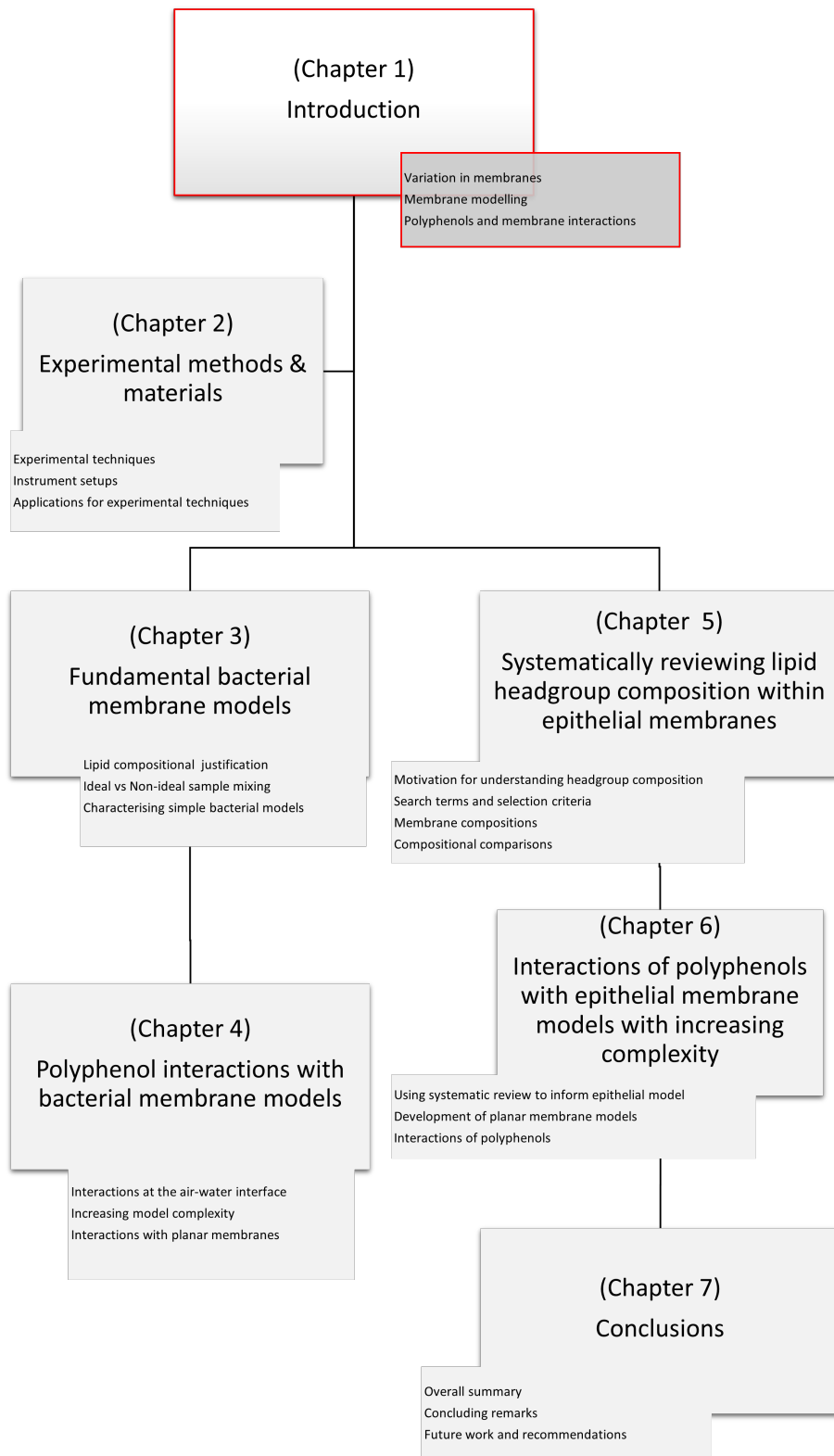
Carlo Rovelli

1

Introduction

Contents

1.1	Lipids and Membrane Architecture	24
1.1.1	Biological Membrane Structure and Function	25
1.2	Variation in Membranes	28
1.3	Reviewing Current Membrane Modelling Techniques	29
1.4	Polyphenols and their Membrane Interactions . . .	34
1.5	Aims and Objectives	36



The cell membrane is an immensely complex structure. Almost 50 years from the inception of the fluid mosaic model, it is still held as a pillar of cell surface science [1]. An understanding of how cell membranes operate at a fundamental level has driven scientific advances for decades. This understanding has been developed using a wide variety of techniques in order to provide information about the membrane in terms of how it functions and interacts with its surroundings. It has been understood for some time that the structure of a lipid bilayer is complex and plays an important role in how the cell membrane functions [2, 3]. Membrane environments are considered to be dominated by glycerophospholipids that are typically supplemented with a diverse range of sphingolipids, sterols, proteins and carbohydrates [4]. Due to the rich diversity found in membranes they can be characterised based on any number of components, structural features, or functions [5]. The lipid diversity within membranes is not well understood, and there are questions that remain unanswered in terms of how lipid headgroup, tail length, and saturation are regulated. Further, mechanisms behind how membrane polarity is established as well as the ratios of lipid headgroups are unclear [6]. Cells spend up to 5% of their genetic information on the synthesis of lipids, which is a staggeringly large amount of genetic code for a such a relatively small portion of the cell architecture, given that the cell membrane is on the order of 30 Å thick. The implications for this are that cell membrane headgroup composition is vitally important, and that cells have a large dependence upon a highly complex catalogue of lipids [7].

1.1 Lipids and Membrane Architecture

There are many components that contribute towards membrane architecture. Historically, lipids have been structurally defined by a hydrophobic portion (tails) and a hydrophilic portion (headgroups) [8]. This simple definition is not inclusive of many lipid types and so a more rigorous nomenclature has been developed including fatty acids, glycerolipids, glycerophospholipids, sphingolipids, and sterol lipids among others [9]. Some of the most common, and in particular those that have a large role in structure, are outlined in figure 1.1. Triacylglycerols form the largest fractions of mammalian fats and are also found within the blood. Crudely, they are made up of a glycerol-derived skeleton that has attached three hydrocarbon based fatty acid groups.

Glycerophospholipids are structurally very similar to triacylglycerols as they have a glycerol based backbone. In the case of glycerophospholipids however, one of the fatty acid tails is replaced by a phosphate linked head group. The headgroups and tails have a large amount of crossover between mammalian and bacterial membranes, likely because they are effective and the task they are performing. The length of the hydrocarbon tail, coupled with the degree of saturation, is what determines the transition temperature of a lipid. This has an impact on the state of the lipid at any given temperature or pressure, which influences how the lipids pack together [10, 11]. Sphingolipids differ from phospholipids in terms of their headgroup base: a sphingoid base rather than glycerol. The tails of sphingolipids are on the whole longer and

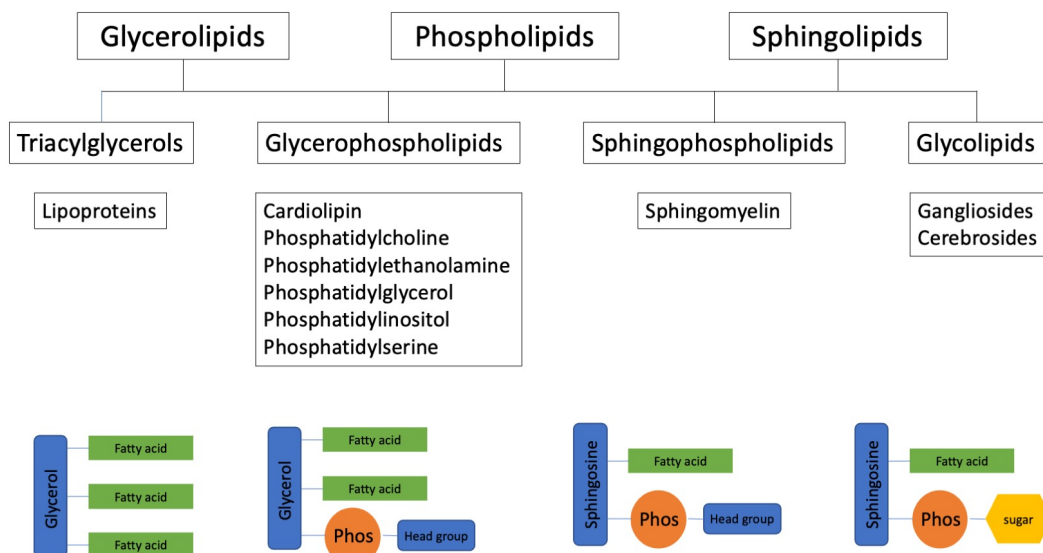


Figure 1.1: Depiction of lipid classes, along with categorical examples of each class and a simplified schematic representation.

more saturated compared to other membrane species which manifests in higher transition temperatures and tighter packing geometries [12]. There is also evidence to show that the difference between how phospholipids and sphingolipids chain packing is involved in the formation of discrete membrane domains that contribute towards lateral heterogeneity [13]. Further, the formation of heterogeneous membrane portions by these different lipid types helps regulate lipid rafts even though it remains a topic of some controversy [14].

Glycolipids are similar to sphingolipids in that they share the same base. Their unique feature being a glycosidic carbohydrate that can be either N-linked or O-linked [15]. In terms of role they also take part in cell recognition and signalling, as well as providing the membrane with some structural stability [16]. Historically, a single lipid species was considered to dominate the membrane environment and that other lipids were only present in much smaller quantities for very localised functions. In fact, the case is that variety is more spread throughout the membrane [17, 18]. Once derivatised phospholipids can become differently distributed throughout the membrane to contribute to different functional roles [19]. Figure 1.2 shows the structures of some of the common cellular phospholipids. They all possess a glycerol based skeleton and an R-group that in reality would be where the long hydrocarbon fatty acid tail resides. Shown in blue are the headgroup regions which are linked to the glycerol via a phosphate ester.

1.1.1 Biological Membrane Structure and Function

The bilayer is required to be sturdy enough to act as a barrier between the intra- and extracellular environments, while still allowing transport and exchange of

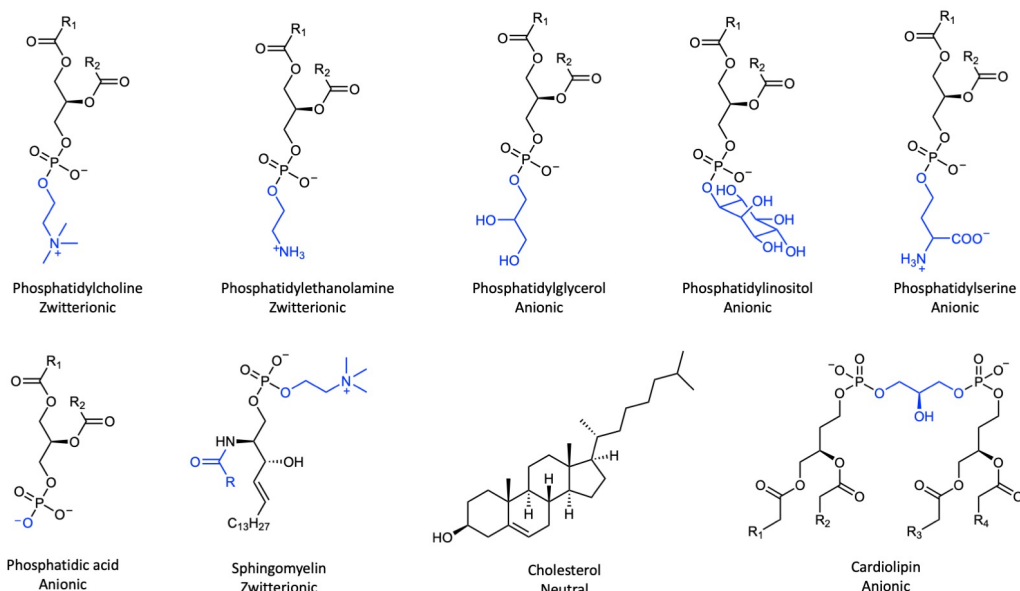


Figure 1.2: Structures of some common membrane lipids. Head groups are shown in blue and are phosphate bound. The glycerol-derivative backbone is also shown along with the positions of the R-groups that can vary in length and saturation.

substances across it [20]. Lipids within the bilayer serve as a solvent for the embedded proteins and carbohydrates, whilst also controlling the short and long range order within the membrane (i.e. lateral heterogeneity) [21]. The interactions between proteins and lipids in the cell membrane provide a number of vital functions. Together they regulate, tune and actuate various cellular pathways and activities. Membrane attached carbohydrates are key in cell signalling and recognition through interactions with other carbohydrates and proteins [22].

It is well understood that the cell membrane takes the form of a bilayer. It has two leaflets of lipids that present their hydrophilic headgroups to the water facing portion of the membrane, while the tail groups of either leaflet face each other creating a hydrophobic core: While the layer is dynamic and fluxional, it maintains a condensed state [23]. Proteins are scattered across the membrane surface and can either be associated only to the headgroups, termed ‘peripheral proteins’, or can pass all the way through the membrane. The latter are known as ‘integral proteins’ [24]. Integral proteins are one means by which the membrane facilitates transport of substances. Carbohydrates too are complex biological molecules that are ubiquitous in their presence at the cell surface, having many important roles themselves [22].

Within membranes, composition is extremely complex and incredibly varied. The structure of the lipid membrane is dependent on the lipids they contain in terms of how they fit together and whether they are bilayer forming types [25]. A primary function of the membrane structure is lipids’ role as a medium within which membrane proteins can be situated [21]. In addition to providing

a barrier, further roles of membrane lipids include provision of a surface for interfacial signalling reactions to take place, and regulating the structure of the surface [26]. The ability of lipids to self-assemble in a non-random fashion allows cell surface structures to have order both across the bilayer and in the lateral plane [27]. The shape and degree of curvature in a membrane is dynamic and is dictated to a large extent by the geometry of individual lipid molecules. Lipids with a headgroup larger than the footprint of the tails will induce 'positive' curvature, while larger tail footprints than headgroup size will result in 'negative' curvature. Naturally, if a lipid headgroup and tail have equivalent relative footprints then this will not have an effect on curvature [23]. The effect of various lipids on the overall shape of the membrane has been understood for some time and are well reported [6, 28, 29].

One of the chief functions of the headgroup of a lipid is to allow the membrane to solubilise in aqueous environments. Some of the most common headgroup structures are shown in figure 1.2, where it can be seen that structurally the headgroups contain a lot of heteroatoms that contribute to their polarity. These polar heteroatoms enable them to interact with water in the extracellular environment through hydrophilic interactions and allows van der Waals forces between the hydrocarbon tails to be maximised [30]. Both of these effects provide stability, which contributes to the membrane persisting as a long-term structural component.

The tail region is responsible for much of the intrinsic order found in the bilayer core, with hydrocarbon saturation being one of the key regulating factors. [3]. The configurations of the tails, along with the presence of one or more C=C double bonds, affects the ability of the lipids to pack together tightly through constraining the tails as they undergo trans-gauche isomerisation [31]. A less tightly packed lipid environment leads to a more fluxional and dynamic layer which in turn will help to promote movement and transport across the hydrophobic region.

The combined effects of both the tail and headgroups influence the membrane structure in the lateral plane. Evidence shows that the lateral order within the bilayer has an impact in turn on how other species interact with the membrane, often with them taking lead and following the lateral order that has been imparted by the lipids in a non-random way. As a result, the nature of the membrane is that it is dynamic and fluxional on time-scales $> 1s$, and because of this it can often be difficult to probe and understand on an atomic level [27, 32]. Further, the impact of lipids across the membrane are observed in domain formation; localised regions of lipids that prefer to reside in self-contained clusters of like-lipids. Such an effect is termed *lateral heterogeneity* and is relatively well understood [27, 33, 34]. These local lipid domains have an effect on various physical properties of the membrane such as rigidity, compressibility, and sites of preferential interactions, as well as on transport through the membrane. By forming areas of composition that are not an ideal mixture of lipids, it is reported that there are levels of compartmentalisation and differentiation across the surface [35].

This understanding that incorporates membranes being separated into distinct domains has been around for some time, and is quite well researched as an area [21]. It can be said that membranes in all their forms contain largely the same lipid specimens, but the ratio of the lipids between membranes can be highly variable and is one way in which membranes differentiate themselves [36]. A foundation of lipid domain composition is that different phases of lipids can coexist within the two-dimensional liquid environment present in the membrane [37]. While lipid rafts remain an area of some controversy, there is evidence to show that there is domain formation in epithelial cells between the lumen-facing portion and the tissue-facing part of the cell [38]. The chemical basis for domain formation is laid out elsewhere; briefly varying the lipid and cholesterol composition of membranes results in altered liquid-disordered and liquid-ordered domains of the membrane through altered transition temperatures. The phase and rigidity effects are responsible for making different portions of the membrane more or less fluid and thus are termed phase separated [12]. There is also reasonable evidence pointing towards the lipid organisation in a membrane acting as a basis for deeper organisation [14].

1.2 Variation in Membranes

Variation in phospholipid composition is observed across membranes as they vary by type, and is to a large extent dependant on species, function, and factors such anatomical geography. There are also estimates that cite phosphatidylcholine (PC) accounting for greater than 50% of the lipids within eukaryotic membranes [7]. One of the hypotheses of this work is to understand lipid composition more accurately so that it can be better represented within model membranes, and is a topic of deeper exploration in the results sections of this thesis.

Epithelial membranes are those that cover anatomical surfaces, for example those lining the lungs or the gastro-intestinal tract. Like other mammalian membrane types they contain a broad variety of lipids, as shown by the structures outlined in figure 1.2, that each have an impact on the membrane. Mammalian membranes are, for the most part, cholesterol rich [39]. Cholesterol is responsible for regulating the rigidity of the membrane, and as the fluidity demands of the layer change, commonly so too will the cholesterol composition [40–42].

Epithelial cells are often characterised by having two separate membrane portions. The lumen facing aspect of the cells is described as *apical*, with the tissue facing surface being termed *basal*. Further, there are separators between two adjacent cells called *tight junctions* that form a tight seal and prevent movement of substances through the trans-cellular space [43]. The basolateral domain is involved in connecting neighbouring cells, as well as underlying tissues, with tight junctions being one of the mechanisms by which the apical and basal portions are kept distinct [44]. One of the properties of heterogeneous lipid domains is in controlling how additives (nutrients, pharmaceuticals,

proteins, native biological compounds etc.) interact and bind with differentiated domains of the bilayer [27].

The apical membrane is the exposed portion of the membrane interface and as such can be subject to harsh biological conditions, be it extreme pH in the stomach or extremes of the gastro-intestinal tract, osmotic pressures, or experience large electric potentials in the myocardium [45]. It tends to be the case that such membrane portions having relative increased levels of cholesterol and sphingomyelin that act to stabilise the membrane [39]. Balancing this level of protection with the need to be so adaptive to absorption and transport is not trivial, and remains an area of investigation. Evidence also suggests that the polarity between the different parts of the epithelial surface is maintained by proteins, with polarisation taking place alongside other structural changes to the layer [46].

Domains are not exclusive to mammalian membranes. Bacterial membranes also show heterogeneity in their composition and variety of species within the bilayer. Bacterial membranes are commonly found to have cardiolipin-rich domains and as with mammalian membranes it has been the focus of various research strands to understand the properties of these domains [47]. It is thought that the clustering of electrically charged lipids also has an impact on lipid domain formation in bacteria. Bacterial membranes are separated into two different classes, with their membrane organisation being a feature that significantly differs between the two.

Gram-positive bacteria only have a single cytoplasmic membrane that is structurally supported by an external peptidoglycan layer, and are understood to contain mainly anionic lipids. Gram negative bacteria have both an inner cytoplasmic membrane surrounding the cell contents and an outer membrane that contain predominantly zwitterionic lipid species [48, 49].

1.3 Reviewing Current Membrane Modelling Techniques

Lipid studies that are focused on membranes and the understanding and replication of their behavior has a wide variety of applications [20]. Given that biological function is intrinsically linked to structure, it is imperative that structures are understood on atomic scales. Only then can enabling steps towards understanding how these structures are important on a wider scale be implemented [50]. Model membranes are a useful tool in investigating how pharmaceutical, medicinal and nutraceutical compounds interact with a model layer [51]. As with any model, it is important that the model membranes attempt to describe their real world counterpart as far as is possible. However, greater accuracy often comes at a cost; as accuracy increases, so too does complexity. Increasing complexity should be carefully considered, with balance being the aim between having a simple enough model that it can be well controlled and understood, while being developed sufficiently that it simulates the necessary system under investigation.

Where studying membranes and their models is concerned, there is a variety of techniques available that cover all manner of length scales, with each providing a unique perspective on the different aspects of the membranes. Figure 1.3 shows various membrane types that are useful as model membranes, each providing insight on different aspects of membrane architecture. Micelles are capable of providing an environment for understanding the ordering of bilayers, and have been used to understand how altering the sample environment conditions might change the physico-chemical properties of the micelle [52]. If membrane specific lipids are used to construct the micelles then information can be obtained about the bilayer environment and how it can be changed to changes to the surrounding medium. Lipid monolayers are appropriate methods of study for individual lipid leaflets at the air-water interface. Vesicles and bilayers both provide opportunities for studying membranes in their *in vivo* geometry, and are critical tools in understanding membrane component dynamics. Moreover they can be assembled to display asymmetry and manipulated to probe different membrane properties spanning a wide range of complexity. The remainder of this section provides more detail for various types of membrane models and gives some insight into the current state of the techniques involved.

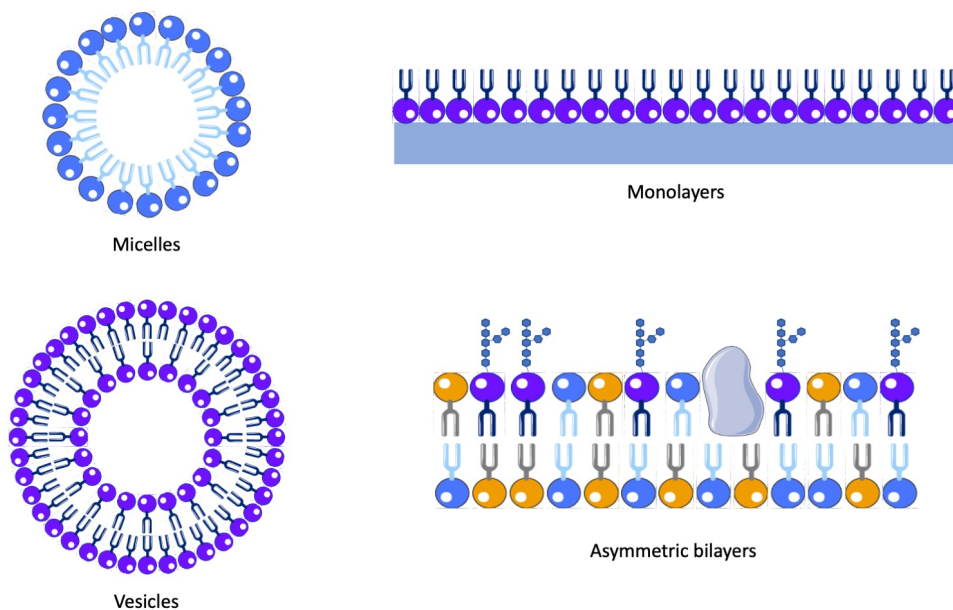


Figure 1.3: Schematics of some typical methods for physical membrane modelling systems and for observing their interactions; Top left – micelles, typical of surfactants and other hydrophobic molecules when introduced to an aqueous environment. Top right – monolayers, very common set-up for Langmuir–Blodgett type experiments for measuring lipid surface pressure and tension. Bottom left – vesicles, these can adopt a large size regime and are frequently used to mimic simple bilayer interactions when formed with lipids. Bottom right – asymmetric bilayers, complex layer formation is taking centre stage in many surface sensitive techniques as they become more accurate and complex.

Langmuir troughs using monolayers played a large part during the formative understanding of lipid behaviour at the air-water interface, including helping to understand some of their most basic physical properties [53]. Experiments using monolayers are beneficial for obtaining information on molecular area and understanding phase behaviour, as well as basic interactions taking place at an interface [54]. In its simplest form, experiments involve measuring surface pressure, π , as a function of area, A , by spreading the lipid in the 2-dimensional gas phase and compressing the area available to the lipid while taking regular readings of the surface pressure. Measurement of the surface pressure at the air-water interface is commonly performed using the Wilhelmy plate method [55]. Using a monolayer the composition of the layer as well as the compression of the material at the surface can be tightly controlled [56]. As well as investigating the individual lipid monolayer components interaction studies can also be performed to understand how the nature of the monolayer changes with the addition of external compounds [57, 58]. Only having one half of a bilayer present for study presents some barriers to investigating certain membrane processes such as lipid flip-flop or bilayer diffusion [59, 60]. Despite its drawbacks, monolayer experiments remain a useful technique that can be used to complement data from other methods.

Another technique that is useful for understanding lipid phases is differential scanning calorimetry (DSC). It is a technique that can be applied to a range of sample morphologies - vesicles (both uni- and multilamellar), multi-bilayer stacks etc. [50]. DSC is useful for probing the phase of the lipid based on a temperature profile of the sample. Lipid phase information from DSC also gives details how well mixed lipid samples are, and also on specific headgroup or hydrocarbon tail interactions [61]. Broadly, lipids can exhibit different phase behaviours depending upon their temperature. Examples of different lipid phases are given in figure 1.4, where the orientation of both the individual lipids and the membranes is shown to change as the sample passes through the transition temperature.

Below the transition temperature T_m , the lipid behaves more as a solid and is described as the *gel phase*. As the lipid passes through the T_m they melt through a *ripple phase* and become more liquid-like. Once in the liquid phase, the lipid molecules are more mobile in the plane of the membrane. DSC is also a useful method for studying biological interactions with lipid membranes [62]. Interactions can be monitored through changes before and after substances are introduced into the membrane environment to understand how the thermal phase transition of the lipid is altered [63].

Fourier transform infrared (FTIR) spectroscopy is a powerful tool for the detection functional chemical groups present at an interface. Analysis of membranes at the solid-liquid interface has been carried out and is capable of showing not only membrane formation and phase states, but also detect emerging changes in a sample environment over time [64, 65]. In the context of this thesis silicon substrates were used for deposition of membranes during FTIR measurements [66]. The FTIR range of interest allows observation of

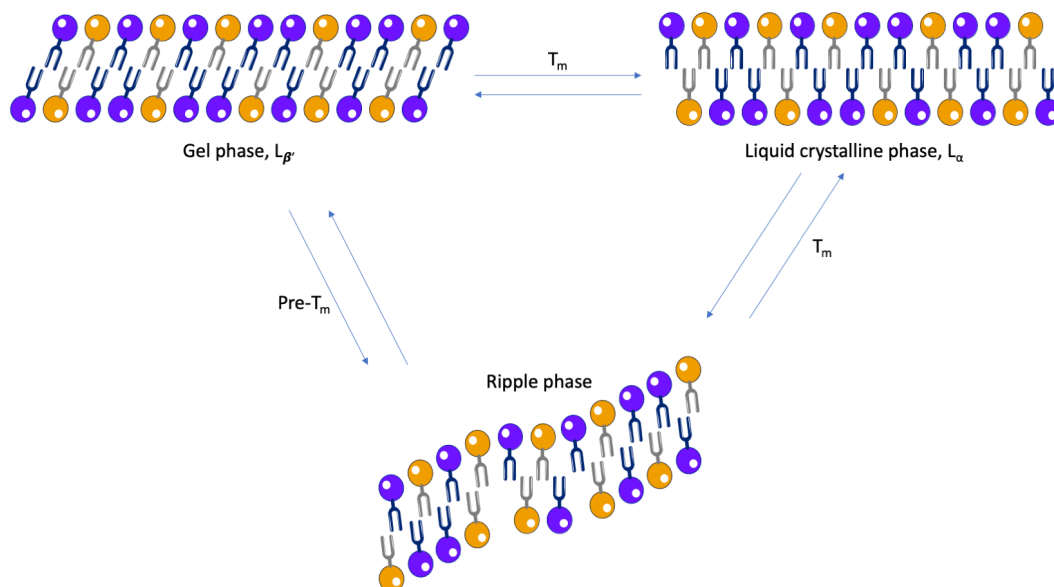


Figure 1.4: Lipid phases within a bilayer, with a schematic representation of how tail chains and headgroups are oriented as the sample passes through the transition temperature.

functional groups and aliphatic chains and falls between *ca.* 1500 - 4000 cm^{-1} [67]. This allows observation of the phosphorous-containing components of the lipids as well as the C-H containing tails. It is common for FTIR experiments involving biological molecules to be carried out in D_2O in order to better observe the amide I region (*ca.* 1645 cm^{-1}) as the H_2O and amide I regions overlap [68]. Using D_2O based solutions allows resolution of some spectral features from the bulk solution signal, by observing changes to the spectra of the membrane before and after interactions at the solid-liquid interface.

Quartz crystal microbalance with dissipation monitoring (QCM-D) is a surface sensitive method for investigating properties and interactions at an interface [69]. The information contained within a QCM-D measurement allows real-time determination of mass and thickness of a film deposited on a substrate and is appropriate for determining how target compounds interact with mimetic biological surfaces in an aqueous environment, as well as being a platform for the development of membrane modelling [70–72]. In the case of investigating model membranes and the bioactivity of different compounds QCM-D experiments show 3 different portions: 1) vesicle adherence to the surface accompanied by a decrease in the measured frequency, 2) vesicle rupture, and 3) loss of trapped water from the surface and a frequency increase. Then frequency (i.e. mass) changes after interaction with a target compound can be studied [67, 73, 74]. As well as frequency changes QCM-D also offers dissipation monitoring. The dissipation measurement offers information pertaining to the rigidity and viscosity of an interfacial layer [74]. Combination of the dissipation data and the changes to the frequency data from the adsorption of materials to the sensor surface providing details about a variety of physical properties [75].

Another powerful candidate for measuring atomic detail and length scales at the Angstrom level is neutron reflectometry (NR). Similarly, advantages to NR include its resolving power and it being a non damaging technique [76]. The neutrons used in NR studies have wavelengths on the Angstrom regime and are therefore appropriate for application to biological samples [77, 78]. It is also desirable that after the neutron studies have taken place, the sample is not spent and can be used for further measurements by other techniques. Unlike X-rays, neutrons are scattered by the nucleus of an atom and as such have a deeper penetrating power. This means that NR is suitable for deep, multilayered sample analysis. Further, neutrons have no electrical charge, and so can pass through the sample unimpeded by Coulombic interactions [20].

In contrast to other scattering techniques, the neutron scattering length of elements across the periodic table is random, where isotopes of the same element do not have the same scattering length values. For example the two most common isotopes of hydrogen have vastly different scattering lengths, such that H₂O has a scattering length density (SLD) of $-0.55 \times 10^{-6} \text{ \AA}^{-2}$ and D₂O of $6.35 \times 10^{-6} \text{ \AA}^{-2}$ [76]. With the prevalence of hydrogen in biological systems, the difference in its isotopic SLD can be taken advantage of to either highlight the biological components from the bulk solution, or to differentiate components from one another through selective deuteration [79].

Due to the fact that NR is deeply penetrating and offers Angstrom scale resolution, the interfacial structure of model membrane systems (e.g. floating lipid membranes, supported lipid bilayers) is well suited to analysis via neutron reflectometry methods. Such powerful structural determination in conjunction with the ability to highlight and locate different parts of the membrane system make neutron reflectometry currently the most advanced tool for biological studies [80]. It shows prevalence over techniques which require crystalline structures for analysis to be performed, or methods that do not allow for aqueous *in vivo* sample environments [81].

Real-world bilayer membranes are highly complex environments, and are composed of many different lipid classes, proteins, carbohydrates, and sugar-based molecules [38]. As previously mentioned, there are challenges that come with the increased accuracy of membrane models. That is why it is important to be able to design and synthesise model systems that allow tight control of the membrane size, composition, and geometry [82]. Further, the overlap between computational models and model membranes provides synergistic benefits. Geometric control over the model system allows experimental design that can be tailored towards particular analytical methods. Naturally, model and mimetic systems come with disadvantages. It is important to understand the relevance and accuracy of a model when drawing conclusions, with an awareness that the real-world counterpart may show differences. In many cases, a balance often needs to be struck between the most complex and accurate systems and pragmatic execution of the model study. There are occasions where compromise must be made in order to carry out a study that is simpler but provides insight into certain membrane aspects

while adhering to practical and experimental limitations. When compared to the cell culture based experimental alternatives, there are some distinct advantages of model and mimetic membrane systems. In general, the chances of chemical or microbial contamination in model systems is much lower. Further, model systems are not susceptible to physical, chemical, or genetic changes that may be induced by the micro-environment as occurs in cell cultures [83, 84].

Chapter 3 investigates the utility of constructing model membrane samples that are suitable for analysis using NR and offers insight into the information that comes from such studies. Chapters 4 and 6 provide details about the use of NR experiments to study, respectively, bacterial and epithelial membranes. Here, differences in composition of the model membranes and their polyphenolic interactions are explored and discussed.

1.4 Polyphenols and their Membrane Interactions

Polyphenols are specialised plant metabolites that have been shown to have a wide range of positive benefits. *Polyphenols* is generally used as an umbrella term and refers to compounds that fall into one of three categories: (1) condensed tannins (proanthocyanidins) which are derived from flavan-3-ol compounds such as epicatechins and epigallocatechins (see later chapter 4 and 6 for experiments involving (-)-epigallocatechin gallate [85]. (2) Gallo- or ellagitannins (also known as hydrolysable tannins) which are derived from gallic acid [86, 87]. (3) phlorotannins that originate from red-brown algae [88].

There are a number of reported benefits for consumption of dietary polyphenols, with bioactivities related to improving cardiovascular health, anti-carcinogenic effects, antimicrobial, anti-inflammatory, and antioxidant properties [88–93]. As anti cancer agents, polyphenols and their extracts have shown the ability to limit the rate of cell proliferation and reduce tumor cell viability through acting as a chemopreventing agent. They also influence apoptosis in cells [90]. Polyphenols are required to be broken down, digested and assimilated through the gut in order to be effective within humans [94]. The ability of humans to absorb polyphenols and their metabolic bioavailability has been extensively reviewed with factors such as polyphenolic type, chemical structure, and dietary source affecting the amount of available polyphenol [95–97]. The cardiovascular effects of polyphenols have been attributed, at least in part, to their multifaceted free radical scavenging properties [97].

While the interactions of polyphenols with lipids is less well understood than for other cell components, they have been reported to interact with lipid bilayers in various ways, often with the gallate motif playing a crucial role [92, 98]. The importance and the effects of changing the number of free galloyl groups is explored in more detail in chapter 4. The partition coefficients of polyphenols goes some way to predicting their ability to interact with membranes [99, 100].

The use of biomimetic models as a method for studying polyphenol interactions has been comprehensively reviewed [101]. The effects of polyphenols have been investigated on various kinds of lipid models. Optical studies on lipid vesicles have shown that flavonoid type polyphenols interact electrostatically with membrane headgroups and make them more rigid [102]. Further, the effects of polyphenols on membrane models can be detected using spectroscopic and calorimetric methods [103]. The structure dependence of polyphenols on their membrane interactions has been established, although the majority of membrane models used to test polyphenol bioactivity are liposomal in nature [92, 102, 104].

This thesis presents findings on the interactions of four compounds with lipid membranes: (i) (-)-epigallocatechin gallate (EGCg), (ii) 1,2,3,4,6-pentagalloyl glucose (PGG), (iii) Tellimagrandin-I (Tel-I), and (iv) Tellimagrandin-II (Tel-II). EGCg and PGG are both polyphenolic compounds that are relatively cheap and commercially available, and have comparatively different molecular weights. These were used for membrane interactions in the first instance to demonstrate proof of concept before more precious and difficult to obtain, such as as Tellimagrandin-I and -II. Studying Tel-I and Tel-II at the molecular level is rare and novel because they are not commercially available and not easy to isolate in quantities needed. Tellimagrandins -I and -II were extracted and purified by the Karonen group (University of Turku, Finland) and gratefully received for interaction studies because often ellagitannin related antimicrobial studies are conducted using polyphenolic containing plant extracts, making it difficult to assess structure-activity relationships [105].

Further, the use of purified Tel-I and Tel-II in this study allowed the physical properties and structural aspects of the four polyphenols to be compared to establish if physical parameters of these kinds of compounds can be used as predictors of interaction. More details of this are provided in chapter 4.

During the course of this thesis, the term “polyphenols” is used to encompass research of all four of the compounds mentioned above, given that they belong to three different classes of compounds. PGG is a gallotannin, and these are often ellagitannin precursors. Tellimagrandins -I and -II are themselves ellagitannins and can be derived from PGG, while EGCg is a flavan-3-ol and belongs to a different class of compound altogether. “Polyphenols” is used throughout at an umbrella term to be able to refer to all four of these particular compounds.

One area that needs further exploration is polyphenolic interactions at planar membranes, such that the effects of polyphenols on various aspects of membrane structure and function can be determined with greater accuracy. Binding of polyphenols to biological membranes, and effects on the cell wall in particular, has been a known phenomenon for some time [106, 107]. Investigation of polyphenolic interaction with membranes is important as type and mechanism of interaction can influence their biological activity [92, 98, 108]. The hydrophobicity of polyphenols is important for determining the mechanism by which they interact with the cell membrane, with increasing hydrophobicity allowing increased penetration into the bilayer core [105, 109]. The phenol

moiety of the polyphenol is capable of hydrogen bonding with the hydrophilic membrane surface by acting as a hydrogen bond donor [110]. Once attracted to the membrane surface polyphenols have been shown to be able to intercalate into the membrane if not completely then via insertion of the galloyl group into the bilayer [111]. This allows perturbation and disruption of the membrane leading to some of the aforementioned antimicrobial properties [112–114].

1.5 Aims and Objectives

This thesis develops advanced model membranes and examines interactions with polyphenols. It is divided into two sections firstly bacterial (chapters 3 and 4) and secondly epithelial (chapters 5 and 6). An attempt to increase the complexity, by migrating from vesicular to planar membranes for characterisation and biological interaction studies. Chapters 3 and 4 deal with bacterial model membranes and epithelial membranes are developed and discussed in chapter 5 and 6.

Throughout this thesis the term “model” is used, and largely refers to two different kinds of model. Firstly, in the context of the physical, “wet” mixtures of chemicals where physicochemical structures (*e.g.* vesicles, supported lipid bilayers, floating membranes) are assembled. In chapters 3 and 4 where the results of the DSC, QCM-D and FTIR experiments are described, this is the intended meaning of the term “model”. Where neutron reflectometry measurements are discussed, the physical models are also present. That is, physical amounts of lipids were assembled upon which experimental analyses were performed. The second meaning of the term “model” is also applicable here which refers to the theoretical, mathematical model that was generated to describe the membrane in terms of its neutron reflectivity. Fitting of the theoretical computational model to the experimental data was used to provide validity to the collected neutron data about the membranes that were assembled and their interactions with polyphenols. Where neutron data are shown and discussed (chapters 4 and 6), the term “model” may be used to discuss either the physical lipid components, or the theoretical mathematical fits of the data.

The overall research focus of this thesis is to develop model membrane systems to understand (i) whether they are capable of interacting with polyphenolic compounds and (ii) if so, whether they can be used to structurally understand interactions on the molecular level.

Membrane construction begins using liposomal and vesicle sample preparation methods to see if the existing methodologies for model membranes are suitable for probing polyphenol bioactivity. Development of these models from vesicles is to the use of supported and advanced floating membrane models is investigated to determine whether they provide a more accurate foundation for membrane modelling. The compositions of these models can be customised and adapted to a variety of membrane types depending on the needs of the model. This level of flexibility makes planar model membrane systems

a powerful tool for modelling both membrane constituents and their interactions.

More simplistic membrane models and initial screening are beginning to understand the ways in which the polyphenols used in this thesis are explored using monolayers and vesicles. The monolayer studies offer some insights into the physical properties of the membrane by being studied as individual leaflets, and vesicle experiments allow calorimetric determination of the phase transitions of individual lipids and lipid mixtures. In adding polyphenols to both of these types of model membranes, the effects on the physical properties being investigated can begin to be understood.

Complexity in the sample environment was increased by moving the membrane models towards planar bilayers for characterisation and interaction studies. The use of FTIR and QCM-D methods allows the detection of the formation of supported bilayers. These membrane models were developed compositionally to reflect more realistic cell membranes in terms of the lipids they contained. The set up was designed such that the membranes were formed on the same solid substrate that would be used for complete characterisation of the bilayers and their interactions with neutron reflectometry. This was important for allowing continuity of model development between rounds of neutron beam time and enabled comparison across all the methods of investigation. The utility of FTIR and QCM-D were both powerful and complementary methods for detecting, respectively, functional group presence and mass change at the interface.

Neutron reflectometry served as the most effective technique for elucidating the mechanics of polyphenolic interactions with model bacterial and epithelial membranes. Using neutron reflectometry allowed analysis of the most complex floating membrane models where quantitative parameters were derived. The development of the model membrane samples from the surface sensitive techniques that had been used prior enabled the use of the most complex human gastrointestinal tract (GIT) epithelial model membrane study [to the author's knowledge at the time of writing]. Comprehensive analysis and modelling in addition to the empirical neutron data enabled a clear picture of the novel membrane models and formed a better understanding of their interactions.

The increase in complexity created a more accurate membrane structure, but at the same time created challenges with regard to the design to enable stable bilayer formation and the study of polyphenolic interactions in a qualitative way. Fundamental physical chemical properties of the membrane architecture was addressed to allow the development of novel supported lipid bilayers to be formed, along with optimising deposition conditions. These challenges are addressed and discussed in due course, largely in chapters 3, 4, and 6 where the results of the interaction studies are reported.

The research focus that is presented in this thesis can be separated in to two parts. First, developing "model membranes", both physical and computational, to mimic the human GIT epithelium and comparing these membranes to a

bacterial membrane mimic. Secondly, to be able use these models for the testing of polyphenolic type compounds in order to structurally understand any interactions that take place. The overall research questions can be summarised as follows:

1. Can the current methods of membrane modelling be extended to develop a more accurate human GIT epithelial membrane model?
2. Can the human GIT model be used to test for polyphenol interactions?
3. Can results for interactions of the same polyphenol be compared between bacterial and epithelial models?

These questions can be related to the map of the thesis presented at the start of each chapter, and repeated below for convenience. The development and optimisation of the experimental techniques is covered first, in chapters 3 and 4, using a bacterial membrane model. The second question is explored in terms of accuracy of epithelial lipid composition in chapter 5 and experimentally in chapter 6. The thesis map makes clear the parallel nature of the bacterial and epithelial work streams.

The comparison of the data concerned in the third research question can be gleaned from the ends of chapters 4 and 6. The comparison culminates in a discussion of the similarities and differences of the interactions with bacterial and epithelial membranes being tied together in the epilogue.

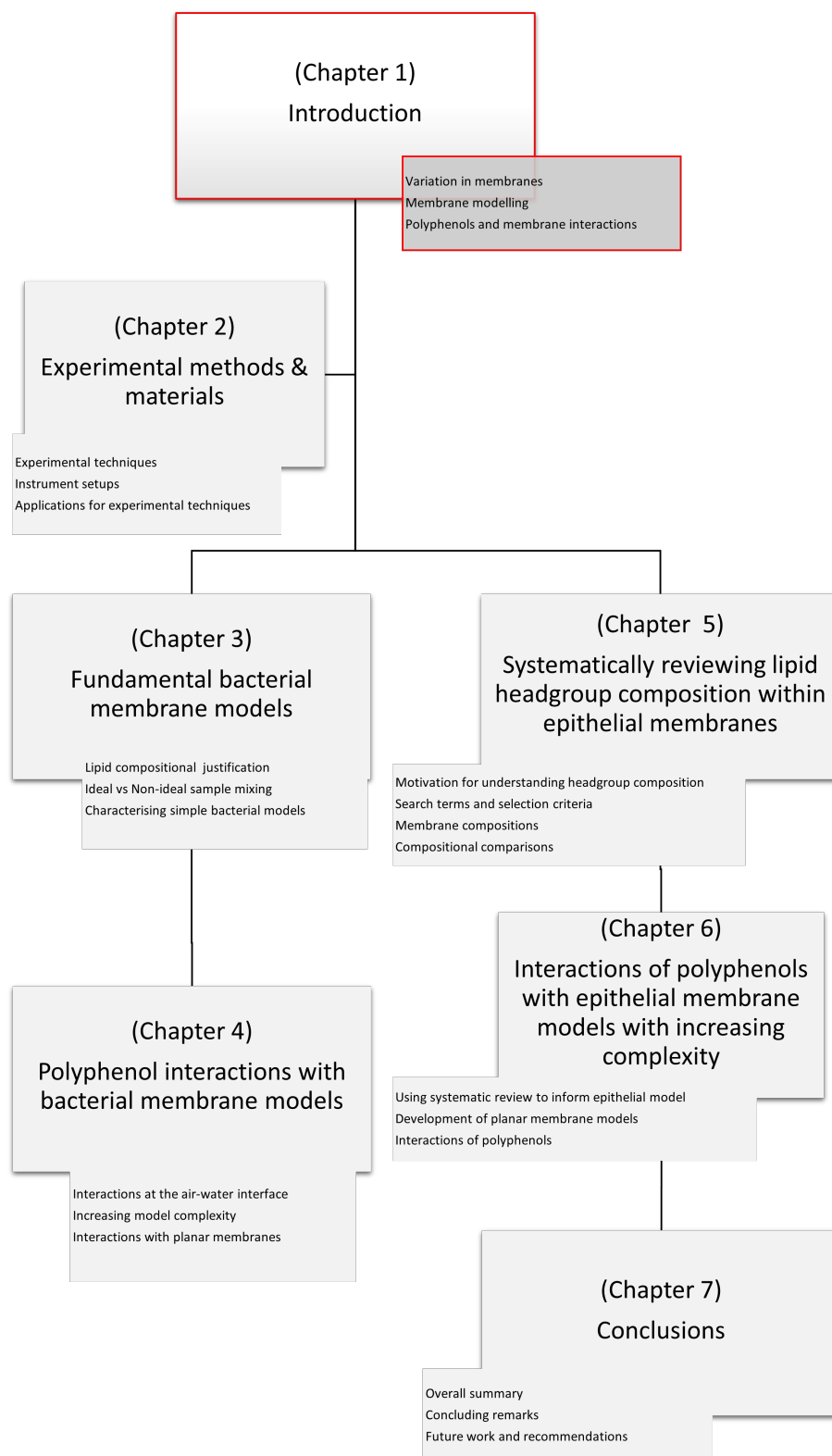


Figure 1.5: A map of the thesis showing the outline of each chapter, and some of the main points to be covered in each section of research. These points can be related to the three research questions set out above.

References

- [1] S. Singer, *The fluid mosaic model of membrane structure*, Springer, 1977, pp. 443–461.
- [2] K. Boesze-Battaglia and R. J. Schimmel, *J. Exp. Biol.*, 1997, **200**, 2927–2936.
- [3] P. L. Yèagle, *FASEB J.*, 1989, **3**, 1833–1842.
- [4] S. C. van IJzendoorn, J. Agnetti and A. Gassama-Diagne, *Biochim. Biophys. Acta - Biomembr.*, 2020, **1862**, 183145.
- [5] J. Ikenouchi, *Tissue Barriers*, 2018, **6**, 1–8.
- [6] S. M. Gruner, *Proceedings of the National Academy of Sciences of the United States of America*, 1985, **82**, 3665–3669.
- [7] G. Van Meer, D. R. Voelker and G. W. Feigenson, *Nature Reviews Molecular Cell Biology*, 2008, **9**, 112–124.
- [8] D. J. Steigmann, *The role of mechanics in the study of lipid bilayers*, Springer, 2017, vol. 577.
- [9] E. Fahy, S. Subramaniam, H. A. Brown, C. K. Glass, A. H. Merrill, R. C. Murphy, C. R. Raetz, D. W. Russell, Y. Seyama, W. Shaw, T. Shimizu, F. Spener, G. V. Meer, M. S. VanNieuwenhze, S. H. White, J. L. Witztum and E. A. Dennis, *Journal of Lipid Research*, 2005, **46**, 839–861.
- [10] H. Goldfine, *J. Lipid Res.*, 1984, **25**, 1501–1507.
- [11] T. K. Lind, M. Cárdenas and H. P. Wacklin, *Langmuir*, 2014, **30**, 7259–7263.
- [12] D. A. Brown and E. London, *J. Biol. Chem.*, 2000, **275**, 17221–17224.
- [13] R. J. Schroeder, S. N. Ahmed, Y. Zhu, E. London and D. A. Brown, *J. Biol. Chem.*, 1998, **273**, 1150–1157.
- [14] I. Levental, K. R. Levental and F. A. Heberle, *Trends Cell Biol.*, 2020, **30**, 341–353.
- [15] L. Rajendran and K. Simons, *J. Cell Sci.*, 2005, **118**, 1099–1102.
- [16] A. Kusumi, I. Koyama-Honda and K. Suzuki, *Traffic*, 2004, **5**, 213–230.

- [17] W. Dowhan, M. Bogdanov and E. Mileykovskaya, in *Biochemistry of lipids, lipoproteins and membranes*, Elsevier, 2008, pp. 1–37.
- [18] D. Marsh, *Biophysical journal*, 2007, **93**, 3884–3899.
- [19] F. Martin-Belmonte, A. Gassama, A. Datta, W. Yu, U. Rescher, V. Gerke and K. Mostov, *Cell*, 2007, **128**, 383–397.
- [20] G. Fragneto, R. Delhom, L. Joly and E. Scoppola, *Curr. Opin. Colloid Interface Sci.*, 2018, **38**, 108–121.
- [21] K. Simons and E. Ikonen, *Nature*, 1997, **387**, 569–572.
- [22] R. Tauber, K. Reher, K. Helling and H. Scherer, *Biol. Sci. Sp. = Uchū seibutsu kagaku*, 2002, **16**, 22–26.
- [23] F. M. Goñi, *Biochim. Biophys. Acta - Biomembr.*, 2014, **1838**, 1467–1476.
- [24] D. Chapman, J. Gomez-Fernandez and F. Goni, *FEBS letters*, 1979, **98**, 211–223.
- [25] B. Cullis, P.R and Kruijff, *Chem. Phys. Lipids*, 1986, **40**, 127–144.
- [26] M. Chabanon, J. C. Stachowiak and P. Rangamani, *Wiley Interdiscip. Rev. Syst. Biol. Med.*, 2017, **9**, 20–22.
- [27] L. A. Bagatolli, J. H. Ipsen, A. C. Simonsen and O. G. Mouritsen, *Prog. Lipid Res.*, 2010, **49**, 378–389.
- [28] W. Helfrich, *Zeitschrift fur Naturforschung - Section C Journal of Biosciences*, 1973, **28**, 693–703.
- [29] R. M. Epanand, N. Fuller and R. P. Rand, *Biophysical Journal*, 1996, **71**, 1806–1810.
- [30] D. Deamer, *Life*, 2017, **7**, 5.
- [31] M. A. Kiselev and D. Lombardo, *Biochimica et Biophysica Acta - General Subjects*, 2017, **1861**, 3700–3717.
- [32] O. G. Mouritsen and K. Jørgensen, *Chemistry and physics of lipids*, 1994, **73**, 3–25.
- [33] D. Marsh, *Biochim. Biophys. Acta - Rev. Biomembr.*, 1996, **1286**, 183–223.
- [34] P. A. Janmey and P. K. Kinnunen, *Trends Cell Biol.*, 2006, **16**, 538–546.
- [35] O. G. Mouritsen, *Eur. J. Lipid Sci. Technol.*, 2011, **113**, 1174–1187.
- [36] G. Van Meer, *Annual Review of Cell Biology*, 1989, **5**, 247–275.
- [37] J. H. Ipsen, G. Karlström, O. Mouritsen, H. Wennerström and M. Zuckermann, *Biochimica et Biophysica Acta (BBA)-Biomembranes*, 1987, **905**, 162–172.

- [38] K. Simons and W. Vaz, *Annual Review of Biophysics and Biomolecular Structure*, 2004, **33**, 269–295.
- [39] K. Simons and G. Van Meer, *Biochemistry*, 1988, **27**, 6197–6202.
- [40] M. Girasole, G. Pompeo, A. Cricenti, A. Congiu-Castellano, F. Andreola, A. Serafino, B. Frazer, G. Boumis and G. Amiconi, *Biochimica et Biophysica Acta - Biomembranes*, 2007, **1768**, 1268–1276.
- [41] E. J. Fernández-Pérez, F. J. Sepúlveda, C. Peters, D. Bascuñán, N. O. Riffo-Lepe, J. González-Sanmiguel, S. A. Sánchez, R. W. Peoples, B. Vicente and L. G. Aguayo, *Frontiers in Aging Neuroscience*, 2018, **10**, 1–14.
- [42] J. Lee, S.-t. Yang, V. Kiessling and L. K. Tamm, *Biophysical Journal*, 2017, **112**, 9a.
- [43] D. G. Drubin and W. J. Nelson, *Cell*, 1996, **84**, 335–344.
- [44] S. Tsukita, M. Furuse and M. Itoh, *Nature reviews Molecular cell biology*, 2001, **2**, 285–293.
- [45] S. Schuck and K. Simons, *J. Cell Sci.*, 2004, **117**, 5955–5964.
- [46] D. Cohen, P. J. Brennwald, E. Rodriguez-Boulan and A. Müsch, *Journal of Cell Biology*, 2004, **164**, 717–727.
- [47] R. M. Epanand and R. F. Epanand, *Biochim. Biophys. Acta - Biomembr.*, 2009, **1788**, 289–294.
- [48] R. P. Huijbregts, A. I. De Kroon and B. De Kruijff, *Biochim. Biophys. Acta - Rev. Biomembr.*, 2000, **1469**, 43–61.
- [49] S. W. Nowotarska, K. J. Nowotarski, M. Friedman and C. Situ, *Molecules*, 2014, **19**, 7497–7515.
- [50] G. Pabst, N. Kučerka, M. P. Nieh, M. C. Rheinstädter and J. Katsaras, *Chem. Phys. Lipids*, 2010, **163**, 460–479.
- [51] F. Foglia, M. J. Lawrence and D. J. Barlow, *Curr. Opin. Colloid Interface Sci.*, 2015, **20**, 235–243.
- [52] P. Scrimin and P. Tecilla, *Model membranes: Developments in functional micelles and vesicles*, 1999.
- [53] V. M. Kaganer, H. Möhwald and P. Dutta, *Reviews of Modern Physics*, 1999, **71**, 779.
- [54] P. Dynarowicz-Latka, A. Dhanabalan and O. N. Oliveira, *Adv. Colloid Interface Sci.*, 2001, **91**, 221–293.
- [55] W. Barzyk, K. Lunkenheimer, P. Warszyński, B. Jachimaska and A. Pomianowski, *Colloids and Surfaces A: Physicochemical and Engineering Aspects*, 2014, **443**, 515–524.

- [56] M. D. Lad, F. Birembaut, L. A. Clifton, R. A. Frazier, J. R. Webster and R. J. Green, *Biophysical Journal*, 2007, **92**, 3575–3586.
- [57] H. Zhu, R. Sun, T. Zhang, C. Hao, P. Zhang, J. Wang and S. Li, *J. Nanomater.*, 2015, **2015**, 7–16.
- [58] F. S. Rocha, G. S. Codeceira, M. D. Oliveira and C. A. Andrade, *Journal of King Saud University - Science*, 2018.
- [59] N. K. Khadka, X. Cheng, C. S. Ho, J. Katsaras and J. Pan, *Biophysical Journal*, 2015, **108**, 2492–2501.
- [60] L. Zheng, Y. Lin, S. Lu, J. Zhang and M. Bogdanov, *Biochimica et Biophysica Acta - Molecular and Cell Biology of Lipids*, 2017, **1862**, 1404–1413.
- [61] A. Arouri, M. Dathe and A. Blume, *Biochim. Biophys. Acta - Biomembr.*, 2009, **1788**, 650–659.
- [62] K. Gardikis, S. Hatziantoniou, K. Viras, M. Wagner and C. Demetzos, *International Journal of Pharmaceutics*, 2006, **318**, 118–123.
- [63] T. Matsuzaki, H. Ito, V. Chevyreva, A. Makky, S. Kaufmann, K. Okano, N. Kobayashi, M. Sukanuma, S. Nakabayashi, H. Y. Yoshikawa and M. Tanaka, *Physical Chemistry Chemical Physics*, 2017, **19**, 19937–19947.
- [64] S. A. Tatulian, *Biochemistry*, 2003, **42**, 11898–11907.
- [65] N. Paracini, L. A. Clifton, M. W. A. Skoda and J. H. Lakey, *Proceedings of the National Academy of Sciences*, 2018, **115**, E7587–E7594.
- [66] S. C. Hall, L. A. Clifton, C. Tognoloni, K. A. Morrison, T. J. Knowles, C. J. Kinane, T. R. Dafforn, K. J. Edler and T. Arnold, *Journal of Colloid and Interface Science*, 2020, **574**, 272–284.
- [67] L. A. Clifton, R. A. Campbell, F. Sebastiani, J. Campos-Terán, J. F. Gonzalez-Martinez, S. Björklund, J. Sotres and M. Cárdenas, *Adv. Colloid Interface Sci.*, 2020, **277**, 102118.
- [68] B. H. Stuart, *Biological applications of infrared spectroscopy*, John Wiley & Sons, 1997.
- [69] C. A. Keller and B. Kasemo, *Biophys. J.*, 1998, **75**, 1397–1402.
- [70] M. C. Dixon, *J. Biomol. Tech.*, 2008, **19**, 151–158.
- [71] A. Alassi, M. Benammar and D. Brett, *Sensors (Switzerland)*, 2017, **17**, 1–41.
- [72] P. Parkkila, M. Elderdfi, A. Bunker and T. Viitala, *Langmuir*, 2018, **34**, 8081–8091.
- [73] B. Seantier, C. Breffa, O. Félix and G. Decher, *Nano Lett.*, 2004, **4**, 5–10.

- [74] F. Höök, B. Kasemo, T. Nylander, C. Fant, K. Sott and H. Elwing, *Anal. Chem.*, 2001, **73**, 5796–5804.
- [75] M. Rodahl, F. Höök, A. Krozer, P. Brzezinski and B. Kasemo, *Review of Scientific Instruments*, 1995, **66**, 3924–3930.
- [76] L. A. Clifton, *Biochem. Soc. Trans.*, 2021, **49**, 1537–1546.
- [77] P. Georgiades, E. Di Cola, R. K. Heenan, P. D. Pudney, D. J. Thornton and T. A. Waigh, *Biopolymers*, 2014, **101**, 1154–1164.
- [78] J. Pencer, T. T. Mills, N. Kucerka, M. P. Nieh and J. Katsaras, *Methods Mol. Biol.*, 2007, **398**, 231–244.
- [79] L. A. Clifton, M. W. Skoda, E. L. Daulton, A. V. Hughes, A. P. L. Brun, J. H. Lakey and S. A. Holt, *Journal of the Royal Society Interface*, 2013, **10**, year.
- [80] E. Sackmann, *Science*, **271**, year = 1996., 43–48.
- [81] H. P. Wacklin, *Current Opinion in Colloid and Interface Science*, 2010, **15**, 445–454.
- [82] Y. H. M. Chan and S. G. Boxer, *Curr. Opin. Chem. Biol.*, 2007, **11**, 581–587.
- [83] L. G. Dickson, R. A. Galloway and G. W. Patterson, *Plant Physiol.*, 1969, **44**, 1413–1416.
- [84] B. M. Turner, *Philos. Trans. R. Soc. B Biol. Sci.*, 2009, **364**, 3403–3418.
- [85] Y. T. H. T. Okuda, T. and H. Ito, *Chemistry and biology of ellagitannins: an underestimated class of bioactive plant polyphenols*, World Scientific, 2009, pp. 1–54.
- [86] E. Haslam and Y. Cai, *Natural Product Reports*, 1994, **11**, 41–66.
- [87] *Flavonoids: Chemistry, Biochemistry and Applications*, ed. O. M. Andersen and K. R. Markham, CRC Press, 1st edn.
- [88] S. Quideau, D. Deffieux, C. Douat-Casassus and L. Pouységu, *Angewandte Chemie - International Edition*, 2011, **50**, 586–621.
- [89] T. P. Kondratyuk and J. M. Pezzuto, *Pharmaceutical biology*, 2004, **42**, 46–63.
- [90] A. N. Li, S. Li, Y. J. Zhang, X. R. Xu, Y. M. Chen and H. B. Li, *Nutrients*, 2014, **6**, 6020–6047.
- [91] P. Bellion, J. Digles, F. Will, H. Dietrich, M. Baum, G. Eisenbrand and C. Janzowski, *Journal of Agricultural and Food Chemistry*, 2010, **58**, 6636–6642.
- [92] M. Karonen, *Plants*, 2022, **11**, 1809.

- [93] A. Reis and V. de Freitas, *Food Chemistry*, 2020, **333**, 127509.
- [94] L. Jakobek, *Food Chemistry*, 2015, **175**, 556–567.
- [95] C. Manach, G. Williamson, C. Morand, A. Scalbert and C. Rémésy, *The American Journal of Clinical Nutrition*, 2005, **81**, 230–242.
- [96] A. Adam, V. Crespy, M.-A. Levrat-Verny, F. Leenhardt, M. Leuillet, C. Demigne and C. Remesy, *The journal of nutrition*, 2002, **132**, 1962–1968.
- [97] P. C. Hollman, A. Cassidy, B. Comte, M. Heinonen, M. Richelle, E. Richling, M. Serafini, A. Scalbert, H. Sies and S. Vidry, *Journal of Nutrition*, 2011, **141**, 989–1009.
- [98] T. Nakayama, T. Hashimoto, K. Kajiya and S. Kumazawa, *Affinity of polyphenols for lipid bilayers*, 2000.
- [99] T. Scheytt, P. Mersmann, R. Lindstädt and T. Heberer, *Water, air, and soil pollution*, 2005, **165**, 3–11.
- [100] O. V. Zillich, U. Schweiggert-Weisz, K. Hasenkopf, P. Eisner and M. Kerscher, *Biomedical Chromatography*, 2013, **27**, 1444–1451.
- [101] A. Reis, J. P. Teixeira, A. M. Silva, M. Ferreira, P. Gameiro and V. de Freitas, *Biomolecules*, 2022, **12**, year.
- [102] H. T. Phan, T. Yoda, B. Chahal, M. Morita, M. Takagi and M. C. Vestergaard, *Biochimica et Biophysica Acta - Biomembranes*, 2014, **1838**, 2670–2677.
- [103] S. Cyboran-Mikołajczyk, R. Żyłka, P. Jurkiewicz, H. Pruchnik, J. Oszmiański, M. Hof and H. Kleszczyńska, *Biochimica et Biophysica Acta - Biomembranes*, 2017, **1859**, 1362–1371.
- [104] N. Caturla, E. Vera-Samper, J. Villalaín, C. R. Mateo and V. Micol, *Free Radical Biology and Medicine*, 2003, **34**, 648–662.
- [105] M. Karonen and V. Virtanen, *Molecules*, 2020, **25**, 3691.
- [106] S. A. Simon, E. A. Disalvo, K. Gawrisch, V. Borovyagin, E. Toone, S. S. Schiffman, D. Needham and T. J. McIntosh, *Biophysical Journal*, 1994, **66**, 1943–1958.
- [107] G. A. Jones, T. A. McAllister, A. D. Muir and K. J. Cheng, *Applied and Environmental Microbiology*, 1994, **60**, 1374–1378.
- [108] V. Virtanen, S. Rääkkönen, E. Puljula and M. Karonen, *Molecules (Basel, Switzerland)*, 2021, **26**, year.
- [109] X. Yu, S. Chu, A. E. Hagerman and G. A. Lorigan, *Journal of Agricultural and Food Chemistry*, 2011, **59**, 6783–6789.

- [110] T. W. Sirk, E. F. Brown, A. K. Sum and M. Friedman, *Journal of Agricultural and Food Chemistry*, 2008, **56**, 7750–7758.
- [111] R. zu Nie, M. zhu Dang, Z. zhen Ge, Y. qiang Huo, B. Yu and S. wen Tang, *Biophysical Chemistry*, 2021, **274**, year.
- [112] H. J. Jung, I. A. Hwang, W. S. Sung, H. Kang, B. S. Kang, Y. B. Seu and D. G. Lee, *Archives of pharmacal research*, 2005, **28**, 557–560.
- [113] E. Puljula, G. Walton, M. J. Woodward and M. Karonen, *Molecules*, 2020, **25**, 3714–3727.
- [114] F. Pires, V. P. Geraldo, B. Rodrigues, A. D. Granada-Flor, R. F. D. Almeida, O. N. Oliveira, B. L. Victor, M. Machuqueiro and M. Raposo, *Langmuir*, 2019, **35**, 6771–6781.

—*The test of all knowledge
is experiment. Experiment
is the sole judge of scientific
truth.*

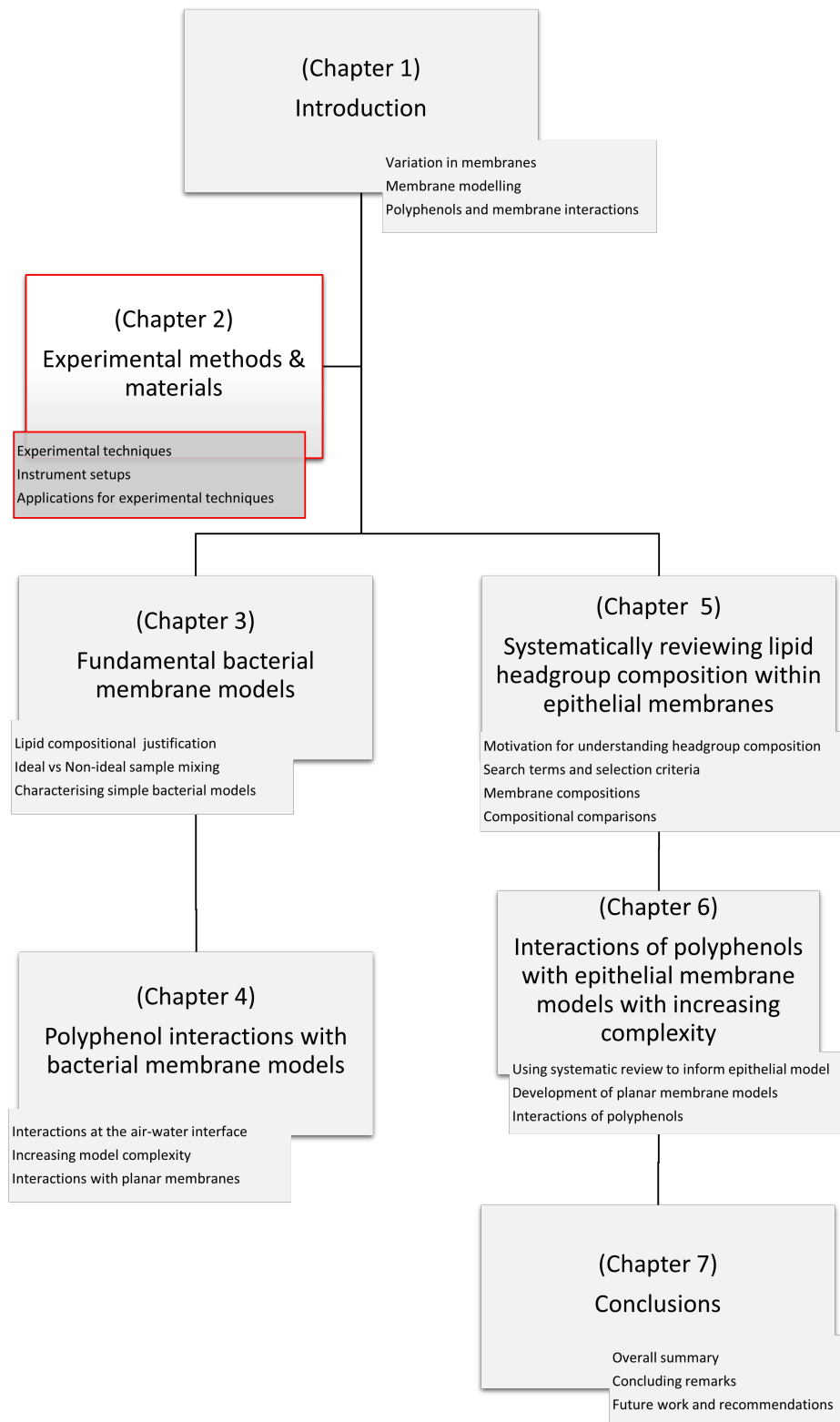
Richard Feynman

2

Instrumentation and Experimental Procedures

Contents

2.1	Membrane Preparation Methods	49
2.2	Addition of Polyphenols to Membranes	49
2.2.1	Vesicle Preparation	49
2.3	Surface Pressure Measurements	50
2.3.1	Langmuir-Blodgett Monolayers & Instrument Setup	50
2.3.2	Pressure-Area Isotherms	50
2.3.3	Compressibility Modulus	52
2.4	Differential Scanning Calorimetry	52
2.4.1	Lipid Phases	52
2.4.2	Instrument Setup	53
2.5	Fourier Transform Infrared Spectroscopy	53
2.5.1	Instrument Setup	53
2.5.2	Applications for FTIR in Membrane Studies	54
2.6	Quartz Crystal Microbalance	55
2.6.1	The Piezoelectric Effect	55
2.6.2	The Sauerbrey Relationship	55
2.6.3	Instrument Setup	56
2.7	Neutron Reflection and Scattering Experiments	58
2.7.1	Theory	58
2.7.2	Instruments and Setup	59
2.7.3	Modelling Methods	59



2.1 Membrane Preparation Methods

For each set of experiments described below, the aim was to use a standard membrane preparation method. For monolayer and Langmuir trough experiments this involved adding lipid sample to the surface drop-wise from a micro syringe. For studies where vesicle preparation was appropriate, these were sought to be prepared using a standardised method to use similarly sized vesicles for each set of studies. The same vesicle preparation methods were also used in neutron studies either for small angle scattering measurements, or for vesicle rupture methods to allow formation of a planar membrane. In each case, the probe sonication time of each sample was suitably adapted. There exists some variation in the techniques used and how they are applied specifically to membrane modelling. In each case, these variations will be detailed in the relevant results chapters.

2.2 Addition of Polyphenols to Membranes

Where vesicle samples were produced, polyphenols were added in lipid:polyphenol amounts in a molar ratio. In SLB and floating bilayer experiments the amount of polyphenol added is specified as the Molar quantity.

2.2.1 Vesicle Preparation

Vesicle stock solutions were prepared by first weighing out the desired amount of vesicle components into a clean glass vial and dissolving in the minimum amount of CHCl_3 . The solvent was then evaporated under constant N_2 flow until a lipid cake was obtained. The lipid cake was then re-hydrated with the appropriate amount of buffer to the desired concentration. Solution based samples were degassed (Fisherbrand™ S-Series Heated Ultrasonic Cleaning Bath) for 10 minutes prior to use. Depending on the sample mixture required, there are differing methods of preparation. Ideal mixing in the sample ensure a more homogeneous mixture with lipids distributed more evenly and well mixed through the membrane. Non-ideal mixing allows non-homogeneous mixing, and subsequently supports lipid domain formation, while still enabling a uniform size distribution within the sample.

Ideally mixed lipid systems were prepared using 5 heating/cooling cycles (65 °C/5 °C respectively) with 1 minute of vortexing in between each hot and cold phase.

Non-ideally mixed vesicle samples were probe sonicated at 20 kHz (model 120 probe sonicator, Fischer Scientific) to produce a monodisperse sample solution for sufficient time to achieve the desired vesicle size. This step was carried out immediately before measurements were taken to minimise vesicle aggregation and polydispersity of the sample.

2.3 Surface Pressure Measurements

2.3.1 Langmuir-Blodgett Monolayers & Instrument Setup

Lipid monolayers were prepared on a Langmuir trough (NIMA model 611, Coventry, England) with a Teflon surface. The size of the surface available for compression with the barriers fully open was $110 \times 10 \text{ cm}^2$. The volume of the trough to be filled with subphase was 80 mL. The trough barriers were movable using electric motors, and were rate controllable to within $\pm 1 \text{ cm}^2 \text{ min}^{-1}$. Prior to lipid being spread on the surface, the air-water interface was cleaned until $\Delta\pi \leq 0.2 \text{ mN.m}^{-1}$. Lipid solutions were spread from the appropriate amount of 0.5 mg/mL stock solutions composed of lipids dissolved in CHCl_3 using a Hamilton micro-syringe. Buffers were made from HEPES (20 mM, 2mM Ca^{2+} , pH 7) dissolved in 80 mL milliQ water (18.2 M Ω) and adjusted using 0.5 M HCl/NaOH until pH 7.2 was achieved.

2.3.2 Pressure-Area Isotherms

Surface pressure versus area isotherms were recorded in order to gain understanding of the behaviour of the monolayers deposited at the air-water interface. Surface pressure was determined by measuring the change in force between the Wilhelmy plate and the subphase surface. Isotherms were collected by compressing the monolayer between the barriers, reducing the area. Upon compression of the monolayer, the amphiphile(s) can adopt a series of phases. At very high area per molecule (APM) the amphiphile obeys a 2-dimensional version of the ideal gas law, and molecules were spaced far enough apart that they did not significantly interact with one another [1]:

$$\Pi A = k_b T \quad (2.1)$$

where Π is the surface pressure at the interface, A is the area available to each molecule, and $k_b T$ is the thermal energy where k_b is the Boltzmann constant and T is temperature. Π is given by the difference in surface tension between a clean (γ_0) and amphiphile containing (γ) interface:

$$\Pi = \gamma_0 - \gamma \quad (2.2)$$

As compression continued, reducing amount of area available to each molecule, the layer progressed through various phases which are well understood and well characterised [2]. As distances between individual amphiphilic molecules decreased, there was an accompanying increase in surface pressure while the molecules begin to coalesce and the surface pressure will plateau as the film reaches a liquid-expanded (LE) phase [3, 4]. Further reducing APM produced transitions through liquid-condensed (LC) and finally a condensed (C) or solid phase. After this, the pressure no longer increased as APM dropped.

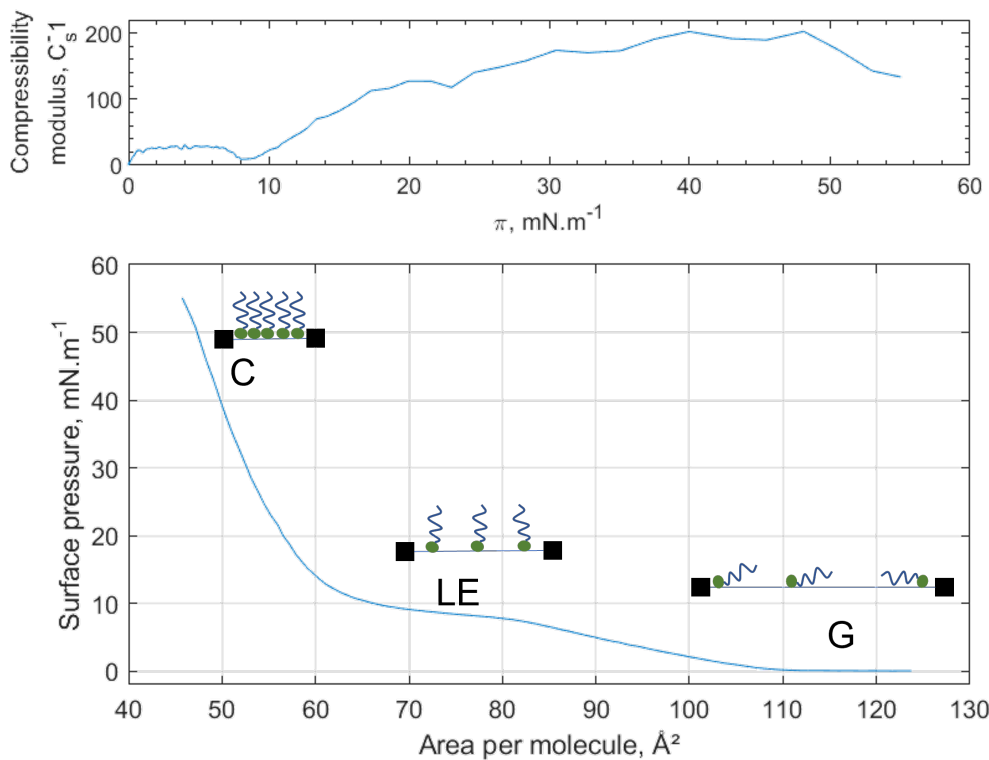


Figure 2.1: A pressure-area isotherm of DPPG (0.5 mg/mL, 20 μL , subphase = NaCl (100 mM)) demonstrating the three phases of compression; the gaseous (G) phase shows no interaction between lipid molecules, the liquid expanded (LE) phase shows some minimal ordering between molecules, and the the condensed (C) phase where the molecules at the surface are tightly packed together. The compressibility modulus shows changes in the lipid phase, for example the minimum at $8 \text{ mN}\cdot\text{m}^{-1}$ shows the G-LE transition.

2.3.3 Compressibility Modulus

The compressibility modulus of the monolayer is useful to help understand some of the physical characteristics of the sample present at the interface. The compressibility modulus, C_s^{-1} , is determined numerically using the slope of the isotherm at various points of compression:

$$C_s^{-1} = -A \cdot \left(\frac{\partial \pi}{\partial A} \right) \quad (2.3)$$

Where A is the area per molecule, π is the surface pressure as in equation 2.2. The compressibility modulus is descriptive of the elasticity of the monolayer, with higher C_s^{-1} values relating to a lower elasticity at the interface [3, 5]. Compressibility modulus is useful for helping to determine phase changes in the sample at the interface [6, 7]. The compressibility modulus is exemplified in the upper panel of figure 2.1. In general, a larger C_s^{-1} value corresponds to a more compressed monolayer and the reference value for a clean air-water interface is 0 [5]. The compressibility modulus shows changes of phase at the surface through local minima in the curve, as can be observed in the top panel of figure 2.1 at around $8 \text{ mN}\cdot\text{m}^{-1}$. This value of $8 \text{ mN}\cdot\text{m}^{-1}$ corresponds to the point on the surface pressure isotherm where the G-LE phase transition has taken place.

2.4 Differential Scanning Calorimetry

DSC, like other forms of calorimetry, relies on the exchange of heat from the instrument through a sample and compares it to the heat exchange in an empty reference cell [8]. This technique is suitable for many lipid systems to understand lipid mixing, as well as for measuring the effects of additives on lipid membrane systems [9, 10]. In the context of lipids and their interactions, DSC allows the measurement of the transitions of lipids between different phases. When interaction studies are performed, alteration to the lipid transition temperatures gives insight into the nature of the interactions. Information such as the enthalpy (ΔH), and subsequently entropy (ΔS) can be taken from a DSC thermogram [11].

2.4.1 Lipid Phases

Lipids are able to adopt and transition between various phases. Generally, there are three possible outcomes of lipid mixing: 1) ideal mixing, where there is no distinguishable phase separation between the membrane components, 2) non-ideal mixing, where there are observable transitions between regions of different phases, and immiscibility which results in individual micron-sized domains of a single component [12, 13]. Lipid phases may also refer to the orientation and fluidity of a membrane. Some examples of lipid phases can also be found in figure 1.4. The more stable a lipid is in its gel phase, the more energy is required to form the liquid crystalline phase, and the higher the

transition temperature will be.

2.4.2 Instrument Setup

For DSC analyses, the samples were analysed in a nanoDSC III (TA instruments) with a reference and sample cell volume of 300 μL . Samples were analysed in heating mode, at a rate of 1°C min^{-1} . All thermograms were recorded in triplicate. Both sample and reference cells were cleaned by flushing the cells with copious amounts of milliQ water (18 M Ω), Decon 90 solution (10%), and MeOH. MilliQ water flushes were done in between and at the end of each of the other cleaning solutions. Scans were processed using NanoAnalyze (version 3.11.0, TA Instruments).

2.5 Fourier Transform Infrared Spectroscopy

Fourier Transform Infrared Spectroscopy (FTIR) involves the measurement of a spectrum of a sample within the infrared range. In practice this requires the illumination of a sample with a multi-wavelength source and measurement of which wavelengths of light are absorbed by the sample. A Fourier transform of the absorbance gives rise to the FTIR spectrum.

Attenuated total reflection (ATR) FTIR is a method of FTIR that allows direct measurement of samples that are pressed up against the surface of a high refractive index prism. The IR source is passed through the prism and totally internally reflects along the surface of the prism, and at each point of reflection allows the measurement of a sample [14]. ATR-FTIR allows multiple measurements to be taken per scan of the sample, due to the beam being reflected and hitting the sample several times, which increases the signal to noise ratio. A schematic of the ATR-FTIR setup is shown in figure 2.2. Any changes in the presence of functional groups at the interface can be monitored through changes in the FTIR spectrum.

2.5.1 Instrument Setup

ATR-FTIR spectra were collected using a Thermo-Nicolet iS50 instrument fitted with an ATR flow cell accessory (Specac). The ATR flow cell housing was kept under a dry air purge to remove the effect of atmospheric water vapour on spectra. The flow cell contained a liquid cooling loop connected to a temperature controlled water bath. The spectrometer used a mercury cadmium telluride (MCT) detector cooled by liquid nitrogen. All spectra were collected at a resolution of 4 cm^{-1} , with 128 interferograms taken per spectrum. Fourier self-deconvolution was performed automatically by the data acquisition software OMNIC 9 (ThermoFisher Scientific).

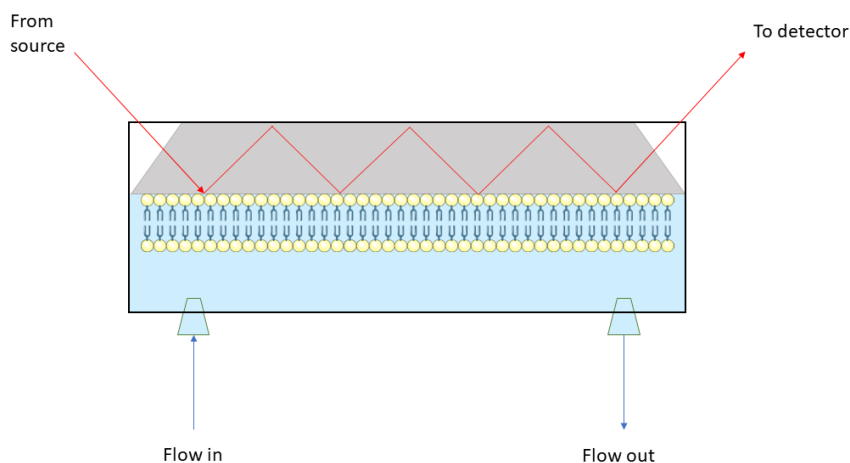


Figure 2.2: Schematic illustration of the ATR-FTIR setup. The IR beam is shown to be internally reflected by the Si substrate and hits the membrane sample at multiple points along the path to the detector.

Single-crystal silicon ATR substrates were cleaned by immersion in 2% (w/v) SDS for 30min before rinsing extensively with ultrapure water and EtOH and drying under a stream of nitrogen. The substrates were ultraviolet-ozone cleaned for 10 min, washed with ultrapure water and then ultraviolet-ozone cleaned a final time for 10 min. The substrate was mounted dry in the flow cell and the volume filled with buffer (20 mM HEPES, 100 mM NaCl, 2mM Ca^{2+} , pD 7.2 in D_2O) heated to 38 °C for background collection. Similar techniques have been described elsewhere [15].

Lipid membrane models were formed *in situ* through vesicle rupture. Largely, the membrane formation is thought to be spontaneous, but bilayer formation was ensured through vesicle rupture by osmotic shock [16, 17]. Supported lipid bilayers allow for a relatively large amount of flexibility and can be bespoke in terms of composition [18]. Once the membrane had been formed interaction studies were carried out, typically through the injection of the polyphenolic compound under investigation in solution.

2.5.2 Applications for FTIR in Membrane Studies

ATR-FTIR provides structural information about functional groups that are present at the solid interface. Experiments that show changes to the structure of the interface can be monitored using this technique [18]. Deposition of supported lipid bilayers (SLBs) on ATR substrates allows measurement of the bilayer formation, as well as changes to in the bilayer region over time when substances are injected to the flow cell to monitor interactions.

Such measurements are carried out in D₂O because the areas of interest for the bilayer are around 2800-3000 cm⁻¹ for the CH₂_{sym} and CH₂_{asym} stretching modes for hydrogenous lipids; this region would be eclipsed by the O–H stretch due to the solvent. Similarly, the lipid ester peaks and peaks of interest for biophysical interactions around 1550-1750 cm⁻¹ are obscured by the H₂O bending mode. In D₂O, these IR features are shifted such that they do not interfere with the measurements [19].

Interactions with SLBs in solution are typically characterised by observing changes in the peak positions and peak areas of the signals in the CH₂ stretching and C=O stretching regions. Measuring the areas of the FTIR peaks as a function of time can be used to give an indication of the kinetics of the interactions. When interacting a membrane with pharmaceutical type compounds the addition of small drugs can also result in the appearance of new FTIR peaks, for example the aromatic C=C or aromatic C–OH features that results from addition of a polyphenolic compound to the interface.

2.6 Quartz Crystal Microbalance

QCM-D makes use of an oscillating quartz crystal as a sensor for measuring mass deposition at a surface. The change in mass at the surface can be monitored in real time, allowing quantitative determination to changes in thickness and rigidity of the films [20]. As such, QCM-D is a useful tool in the analysis of understanding the formation of supported lipid bilayer (SLB) deposition and interactions therein. Typically, small unilamellar vesicles (SUVs) are adsorbed and ruptured on the SiO₂ sensor surface [21].

2.6.1 The Piezoelectric Effect

The operation of the QCM as a mass sensitive technique relies on the piezoelectric effect - that is, when an AC voltage is applied across the quartz crystal, the crystal lattice is caused to repeatedly expand and contract that results in a standing wave. When the AC voltage has a frequency that is close to the resonant frequency (f_0) of the crystal, resonance is produced [22]. This resonance can be related to mass changes at the surface of the crystal as demonstrated by Sauerbrey and colleagues [23].

2.6.2 The Sauerbrey Relationship

In 1959, Sauerbrey showed that a change in frequency of an oscillating crystal could be used as a method of measuring mass changes at an interface [23]. The relationship is given by:

$$\Delta m = -\frac{C}{n} \Delta f \quad (2.4)$$

where n is the harmonic number, and:

$$C = \frac{t_q \rho_q}{f_0} \quad (2.5)$$

with t_q being the thickness of the quartz, ρ_q being the quartz density, and f_0 being the resonant frequency of the quartz. For the Sauerbrey relationship to be reasonably applied, there are some assumptions that need to hold. The mass adsorbed to the crystal must be small compared to the mass of the crystal, the mass change must be due to the formation of a thin, rigid film, and the mass change must be uniform across the crystal [20, 22, 23].

2.6.3 Instrument Setup

QCM-D experiments were performed on a QSense E4 system (QSense, Biolin Scientific, Stockholm, Sweden). Silicon dioxide sensors (QSense, Biolin Scientific, Stockholm, Sweden) were used after cleaning (protocol described below). Sample solution was pumped through the flow cell onto the sensor using a calibrated peristaltic pump, with a flow rate of 0.2 mL/min. The peristaltic pump was connected to the outlet line of the QCM-D flow cell. A baseline was acquired for 5 min in buffer solution to allow for temperature equilibration before starting any measurements. Frequency and dissipation changes (Δf and ΔD) were monitored using various overtone harmonics ($n = 3, 5, 7, 9, 11$) of the resonant frequency. A simple schematic of the QCM-D setup is shown below in figure 2.3.

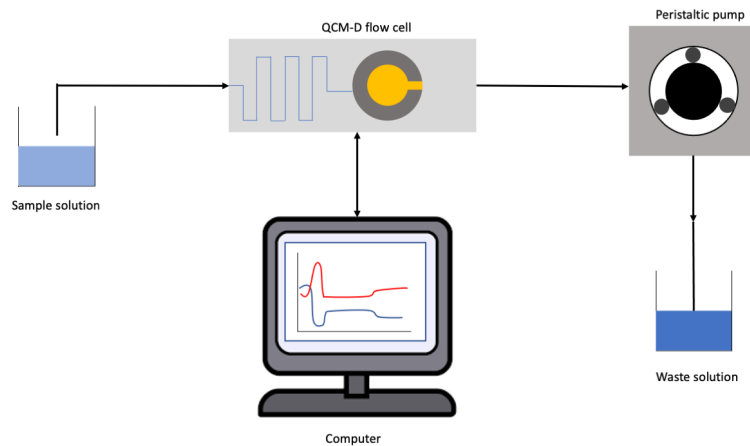


Figure 2.3: A simple schematic of the QCM-D setup.

Sensor Surface Preparation

Silicon dioxide sensors were subjected to a cleaning protocol that included a long (*ca.* 20 minute) UV-ozone clean, followed by soaking in SDS (2% w/v) solution, rinsing with copious amounts of milliQ water (18.2 M Ω), drying under N₂ stream, and UV-ozone cleaned for 10 minutes immediately before use. Fluid was drawn through the flow cells using a peristaltic pump on the out-flow end of the instrument.

After experiments had been completed, the cells were flushed with multiple cell volumes of SDS (2% w/v), Hellmenex (2% v/v), analytical grade EtOH, and milliQ water (18.2 M Ω). The flow cells were pumped dry and disassembled, and the SiO₂ sensors were removed and UV-ozone cleaned again. Following the ozone treatment, they were washed with milliQ water, dried under N₂ flow and stored dry in a sealed container.

Lipid Sample Preparation

Lipid solutions were prepared as in section 2.2.1. The buffer solution used contained HEPES (20 mM), CaCl₂ (2 mM), NaCl (200 mM) and was prepared in H₂O at pH 7.2. Lipids and analyte solutions were flowed through the QCM-D flow cell at 0.2 mL.min⁻¹, and the sample environment was set to 38 °C for the duration of the experiment.

The prepared sample, once sonicated, was injected into the flow cell and the process of SLB formation is carried out [24]. The decreasing initial frequency at (1) occurs from the injection of the lipid sample and the initiation of deposition at the sensor surface: from equation 2.4 we know decreasing frequency is proportional to increasing mass. Point (2) corresponds to vesicle rupture, and the decrease in mass corresponds to the loss of trapped buffer from inside the vesicles to the bulk solution. SLB formation has largely taken place by point (3). To ensure bilayer formation point (4) shows the changing of the bulk solution from D₂O based buffer to pure D₂O to force any remaining adsorbed vesicles to rupture via osmotic shock. The increase in frequency here corresponds to the lower density of the pure D₂O. Point (5) shows the return to the frequency of the SLB. Changes to ΔD typically mirror that of the changes in Δf , with lower values of ΔD corresponding to thinner more rigid layers.

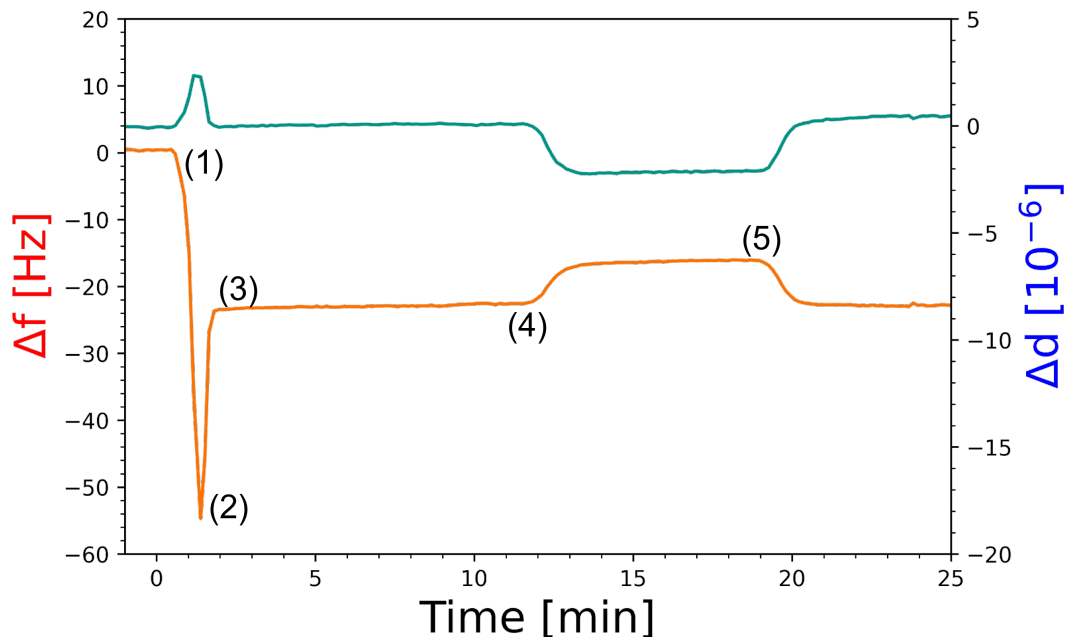


Figure 2.4: A typical example of changes to frequency and dissipation during the deposition of a supported lipid bilayer at the Si-water interface. Here a single overtone is shown for both Δf (frequency) and ΔD (dissipation) with the important times labelled: (1) lipid vesicle injections, (2) vesicle adsorption and spontaneous rupture (3) SLB formation, (4) osmotic shock with pure D_2O , and (5) buffer wash.

2.7 Neutron Reflection and Scattering Experiments

Neutron scattering is a facility type technique that allows detailed atom-scale analysis of experimental systems. Generally, the techniques used are non-damaging and are capable of deep interfacial analysis in a way that X-ray scattering experiments are not. Neutron scattering length densities (nSLDs) vary across the periodic table in a random way, and are even different amongst isotopes - for example 1H and 2H have vastly different nSLDs. This fundamental property of neutron scattering allows for the use of *isotopic contrast* as an extremely useful tool for the analysis of biological systems that contain a lot of water, enabling different parts of the system to be highlighted.

2.7.1 Theory

The study of matter using neutrons relies on the measurement of the transfer of momentum from incident neutrons and scattered, reflected or transmitted neutrons after interacting with a sample. Since it is not always possible to resolve individual scattering components an average nSLD value, ρ , is used. The fitting of a model to empirical data is then used to best describe the measurements that are taken, often with an associated amount of uncertainty. In the case of small angle scattering measurements, the scattering intensity,

$I(Q)$, is measured after the sample, and is recorded as a function of the angle of the scattering that has taken place [25].

Reflectivity measurements are recorded as R vs Q plots, and are converted into one dimensional nSLD profiles. These nSLD profiles can be used to determine the density, roughness, and thickness of each of the layers in the model being fit to the data. This is usually achieved through a least-squares type fit between the calculated and experimentally obtained reflectivity profiles [26].

In both cases, the use of hydrogen and deuterium containing water can be used to highlight various parts of the system with different solution $^1\text{H}/^2\text{H}$ ratios. This means that the substrate and solvent can be contrast matched, that is, that the solvent is mixed with the appropriate amount of H_2O and D_2O in order that the solvent and substrate are indistinguishable in terms of their component nSLDs. This is a method of allowing the desired parts of the system to be better resolved during analysis. Further, by fitting multiple sets of contrast data using a single set of parameters, one can avoid over-fitting the data, and is also able to reduce the uncertainty bounds the data carries.

2.7.2 Instruments and Setup

Neutron Reflectometry

NR measurements were carried out using the white beam OFFSPEC reflectometer at the ISIS Spallation Neutron and Muon Source, Rutherford Appleton Laboratory (Oxfordshire, U.K.), which use neutron wavelengths from 1 to 14 Å. The reflected intensity was measured at incidence angles of 0.7° and 2.0° . Reflectivity was measured as a function of the momentum transfer, Q_z ($(4\pi \sin \theta)/\lambda$, where λ is wavelength and θ is the incident angle).

Purpose built liquid flow cells for analysis of the silicon-liquid interface were placed on a variable angle sample stage in the NR instrument and the inlet to the liquid cell was connected to a liquid chromatography pump (L7100 HPLC pump, Merck, Hitachi) to enable exchange of the solution contrasts within the sample cells. For each isotopic contrast, 22.5 mL of 20 mM pH/pD 7.2 HEPES 2 mM CaCl_2 buffer solution was pumped through the cell at a rate of 1.5 mL/min, ensuring that the new contrast had filled the cell and the previous contrast solution was fully washed out.

2.7.3 Modelling Methods

Neutron Reflectometry

NR data were analyzed using the RasCAL fitting package (version 2014b, A. Hughes, ISIS Spallation Neutron Source, Rutherford Appleton Laboratory) to fit layer models of the interfacial structure to the experimental reflectivity data

[27]. The program allows simultaneous fitting of multiple data set parameters such as the layer thickness and roughness. The custom fitting area of the program is used to define relationships between the scattering length density (SLD), layer thickness, and the lipid/SAM area per molecule [28].

Models describing the interfacial layer structure between the silicon substrate (super phase) and the buffered water (subphase) consisted of an SiO₂ layer, a Nickel-Iron *permalloy* layer, a gold layer, a self-assembled monolayer (SAM), a water interlayer, inner bilayer headgroups, bilayer tails, and outer bilayer headgroups. NR data were obtained using HEPES buffered subphases (20 mM HEPES pH/D 7.2) with the following solution contrasts:

- D₂O
- H₂O
- Silicon matched water (SiMW, 75% D₂O)
- Gold matched water (AuMW, 37% D₂O)

The fitting parameters for SiO₂, gold, and *permalloy* under-layers were assumed to be the same across all data sets obtained under varying solution isotopic contrast conditions. The organic layers, SAMs and the bilayers were fitted by area per molecule with associated percentage bilayer coverage parameters. This allowed for the linking of the lipid headgroup and tail parameters such that the number density of these components was the same (as they are part of the same molecule). This approach minimized the number of free parameters in the model, and it yields useful quantities, such as hydration or area per molecule [29]. All model fits used in the results chapters that follow assumed the presence of the underlayers before and after bilayer deposition, and the models were designed with flexibility in mind so as to avoid over-fitting of the data. The flexibility seeks to let the interaction(s) happen, if at all, by allowing the experimental data to best fit to the model without attempting to prescribe anything within the model. A schematic of the rudimentary bilayer model that was used to resolve lipid-polyphenol interactions is given in figure 2.5. It shows the silicon, *permalloy*, and gold underlayers along with the SAM (purple) and floating lipid bilayer (yellow) along with the bulk solution.

Reflectivity data sets were obtained for the SAM/gold/*permalloy* coated silicon surfaces in the absence of the bilayer at the interface. These data sets were further used to constrain the fitting of the SAM, gold, and *permalloy* layers of the interfacial structure in order to achieve low ambiguity solutions for the interfacial structures. Bayesian error estimate routines were run in RasCAL to provide errors on the model fits and to help resolve the data with reduced ambiguity [30]. The best fit parameters were taken as the distribution maxima and the uncertainties were given from the shortest 95% confidence intervals of each distribution.

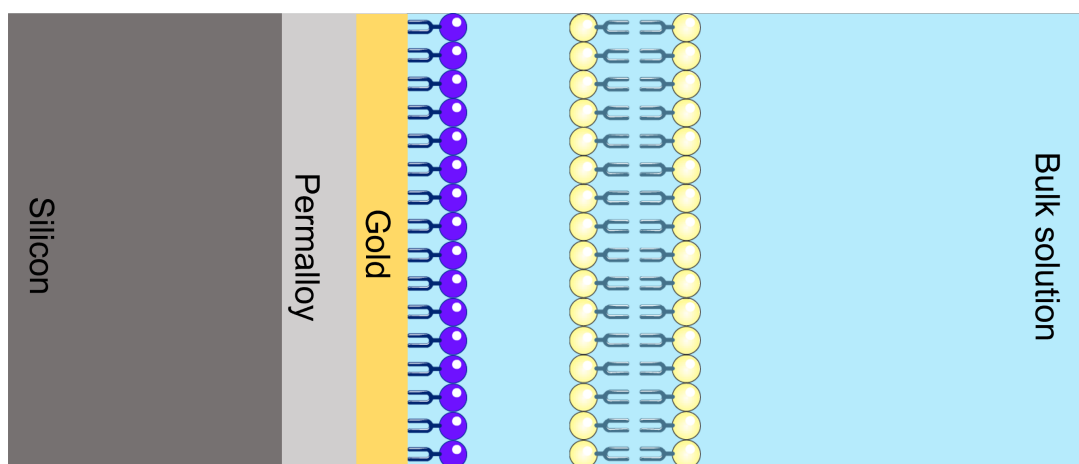


Figure 2.5: Schematic depicting the layers assumed to be present and used for all initial neutron reflectometry fits showing the under layers, SAM (purple), floating lipid bilayer (yellow), and bulk solution.

References

- [1] F. Bordi and C. Cametti, *Biomembranes*, Elsevier, 2005.
- [2] W. D. Harkins, *The physical chemistry of surface films*, Reinhold, 1952.
- [3] H. Zhu, R. Sun, T. Zhang, C. Hao, P. Zhang, J. Wang and S. Li, *J. Nanomater.*, 2015, **2015**, 7–16.
- [4] M. R. Sanders, L. A. Clifton, R. A. Frazier and R. J. Green, *Langmuir*, 2016, **32**, 2050–2057.
- [5] K. Gong, S. S. Feng, M. L. Go and P. H. Soew, *Colloids Surfaces A Physicochem. Eng. Asp.*, 2002, **207**, 113–125.
- [6] M. Arczewska and M. Gagoś, *Biochim. Biophys. Acta - Biomembr.*, 2011, **1808**, 2706–2713.
- [7] J. Hu, X. Li, M. Li, Y. Shang, Y. He and H. Liu, *Colloids and Surfaces B: Biointerfaces*, 2020, **190**, 110922.
- [8] G. Höhne, J. McNaughton, W. Hemminger, H.-J. Flammersheim and H.-J. Flammersheim, *Differential scanning calorimetry*, Springer Science & Business Media, 2003.
- [9] R. N. Lewis, D. A. Mannock and R. N. McElhaney, *Methods in Membrane Lipids*, 2007, 171–195.
- [10] S. Mabrey and J. M. Sturtevant, *Proc. Natl. Acad. Sci. U. S. A.*, 1976, **73**, 3862–3866.
- [11] M. H. Chiu and E. J. Prenner, *Journal of Pharmacy and Bioallied Sciences*, 2011, **3**, 39.
- [12] T. Baumgart, S. Hess and W. Webb, *Nature*, 2003, **425**, 821–824.
- [13] S. L. Veatch, I. V. Polozov, K. Gawrisch and S. L. Keller, *Biophys. J.*, 2004, **86**, 2910–2922.
- [14] A. R. Hind, S. K. Bhargava and A. McKinnon, *Advances in Colloid and Interface Science*, 2001, **93**, 91–114.
- [15] G. W. Hughes, S. C. Hall, C. S. Laxton, P. Sridhar, A. H. Mahadi, C. Hatton, T. J. Piggot, P. J. Wotherspoon, A. C. Leney, D. G. Ward, M. Jamshad, V. Spana, I. T. Cadby, C. Harding, G. L. Isom, J. A. Bryant, R. J. Parr, Y. Yakub, M. Jeeves, D. Huber, I. R. Henderson, L. A. Clifton, A. L. Lovering and T. J. Knowles, *Nat. Microbiol.*, 2019, **4**, 1692–1705.

- [16] J. A. Jackman and N. J. Cho, *Langmuir*, 2020, **36**, 1387–1400.
- [17] F. Evers, C. Jeworrek, S. Tiemeyer, K. Weise, D. Sellin, M. Paulus, B. Struth, M. Tolan and R. Winter, *Journal of the American Chemical Society*, 2009, **131**, 9516–9521.
- [18] L. A. Clifton, R. A. Campbell, F. Sebastiani, J. Campos-Terán, J. F. Gonzalez-Martinez, S. Björklund, J. Sotres and M. Cárdenas, *Adv. Colloid Interface Sci.*, 2020, **277**, 102118.
- [19] B. H. Stuart, *Biological applications of infrared spectroscopy*, John Wiley & Sons, 1997.
- [20] N. J. Cho, C. W. Frank, B. Kasemo and F. Höök, *Nat. Protoc.*, 2010, **5**, 1096–1106.
- [21] P. Parkkila, M. Elderdfi, A. Bunker and T. Viitala, *Langmuir*, 2018, **34**, 8081–8091.
- [22] M. C. Dixon, *J. Biomol. Tech.*, 2008, **19**, 151–158.
- [23] G. Sauerbrey, *Zeitschrift für Phys.*, 1959, **155**, 206–222.
- [24] C. A. Keller, K. Glasmästar, V. P. Zhdanov and B. Kasemo, *Physical Review Letters*, 2000, **84**, 5443–5446.
- [25] G. Fragneto, R. Delhom, L. Joly and E. Scoppola, *Curr. Opin. Colloid Interface Sci.*, 2018, **38**, 108–121.
- [26] G. Fragneto and M. Rheinstädter, *Comptes Rendus Phys.*, 2007, **8**, 865–883.
- [27] L. G. Parratt, *Physical review*, 1954, **95**, 359.
- [28] L. A. Clifton, N. Paracini, A. V. Hughes, J. H. Lakey, N.-J. J. Steinke, J. F. Cooper, M. Gavutis and M. W. Skoda, *Langmuir*, 2019, **35**, 13735–13744.
- [29] A. V. Hughes, S. A. Holt, E. Daulton, A. Soliakov, T. R. Charlton, S. J. Roser and J. H. Lakey, *Journal of The Royal Society Interface*, 2014, **11**, 20140447.
- [30] D. S. Sivia and J. R. Webster, *Physica B: Condensed Matter*, 1998, **248**, 327–337.

—You don't have to know
how to finish the project, you
just have to know what the
next step is.

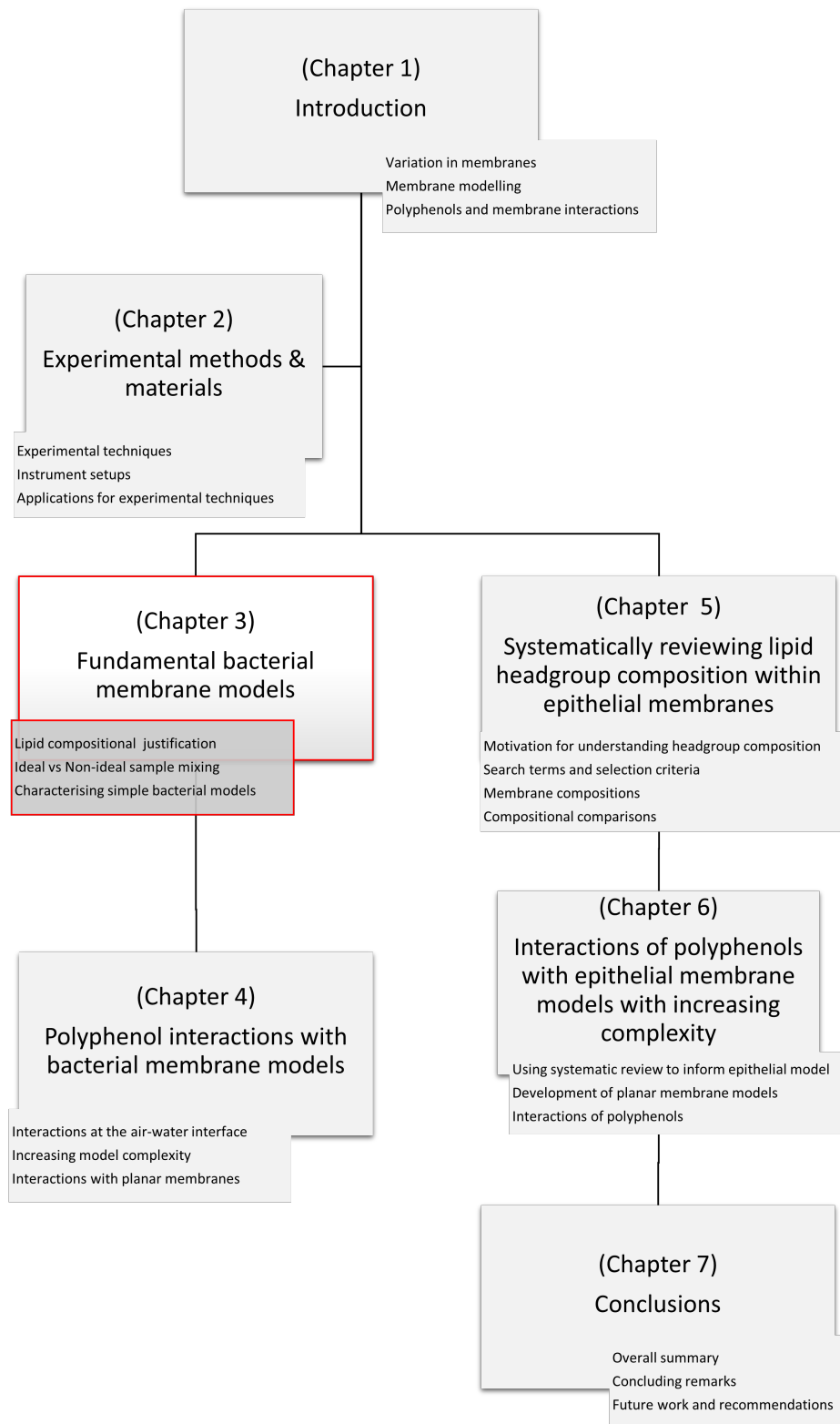
Adam Savage

3

Design & Synthesis of a Bacterial Membrane Model

Contents

3.1	Bacterial Membrane Composition	66
3.1.1	Lipid Compositional Justification	66
3.2	Results & Discussion	67
3.2.1	Fundamental Bacterial Membrane Models	67
3.2.2	Calorimetric Behaviour of Bacterial Model Membranes	68
3.3	Model Membrane Characterisation with Supported Lipid Bilayers	71
3.3.1	Structural Evaluation of Model Bacterial Membrane using Neutron Reflectometry	74
3.3.2	Discussion	76
3.4	Summary	80



3.1 Bacterial Membrane Composition

Bacterial membranes come in many forms. Considered here are two major classifications of bacterial membranes; Gram-positive, and Gram-negative. Gram-positive membranes have only one cell membrane which is supplemented by thick layers of peptidoglycan. By contrast Gram-negative bacteria have both an inner and an outer membrane, along with thinner peptidoglycan layers. Further, there are distinct difference in the lipopolysaccharide (LPS) compositions of the two bacterial membrane types along with greater thickness of the external peptidoglycan layers in Gram-positive bacteria [1]. In terms of lipid composition, the most predominant zwitterionic lipid headgroup is PE, along with PG lipids and cardiolipin (CL) [1, 2].

3.1.1 Lipid Compositional Justification

The compositional justification for bacterial membrane models is covered in detail in Chapter 5. The literature at large shows that model bacterial membranes contain PE-lipids in order to reflect their prevalence in nature, and this holds true in the case of Gram-negative bacteria [3]. Further, PG-lipids are frequently combined with PE as they too form a large portion of the Gram-negative membrane. This mixed PE/PG system is more relevant than a PE system alone and functions as a bacterial membrane model [1, 4–6]. Often for simplicity and reliability, a two component membrane is used with cardiolipin being omitted from the mixture [7–10]. The use of a two component mixture allows good control over the membrane and allows interactions with the model membrane to show how the two major membrane lipids behave. Single lipid component models were initially tested, serving as a baseline to better characterise and understand more complex lipid mixtures and their interactions in the work that follows.

The wider goal of the membrane modelling and mimetics is to more accurately replicate naturally occurring biological systems so as to understand a particular element or property of that system. Through increasing accuracy one can apply the model to better test and understand its behaviour [11]. To be able to have a more complex and relatively more accurate membrane model, first the building blocks of the model system have to be well understood and appropriately characterised. To that end, this chapter sets up the foundations for more complex and accurate models that follow later that investigate at the interactions of model membranes with polyphenolic compounds.

Lipid vesicle samples are often prepared through vortexing or bath sonication procedures [8, 12]. These do allow control of the size of the lipid vesicles but for lipid mixtures they only show a single DSC peak corresponding to a lipid phase transition. This does not allow for resolution of individual membrane components and thus does not account for lipid domain formation in model membranes. Since, as addressed above, lipid domain formation is known to be a genuine phenomenon, model membranes should be able to reflect this [13, 14]. This is a subject that is explored further in the sections of the chapter that

follow in an effort to mimic real biomembranes. A variety of factors beyond sample preparation can affect the homogeneity of the lipid mixing, such as the differing chain lengths and head groups charges[15]. Differences between the lipid headgroups in terms of size or charge can be enough to induce non-ideal mixing[5]. The individual lipid components here have transition temperatures that are consistent with other literature values [3, 8, 16, 17].

3.2 Results & Discussion

3.2.1 Fundamental Bacterial Membrane Models

The first step in understanding a complex multi-component model set about characterising the individual lipids that were going to be used as constituent parts of multi-lipid mixtures in future work. For the most part, this involved experiments using a Langmuir Trough and Differential Scanning Calorimetry (DSC). The details for the experimental setups for these techniques is given in chapters 2.3.2 and 2.4. There were 5 individual lipids used for this initial characterisation for the monolayer work: DPPC, DPPG, DPPE, DOPC, and DOPG. Their structures are shown in figure 3.1.

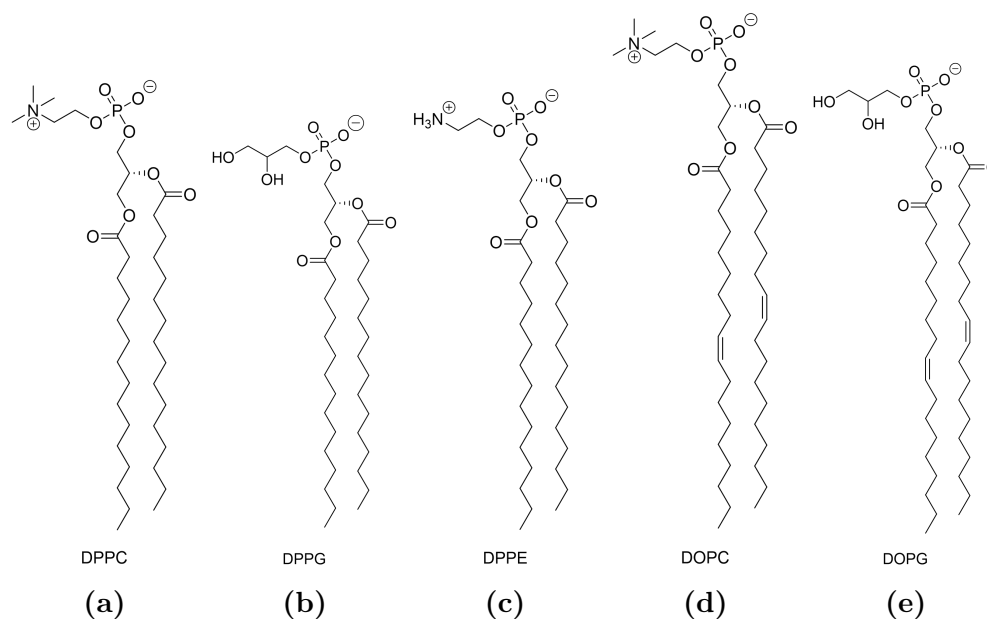


Figure 3.1: Skeletal lipid structures for (a) DPPC, (b) DPPG, (c) DPPE, (d) DOPC, and (e) DOPG.

Surface Pressure Isotherms of Individual Lipid Components

Isotherms for individual lipid components are given in figure 3.2. DPPC and DPPG both show 3 distinct lipid phases, confirmed by minima (4 and 8 $\text{mN}\cdot\text{m}^{-1}$ respectively) in their compressibility modulus. The phase transitions accompanied by these minima are from the liquid expanded (LE) to the

condensed (C) phase, where the individual lipids in the monolayer go from sometimes interacting with a neighbour as compression occurs to being packed like a solid where all lipids are in physical contact with all lipids immediately adjacent to themselves. The LE phase then becomes a more solid and condensed (C) phase where the lipids are tightly packed with their neighbours on all sides. As compression continues, the layer loses its elasticity until no more compression will change the individual area per molecule. For a more complete description of the lipid phases at the air-water interface the reader is referred back to figure 2.1.

By comparison DPPE shows a biphasic isotherm with only one phase transition from the gaseous to the condensed phase at around 100 \AA^2 per molecule [18, 19]. Here, DPPE behaves immediately much more like a solid layer and is much less elastic when compared to DPPC and DPPG despite the tail length and unsaturation being identical. This inelasticity is shown in the compressibility modulus by the C_s^{-1} value becoming very large at comparatively low surface pressures. The isotherms for DOPC and DOPG are much more amorphous in terms of the phase information they contain. Due to the *cis* geometry of the double bond in DOPC and DOPG the two tails diverge from one another. This leads to the tails of DOPC and DOPG lipids taking up far more three dimensional space, and so during compression they pack in a less perfect manner than the other lipid isotherms shown. As a result the monolayer collapses at a larger area per molecule (APM) when compared to lipids with identical headgroups and fully saturated tails. The lack of packing order is evidenced in the compressibility modulus plots for DOPC and DOPG where there are no observable minima corresponding to a phase transition. DOPC and DOPG behave far more like elastic and gaseous layers throughout compression, and the collapse of the DOPG monolayer is apparent where the C_s^{-1} begins to drop to 0. The isotherms shown in figure 3.2 were taken from the second repeat of a set of 3 measurements and show phase transitions consistent with the literature [11, 20–25]. The compressibility moduli are vertically offset for clarity.

3.2.2 Calorimetric Behaviour of Bacterial Model Membranes

Lipid Vesicle Preparation: Ideal versus Non-Ideal Mixing

During the preparation of early bacterial membrane models, as described in chapter 2, it was noticed that the method of liposome preparation would yield varying results in DSC scans of the lipid samples, and the results showing this are given later (figure 3.3) and are explored. The difference between the two preparation methods (from chapter 2) is exemplified in figure 3.3 through the non-ideally mixed vesicles displaying signs of phase separation. In the DSC scans, this manifests as separation of the two individual component peaks for the non-ideal sample compared to the one broad peak for the homogeneously mixed sample [26]. The presence of domain formation is also indicated by the shoulder on the highest temperature peak, in this case corresponding to DPPE,

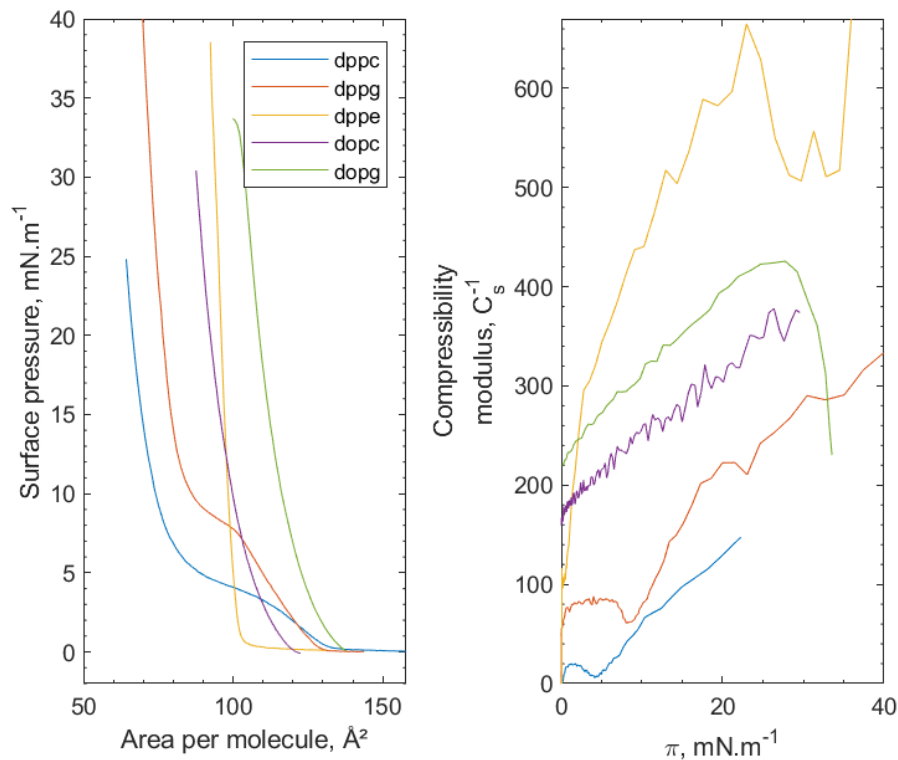


Figure 3.2: (Left) Pressure-area isotherms of the individual lipid components used in the process for forming a bacterial membrane model. DPPC (blue) and DPPG (orange) show 3 distinct phases, while DOPC (purple) and DOPG (green) show condensed phases at relatively large APM compared to their longer, more saturated, chain counterparts. DPPE (yellow) also shows only two phases. (Right) Compressibility moduli for each lipid are given, depicting the elasticity of the monolayer. Colours of the compressibility moduli are matched to the pressure-area isotherms, and have been vertically offset for clarity.

for the non-ideal DPPE/DPPG (3:2) sample which indicated non-ideal mixing [8].

Similarly to characterising lipids in a monolayer format the membrane models also need characterising as bilayers. In differential scanning calorimetry (DSC) we investigated lipid vesicles in solution, thus allowing measurements of lipids in a bilayer form, providing another angle of investigation when combined with the monolayer experiments. DSC also allowed investigation of the transition temperatures of lipid vesicles to be monitored with the presence of polyphenol in the liposome, and this is discussed later in chapter 4. Figure 3.3 shows DSC thermograms of 3 individual lipid components, DPPC, DPPE, and DPPG, along with ideally and non-ideally mixed lipid samples composed of DPPE/DPPG (3:2) mixtures. The rationale for ideal versus non-ideal mixing are considered in section 3.2.2. The thermograms for each lipid show the transition temperature from the gel phase (L_β) to the liquid crystalline phase (L_α) through a shift in the orientation of the tail groups. For a schematic see figure 1.4.

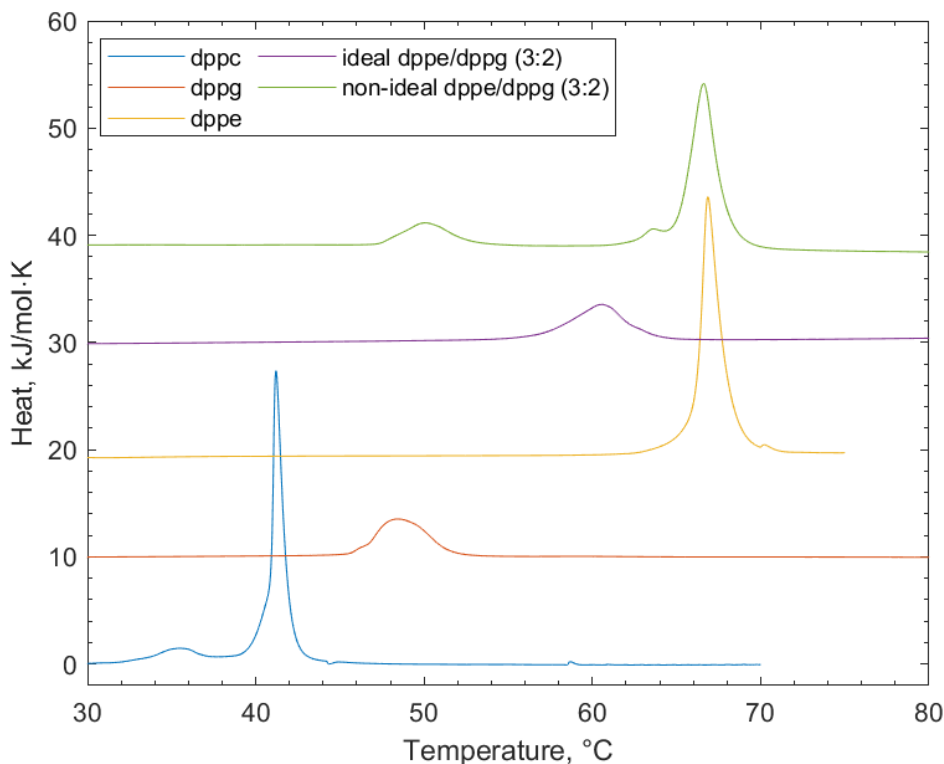


Figure 3.3: DSC thermograms for the single lipids and the bacterial mixtures to demonstrate the phase transition temperatures of the individual and mixed components.

The ideal mixture allows for components that ordinarily would not coexist in the perfect sense to be forced into a state where the long range average of each of the components over a given space are equal in ratio. That is, for any given area of 10 selected lipids in a two component mixture, there would be

precisely 5 of one type and 5 of another. Non-ideal mixing on the other hand gives more freedom to the components in the membrane, allowing them to diffuse laterally as their equilibrium state dictates. In this way, lateral domain formation is enabled giving rise to so-called *lipid rafts* [27–31]. Lipid rafts are sections of the membrane that contain disproportionate amounts of some components compared to their amounts in the membrane as whole.

The ideally mixed lipid samples show a T_m that lies between the two peaks for the two individual lipids in the ratio of the two lipids. We can see from table 3.1 that the measured transition temperature for the ideal mixture does fall between the two individual lipid peaks at 60.5 °C. The non-ideal lipid mixture shows two peaks - one for each of the lipid components. Due to the nature of the sample preparation, distinct lipid domain formation is enabled. As a result of these stable lipid domains each lipid component is responsible for producing a peak in the thermogram in figure 3.3. The shoulder on the DPPE peak in the non-ideally mixed lipid sample is indicative that there exists non-uniform mixing of components in the sample consistent with phase separation of the lipids [8, 26]. Value for all transition temperatures of lipid samples from figure 3.3 are given in table 3.1 along with their associated error values.

Table 3.1: Mean transition temperatures for the individual lipids and ideal plus non-ideal lipid mixtures along with associated standard deviation (S.D.) and standard error (S.E.) values.

	Mean Temp, °C	S.D.	S.E.	Mean Temp, °C	S.D.	S.E.
DPPC	41.16	0.01	0.01	-	-	-
DPPG	47.93	0.45	0.22	-	-	-
DPPE	66.90	0.08	0.04	-	-	-
ideal DPPE/ DPPG (3:2)	60.51	0.17	0.10	-	-	-
non-ideal DPPE DPPG (3:2)	51.57	1.29	0.58	67.02	0.32	0.14

3.3 Model Membrane Characterisation with Supported Lipid Bilayers

Building on the foundation from the membrane models that were analysed using the Langmuir trough and DSC methods supported lipid bilayer models have also been investigated. SLBs are one of the main methods for forming lipid bilayers at an interface and performing interaction studies. The methods for forming these types of systems are covered in sections 2.5 and 2.6. The advantage of SLBs is that they allow experimentation on planar lipid bilayers where, compared to vesicles, the geometry of the membrane can be more precisely controlled. This offers more structural insight than perhaps a monolayer or vesicle experiment might offer.

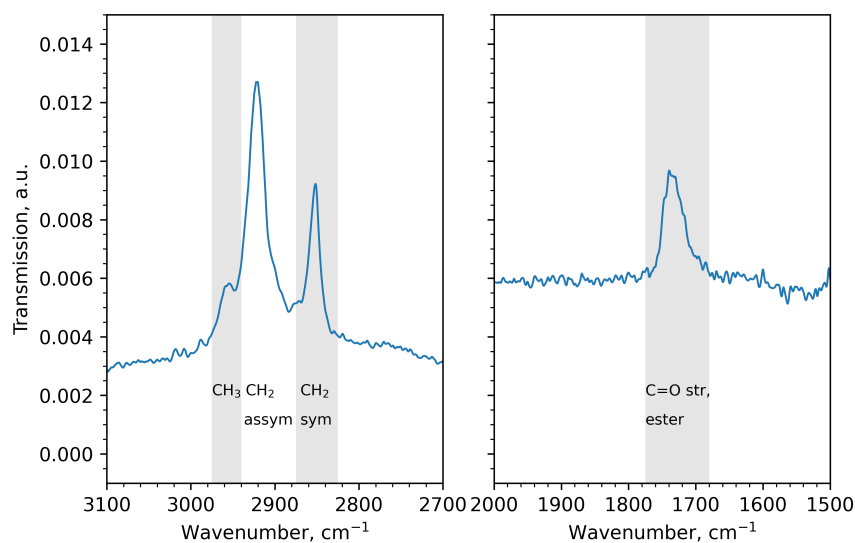
For analysis of SLBs using FTIR and QCM-D, and for the more sophisticated neutron reflectometry (NR) experiments that followed, there are issues of membrane fluidity that need to be considered when trying to spontaneously form bilayers. To ensure that the ability to physically form a bilayer did not become a barrier to working with lipid membranes with these kinds of surface sensitive techniques, the amount of PC-containing lipids was increased to both reduce the effects of the PG-lipid headgroup charge and to encourage spontaneous bilayer formation and avoid hexagonal phase formation [32].

The ATR-FTIR spectrum for a DOPC/DOPG (7:3) SLB system is shown in figure 3.4b with the features for the bilayer being highlighted in red and green. The features in red show the part of the spectrum that contains the vibrational modes associated with the aliphatic C-H part of the hydrocarbon tail. The green highlighted features contain the ester C=O vibrational modes associated with the linker group of the lipid headgroup and tail region. In yellow are highlighted the features that are associated with the buffer solutions. In particular, the major peak at around 2500 cm^{-1} is related to the D_2O in the sample while the smaller feature at *ca.* 3300 cm^{-1} indicates the presence of any residual H_2O vapour [33–36]. Full assignment of the peaks from the lipid DOPC/DOPG (7:3) SLB are given in table 3.2, and a visual breakdown of the CH_3 and CH_2 stretching modes are given in figure 3.4a. The presence of these peaks, and their persistence after washing the flow cell with buffer solution, is assumed to be indicative of the formation of a supported lipid bilayer.

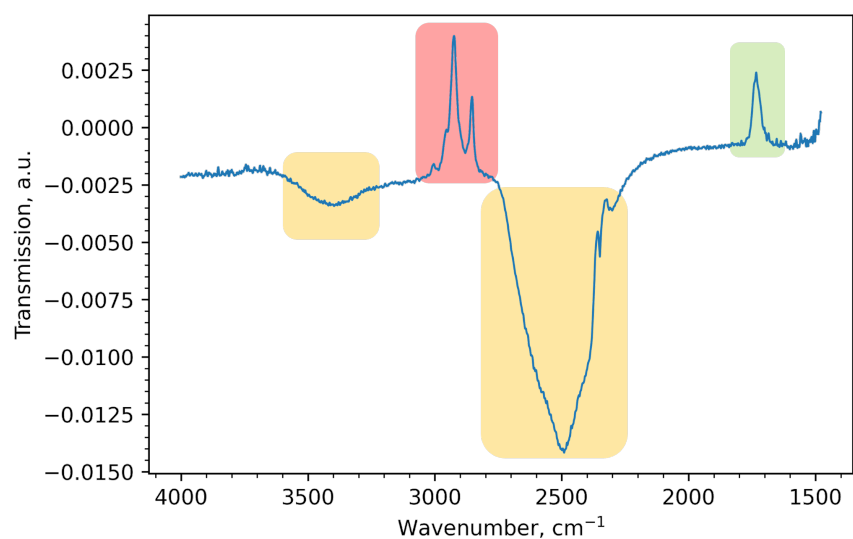
Table 3.2: FTIR peak assignments for aliphatic lipid regions as well as H_2O and D_2O from the buffer. *ss* - symmetric stretch; *as* - asymmetric stretch

Peak assignment	Wavenumber, cm^{-1}
CH_3 <i>as</i>	3000
CH_2 <i>as</i>	2950
CH_2 <i>ss</i>	2860
$\text{C}=\text{O}$ <i>ss</i>	1730
OD <i>ss</i>	2450
OD <i>as</i>	2540
OH <i>ss</i>	3280
OH <i>as</i>	3490

To complement FTIR as a method for investigating interactions with membranes at a sensor interface, QCM-D is useful for quantifying changes in mass at the surface of a sensor. The stages of SLB formation using QCM-D have already been outlined in figure 2.4. The formation of a DOPC/DOPG (7:3) bilayer using QCM-D is shown in figure 3.5. The key stages of the SLB formation process are annotated in the figure, with clear similarities to those shown previously in figure 2.4. The sudden loss of mass at around $t = 30$ mins is likely due to the washing out of a small air bubble attached to the surface of the sensor given that it is accompanied by a slight increase in ΔD , indicating a slight softening of the layer. The frequency changes (*ca.* -25 Hz), along with



(a)



(b)

Figure 3.4: ATR-FTIR spectrum for DOPC/DOPG (7:3) supported at the Si-water interface cropped to show the (a) aliphatic C-H vibrational modes for the lipid hydrocarbon tails and the ester stretching mode. The full spectrum is shown in panel (b) with areas of interest highlighted in coloured boxes. Features for O-D and O-H are coloured in yellow, aliphatic C-H features are in red and the ester C=O in green. Peak assignments are given in table 3.2.

the dissipation changes, are consistent with literature reports of SLB formation [37–40]. Differences in terms of the gap between the traces for Δf and ΔD are not important, and varying gaps between QCM-D figures are the results of having applied different offsets. Small amounts of drift in the Δf and ΔD are attributed to noise with the measurement, and can be explained by keeping the flow cell under constant solution flow manifesting as artificial mass changes due to the pressure of the solution on the sensor.

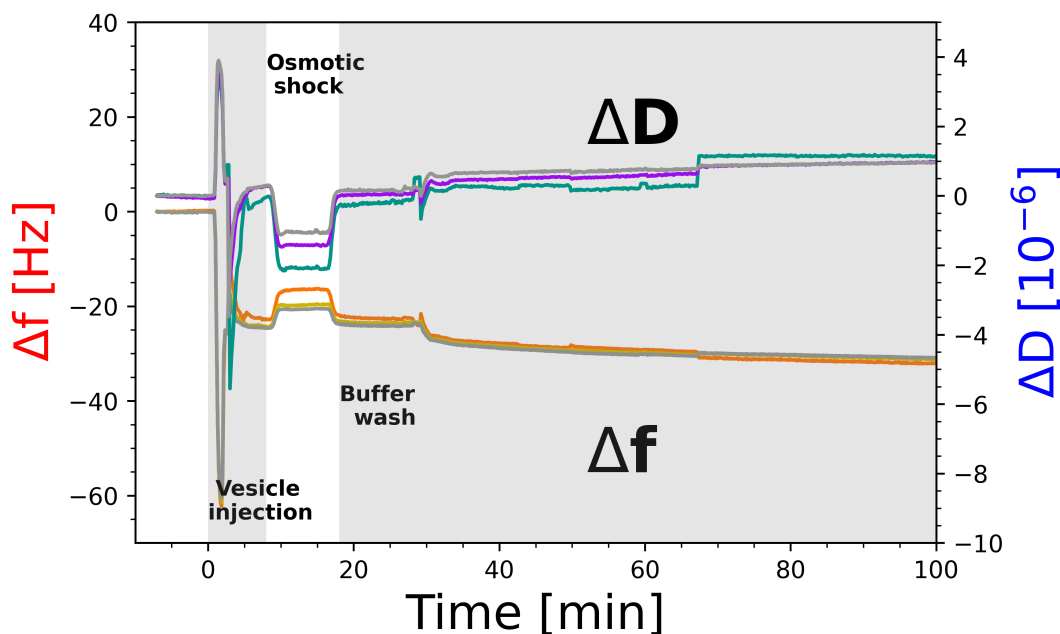


Figure 3.5: Example of changes to frequency and dissipation during the deposition of a DOPC/DOPG (7:3) SLB at the Si-water interface. Critical changes to the system are indicated in the in-figure annotations highlighting vesicle adsorption, rupture, and buffer wash to remove any loosely bound unruptured vesicles.

3.3.1 Structural Evaluation of Model Bacterial Membrane using Neutron Reflectometry

The systems used for forming SLBs are developed and modified to make them suitable for analysis using neutron reflectometry (NR). The experimental setup and detail have already been covered in chapter 2. The major difference between the membranes formed for the FTIR and QCM-D analysis above and the membranes used in NR is that the neutron samples used a *floating membrane*. The membrane for NR is suspended over a gel-like water gap that sits between the functionalised underlayers and the membrane [41]. The functionalisation here refers to a terminal group charged oligo (ethylene glycol) alkanethiol self-assembled-monolayers (SAMs) that was used as a support for membrane formation via vesicle fusion [41].

A key point to note: the floating bilayer systems for neutron reflectometry are at the cutting edge of surface science research. As membrane modelling

methods, compared to monolayers or to tethered bilayers they are still relatively in their infancy. While the technique nor the bacterial model membrane systems are not novel, they are important at the outset of this work to set a solid foundation for which later work can be based upon.

Reflectivity profiles for a DOPC/DOPG (7:3) model bacterial membrane are shown in figure 3.6 panels A-D for the H₂O, gold (AuMW) and silicon matched water (SiMW), and D₂O solution contrasts. The scattering length density (SLD) profiles are shown in panel E, and describe how the SLD of the material changes based on the distance from the underlayers. Because of the hydrogenous nature of the lipids used in the membrane the changes to the reflectivity of the surface can most clearly be seen in the D₂O contrast (figure 3.6, panel A). The colour in the reflectivity profiles and the SLD profiles are matched for clarity. The error bounds on the SLD profile (shaded red/blue areas) are derived from the Bayesian error estimation routines in the RasCAL program (see section 2.7.3). The fits of the model membrane data show that a high coverage bilayer (95%) was formed, and was floating on a 6 Å thick water gap. The area per molecule for the DOPC/DOPG lipid mixture was (73 Å²) is consistent with the area required in the condensed lipid phase from the pressure-area isotherms of the two lipid components shown in figure 3.2. Some other key parameters from the fitting are shown in table 3.3 along with their associated errors.

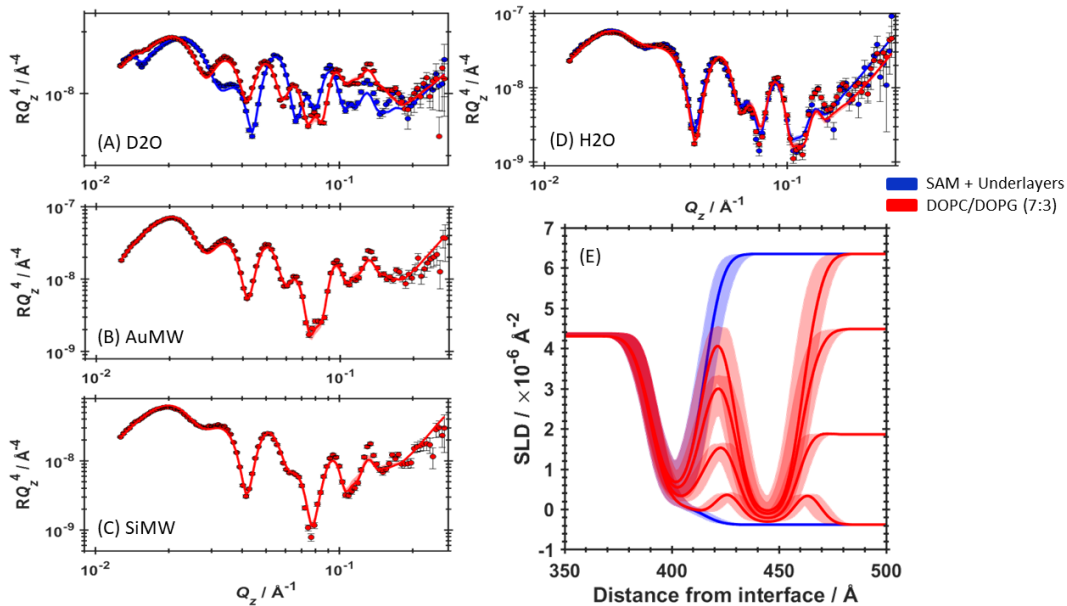


Figure 3.6: Panels (A-D) showing neutron reflectivity profiles for data (points) and model fits (lines) for a COOH-SAM/Gold/Permalloy coated silicon substrate (blue) with DOPC/DOPG (7:3) model membrane (red) in various contrast solutions. (E) Neutron SLD profiles showing the Si-Py-SAM-COOH underlayers (blue) with DOPC/DOPG (7:3) bilayer (red) interaction in H₂O, gold and silicon matched water, and D₂O contrasts. The SLD profile (E) has been cropped to show membrane regions more clearly, leaving out the underlayers.

Table 3.3: Parameter values and error bounds (upper bound, lower bound) for key parameters from the fitting and error estimation routines for a DOPC/DOPG (7:3) model bacterial floating membrane.

Parameter	Value
Central water thickness, Å	6.53 (5.94, 6.59)
Bilayer coverage, %	95.3 (94, 97)
Bilayer roughness, Å	5.69 (5.49, 5.95)
Lipid APM, Å ²	73.95 (73.68, 75.21)

In order to best highlight the different areas of the SLD profile the DOPC/DOPG (7:3) SLD profile from figure 3.6 has been overlaid on top of a schematic of a lipid membrane in figure 3.7. Again, the underlayers have been cropped out to better showcase the crucial bilayer components. Diagrammatically, the gold and the underlayers are depicted by the gold block from 360-385 Å from the interface. Grafted onto the gold is the SAM shown at around 400 Å from the interface. The two peaks in the H₂O contrast at 425 and 465 Å show the inner and outer lipid headgroups of the bilayer with the tail regions situated in between. The bulk solution is the buffer that fills the cell outside the bilayer distal to all the underlayers and the SAM. When interaction studies are performed by injecting compounds into solution, it is in this space away from the underlayers where the injection takes place. The setup for these cells is analogous to that shown in figure 2.2 for FTIR experiments.

3.3.2 Discussion

The use of monolayers (Langmuir trough measurements, figure 3.2) and lipid vesicle (DSC) experiments (figure 3.3) gives insight into some of the physical properties of the lipids that are appropriate for use in model bacterial membranes. Understanding how the lipids pack together and the phases that they can occupy is useful when trying to understand how each lipid will behave in both single and multi-component membranes. DPPC and DPPG both showed 3 different phases depending on the area available to each molecule, where DPPE showed only a single phase transition (*ca.* 103 Å²) and behaved very much like a solid at the interface despite the tails being identical in length and unsaturation in all 3 lipids. This demonstrates that DPPE has a very high packing order and forms an incredibly stable monolayer. DPPC and DPPG do also display packing order, but only when sufficiently compressed, having gone through a less well ordered LC phase. Increasing the unsaturation and decreasing the length of the tails leads to a stark decrease in the packing of the lipids, evidenced by the isotherms of DOPC and DOPG with transitions at *ca.* 120 and 135 Å² respectively. The increased fluidity results in a very gaseous layer at the interface with much less regularity in the packing of the lipids, and as such, a less stable membrane model. The effects of polyphenols on the compressibility of the monolayer and the packing effects of lipids are explored later on in chapter 4.

The stability contributions of each lipid can be gained from DSC experiments,

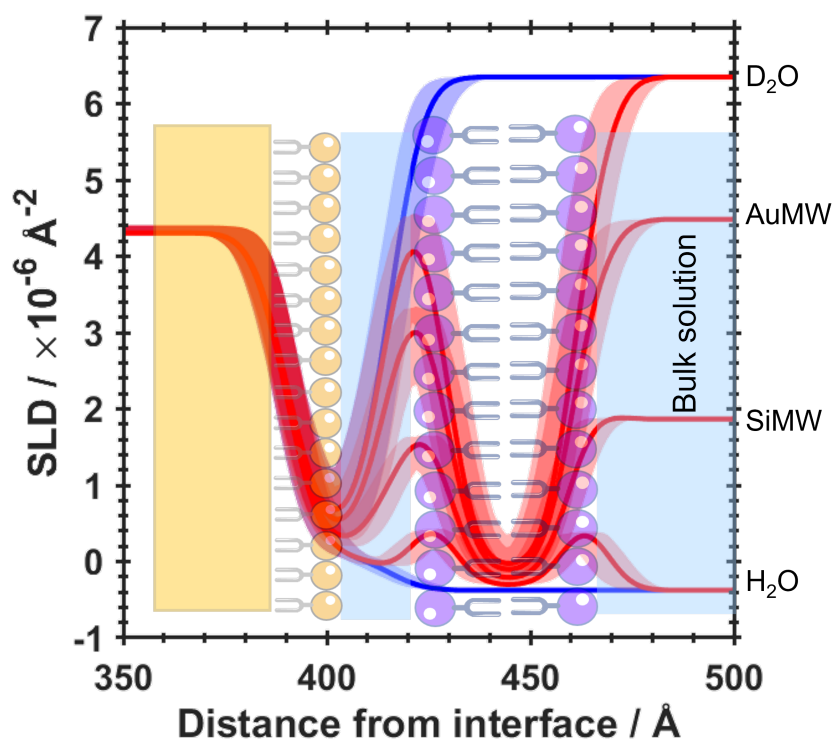


Figure 3.7: Neutron SLD profile for a DOPC/DOPG (7:3) model membrane system showing the Si-Py-SAM-COOH underlayers (blue) with DOPC/DOPG (7:3) bilayer (red) interaction in H_2O , gold and silicon matched water, and D_2O contrasts. The overlaid cartoon shows the functionalised gold surface and the attached SAM, the water gap between the underlayers and the model membrane, and the two leaflets of the membrane itself.

where higher transition temperatures for a given lipid represent a more stable lipid phase. DPPE has a much higher transition temperature (66.9 °C) than DPPC (41.2 °C) and DPPG (47.9 °C) because a lot more energy is required to transition out of a very stable lipid packing phase, corresponding to the behaviour displayed in the isotherm of DPPE. In forming a bacterial membrane model composed of DPPG and DPPE (see figure 3.3) the DSC thermograms display phase behaviour that falls between that of the two individual components.

Lipid Fluidity Challenges Surrounding Floating Bilayer Formation

At the beginning of our studies, bilayers formed by vesicle rupture had not been successful where high amounts of charged anionic lipids were used. Making the transition from vesicles to planar membrane systems can present some challenges during the process of bilayer formation. In order to form a bilayer by vesicle rupture the lipids in the system are required to be in a fluid state. Two factors that affect fluidity are the length of the tail region, and the extent of unsaturation. Externally, the temperature of the sample can be increased to push the lipid past its melting transition. Keeping in mind the accuracy of the membrane model, it is not then realistic to use lipids with melting points greater than 40 °C because it is not physiologically appropriate. For the purposes of this modelling, the compromise is to set the sample environments for lipid bilayer formation to 37 °C, and also select a lipid that has an appropriately short or unsaturated tail group that means that it is in the fluid phase below 37 °C.

If the lipid sample is suitably fluid based on the physical properties of the lipid outlined above and the temperature of the sample environment is appropriate, then SLB formation on silica for the QCM-D and FTIR samples is often spontaneous. While the samples are deposited at the interface in buffers high in salt (100 mM NaCl), the osmotic shock procedure outlined in chapter 2 will help ensure that any vesicles that have adsorbed to the surface do rupture when flushed with buffer solution containing no salt. In order to help encourage the vesicles to the surface of the substrate, be it for SLB formation or in the NR floating sample deposition, Ca^{2+} is included in the buffer solutions [41]. For NR studies, this is a critical step and without the addition of calcium to the buffer this will impact the chance of forming a high coverage membrane. The calcium acts to bridge the gap between the charged SAM surface and the lipid headgroups in the injected vesicle solution. Often, in using SLBs for FTIR and QCM-D experiments, the use of bilayers containing high amounts of PE or PG lipids would not adversely affect the formation of a bilayer. Characterisation of these membranes and understanding qualitatively if the bilayers would form (and indeed if interactions would take place) was both possible and appropriate. Unfortunately this was not the case for the formation of floating bilayer in NR experiments.

In contrast to FTIR data (figure 3.4a) and QCM-D data (3.5) the membrane

formation protocol for NR needed some development and optimisation. The addition of the calcium (*ca.* 2 mM) to the buffer solutions for the vesicle adsorption in NR experiments will keep the vesicles adsorbed to the surface once they are close enough to electrostatically interact. To help maximise adsorption further vesicles were allowed to incubate for at least 30 minutes, and during injection vesicle solution was washed back and forth over the surface repeatedly to give a high chance of surface adsorption [41, 42]. Because of the non-spontaneous floating bilayer formation in NR compared to SLB formation the osmotic shock protocol is critical for successful formation of a floating membrane, where perhaps it is not strictly necessary for SLB formation.

pH Effects During Vesicle Adsorption

Another consideration around surface charge and vesicle interactions with the surface when depositing membranes for NR studies (see figure 3.7) is balancing the charge and any potential interactions between the SAM and the bilayer lipids. In depositing bacterial membrane models containing PG-headgroups, which are anionic, there were issues getting high enough vesicle coverage of the surface to promote good bilayer formation. Given that the SAM terminates in a carboxyl group it is likely that deposition of a lipid mixture containing significant amounts of PG-lipids was going to result in large repulsive interactions between the vesicles and the SAM that the Ca^{2+} could not overcome at a neutral pH.

The method for deposition of a floating lipid membrane was developed and adapted here to allow for PG-containing bilayer to be formed. As for DSC, FTIR, and QCM-D sample and buffer solutions were kept at either pH or pD 7.2, for H_2O or D_2O solvents respectively. To address this, NR samples containing PG headgroups were deposited at pD 3. Acidic buffers for deposition would help protonate the $\text{SAM}-\text{COO}^-$ terminus and so prevent any repulsive interactions. Once osmotic shock had resulted in a floating membrane, the contrast solution would be changed to a pD 7.2 running buffer. This was both more physiologically appropriate, and when polyphenol interactions took place would not result in acid-catalysed hydrolysis of any ester moieties in the polyphenol structure.

Phase Preferences of Membrane Lipids

As well as the fluidity concerns presenting barriers to overcome during membrane formation, so too must the preference of the fluid phase for each lipid be considered. So far PC and PG lipids do not present any challenges as they have a preference for forming bilayer phases, and later in chapter 6 and beyond, phosphatidylserine (PS) lipids also form bilayers. PE by contrast forms hexagonal phases which presents complex problems in planar membrane formation [43]. Naturally, for a monolayer, there are no phase considerations that can cause problems. In DSC studies where sonication of the lipid solution immediately before measurement was viable, the presence of PE lipids in the sample did not present such a problem. With SLBs where spontaneous bilayer

formation is important and where repeated measures forcing a particular bilayer geometry, be it spherical or planar, cannot be taken then alternative lipids were sought. In this case DOPC was used instead of DPPE to overcome both the hexagonal phase problem in solution as well as avoiding any further complications with charge based SAM interactions. To match the fluidity, DOPG was selected for the PG-containing lipid. In this way the model kept a major bacterial membrane component (PG-lipids) and DOPC was used to overcome practical problems presented in membrane formation.

Once the model membranes had been formed and were deemed of sufficient quality they could be used for interaction studies. Chapter 4 introduces interactions of bacterial membrane models with polyphenolic compounds. By compromising the accuracy of the model with the introduction of more DOPC than would be found in *in-vivo* bacterial membranes, problems that would prevent any interaction studies being performed were arrested.

3.4 Summary

This chapter has outlined methods of characterisation of some model bacterial membranes, taking on various geometries. Monolayers and vesicles are used primarily to understand the phase behaviour of the lipids. They have a number of advantages including being quick to setup and easy to operate, which means they have use as a relatively high throughput method compared to SLBs, and neutron experiments which require large facilities to operate. They also help to form the foundation for more complex bilayer methods, such as ATR-FTIR and QCM-D, which allow study of planar membrane systems where more complex aspects of bilayer properties and interactions can begin to be investigated. These techniques were useful tools to develop the model membrane systems used in neutron reflectometry experiments with a more complex floating bilayer system. Practical compromises had to be made in some cases to allow formation of repeatable, robust membranes to allow analyses to be carried out. These compromises were made to enable floating model membranes with high surface coverage.

The techniques used here are not new, but serve as a methodological foundation that can be developed into something novel. Further, repeating studies with well characterised membrane models will demonstrate the appropriateness of the techniques for characterising novel membrane models. With these model membranes, interactions with polyphenols that were previously unexplored using this kind of interfacial analysis can be investigated for the first time.

Moving forward, FTIR, QCM-D, and NR will be used to investigate interactions at the the lipid membrane surface. QCM-D allows changes of mass at the surface on a nanogram scale to be detected. This is appropriate for both the formation of a bilayer and for its interaction with small molecules as we see in the next chapter. Further, the dissipation information tells us something about the nature of the interaction, and how the rigidity of the layer(s) at

the surface is changing before and after the introduction of samples into the instrument. FTIR is powerful in that it is capable of detecting the presence of functional groups at the interface. When trying to gauge whether interactions are taking place, and if these interactions are persistent, this is an immensely useful technique to understand the kinds of fundamental processes taking place at the interface.

Neutron reflectometry then allows an understanding of the model membranes structurally, and will give a description of the distribution of the membrane components across the interfacial surface. While the information from NR is far more detailed and precise than for alternative surface sensitive techniques, it comes at a cost. The setup required for NR experiments needs access to a neutron source, either spallation or reactor based, which are incredibly complex and expensive to build, operate, and maintain. As such access to them is not trivial. Further, the sample environments are often greater in complexity, and as outlined above, steps must be taken to ensure that fundamental properties of the materials used in sample construction (i.e. surface charges, temperature etc.) do not adversely impact measurements.

References

- [1] R. F. Epand and R. M. Epand, *Biochim. Biophys. Acta - Biomembr.*, 2009, **1788**, 289–294.
- [2] B. Pozo Navas, K. Lohner, G. Deutsch, E. Sevcsik, K. A. Riske, R. Dimova, P. Garidel and G. Pabst, *Biochim. Biophys. Acta - Biomembr.*, 2005, **1716**, 40–48.
- [3] Á. Oszlánzi, A. Bóta and E. Klumpp, *Biophysical Chemistry*, 2007, **125**, 334–340.
- [4] T. K. Lind, H. Wacklin, J. Schiller, M. Moulin, M. Haertlein, T. G. Pomorski and M. Cárdenas, *PLoS ONE*, 2015, **10**, year.
- [5] K. Lohner and E. J. Prenner, *Biochimica et Biophysica Acta - Biomembranes*, 1999, **1462**, 141–156.
- [6] K. Lohner, A. Latal, G. Degovics and P. Garidel, *Chemistry and Physics of Lipids*, 2001, **111**, 177–192.
- [7] F. Separovic and K. Gawrisch, *Biophysical Journal*, 1996, **71**, 274–282.
- [8] A. Aroui, M. Dathe and A. Blume, *Biochim. Biophys. Acta - Biomembr.*, 2009, **1788**, 650–659.
- [9] C. Suárez-Germà, M. T. Montero, J. Ignés-Mullol, J. Hernández-Borrell and Òscar Domènech, *Journal of Physical Chemistry B*, 2011, **115**, 12778–12784.
- [10] L. Yang, V. D. Gordon, A. Mishra, A. Som, K. R. Purdy, M. A. Davis, G. N. Tew and G. C. Wong, *Journal of the American Chemical Society*, 2007, **129**, 12141–12147.
- [11] D. Sanver, B. S. Murray, A. Sadeghpour, M. Rappolt and A. L. Nelson, *Langmuir*, 2016, **32**, 13234–13243.
- [12] R. F. Epand, P. B. Savage and R. M. Epand, *Biochimica et Biophysica Acta - Biomembranes*, 2007, **1768**, 2500–2509.
- [13] A. Latal, G. Degovics, R. F. Epand, R. M. Epand and K. Lohner, *European journal of biochemistry*, 1997, **248**, 938–946.
- [14] R. F. Epand, M. A. Schmitt, S. H. Gellman and R. M. Epand, *Biochimica et Biophysica Acta (BBA)-Biomembranes*, 2006, **1758**, 1343–1350.

- [15] A. Raudino, M. G. Sarpietro and M. Pannuzzo, *Differential scanning calorimetry (DSC): Theoretical fundamentals*, Woodhead Publishing Limited, 2013, pp. 127–168.
- [16] K. Gardikis, S. Hatziantoniou, K. Viras, M. Wagner and C. Demetzos, *International Journal of Pharmaceutics*, 2006, **318**, 118–123.
- [17] Á. Oszlanczi, A. Bóta, S. Berényi and E. Klumpp, *Colloids and Surfaces B: Biointerfaces*, 2010, **76**, 519–528.
- [18] F. Gambinossi, B. Mecheri, G. Caminati, M. Nocentini, M. Puggelli and G. Gabrielli, *Materials Science and Engineering C*, 2002, **22**, 283–288.
- [19] P. Wydro, M. Flasiński and M. Broniatowski, *Biochimica et Biophysica Acta - Biomembranes*, 2012, **1818**, 1745–1754.
- [20] G. Ma and H. C. Allen, *Langmuir*, 2006, **22**, 5341–5349.
- [21] E. M. Adams, C. B. Casper and H. C. Allen, *Journal of Colloid and Interface Science*, 2016, **478**, 353–364.
- [22] A. Hädicke and A. Blume, *Langmuir*, 2015, **31**, 12203–12214.
- [23] P. Wydro and K. Witkowska, *Colloids and Surfaces B: Biointerfaces*, 2009, **72**, 32–39.
- [24] C. C. Hao, R. G. Sun and J. Zhang, *Chinese Journal of Chemical Physics*, 2012, **25**, 691–696.
- [25] V. Vié, N. Van Mau, L. Chaloin, E. Lesniewska, C. Le Grimellec and F. Heitz, *Biophysical Journal*, 2000, **78**, 846–856.
- [26] G. Pabst, N. Kučerka, M. P. Nieh, M. C. Rheinstädter and J. Katsaras, *Chem. Phys. Lipids*, 2010, **163**, 460–479.
- [27] L. Rajendran and K. Simons, *J. Cell Sci.*, 2005, **118**, 1099–1102.
- [28] G. Van Meer, D. R. Voelker and G. W. Feigenson, *Nature Reviews Molecular Cell Biology*, 2008, **9**, 112–124.
- [29] K. Simons and W. Vaz, *Annual Review of Biophysics and Biomolecular Structure*, 2004, **33**, 269–295.
- [30] K. Simons and E. Ikonen, *Nature*, 1997, **387**, 569–572.
- [31] K. Simons and G. Van Meer, *Biochemistry*, 1988, **27**, 6197–6202.
- [32] B. Cullis, P.R and Kruijff, *Chem. Phys. Lipids*, 1986, **40**, 127–144.
- [33] S. C. Hall, L. A. Clifton, C. Tognoloni, K. A. Morrison, T. J. Knowles, C. J. Kinane, T. R. Dafforn, K. J. Edler and T. Arnold, *Journal of Colloid and Interface Science*, 2020, **574**, 272–284.
- [34] S. A. Tatulian, in *Lipid-Protein Interactions*, Springer, 2019, pp. 281–325.

- [35] L. K. Tamm and S. A. Tatulian, *Quarterly Reviews of Biophysics*, 1997, **30**, 365–429.
- [36] U. P. Fringeli and H. H. Günthard, *Membrane spectroscopy*, 1981, 270–332.
- [37] N. J. Cho, C. W. Frank, B. Kasemo and F. Höök, *Nat. Protoc.*, 2010, **5**, 1096–1106.
- [38] H. P. Wacklin, *Langmuir*, 2011, **27**, 7698–7707.
- [39] K. F. Wang, R. Nagarajan, C. M. Mello and T. A. Camesano, *Journal of Physical Chemistry B*, 2011, **115**, 15228–15235.
- [40] S. B. Nielsen and D. E. Otzen, *Journal of Colloid and Interface Science*, 2010, **345**, 248–256.
- [41] L. A. Clifton, N. Paracini, A. V. Hughes, J. H. Lakey, N.-J. J. Steinke, J. F. Cooper, M. Gavutis and M. W. Skoda, *Langmuir*, 2019, **35**, 13735–13744.
- [42] L. A. Clifton, R. A. Campbell, F. Sebastiani, J. Campos-Terán, J. F. Gonzalez-Martinez, S. Björklund, J. Sotres and M. Cárdenas, *Adv. Colloid Interface Sci.*, 2020, **277**, 102118.
- [43] W. Dowhan and M. Bogdanov, in *Biochemistry of Lipids: Lipoproteins and Membranes*, ed. D. E. Vance and J. E. Vance, Elsevier Science, 4th edn., 2002, vol. 36, pp. 1–35.

—You dig deeper and it gets more and more complicated, and you get confused, and it's tricky and it's hard, but... It is beautiful.

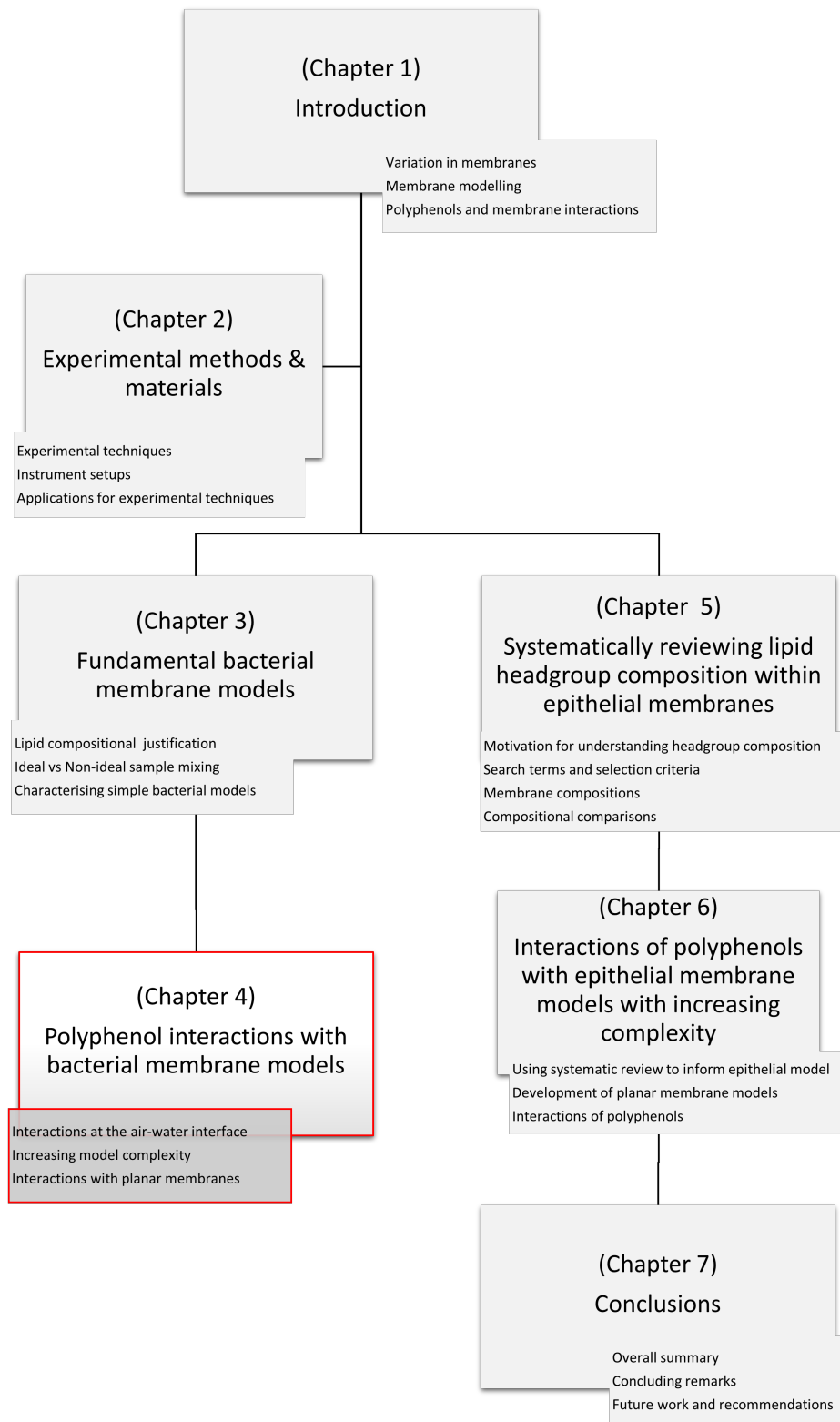
Brian E. Cox

4

Investigating the Interactions of Polyphenolic Compounds with a Bacterial Membrane Model

Contents

4.1	Lipid-Polyphenol interactions at the air water interface	87
4.2	Increasing Complexity: Interactions with Vesicles .	89
4.2.1	Ideal versus Non-ideal Lipid Interactions in Bacterial Model Membranes	92
4.2.2	Bacterial Model Membranes' Interactions with Tellimagrandins I and II	95
4.3	Characterising Interactions with Supported Lipid Bilayers	101
4.3.1	Interactions of EGCg with a Model Bacterial Membrane	103
4.3.2	Interactions of Tellimagrandin II with a Model Bacterial Membrane	107
4.3.3	Interactions of Tellimagrandin I with a Model Bacterial Membrane	110
4.4	Floating Model Bacterial Membrane Interactions with EGCg using Neutron Reflectometry	115
4.4.1	Interactions with EGCg from the Bulk Solution	116
4.5	Analysis of Model Bacterial Membranes Containing Pre-Mixed EGCg	119
4.6	Floating Model Bacterial Membrane Interactions with Tellimagrandin-II using Neutron Reflectometry	122
4.7	Summary	126



4.1 Lipid-Polyphenol interactions at the air water interface

Just as phase and packing information can be gained from single lipids, such as those in figure 3.2, insight into the effects of pharma- or neutraceutical compounds on lipid layers can be gained from measuring compression isotherms where there is both lipid and drug present at the air-water interface. It was important to build up the complexity of the model in a methodical way. The first step taken was to see the effects of a model polyphenol, 1,2,3,4, 6-penta-O-galloyl d-glucose (PGG), with a bacterial model membrane. For the model membrane DPPG was used as it is a major bacterial membrane component [1, 2]. The structure of PGG is shown in figure 4.1.

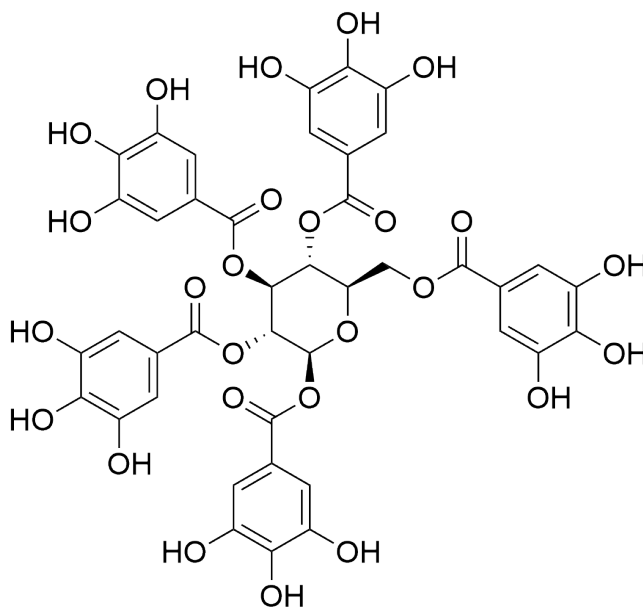


Figure 4.1: Chemical structure of 1,2,3,4,6-penta-O-galloyl d-glucose (PGG).

The effects of PGG on a bacterial model membrane at the air-water interface are explored in figure 4.2. When compared to a pure DPPG monolayer it is clear that there is a loss of phase information as the amount of PGG in the mixture increases. In particular, it is the LE-phase that is lost as the mixture appears to move towards more typical binary phase mixture behavior. The loss of the phase information and the disappearance of the LE-phase is shown through the loss of the local minimum around 10 mN/m in the compressibility modulus. As the concentration of PGG increases in the mixture the values for the compressibility modulus at any given π -value are lower, which indicates that the layer is becoming more elastic when compared to the pure DPPG monolayer. Note, that for a clean air-water interface $C_s^{-1} = 0$.

At very high areas per molecule, the gaseous phase in each isotherm was still observed which shows that there was still enough space initially for compression to take place and no intermolecular interactions occur. Because of the increasing elasticity of the monolayer that is shown in the compressibility (C_s^{-1}) plots,

one can infer that as the molecules are being compressed into one another at the interface, they are not orienting themselves as uniformly as they do in the pure lipid layer. Instead of a clear LE phase transition when PGG is added to the lipid layer, the LE-phase is apparently more drawn out. This indicated that the PGG is forcing alignment of lipid molecules earlier on at higher area per molecule. When compared to the lipid layer without PGG the effects of intermolecular interactions can be seen earlier on in the compression and continues at a steady rate until a condensed layer is reached. Once there is no space left available at the interface for the lipid and PGG molecules to rearrange themselves such that compression can continue the surface pressure climbs at a rapid rate, indicating the material at the interface.

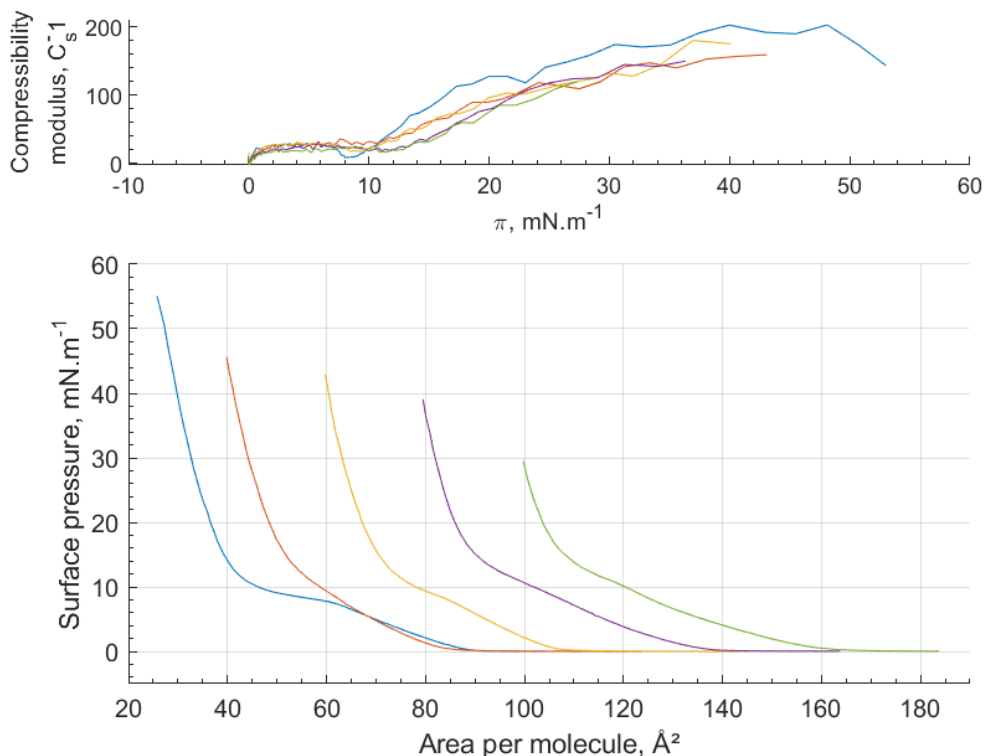


Figure 4.2: Compression isotherms of DPPG where the fraction of PGG in the sample increases from pure DPPG (blue), DPPG:PGG = 10:1 (orange), DPPG:PGG = 5:1 (yellow), DPPG:PGG = 3:1 (purple), DPPG:PGG = 2:1 (green). Compressibility moduli of the isotherms are shown above the compression isotherms.

To understand how the lipid and polyphenol interact in the layer, the mean molecular area at 5, 15, 25, and 35 mN/m was plotted against the mole fraction (χ) of DPPG in the layer. It is established that plotting mean area per molecule against χ for an ideal mixture will give a straight line [3]. Clearly, from figure 4.3, the DPPG/PGG mixtures are non-ideal and so the two components are not perfectly miscible. As the mean molecular area values for the DPPG/PGG mixture are less than the ideal (dashed black line) we can infer that the interactions between the two components are attractive in nature [3]. The highly

miscible nature of the two components may be attributed in part to the ability of the polyphenol to dissolve into the subphase in the trough when the monolayer is saturated. Here, to show that the mean area per molecule was not linear it was fit to a parabolic polynomial using the Matlab *polyfit* function (MATLAB, 2021b).

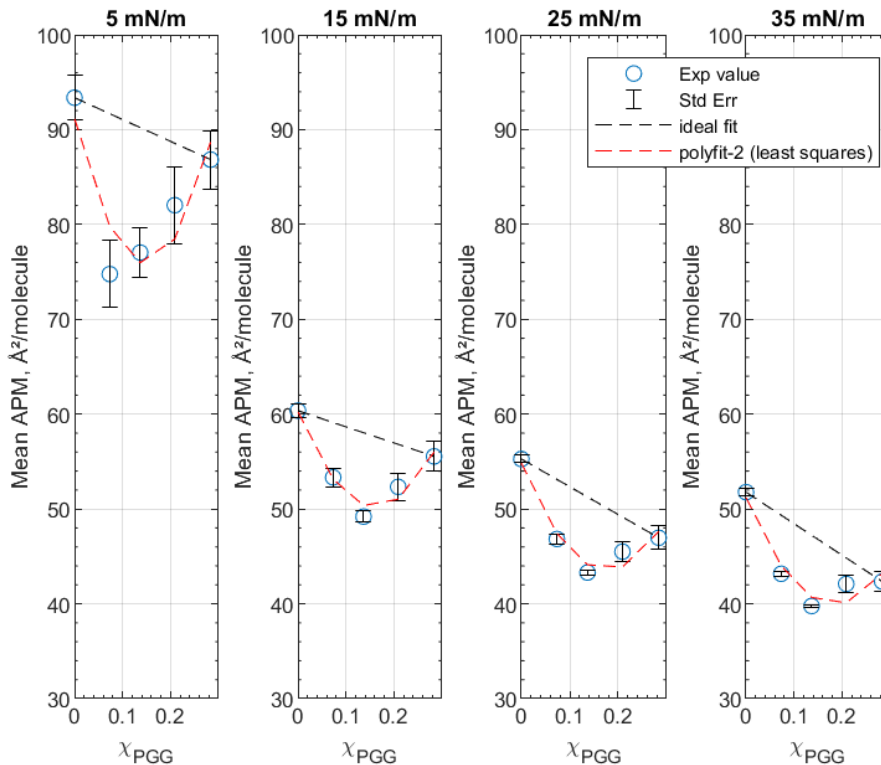


Figure 4.3: Mean molecular area versus composition of PGG for DPPG/PGG monolayers at the air-water interface at the fixed surface pressure values. The data were fit to a parabolic polynomial to demonstrate their non-linearity using Matlab’s *polyfit* function.

The changes to the LE-phase transition caused by PGG to a single DPPG leaflet in this set of isotherms (figure 4.2) and the comparison of the mean molecular areas of the mixtures to the ‘ideal’ has shown that there are some effects taking place at the membrane interface. These fundamental interactions can be explored in more depth using a variety of polyphenols, lipid membrane models, and techniques. Using different techniques will allow different aspects of the interactions to be understood.

4.2 Increasing Complexity: Interactions with Vesicles

Vesicles provide an opportunity for interactions with bilayer systems and largely builds on the bacterial membrane models described in chapter 3. Compared to SLBs or floating bilayers used in neutron reflectometry studies, the vesicle sample preparation is better suited to high sample throughput. From figure

3.3, a non-ideal lipid sample has been chosen as the most appropriate vesicle preparation method given that distinct lipid domains are a real membrane phenomenon and afford this model membrane an extra level of accuracy. This section of the chapter involves measuring the effects of a series of polyphenolic compounds on lipid bilayers in vesicle form. In practice this was achieved using DSC and will manifest as changes in the transition temperature peaks in the DSC thermogram. The changes that appear upon addition of an external compound in the DSC thermograms can be characterised in two main ways. Increases in the transition temperature result from the gel-phase becoming more stable through attractive headgroup interactions. Decreases in the position of the transition temperature are as a result of sterics from large molecules at or near the membrane surface interrupting and destabilising the gel-phase of the membrane [4]. This is summarised in table 4.1.

Table 4.1: Summary of changes to DSC thermograms upon polyphenol addition, along with associated causes for temperature shifts in lipid samples.

Temperature shift	Cause	Mechanism
Increase	Increased stability of gel phase	Electrostatic headgroup interactions
Decrease	Steric effects	Large molecules at the membrane surface interrupting headgroup-headgroup interactions

The addition of PGG to the non-ideally mixed DPPE/DPPG (3:2) vesicles shifts the transition temperatures of both DPPE and DPPG to higher temperature as shown in figure 4.4. PGG at a lipid:PGG ratio of 2:1 moves the T_m for the DPPE and DPPG peaks an average of 1.3 and 0.4 °C respectively. Transition temperatures and standard deviation values are shown in table 4.2. This indicates that the presence of PGG in the membrane stabilises the gel-phase. Beyond stability of both lipids in the gel-phase it is clear that the peak for DPPG is shifted further than the T_m for DPPE. From this it can be inferred that the PGG here has a preference for the DPPG headgroup over DPPE. In chapter 3 the idea of non-uniform mixing in lipid samples is introduced, with a shoulder on a peak in a DSC thermogram being an indicator of imperfect mixing in the multi-component membrane. The non-ideal lipid scan shows a shoulder on the DPPE peak at *ca.* 64 °C. Addition of PGG in increasing amounts in the mixture results initially in the shrinking of the magnitude of the shoulder before it finally becomes a very broad feature with very low intensity, lying between the main DPPG and DPPE transition peaks. It is likely that this arises due to the DPPG headgroups that have interacted with PGG molecules at the membrane surface, when have themselves becomes

more stable in their gel-phase than the pure DPPG. As such the pure DPPG and the PGG-bound DPPG show distinct transition temperatures due to the difference in stability.

The results of the DSC studies with PGG on the bacterial membrane model, in addition to the Langmuir trough data from figure 4.2, demonstrates that a model polyphenol will interact with a bacterial membrane mimetic. It shows that the preference for lipids is not symmetric and that the behaviours of the lipids after the interaction are altered.

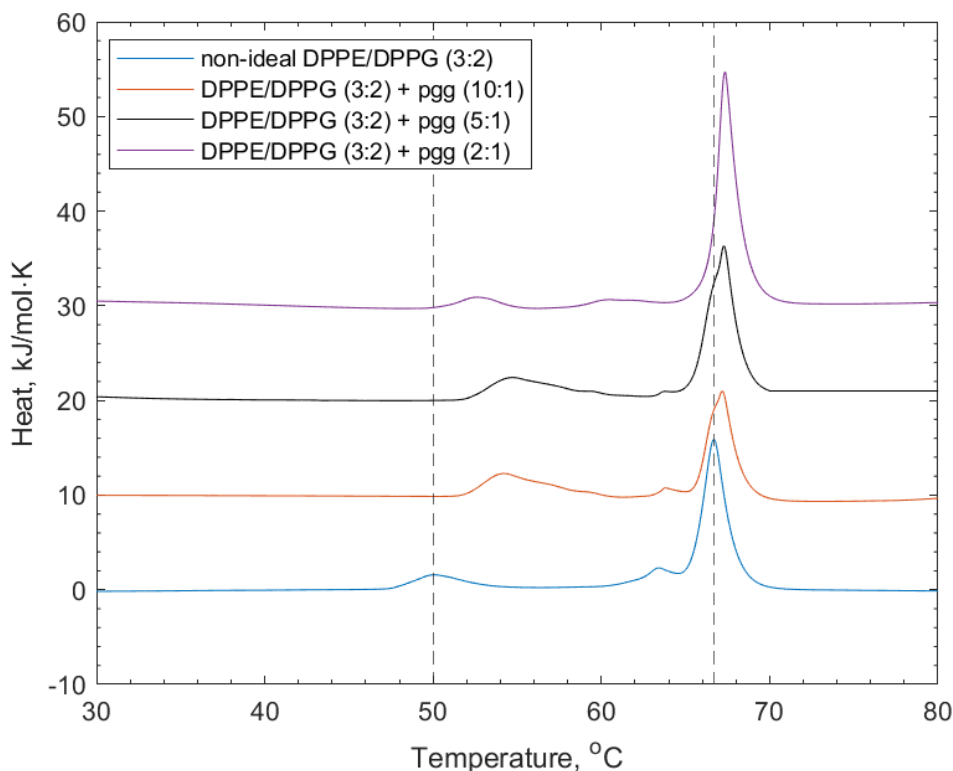


Figure 4.4: DSC thermograms for non-ideal DPPE/DPPG (3:2, blue) with the addition of 1,2,3,4,6-pentagalloylglucose (PGG) at lipid:PGG ratios of 10:1 (orange), 5:1 (black), and 2:1 (purple).

Table 4.2: Transition temperatures for non-ideal DPPE/DPPG (3:2) + PGG. Associated standard deviation values and standard error of the mean values are also given.

	Peak 1, °C	S.D. (n=3)	S.E.	Peak 2, °C	S.D. (n=3)	S.E.
DPPE/DPPG (3:2)	51.6	0.6	0.58	67	0.1	0.14
+ PGG (10:1)	57	1.2	1.17	65.7	0.1	0.72
+ PGG (5:1)	55.9	0.8	0.81	66.2	0.9	0.94
+ PGG (2:1)	52.9	0.2	0.2	67.4	1.1	1.06

4.2.1 Ideal versus Non-ideal Lipid Interactions in Bacterial Model Membranes

To understand the effect of sample preparation on both lipid behaviour, and also on lipid-polyphenol interactions, another set of experiments were conducted. The questions being asked of this study were two-fold: (i) can differences in sample preparation methods be measured using DSC? (ii) Does the sample preparation method affect lipid-polyphenol interaction? For this comparative study a green tea polyphenol, (-)-epigallocatechin gallate (EGCg), was selected. EGCg has been shown to interact with model membranes, with galloylated polyphenols showing a higher affinity for membrane interactions compared to their non-galloylated counterparts [5–7]. EGCg was selected for these studies in place of PGG because EGCg was a good candidate for a neutron reflectometry experiment. Confirming its interactions with membranes was important to both provide complementary results and ensure the viability of the neutron study.

Ideal Lipid Membrane Interaction: DPPE/DPPG (3:2) + EGCg

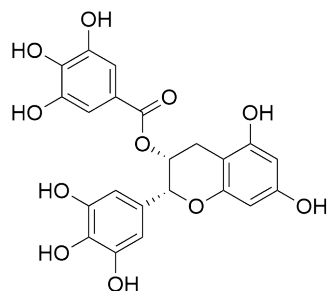
Figure 4.5b shows the thermograms of ideally mixed DPPE/DPPG (3:2) with EGCg at various concentrations. From the single peak of the ideally mixed sample at *ca.* 60°C the peak gets first of all much broader at a lipid:EGCg ratio of 10:1 and shows the emergence of a very small shoulder at 5:1 and a shifting of the peak to 64°C, towards that of pure DPPE. At 2:1, there is total separation of the two lipid features, for a DPPE-like transition at 66.1°C and a DPPG-like transition at 50.4°C. The value of the DPPG-like transition is consistent with that of the DPPG peak at 51.6°C, with the difference resulting from EGCg offering lower stability compared to the lipid gel-phase. The splitting of the two lipid transitions indicates apparent *demixing*, which is confirmed by the presence of a shoulder on the DPPE transition peak. Comparing the two lipids with their ideal starting point, once again shows a preference for the DPPG headgroup compared to DPPE. Values for the transition temperatures and their associated errors are shown in table 4.3.

Table 4.3: Transition temperatures for ideal DPPE/DPPG (3:2) + EGCg. Associated standard deviation values and standard error of the mean values are also provided.

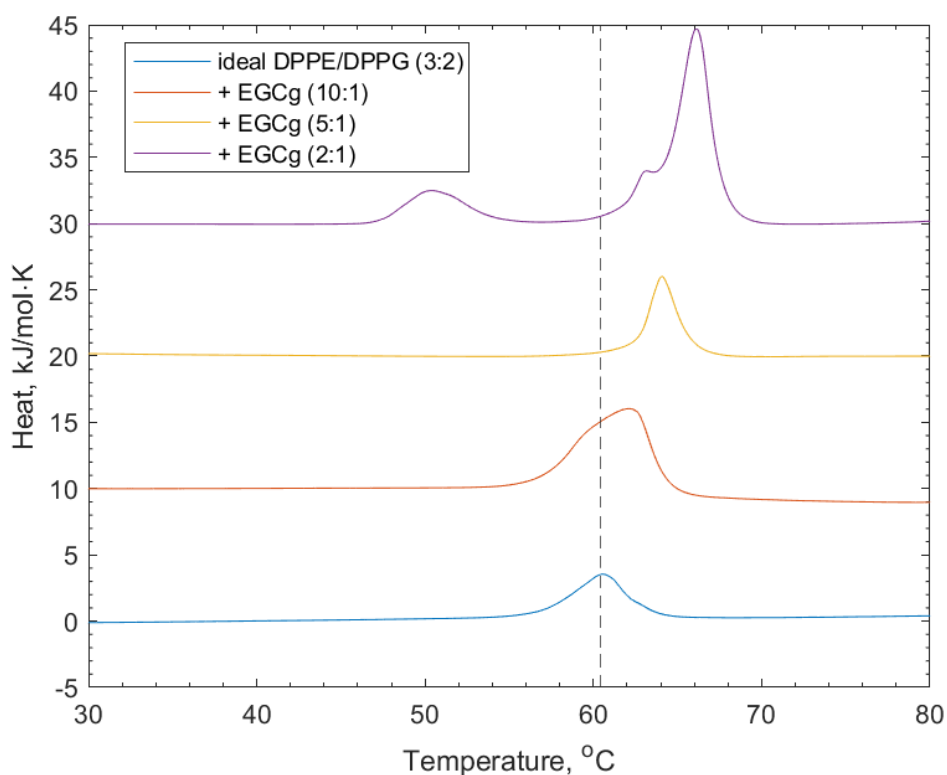
	Peak 1, °C	S.D. (n=3)	S.E.	Peak 2, °C	S.D. (n=3)	S.E.
DPPE/DPPG (3:2)	60.51	0.17	0.10	-	-	-
+ EGCg (10:1)	62.10	0.07	0.05	-	-	-
+ EGCg (5:1)	63.99	0.15	0.09	-	-	-
+ EGCg (2:1)	50.46	0.23	0.13	66.12	0.06	0.03

Non-ideal Lipid Membrane Interaction: DPPE/DPPG (3:2) + EGCg

In contrast to the ideal lipid vesicles' interactions with EGCg, the non-ideal lipid mixture showed signs of induced mixing as the concentration of EGCg



(a)



(b)

Figure 4.5: (a) Structure of (-)-epigallocatechin gallate (EGCg). (b) DSC thermograms for ideally mixed DPPE/DPPG (3:2, blue) vesicles. Lipid:EGCg ratios increase from 10:1 (orange), 5:1 (yellow), and to 2:1 (purple) showing that increasing the EGCg concentration induced demixing of the lipid membrane components.

in the sample increased. Thermograms are shown in figure 4.6. The peak associated with DPPE dropped to a lower temperature, suggesting that the gel phase of the lipid became less stable. At the highest lipid:EGCg concentration the DPPG-associated transition was not observed. The shoulder on the DPPE peak was much broader and reduced in intensity, which would point to polyphenol-induced disruption to the membrane microdomains that are able to form in the sample with no EGCg present. The values and associated errors for the non-ideal lipid sample with EGCg are given in table 4.4.

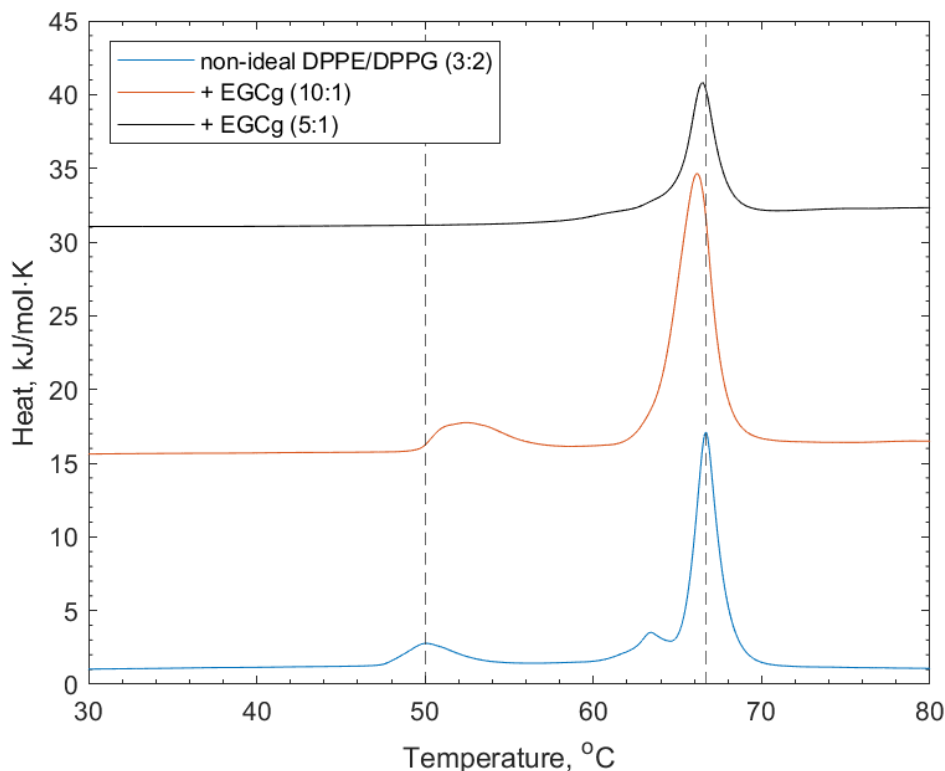


Figure 4.6: DSC thermograms for non-ideal DPPE/DPPG (3:2, blue) with interactions with (-)-epigallocatechin gallate (EGCg) at lipid:EGCg ratios of 10:1 (orange) and 5:1 (black).

Table 4.4: Transition temperatures for non-ideal DPPE/DPPG (3:2) + EGCg. Associated standard deviation values and standard error of the mean values are also provided.

	Peak 1, °C	S.D.(n=3)	S.E.	Peak 2, °C	S.D. (n=3)	S.E.
DPPE/DPPG (3:2)	51.6	0.6	0.58	67	0.1	0.14
+ EGCg (10:1)	52	0.5	0.45	66.2	0.1	0.11
+ EGCg (5:1)	-	-	-	66.4	0.1	0.05

The non-ideal sample, without polyphenols present, shows more inherent disorder and allows for spontaneous microdomain formation in the model membrane. The microdomain formation allows the individual lipid peaks within

the mixture to be resolved calorimetrically, and as a result preferences for individual membrane components within model membranes can be observed. Further, as previously mentioned, the formation of stable lateral microdomains within real lipid membranes is relatively well documented and affords this method of sample preparation an extra layer accuracy compared to its ideally mixed counterpart. To help reflect the asymmetric nature of real cell membranes, the non-ideal mixture was used instead of the ideal in subsequent experiments.

Observing Membrane Changes as a Function of Time

Using a single DSC sample the effects of EGCg on the non-ideally mixed bacterial model (DPPE/DPPG (3:2) + EGCg, lipid:EGCg = 2:1) were observed over the course of approximately 1 day. The sample containing polyphenol at a lipid:EGCg ratio of 2:1 was used because previous experiments showed the greatest change in samples containing the highest polyphenol ratio. The plots of peak position as a function of time shown in figure 4.7 display signs of the initial shifting of the DPPG associated peak to higher temperatures, with more drastic shifts being observed at 24h (purple) and 26h (green). At $t = 26\text{h}$ there is also the disappearance of the shoulder on the DPPE peak, indicating that uniform mixing is beginning to take place, along with the decrease in the value of the T_m of the DPPE peak. The destabilisation of the DPPE gel-phase likely comes from the EGCg-lipid headgroup interactions. The positively charged PE-headgroup provides a formal charge for interaction with the phenolic moieties on the EGCg. The lipid-lipid interactions may be disrupted as a result and thus the T_m of the lipid is decreased. The bottom panel of figure 4.7 shows the thermograms overlaid in 2-D to better highlight temperature shifting in the initial scans that show only small increases in the DPPG T_m .

Unfortunately, again as a result of the nanoDSC being unusable, repeat of this experiment with a longer data collection time was not possible. As it stands, this experiment only had a single run, with each thermogram being collected in triplicate. As before, the second scan from each set is shown.

4.2.2 Bacterial Model Membranes' Interactions with Tellimagrandins I and II

Similarly to EGCg, Tellimagrandin II (Tel-II) causes the stabilisation of the PG headgroup in the membrane, increasing its melting temperature from 51.6 to 53.3°C. Further, the T_m of PE is reduced from 67 to 65.4°C. As the concentration of the Tel-II increased, the effects of the polyphenol on the membrane showed apparent induced mixing. In the DSC thermogram shown in figure 4.8b this manifests as the peaks of the two lipid components move closer together. The structure of Tel-II is given in figure 4.8a. Table 4.5 provides temperature values, standard deviations and standard error values. The shoulder of the PE peak also broadened and becomes more dissociated from the

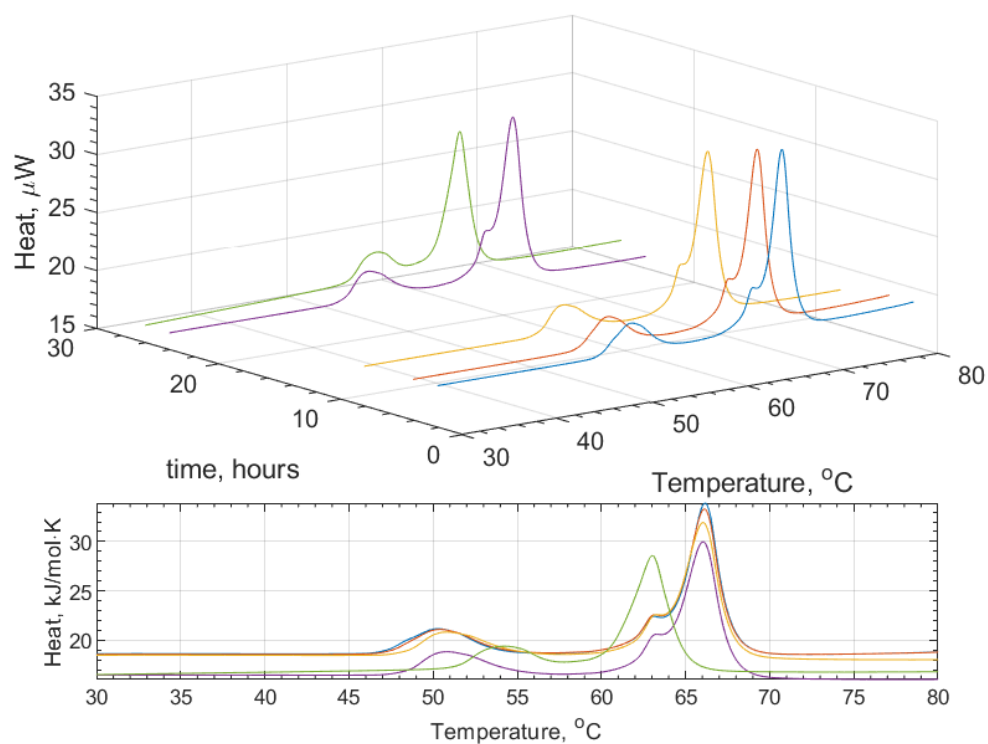


Figure 4.7: Exploring the effects of induced mixing with an ideally mixed DPPE/DPPG (3:2) + EGCg at a lipid:EGCg ratio of 2:1. Scans of the same sample were taken at $t = 2$ (blue), 4 (orange), 8 (yellow), 24 (purple), and 26h (green) to measure the evolution of the lipid layer due to the addition of EGCg.

PE-peak, showing that lateral lipid domains persist during the addition of Tel-II.

Table 4.5: Transition temperatures for non-ideal DPPE/DPPG (3:2) + Tellimagrandin II. Associated standard deviation values and standard errors of the mean are also given.

	Peak 1, °C	S.D.(n=3)	S.E.	Peak 2, °C	S.D. (n=3)	S.E.
DPPE/DPPG (3:2)	51.6	0.6	0.58	67	0.1	0.14
+ Tel-II (10:1)	53	0.8	0.83	66.4	0.1	0.03
+ Tel-II (5:1)	54.6	1.3	1.31	66.5	0.1	0.05
+ Tel-II (2:1)	53.3	0.4	0.42	65.4	0.2	0.15

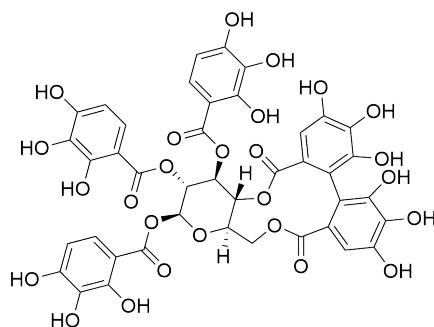
Tellimagrandin-I (Tel-I) shows the same trend as Tel-II, along with almost identical shifts in the temperature for both PG and PE peaks, which given the similarity in chemical structure this is not surprising. The structure for Tel-I is given in figure 4.9a. The thermograms, in figure 4.9b, show a PG-peak that has an increasing T_m with Tel-I concentration, from 51.6 to 53.25°C, and a PE-peak that decreases in temperature from 67 to 65.3°C. At a lipid:Tel-I ratio of 2:1, however, the PE peak shows greater reduction in intensity for Tel-I than any of the other polyphenols. The reduced area under the curve for the PE-peak at the 2:1 ratio is indicative of a lower ΔH for this lipid-polyphenol interaction. For any given T_m , a lower ΔH value corresponds to a lower entropy, which indicates increased order in the system.

The shoulder on the PE-peak for the Tel-I interaction was broader than for previous polyphenol interactions, but remains on the PE-peak. It is clear that formation of lipid rafts in the vesicle membrane are not disrupted completely during the interaction with Tel-I. At the highest lipid:EGCg concentration the shoulder that previously resided on the DPPE peak has shifted to a T_m somewhere between DPPE and DPPG. This may indicate the formation of a DPPE-DPPG-Tel-II domain that is phase separated from the rest of the lipids in the vesicle.

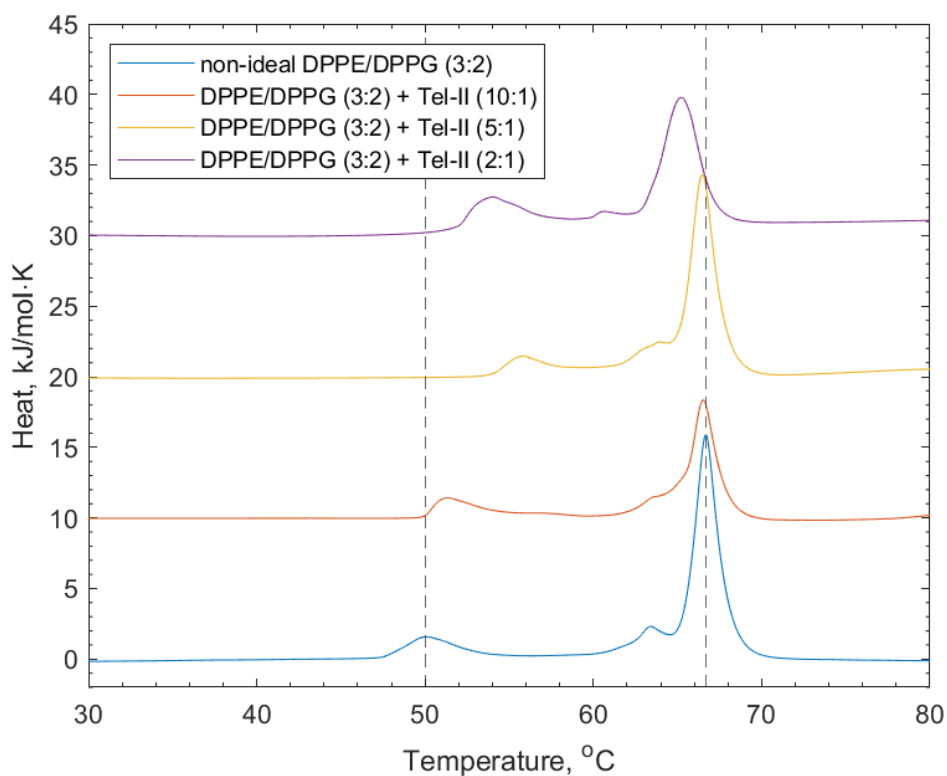
Table 4.6: Transition temperatures for DSC thermograms of non-ideal DPPE/DPPG (3:2) + Tellimagrandin I interactions. Associated standard deviation values and standard errors of the mean are also given.

	Peak 1, °C	S.D. (n=3)	S.E.	Peak 2, °C	S.D. (n=3)	S.E.
DPPE/DPPG (3:2)	51.6	0.6	0.58	67	0.1	0.14
+ Tel-I (10:1)	50.6	0.1	0.83	66.5	0.1	0.12
+ Tel-I (5:1)	52	0.8	1.31	66.1	0.1	0.14
+ Tel-I (2:1)	53.25	0.73	0.42	65.26	1.36	0.96

As described earlier in table 4.1, there are two major physical factors that influence the lipid-polyphenol interactions: electrostatics and sterics. Based on

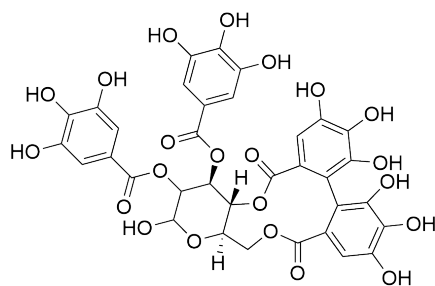


(a)

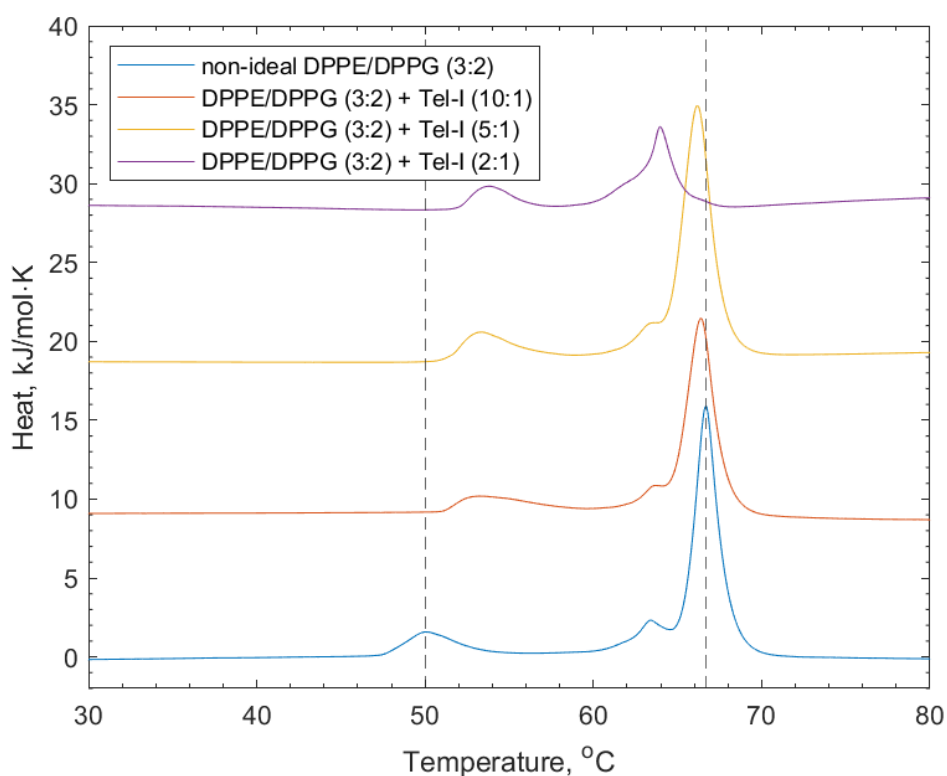


(b)

Figure 4.8: (a) Structure of Tellimagrandin II. (b) DSC thermograms for ideally mixed DPPE/DPPG (3:2, blue) vesicles. Lipid:Tel-II ratios increase from 10:1 (orange), 5:1 (yellow), and to 2:1 (purple) showing that increasing the Tel-II concentration results in induced mixing of the lipid membrane components.



(a)



(b)

Figure 4.9: (a) Structure of Tellimagrandin I. (b) DSC thermograms for ideally mixed DPPE/DPPG (3:2, blue) vesicles. Lipid:Tel-I ratios increase from 10:1 (orange), 5:1 (yellow), and to 2:1 (purple) showing that increasing Tel-I concentration results in induced mixing of the lipid membrane components.

the trends of these DSC studies it is apparent that there are other factors that should also be taken into account. The logP values of the polyphenols above indicated the preference for each compound to reside in either an aqueous or organic environment based on the octanol-water partition:

$$\log P = \log_{10} \left(\frac{[\text{solute}]_{\text{octanol}}}{[\text{solute}]_{\text{water}}} \right) \quad (4.1)$$

where [solute] is the concentration of the compound of interest in both octanol and water respectively. For any given compound, the larger the logP value the greater its affinity for an organic environment. In the context of lipid membranes, the organic environment within the cell would be the core tail region of the bilayer. The surrounding cellular space, or the cytoplasm within the cell, would serve as the aqueous environment.

The logP values of the polyphenols, listed in table 4.7 can be used as a guide for the affinity of interaction with the lipid membrane [8, 9]. It has been reported previously with NMR experiments that these interactions take place predominantly with the lipid headgroups [10]. In conjunction with the DSC experiments conducted here, we show that there are other factors that should be considered. As well as logP being an indicator of interaction so too is the number of free galloyl groups contained on the polyphenol. Free galloyl groups can be characterised by a galloyl group (see figure 4.1 for reference) that contains only one connected branch to the main molecule skeleton, allowing free rotation in real space. Molecular area is also an important factor, and one that eventually becomes self limiting, as can be seen in the case of PGG; despite increasing molecular area there is no associated change in the transition temperature. This demonstrates that molecular size can inversely affect interactive groups accessing the bilayer surface.

Table 4.7: Table of values for logP, DSC transition temperature shift for each lipid component, number of free galloyl groups and molecular area of each of the polyphenols investigated for lipid interactions with DSC calorimetry. ^a taken from the highest lipid:polyphenol concentration sample. ^b Molecular area estimated using the Chemdraw Professional (v20.0.0.41) molecular area tool.

Polyphenol	logP	PG shift ^a , °C	PE shift ^a , °C	Free galloyl groups	Mol. area ^b , Å ²
EGCg (ideal)	2.38	-	5.61	1	398.2
EGCg	2.38	-	-0.6	1	398.2
PGG	1.48	1.3	0.4	5	737.5
Tel-II	0.75	1.7	-1.6	3	688.8
Tel-I	-0.45	1.7	-1.7	2	582.8

For EGCg interacting with the ideally mixed sample, with a relatively small molecular area compared to the other polyphenols here, the steric impacts are relatively small. Thus, the observed temperature increase in the place of the PE peak indicates that electrostatic effects prevail. As molecular area increases

through the polyphenol series (from smallest to largest: Tel-I, Tel-II, PGG) the degree of temperature shift in the PE decreases. Given the number of free galloyl groups in these molecules is similar for Tellimagrandins I and II this likely does not play a major role. PGG has the most free galloyl groups, although it is unlikely that all 5 are able to interact with the membrane surface at any time. The direction of temperature shift of the PE peak for Tel-I and II is always negative which confirms sterics as the dominant effect here. For the DPPG peak, the direction of shift in all cases was to a higher temperature, showing that the effects of having added polyphenols to the membrane stabilises the DPPG electrostatically. Mechanistically, this is proposed to be through hydrogen bonding interactions between H-bond donors on the galloyl groups of the polyphenol's polar lipid headgroups, and specifically in this case, the anionic DPPG headgroup [7, 11–13]. The interaction of the lipid-polyphenol being hydrogen bond mediated is depicted schematically in figure 4.10.

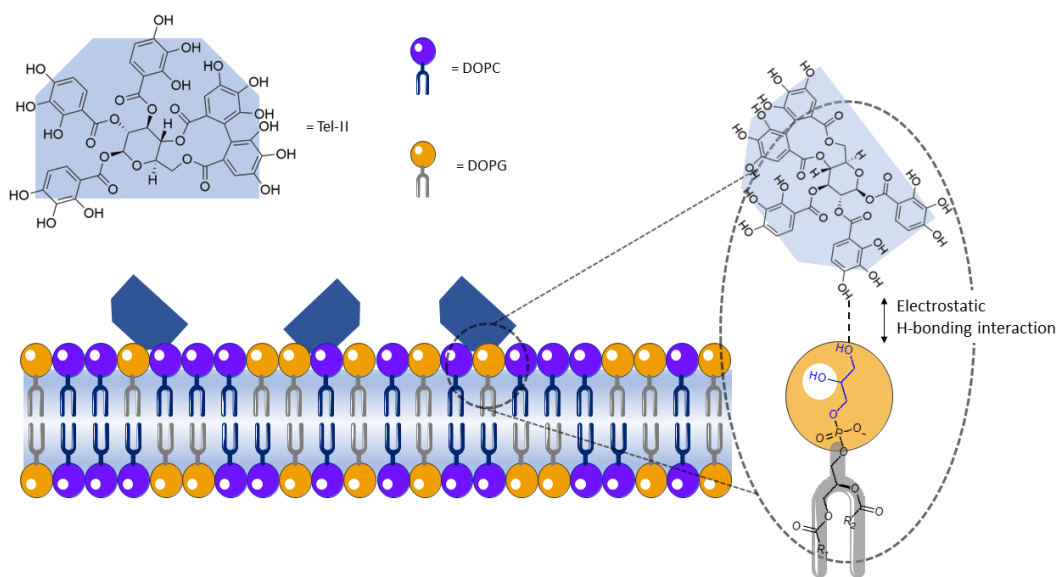


Figure 4.10: Schematic representation of a polyphenol interacting electrostatically at the lipid bilayer surface. The anionic DPPG headgroup is shown here to offer a lone electron pair from one of the glycerol oxygen atoms that protrudes at the bilayer surface for hydrogen bond donation from the polyphenol. The polyphenol example given here is Tellimagrandin II and the bilayer depicted represents the DOPC/DOPG (7:3) bilayer used in SLB and neutron experiments.

4.3 Characterising Interactions with Supported Lipid Bilayers

While allowing the investigation of changes to a lipid bilayer, DSC as a technique does not allow investigation on planar membranes in the sense that they would be found *in situ*. Further, due to the nature of the sample environment in DSC experiments the polyphenol, must be mixed into the lipid sample at the time of

sample loading into the instrument. This, potentially admits inclusion of some undesired bias in to the experiment. By first forming the a lipid membrane on a supported substrate (supported lipid bilayer, or SLB) and then injecting a polyphenol solution after membrane formation, we give the polyphenol a chance to interact, or not, with the membrane. Moreover, as indicated earlier, this aids the realistic nature of interaction *in situ*.

SLBs allow membrane formation on a substrate support and are appropriate as methods for forming model membranes [14]. The lipid composition of the model membrane needs to be selected such that the accuracy of the membrane is maintained as far as possible, while ensuring practical factors such as membrane charge and fluidity do not create barriers to SLB formation. Further, SLBs do not suffer the same instability that vesicle samples are susceptible to, i.e. potential changes to the size of the vesicle or aggregation [15]. This makes SLBs an ideal candidate for use as a model membrane system that are applicable to a wide range of interfacial analyses. To investigate lipid-polyphenol interactions, two particular techniques have been utilised: ATR-FTIR and QCM-D. These techniques and their applications are introduced in detail in sections 2.5 and 2.6 respectively but a brief summary is included below. ATR-FTIR allows the measurement of changes in functional groups at the interface. In the context of membrane formation and subsequent interactions this allows the process to be shown in stages, from the formation of a membrane on a blank substrate and showing that the membrane is robust enough to withstand laminar flow of buffer solution to the injection and persistence of polyphenols at the membrane surface after rinsing. Changes to the FTIR spectrum during interactions are often observed through the appearance of additional peaks in the spectrum or through shifting of peaks that were already present. Differentiation of lipid components in the membrane can be used using deuteration, due to the differences in stretching modes between C–H and C–D tails of the lipids.

QCM-D enables detection of mass changes at the sensor surface on the nanogram scale through measuring changes in the frequency of an oscillating crystal sensor [14, 16]. This allows the formation of SLBs at the sensor surface and can show interactions through persistent mass changes after injection of substances after bilayer formation. Dissipation monitoring allows determination of how rigid or diffuse the film formed at the sensor surface is, which is helpful both in confirmation of the formation of a thin, rigid bilayer as well as giving information about the nature of an interaction after a membrane interaction.

In all experiments carried out by the author, SLBs were formed using vesicle adsorption-rupture methods on SiO₂ substrates for both ATR-FTIR and QCM-D [17]. The SiO₂ substrate and lipid vesicles show an attractive interaction towards one another, where the vesicle bound irreversibly to the substrate [18]. At some critical coverage, vesicle fusion occurred with a combination of vesicle-substrate and vesicle-vesicle interactions which promoted vesicle rupture. Localised patches of ruptured vesicles then formed, where the edges provided a site for an “autocatalytic SLB formation process” [19]. To aid SLB formation through maximal lipid fluidity the temperature for deposition

was generally set above the T_m of the lipid(s) being used [20]. When depositing SLBs that contained charged lipids, the use of salts in the buffer solution are important. To help screen the vesicle/surface charge the use of high salt concentration (e.g. >100 mM NaCl) and the inclusion of divalent cations (i.e. CaCl_2 , *ca.* 2mM) will aided SLB formation. For bacterial membrane models containing PG-headgroup lipids this was vital [17, 21]. An alternative SLB formation method was Langmuir Blodgett/Langmuir Schaefer deposition, which involves dipping the solid support onto a a series of monolayers, and allows the bilayer composition and asymmetry to be controlled through the monolayer composition [22].

To align with the DSC experiments, a bacterial membrane model was required as a planar membrane rather than vesicles. The membrane composition was constructed such that it reflected the charge of the bacterial outer membrane whilst avoiding possible practical concerns. We used a 7:3 mixture of DOPC and DOPG, where DOPG was the charged anionic lipid, but DOPC replaces the PE lipid such that the membrane geometry remained planar rather than curved [23]. Further, DOPC also is zwitterionic and does not have any unfavourable interactions with the SiO_2 substrate in the same way that anionic lipids might, thus providing fewer barriers to SLB formation. For a diagnostic breakdown of the FTIR features for lipid membranes and the experimental solutions, refer to figures 3.4a and 3.4b.

4.3.1 Interactions of EGCg with a Model Bacterial Membrane

The FTIR spectrum for a bacterial membrane model, DOPC/DOPG (7:3), can be seen in figure 4.11. It was predominantly characterised by both the symmetric and asymmetric CH_2 stretching modes at 2840 and 2920 cm^{-1} respectively. The height difference in the peaks is related to the ratio of available stretching modes for each band (approximately 2:1 asy:sym). The feature at 1724 cm^{-1} can be assigned to the ester linkages between the lipid headgroups and tail regions. The region for the phosphorus FTIR features occur at around 1220-1260 cm^{-1} which is below the cutoff for these measurements and as such they are not seen [24]. After the addition of EGCg (100 μM) the changes to the spectrum were twofold: the peak at 1724 cm^{-1} increased in area, as the lower wavenumber edge of the peak broadened and tailed off. There was also the emergence of a peak at 1603 cm^{-1} which is assigned to the presence of aromatic C=C, C-H, C-O, and C-OH stretching at the membrane surface [25, 26].

The kinetics of the interaction with the SLB are shown in figure 4.12. Given the small size of the EGCg molecule, the membrane surface saturated quickly, with no further detectable change to the peak areas after approximately 15 minutes. As with the DSC experiments involving EGCg it appears as though the interaction was entirely mediated by electrostatics with the sterics of the molecule having little to no impact on the ability of EGCg to reach the

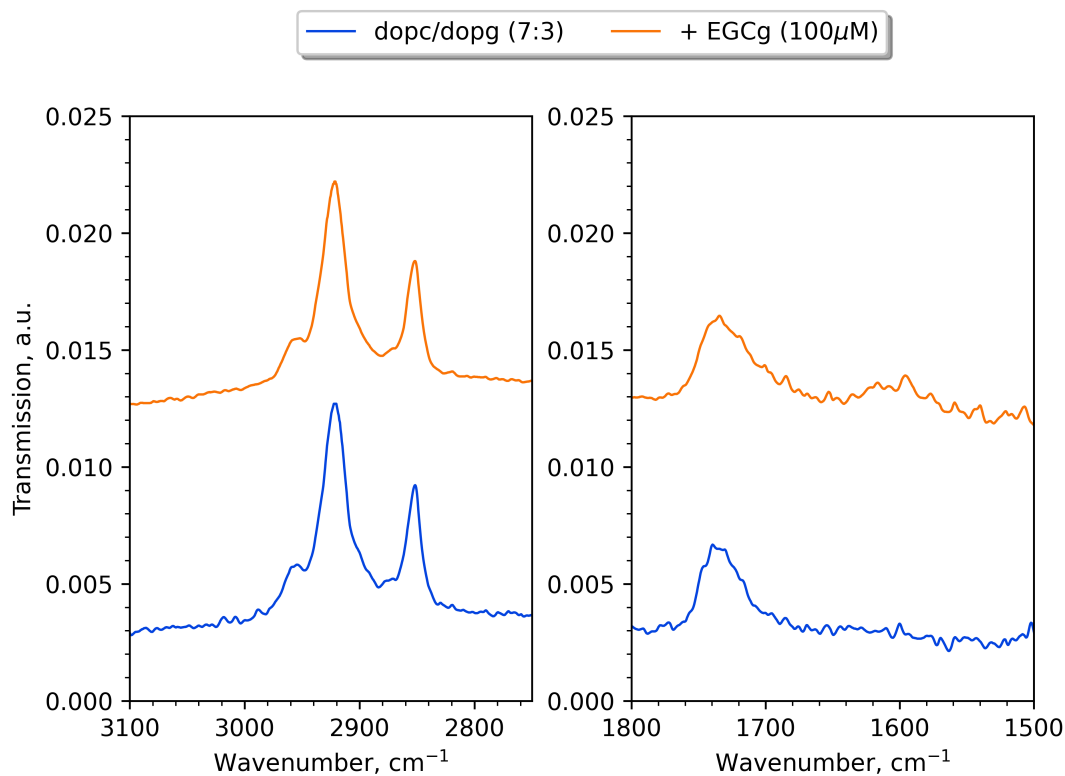


Figure 4.11: FTIR spectrum for a DOPC/DOPG (7:3) SLB before (blue) and after (orange) addition of EGCg ($100 \mu\text{M}$), showing relevant sections to highlight the asymmetric (2920 cm^{-1}) and symmetric (2840 cm^{-1}) C–H stretching modes as well as the C=O stretching mode (1724 cm^{-1}). After the addition of EGCg ($100 \mu\text{M}$) a peak can be seen having appeared (1603 cm^{-1}) as a result of the presence of EGCg at the interface, as well as an increase in the area under the peak at 1724 cm^{-1} .

membrane surface. The FTIR spectrum (figure 4.11, orange) was recorded after copious washing of the surface with buffer solution indicating that the binding of the EGCg with the SLB surface was strong enough to withstand laminar flow of the bulk solution.

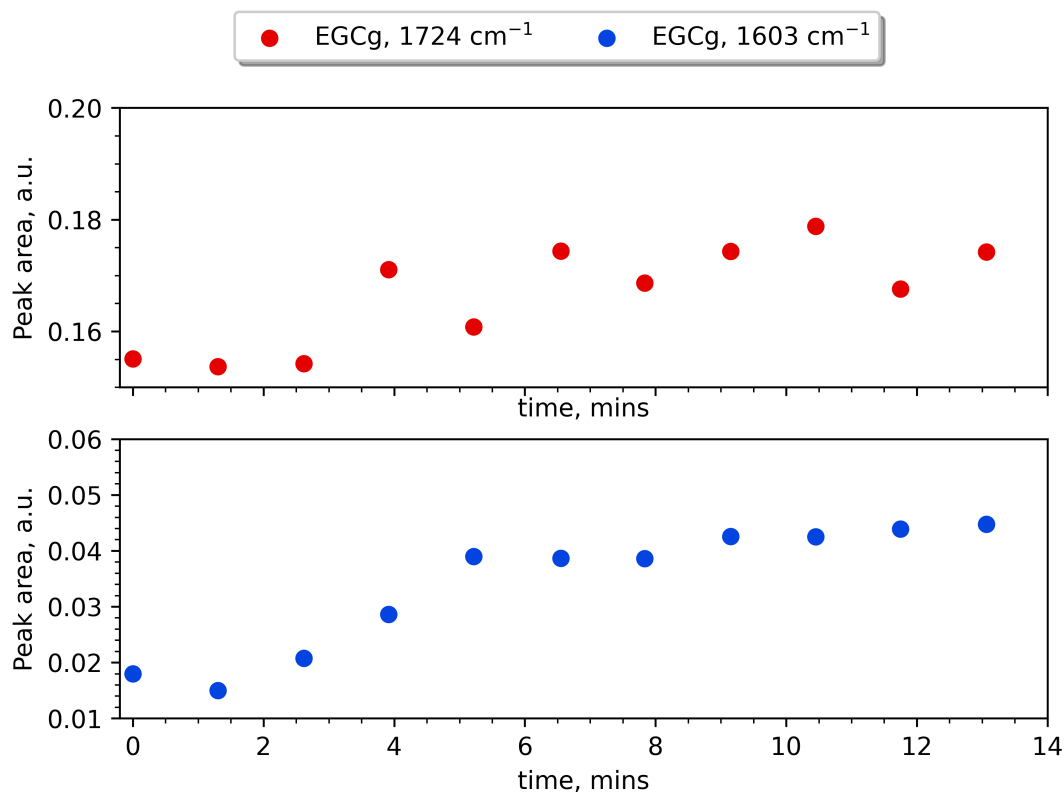


Figure 4.12: Kinetics of interaction of EGCg ($100\mu\text{M}$) with the bacterial model DOPC/DOPG (7:3) membrane. The top panel (red) shows the small increases in the area under the peak at 1724 cm^{-1} corresponding the ester groups in the lipid tails. The EGCg ester groups are thought to cause the increased peak area. For the feature that appears at 1603 cm^{-1} (blue) the aromatic C=C, C-H and C-OH are likely responsible.

Interaction of EGCg with a DOPC/DOPG (7:3) SLB was also investigated using QCM-D. This allowed further evidence of bilayer interaction to be observed, i.e. if the EGCg stayed in solution it would simply wash over the sensor after SLB formation and there would be no substantial or long lasting mass changes at the surface. The change to both frequency and dissipation by the interaction of EGCg with the model DOPC/DOPG (7:3) membrane is shown in figure 4.13. The changes in ΔF and ΔD were measured in multiple overtones (3rd, 5th, 7th, and 9th) simultaneously.

The ΔF changes in figure 4.13, shown in red/orange/yellow/grey for the 3rd/5th/7th/9th overtones respectively, highlight the key parts of SLB formation [15, 27]. Injection of the DOPC/DOPG (7:3) vesicle solution and vesicle adsorption corresponds to the initial decrease in frequency (i.e. increase

in mass) and an associated increase in the dissipation value due to the soft, non-rigid nature of the vesicles. Upon vesicle rupture via osmotic shock and water loss from buffer trapped in the centre of the vesicle to the bulk solution during SLB formation there is mass loss at the surface (i.e. increase in ΔF and a decrease in ΔD) as the layer becomes thinner and more rigid. The bilayer was then washed with buffer solution to ensure any intact vesicles still adhering to the sensor surface were washed away. During the washing with buffer solution the traces in ΔF and ΔD become more stable, settling at *ca.* -25 Hz which is characteristic of bilayer formation [15, 21, 28]. Various stages in the SLB formation process are annotated in figure 4.13.

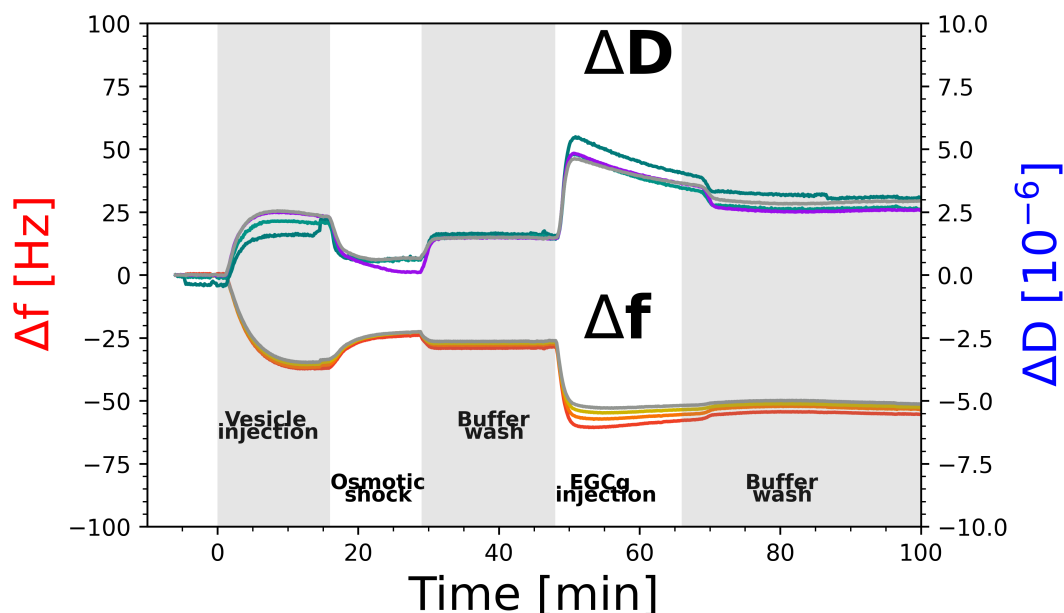


Figure 4.13: QCM-D plots showing changes to both frequency and dissipation (ΔF , ΔD respectively) in the 3rd (red, green) 5th (orange, teal), 7th (yellow, purple), and 9th (grey, grey) overtones for formation of a DOPC/DOPG (7:3) SLB followed by interaction with EGCg (100 μM). Bilayer formation was ensured through osmotic shock after vesicle adsorption. The change in ΔF shows that the interaction at the bilayer surface was strong enough such that the EGCg remained bound at the membrane surface under constant flow of buffer solution.

Addition of EGCg (100 μM) to the SLB shows further significant mass change at the surface, with another large decrease in the frequency. The dissipation change indicates the addition of a layer that reduces the overall rigidity of the film at the sensor surface, as it became more viscous and hydrated. The fact that the SLB was able to remain stable, evidenced by a stable frequency, under laminar flow of the buffer solution points to the mass change coming from the addition of EGCg on top of the model bacterial membrane. After injection of the polyphenol solution the membrane and anything bound to it was washed with buffer solution. During the washing the mass change caused by addition of EGCg at the membrane surface distal to the

SiO₂ sensor showed a small decrease in mass (i.e. a slight increase in frequency as slight decrease in dissipation) as any loosely bound EGCg was washed away. A large proportion of the EGCg introduced to the membrane surface was bound tightly enough such that it remained adhered to the bilayer after rinsing. This mass change from EGCg addition also corresponded to a frequency change of approximately -25 Hz. Much like the FTIR study, the kinetics of the EGCg interacting at the membrane surface are rapid in the QCM-D scenario. Apparent saturation of the EGCg at the bilayer-water interface takes place in ≤ 5 minutes, at a relatively low flow rate (0.2 mL.min⁻¹). This indicates that the affinity of the membrane surface for EGCg is relatively high, with most polyphenol coming near the membrane surface being attracted to interact.

Both FTIR and QCM-D have shown that the addition of EGCg to a DOPC/DOPG (7:3) SLB shows persistent changes at the membrane interface, and further that the interactions were strong enough to withstand the flow of solution without complete removal of polyphenol from the interface. This characterisation using SLBs makes investigation of EGCg at the bacterial membrane surface a strong candidate for further examination, for example, using neutron reflectometry.

4.3.2 Interactions of Tellimagrandin II with a Model Bacterial Membrane

Tellimagrandin II shows similar effects in the FTIR spectrum to EGCg, in that the lipid CH₂ and CH₃ peaks are unaffected, while the carbonyl peak at 1724 cm⁻¹ increased in both magnitude and breadth with the addition of the polyphenol to the DOPC/DOPG (7:3) membrane surface. From the structure of Tel-II (see figure 4.8a) it is posited that the new peak that appears at 1595 cm⁻¹ comes from the presence of aromatic C=C, C=O, and aromatic C-OH groups at the membrane interface. There are no major shifts or peak areas to the symmetric (2920 cm⁻¹) and asymmetric (2840 cm⁻¹) C-H stretching modes of the lipid tails.

The kinetics of the interaction of Tel-II with a DOPC/DOPG (7:3) model bacterial membrane are given in figure 4.15, in terms of the increasing in the area under the curve of the FTIR peak area. In contrast to EGCg which took around 15 mins until the peak areas plateaued the Tel-II peak areas continued to increase for 1050 mins; approximately 70 times longer for Tel-II than EGCg. There is some inflexibility in the structure of Tel-II through a fused ring system, and so the increased time taken for the peak area to reach a maximum value is rationalised in terms of the slow equilibration of Tel-II molecules becoming optimally oriented at the membrane surface. The larger surface area of Tel-II, compared to EGCg, provided a steric barrier for additional Tel-II reaching the headgroups of the outer leaflet.

The kinetics of Tel-II addition to the DOPC/DOPG(7:3) membrane surface were observed in 3 parts. Initially, changes to the peak areas immediately

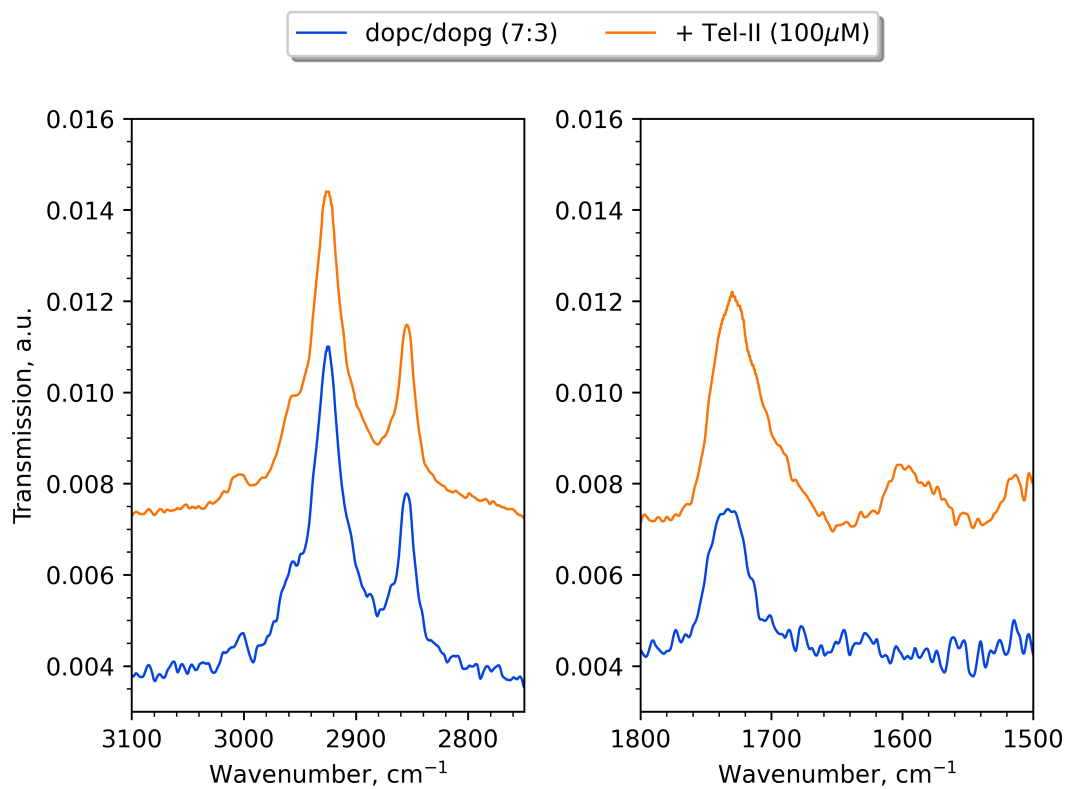


Figure 4.14: FTIR spectrum for a DOPC/DOPG (7:3) SLB before (blue) and after (orange) addition of Tel-II ($100 \mu\text{M}$), showing relevant sections to highlight the asymmetric (2920 cm^{-1}) and symmetric (2840 cm^{-1}) C–H stretching modes as well as the C=O stretching mode (1724 cm^{-1}). With the addition of Tel-II ($100 \mu\text{M}$) a peak appears at 1595 cm^{-1} along with an increase in the area under the peak at 1724 cm^{-1} .

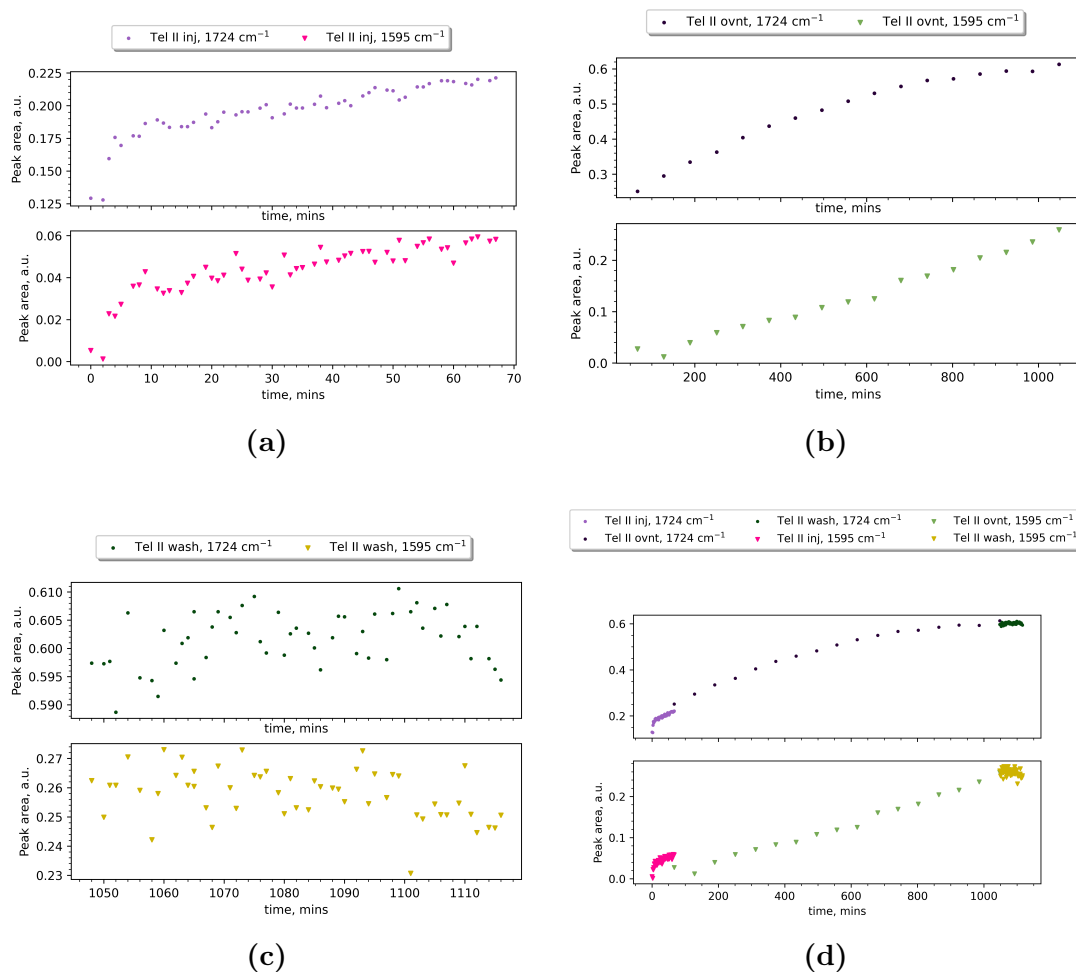


Figure 4.15: Figure showing changes to FTIR peak areas for Tel-II ($100 \mu\text{M}$) with the bacterial model DOPC/DOPG (7:3) membrane. The top panel (red) in each shows increases in the area under the peak at 1724 cm^{-1} corresponding to the ester groups in the lipid tails. The ester linkages in the polyphenol are likely the cause of the increased peak area. For the feature that appears at 1595 cm^{-1} (blue) the aromatic C=C, C-H and C-OH are likely responsible. The changes to the peak area was measured in 3 parts with (a) the initial changes as the Tel-II was injected across the membrane, (b) longer timescale increases as measured overnight, and (c) reaction termination after excess Tel-II was rinsed away from the surface. (d) shows all three sets of changes overlaid.

following injection of Tel-II was monitored, with changes are shown in 4.15a. After over 1h the area underneath both the 1724 and 1595 cm^{-1} continued to increase. To understand better the rate at which Tel-II interacted with the model membrane surface the sample was left collecting overnight at *ca.* 1h time intervals in figure 4.15b. For the overnight run, the area under both peaks continues to increase, and only begins to stall after *ca.* 17h. The data for the the interaction after being washed with buffer is shown at 4.15c and shows no further increase to the peak area for both 1724 and 1595 cm^{-1} peaks. All three data sets are overlaid in 4.15d.

QCM-D was employed to check the changes in mass at the surface of the model bacterial membrane, with changes in Δf and ΔD being shown in figure 4.16. As for EGCg, the lipid vesicles show spontaneous adsorption ($t = 0$ min) and rupture, with frequency and dissipation changes that correspond to a suitably thin rigid bilayer. Again, this model bilayer showed the characteristic frequency change of *ca.* -25 Hz after the osmotic shock process had been completed. Addition of Tel-II shows a mass change that occurs over approximately 35 mins, which is far longer than observed for EGCg, and a total frequency change of *ca.* 20 Hz. Again, upon washing the membrane with buffer solution, the mass change that resulted from the Tel-II interaction is persistent. The mass change was accompanied by an increase in the Δd values, indicative of a more viscous layer being formed and the bilayer losing some of its rigidity. Finally, when the sample cell was washed with buffer solution, the dissipation values returned to similar values observed for bilayer formation. This indicates that any loosely bound Tel-II at the membrane surface was washed away leaving any change in frequency as a result of strong binding at the bilayer surface.

Addition of Tel-II to a DOPC/DOPG (7:3) model membrane, much like for ECGg, shows an interaction at the interface that is strong enough to withstand laminar solution flow. The larger molecular area of Tel-II (688.8 \AA^2) compared to EGCg (398.2 \AA^2) may have resulted in restricted access of the galloyl groups to the lipid surface and resulted in an increased time for the mass or peak area changes to take place. For area per molecule values the reader is referred back to table 4.7.

4.3.3 Interactions of Tellimagrandin I with a Model Bacterial Membrane

Tellimagrandin I (figure 4.9a) is structurally very similar to Tel-II, and so it follows that there would also be some interaction with a model bacterial bilayer. As was the case for previous interactions, the FTIR features for the lipid tails' CH_2 sym, CH_2 asym, and CH_3 sym stretching modes were unaffected through the interaction. The peak at 1726 cm^{-1} is attributed to the C=O group in and around the lipid headgroup. Upon addition of Tel-I to the surface the area under the 1726 cm^{-1} peak increased from the presence of Tel-I carbonyl groups near the interface. A further peak appeared at 1577 cm^{-1} , which is assigned to the Tel-I aromatic C=C, C-H, and C-OH moieties. The FTIR spectrum of a

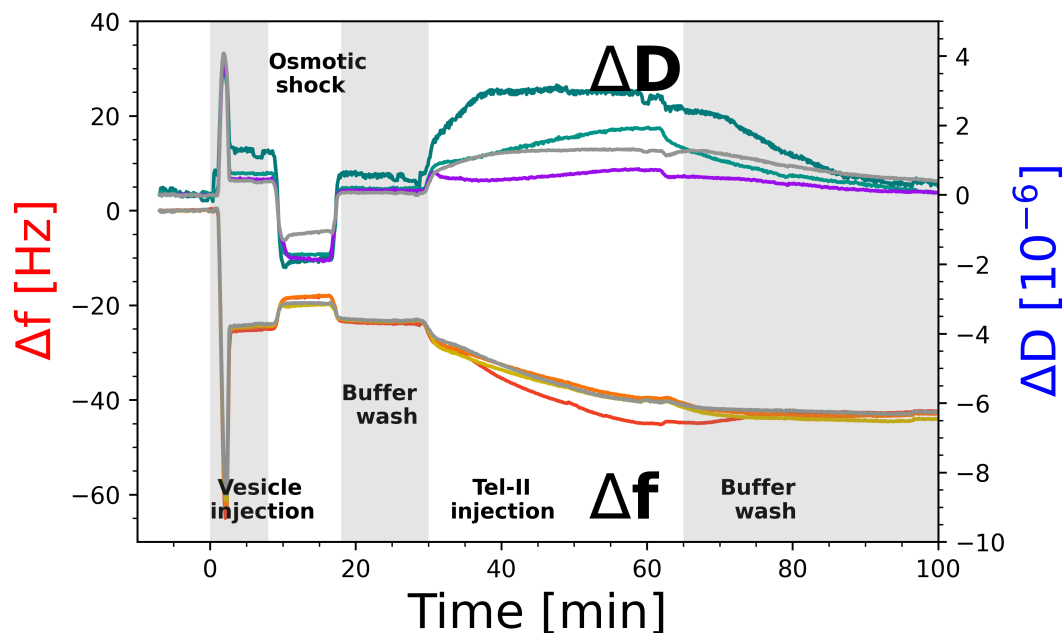


Figure 4.16: QCM-D plots showing changes to both frequency and dissipation (ΔF , ΔD respectively) in the 3rd (red, green) 5th (orange, teal), 7th (yellow, purple), and 9th (grey, grey) overtones for formation of a DOPC/DOPG (7:3) SLB followed by interaction with Tellimagrandin II (100 μM). Bilayer formation was ensured through osmotic shock after vesicle adsorption. The change in ΔF shows that the interaction at the bilayer surface was strong enough such that the Tel-II remained bound at the membrane surface under constant flow of buffer solution.

DOPC/DOPG (7:3) model membrane before and after the addition of Tel-I is shown in figure 4.17. Addition of Tel-I to the bilayer interface produced smaller changes in the peak areas than for both EGCg and Tel-II (see figures 4.12 and 4.15 respectively), and showed delayed appearance of the aromatic polyphenol peak at 1577 cm^{-1} .

In the instance of QCM-D, the interaction of Tel-I (100 μM) with the model bacterial membrane more closely resembled that of Tel-II than EGCg in terms of rate of mass change. The bilayer formed after osmotic shock, characterised by $\Delta f = -30\text{ Hz}$, showed an interaction that changed the mass at the surface more gradually than the two polyphenols that were shown above. After *ca.* 20 minutes of Tel-I injection the mass change began to flatten ($t = 56\text{ mins}$), and then the mass change was persistent when washed with buffer. The amount of interaction with the surface was suggested to be less than that for both Tel-II and EGCg based on the magnitude of the frequency changes (Tel-II = -20 Hz ; EGCg = -25 Hz).

The use of SLBs to investigate interactions of Tel-I with a model bacterial membrane (DOPC/DOPG (7:3)) show that an interaction does take place, but reduced in intensity from interactions measured with EGCg and Tel-II. The increasing in the area under the peaks in FTIR measurements were of a lower

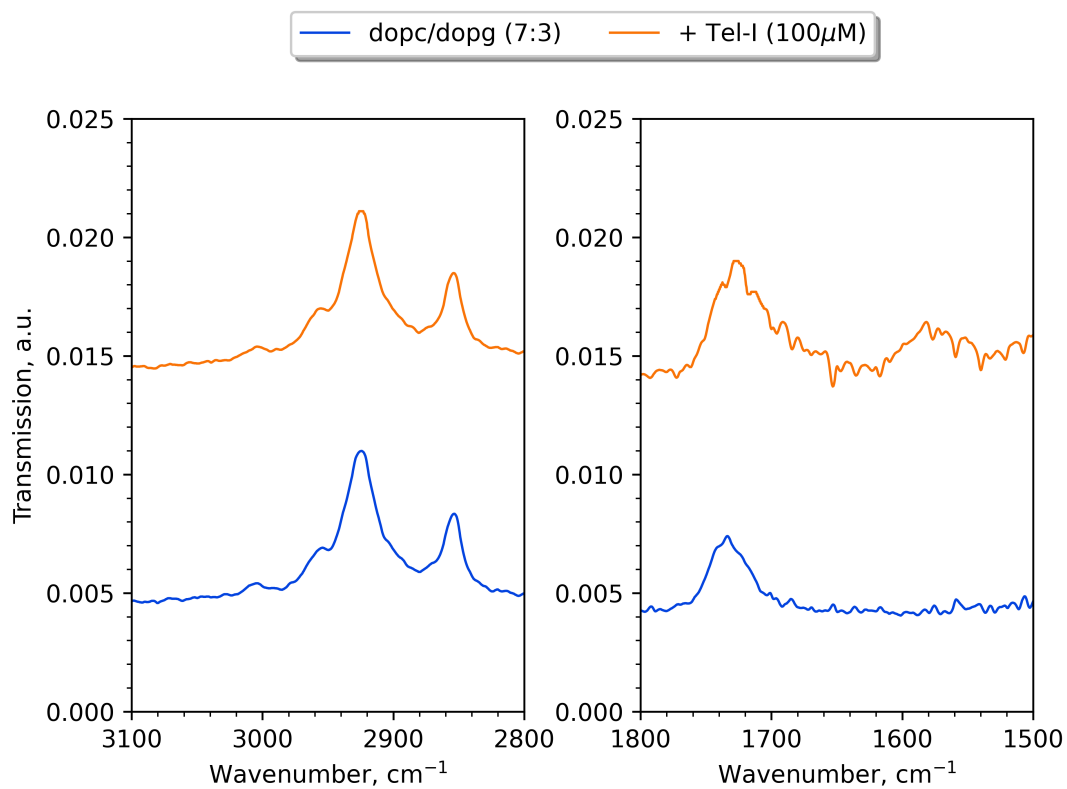


Figure 4.17: FTIR spectrum for a DOPC/DOPG (7:3) SLB before (blue) and after (orange) addition of Tel-I ($100 \mu\text{M}$), showing relevant sections to highlight the asymmetric (2920 cm^{-1}) and symmetric (2840 cm^{-1}) C–H stretching modes as well as the C=O stretching mode (1726 cm^{-1}). With the addition of Tel-I ($100 \mu\text{M}$) a peak appears at 1577 cm^{-1} along with an increase in the area under the peak at 1726 cm^{-1} .

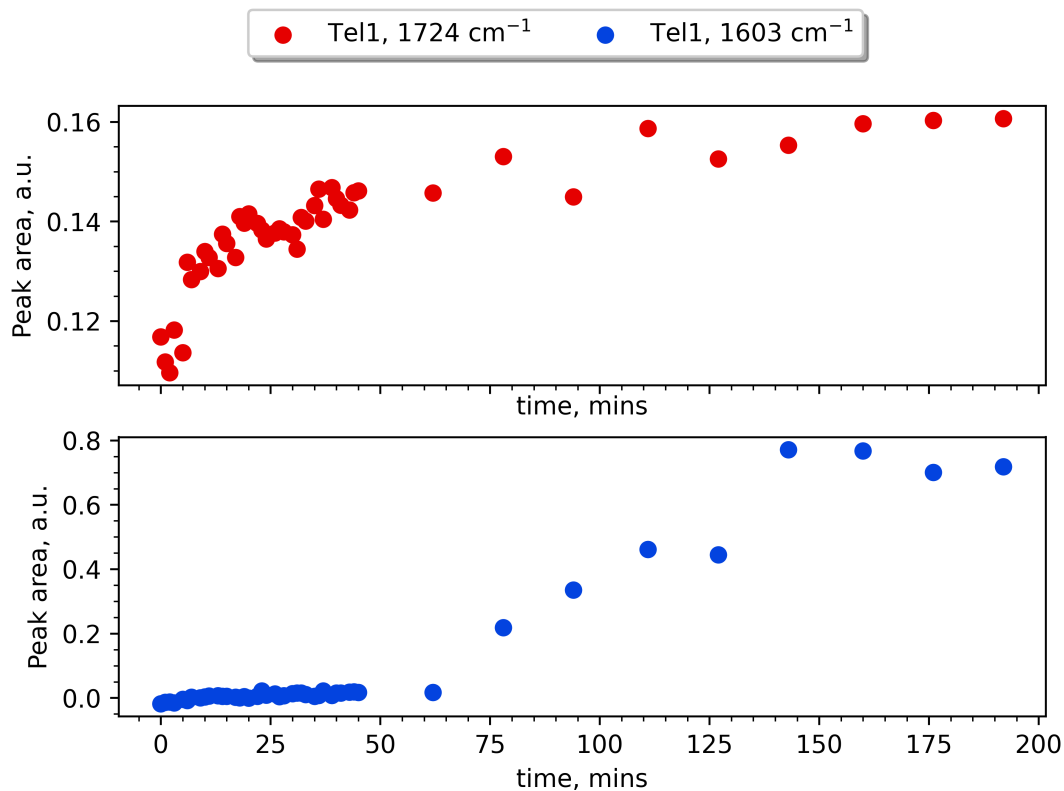


Figure 4.18: Plots to show the kinetics of interaction of Tel-I ($100 \mu\text{M}$) with the bacterial model DOPC/DOPG (7:3) membrane. The top panel (red) shows the small increases in the area under the peak at 1726 cm^{-1} corresponding to the ester groups in the lipid tails. The EGCg ester groups are thought to cause the increased peak area. For the feature that appears at 1577 cm^{-1} (blue) the aromatic C=C, C-H and C-OH are likely responsible.

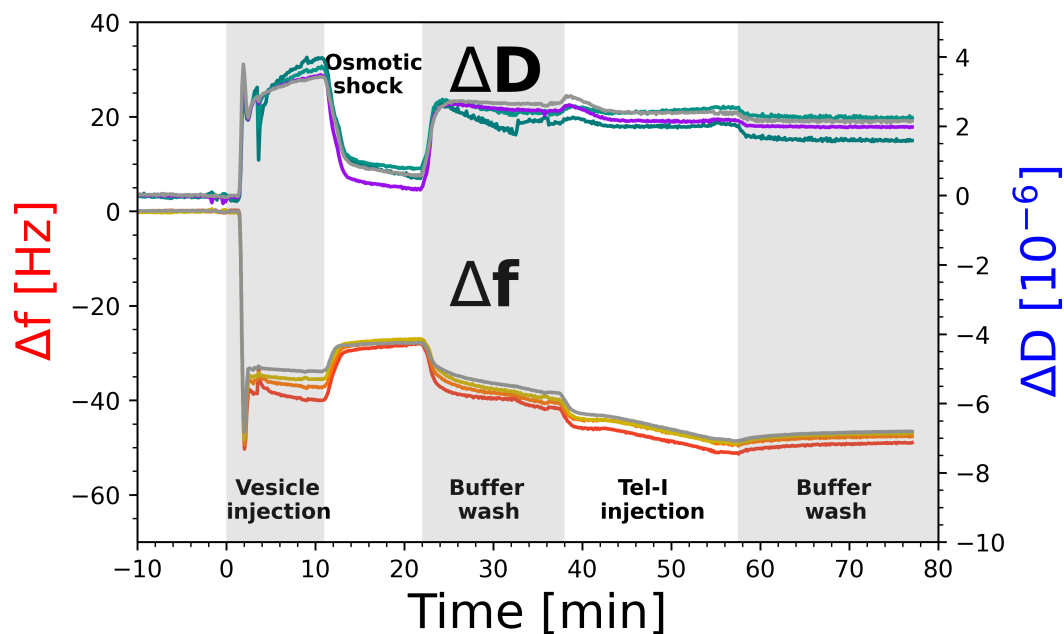


Figure 4.19: QCM-D plots showing changes to both frequency and dissipation (ΔF , ΔD respectively) in the 3rd (red, green) 5th (orange, teal), 7th (yellow, purple), and 9th (grey, grey) overtones for formation of a DOPC/DOPG (7:3) SLB followed by interaction with Tellimagrandin I ($100 \mu\text{M}$). Bilayer formation was ensured through osmotic shock after vesicle adsorption. The change in ΔF shows that the interaction at the bilayer surface was strong enough such that the Tel-I remained bound at the membrane surface under constant flow of buffer solution.

magnitude and took longer to be observed for Tel-I, and further the overall frequency change in QCM-D experiments showed less adsorption of Tel-I to the membrane surface. Furthermore, the dissipation in the QCM-D measurements shows less viscosity in the layer after Tel-I when compared to Tel-II or EGCg. This could point to simply less material aggregation at the membrane surface. Alternatively, it could speak to the nature of the interaction, with EGCg and Tel-II being more intercalated into the bilayer, where Tel-I simply adsorbs to the headgroups in the outer leaflet, perhaps.

4.4 Floating Model Bacterial Membrane Interactions with EGCg using Neutron Reflectometry

Floating lipid bilayers offer the greatest accuracy for membrane models, as they are not bound to the surface in any formal way [14]. Floating membranes, unlike SLBs, have bulk solution on both sides of the membrane, and can be formed either above an SLB already at the interface or above a grafted self assembled monolayer (SAM) [29–32]. The separation of the membrane from the SAM surface is due to a balance of both electrostatic and van der Waals forces that are countered by entropic repulsion. That is, floating bilayers are kept supported on a water interlayer, as total adherence of the bilayer to the substrate prevents out of plane fluctuations resulting in a decrease in the membrane entropy [31, 33]. The main drawback of the more accurate floating membrane systems is the complexity of their preparation. SLBs can be formed with relative ease, whereas floating membrane preparation requires extra steps.

As mentioned in chapter 3, the techniques and bacterial membrane composition used in this portion of work are not novel, but are useful in demonstrating the appropriateness of neutron measurements to model membrane samples. However, the characterisation of the interactions of EGCg and Tellimagrandin-II with model bacterial membranes in this chapter is novel, and has not been studied using neutron reflectometry before.

Floating bacterial model membranes were formed and analysed using neutron reflectometry (NR), for which the experimental detail was covered in chapter 2. NR is a powerful technique that allows structural detail of materials to be resolved on a nanometer scale through measuring changes in the scattering length of constituent atoms in the layers of a material [34, 35]. As the neutron waves move through the layers, constructive and destructive interference between the reflected neutrons result in the appearance of fringes in the data [36, 37].

Since the scattering length of atoms varies between isotopes, (e.g. $6.35 \times 10^{-6} \text{ \AA}^{-2}$ for D_2O and $-0.56 \times 10^{-6} \text{ \AA}^{-2}$ for H_2O) it is possible to tailor the solution scattering length density (SLD) to be able to hide or highlight certain

aspects of the sample system via contrast matching [38]. Simultaneous analysis of data from multiple solution contrasts allows the determination of the relative proportions of each component in the sample, giving information about the structure of the sample [14].

When reduced to its most fundamental aspect, the neutron reflectivity experiments were designed to observe changes before and after a process had occurred. Samples were exposed to the neutron beamline to monitor changes before and after vesicle adsorption, bilayer formation, and polyphenol interaction. The changes that can be seen in the reflectivity plots were accounted for in alterations to the computational model and fitting.

4.4.1 Interactions with EGCg from the Bulk Solution

EGCg interactions with a bacterial membrane model has shown positive results using both vesicles (chapter 4.2.1) and supported lipid bilayers (chapter 4.3.1). The increases in FTIR peak area and the persistent increase in mass at the SLB surface are good indicators that there is a strong lipid-EGCg interaction which is suitable for further study. The quality of the preliminary characterisations make the lipid-EGCg system a strong candidate for structural investigation using NR.

The experimental detail for these experiments has been covered in chapter 2.7.2. In brief, a floating lipid bilayer was formed using vesicle rupture via osmotic shock. The buffer solutions contained sufficient salt species such that a water gap between the functionalised underlayers and the model membrane was maintained at approximately 10 Å. The bilayer before and after interaction with EGCg (100 μ M) was measured in 4 solution contrasts (H_2O , silicon matched water (SiMW), gold matched water (AuMW), and D_2O).

Reflectivity plots for the interaction of EGCg with the DOPC/DOPG (7:3) model bacterial membrane are shown in figure 4.20 along with the SLD profile. The underlayers (Silicon, gold, permalloy) have been cropped out of the SLD profile for clarity. In the reflectivity plots (figure 4.20 panels A-D) and the SLD profiles (panel E) the bare SAM is shown in green and displays no features in either the H_2O and D_2O contrasts other than for the SAM at around 400 Å from the interface.

Blue lines in all plots (A-E) show the bilayer features in the four solution contrasts before interaction with EGCg. The SLD profile shows a high coverage lipid bilayer (95%) with an appropriately sized (6 Å) gel-phase water gap between the SAM and the floating membrane. The thickness of the tail region of the bilayer before (21 Å) and after (20 Å) the addition of EGCg (100 μ M, red lines) remains relatively unchanged indicating that there is no alteration to the hydrophobic tail core due to the presence of the polyphenol. Despite limited changes to the tail region, the model allowed EGCg to be on either side of the bilayer, or associate with either the headgroups or tail regions within the membrane. The best fit of the model came from allowing three distinct

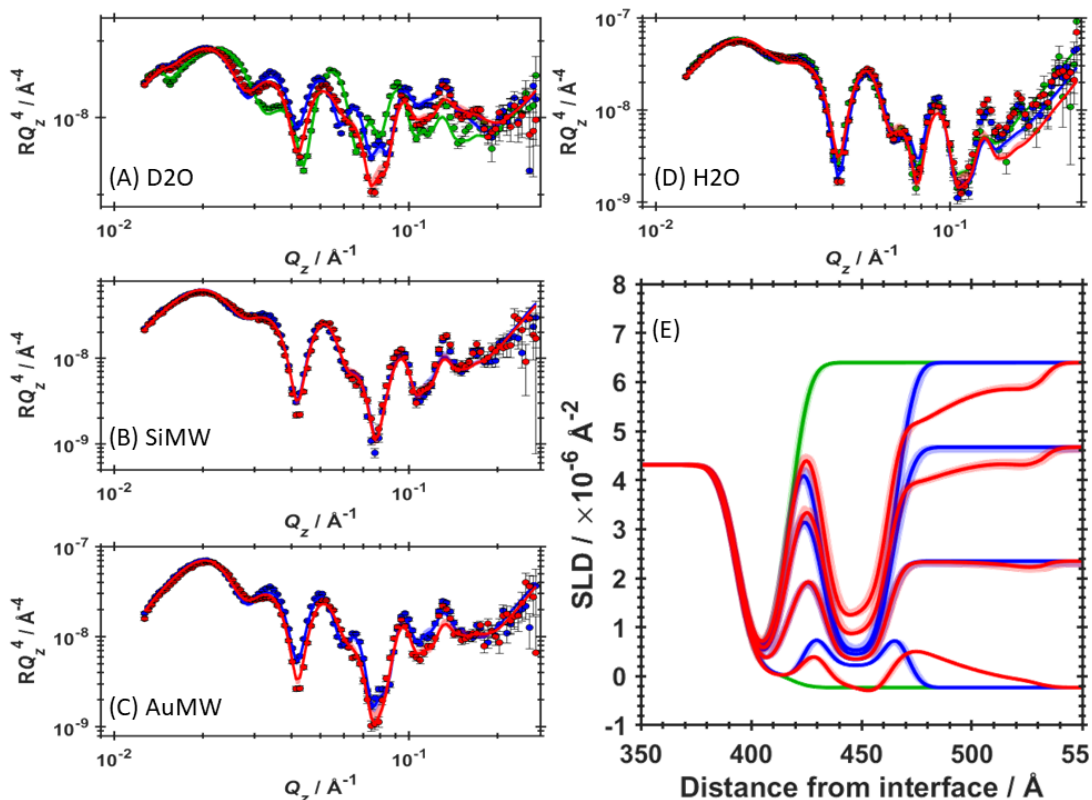


Figure 4.20: Panels (A-D) showing neutron reflectivity profiles for data (points) and model fits (lines) for a COOH-SAM/Gold/Permalloy coated silicon substrate (green) with DOPC/DOPG (7:3) model membrane before (blue) and after (red) interaction with (-)-EGCg (100 μM) in various contrasts. (E) Neutron SLD profiles showing the Si-Py-SAM-COOH underlayers (green) with DOPC/DOPG (7:3) bilayer both before (blue) and after (red) interaction with (-)-EGCg (100 μM) solution in H₂O, gold and silicon matched water, and D₂O contrasts. The SLD profile (E) has been cropped to show membrane regions more clearly, leaving out the underlayers.

EGCg layers on the outer leaflet (most distal to the silicon substrate) each more hydrated than the last, as well as one inner EGCg layer between the membrane and the SAM. The thickness of this layer (0.16 \AA) suggests that movement through the membrane is not active, and that the amount of EGCg contained in the central water gap is not high. Likely, the EGCg in this later is planar due to the low thickness value from the model fit. The thickness of the central water gap increases slightly after addition of EGCg, from 6.53 \AA to 6.93 \AA , to accommodate the movement of EGCg across the membrane. Output values from the model fits and the associated error bounds are given in table 4.8, with a full list of fitting parameters given in table A.1.

The interaction is depicted schematically in figure 4.21. A diagrammatic representation of the membrane system including the gold layer and the SAM, is shown overlaid on the SLD plot taken from figure 4.20. The external layers of EGCg show that at the surface the solution is most densely populated with EGCg

Table 4.8: Parameter values and error bounds (upper bound, lower bound) for key parameters from the fitting and error estimation routines for the DOPC/DOPG (7:3) model bacterial membrane before and after interaction with EGCg (100 μ M). Parameters with no associated error bounds have been derived from the appropriate SLD profiles.

Parameter	Before (-)-EGCg	After (-)-EGCg
Central water thickness, \AA	6.53 (6.25, 6.89)	6.93 (6.87, 7.09)
Bilayer coverage, %	95.3 (94, 96.6)	98.9 (98.9, 99.24)
Bilayer roughness, \AA	5.69 (5.49, 5.95)	5.18 (5.09, 5.34)
Lipid APM, \AA^2	73.95 (73.93, 75.21)	74.33 (73.85, 74.82)
Outer HG thickness, \AA	15	59
Tail region thickness, \AA	21	20
Inner tannin thickness, \AA		0.16 (0.16, 0.16)
Outer tannin total thickness, \AA		15

interacting with the lipid headgroups. As the distance away from the membrane surface into the bulk solution increases we see on the SLD profile that the fit tapers to match the SLD of the bulk solution. To echo that, the EGCg shows three layers (as per the mathematical model) with each layer moving into the bulk solution becoming less densely populated with EGCg and more hydrated in nature.

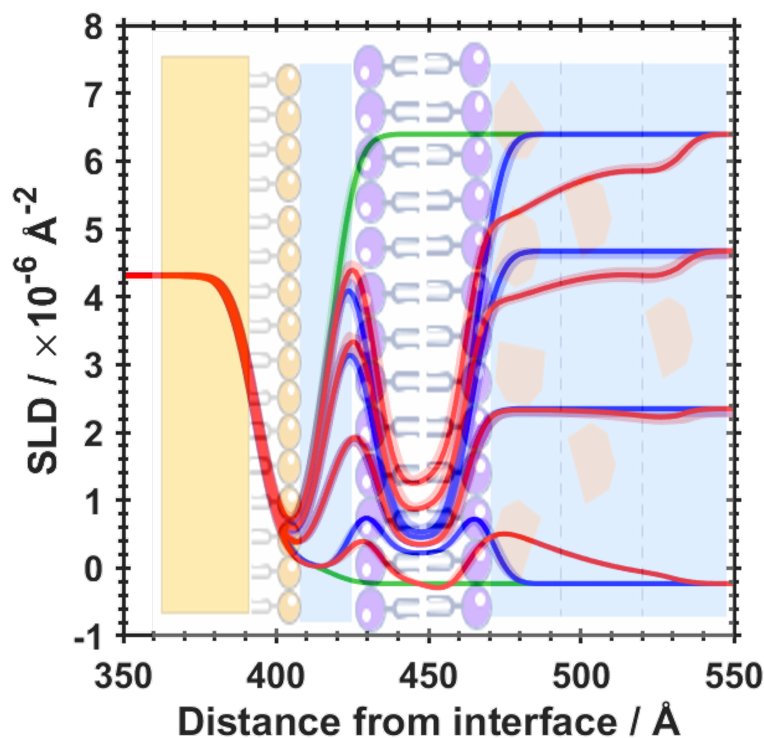


Figure 4.21: SLD plot for the DOPC/DOPG (7:3) model membrane system overlaid with a schematic illustration of the underlayers, SAM, and bilayer with EGCg interactions included. The amount of EGCg in the external layers reduces as the distance away from the membrane increases, leaving a less EGCg-dense, and more hydrated layer to match the tapering of the SLD profile into the bulk solution.

4.5 Analysis of Model Bacterial Membranes Containing Pre-Mixed EGCg

In order to reflect the sample preparation method for the DSC samples that showed interaction of EGCg with a model bacterial membrane (see figure 4.6) an analogous NR sample was prepared and deposited. The SLD profile for the membrane region of interest is shown in figure 4.22 and is quite different to the SLD profile for the DOPC/DOPG (7:3) membrane back in section 3.6, particularly in the outer headgroup region. By contrast the inner headgroup region of both the lipid only membrane (9 Å) and the EGCg-doped membrane (15 Å) remained comparatively less affected. Other key parameters from the fitting and error estimation routines are given in table 4.9.

From the SLD profile in figure 4.22, and from table 4.9, the effects of EGCg on the outer headgroup region can be compared. A full list of fitting parameters can be found in table A.2. Introduction of EGCg at the sample preparation and sonication stage results in a thinner outer headgroup (48 Å) compared to the interaction from solution (59 Å). The energy input from the probe sonication could potentially allow more EGCg into the tail region, which might give rise

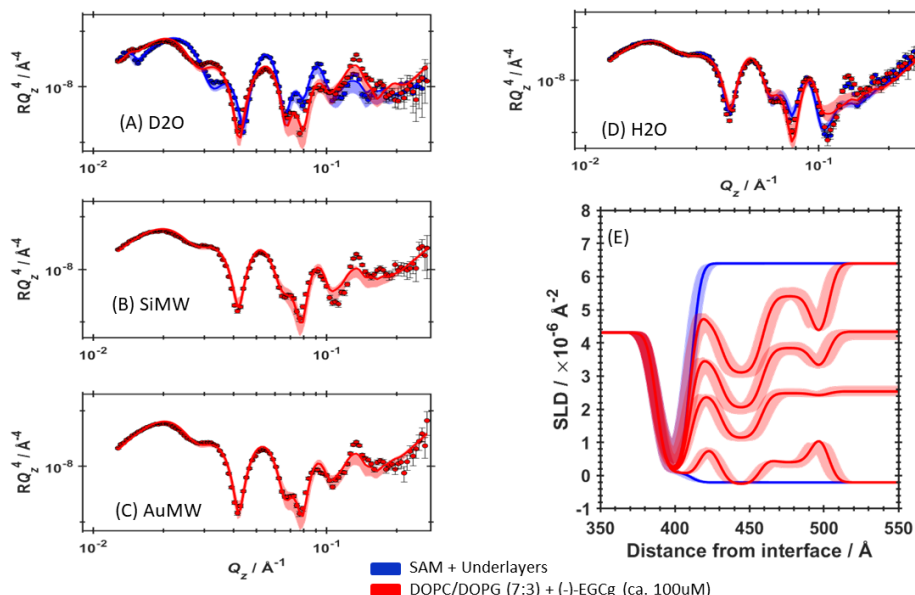


Figure 4.22: Panels (A-D) showing neutron reflectivity profiles for data (points) and model fits (lines) for a COOH-SAM/Gold/Permalloy coated silicon substrate (blue) with DOPC/DOPG (7:3) pre-mixed (doped) with (-)-EGCg (100 μ M) model membrane (red) in various contrasts. (E) Neutron SLD profiles showing the Si-Py-SAM-COOH underlayers (green) with DOPC/DOPG (7:3) bilayer both before (blue) and after (red) interaction with (-)-EGCg (100 μ M) solution in H₂O, gold and silicon matched water, and D₂O contrasts. The SLD profile (E) has been cropped to show membrane regions more clearly, leaving out the underlayers.

to the EGCg-doped membrane having a thicker tail region (26 \AA) compared to the interaction from solution (20 \AA). The mixing of EGCg into the membrane during sonication likely provided enough energy for each individual EGCg molecule to find a conformation where it most efficiently packed with the lipid headgroups and tails with its nearest neighbours, resulting in a lower thickness.

However, the slight reduction in the packing efficiency of the lipid molecules after the addition of EGCg comes at a potential cost. The fit values for the lipid area per molecule (APM) after addition of EGCg in both cases is increased, although the increase in the EGCg-doped membrane (from 73.95 to 76.28 \AA^2) is greater than for the solution based interaction (to 74.33 \AA^2). This points to the individual membrane components requiring more space per molecule in the plane of the membrane, suggesting a more diffusely packed layer. As a result of the less efficient packing, the membrane has more defects and this manifests as a much lower coverage membrane (49.3%) than compared to the model membrane after formation (95.3%) and after the solution based interaction (98.9%). The increase in coverage after the solution based interaction can be explained by free EGCg from solution occupying any pores or defects in the bilayer.

The increasing APM for the doped EGCg membrane can be rationalised as a

Table 4.9: Parameter values and error bounds (upper bound, lower bound) for key parameters from the fitting and error estimation routines for the DOPC/DOPG (7:3) model bacterial membrane before and after interaction with EGCg (100 μ M) and a pre-mixed with EGCg (100 μ M). Parameters with no associated error bounds have been derived from the appropriate SLD profiles. The values from table 3.3 have been repeated here for convenience.

Parameter	Before (-)-EGCg	After (-)-EGCg	Doped (-)-EGCg
Central water thickness, \AA	6.53 (6.25, 6.89)	6.93 (6.87, 7.09)	5.48 (5.26, 5.81)
Bilayer coverage, %	95.3 (94, 96.6)	98.9 (98.9, 99.24)	49.27 (48.29, 50.37)
Bilayer roughness, \AA	5.69 (5.49, 5.95)	5.18 (5.09, 5.34)	5.55 (5.3, 5.88)
Lipid APM, \AA^2	73.95 (73.93, 75.21)	74.33 (73.85, 74.82)	76.28 (75, 77.46)
Inner HG thickness, \AA	11	15	14
Outer HG thickness, \AA	14	59	48
Tail region thickness, \AA	21	20	26
Inner tannin thickness		0.16 (0.16, 0.16)	9.07 (8.53, 9.33)
Outer tannin total thickness, \AA		15	36.99

manifestation of the physical effects within the membrane. Given the rigid and planar structure of EGCg (see figure 4.5a) it follows that EGCg in the doped membrane is willing to occupy the tail region of the bilayer. This is apparent from the SLD profile in figure 4.22 that shows an extended region between the peaks corresponding to the two lipid headgroups at 420 \AA and 500 \AA from the interface. Figure 4.23 gives a visual representation of the EGCg molecules intercalated into the bilayer and the tail region of increased thickness compared to both the lipid only bilayer or the bilayer after interaction with EGCg from solution. Further, compared to the solution based interaction (figure 4.20 the membrane doped with EGCg the fit was not improved by forcing a layer of EGCg outside the membrane. This indicated that the preference for the EGCg is within membrane, and likely in the tail region as shown by the data here based on polarity considerations.

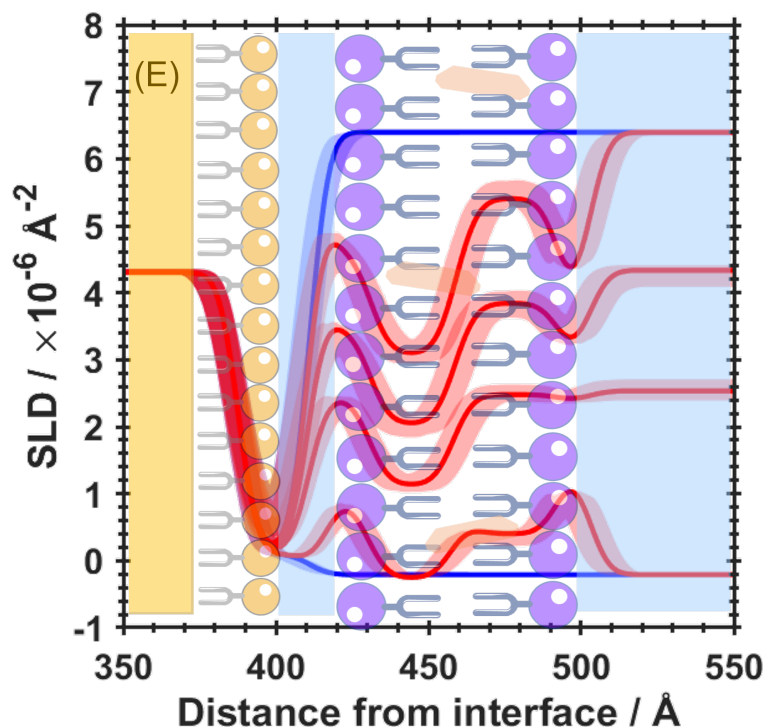


Figure 4.23: SLD plot for the DOPC/DOPG (7:3) model membrane system doped with EGCg (100 μM) overlaid over a schematic illustration of the underlayers, SAM, and bilayer with intercalated EGCg. The inclusion of EGCg in the tail region corresponds to a thicker tail group compared to the either the lipid only bilayer or the bilayer after interaction with EGCg from solution.

4.6 Floating Model Bacterial Membrane Interactions with Tellimagrandin-II using Neutron Reflectometry

When considering the results from sections 4.3.2 4.3.3 during the search for other suitable polyphenolic species to investigate interactions with model membranes, the FTIR data showed similar results in terms of the peaks that appeared after injection of the respective polyphenols. Tellimagrandin-II (Tel-II) showed more drawn out kinetics in terms of the FTIR peak area, but the analysis of Tel-II showed a larger peak area compared with Tellimagrandin-I. Furthermore, QCM-D results showed interaction of Tel-II with model membrane at the sensor surface resulted in larger mass changes at the interface (*ca.* -20 Hz) after interaction compared with Tellimagrandin-I (*ca.* -10 Hz). Based on these results, and including the interactions seen in the DSC experiments, Tel-II was selected as the next polyphenol to investigate interactions with a floating model bacterial membrane.

The composition of the model bacterial membrane was retained

(DOPC/DOPG, 7:3) from the previous NR experiment for two main reasons. First, this membrane composition has been method tested and optimised for deposition, with challenges being accounted for and overcome, as discussed in the previous chapter (see section 3.3.2). While some accuracy in the model is sacrificed, and has not been developed to the same extent as the interaction portion of the experimental setup, there is a degree of repeatability and robustness to using a floating membrane that can be formed with a high degree of confidence. This composition still allows for interaction with DOPG in the membrane, where PG lipids are abundant in bacterial membranes whilst retaining the fluidity for bilayer formation using vesicle rupture methods. Second, keeping the membrane the same allows for direct comparisons between the two polyphenols: EGCg and Tel-II, the effects of which are similar in nature yet contain some subtle, but key differences.

Results of the model fits (lines) to the experimental data (points) for the interaction of Tel-II with a model bacterial membrane are shown in figure 4.24 and values are given in table 4.10. A complete list of fitting parameters is given in table A.3. The SLD profile shows the effects of the Tel-II interaction on the membrane (red). Rather than addition of the polyphenol into the bilayer, the best fits were generated by allowing lamellar stacking of the membrane to take place. This phenomenon is straightforward to explain, but first the reader should be reminded that the floating bilayer systems are constructed inside a closed cell. Therefore, once Tel-II interacted with the initial floating membrane and penetrated the tail region, the lipid molecules that were displaced had to go somewhere. Here the SLD profile shows repeated bilayer formation further into the bulk solution of 3 extra bilayers stacked towards the bulk solution. It could also be the case that the addition of the bulky Tel-II structure inserting into the bilayer causes faults and defects in the membrane along which the bilayer shears when there is not any more space for Tel-II addition into that layer. The “new” sequential bilayers could be formed from portions of the membrane that are separated along these faults.

Practically these extra lamellar layers were all modelled with their own set of bilayer parameters, including a coverage parameter. From table 4.10 the coverage parameters of the each bilayer sequentially decrease from 98% in the initial membrane, showing less coverage and increased roughness and hydration moving away from the Si interface to bilayers 2 (59% coverage), 3 (29%, coverage), and 4 (6% coverage). The larger size of Tel-II (versus EGCg) once a critical amount has penetrated the membrane into the tail region, folds and shears the membrane, creating fragments in the bulk solution.

The system was modelled as: UNDERLAYERS; CW; MEMBRANE; CW2; MEMBRANE2; CW3; TANNIN_PROX; MEMBRANE3; CW4; TANNIN_MED; MEMBRANE4; TANNIN_DIST where each membrane layer has its own associated coverage and roughness parameter. UNDERLAYERS is characterised as Cr; GOLD; SAM, while MEMBRANE layers are defined as HG; TAILS; TAILS; HG. Tel-II was allowed into the layers by including a parameter relating to the volume fraction of the bilayer that described the

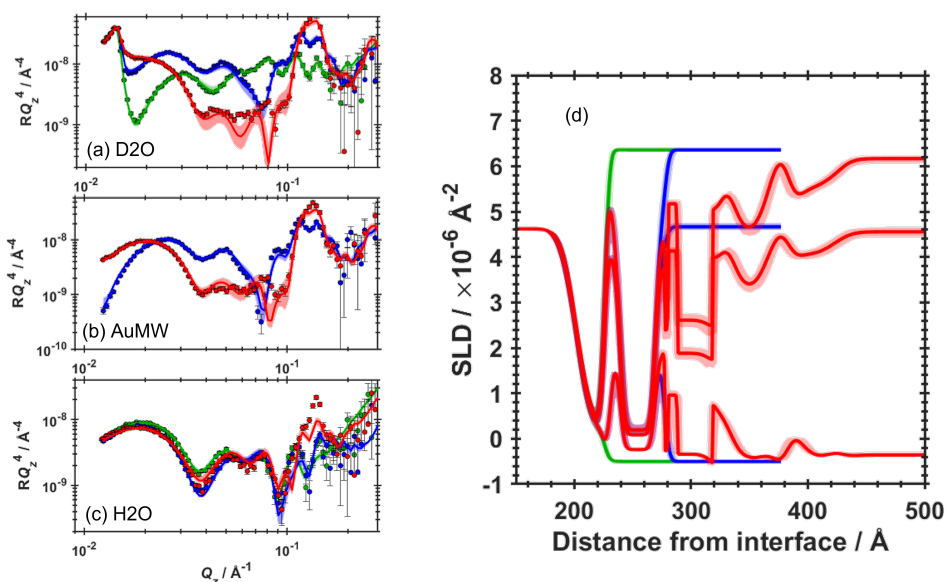


Figure 4.24: Panels (A-C) showing neutron reflectivity profiles for data (points) and model fits (lines) for a COOH-SAM/Gold/Chromium coated silicon substrate (green) with DOPC/DOPG (7:3) model membrane before (blue) and after (red) interaction with Tel-II (100 μM) in various contrast solutions. (D) Neutron SLD profiles showing the Si-Cr-Au-SAM-COOH underlayers (green) with DOPC/DOPG (7:3) bilayer both before (blue) and after (red) interaction with Tel-II (100 μM) solution in H_2O , gold and silicon matched water, and D_2O contrasts. The SLD profile has been cropped to show membrane regions more clearly, leaving out the underlayers.

amount of substance that was *not bilayer*. Tel-II was allowed outside the membrane using distinct regions of the model described by Tel-II layers. The distinct Tel-II layers are described in terms of their thickness and hydration in table 4.10, and was associated with a central water gap between each layer of the multilamellar structure. The most proximal region of Tel-II external to the membrane shows a thickness of zero, while further away from the membrane towards the bulk solution, the Tel-II layers begin to increase in thickness. The most distal layer of polyphenol is this thickest, 83 \AA , although the associated hydration (93%) of that layer suggests that the layer is not purely Tel-II and is relatively polyphenol diffuse. The apparent purpose of the external Tel-II layer outside all the membrane regions in the bulk solution is as a reservoir for Tel-II to move into the bilayer. This is also concordant with the amount of hydration in the distal Tel-II layer from the fitting output. Figure 4.25 shows schematically the nature of the diminishing bilayer coverage as membranes increase in distance from the interface. The volume fraction of Tel-II is 4% within the membranes, and the amount of Tel-II between the membranes is determined by the thickness and hydration of the defined polyphenol layers.

After the addition of Tel-II to the solution, the fitted APM drops from 70

Table 4.10: Values and error bounds (upper bound, lower bound) for key parameters from the fitting and error estimation routines for the DOPC/DOPG (7:3) model bacterial membrane before and after interaction with Tel-II (100 μ M) and a pre-mixed with EGCg (100 μ M). Parameters with no associated error bounds have been derived from the appropriate SLD profiles.

Parameter	Before Tel-II	After Tel-II
Central water thickness, \AA	8.45 (8.40, 8.54)	4.87 (4.76, 4.99)
Bilayer coverage, %	99 (98, 99)	0.98 (0.97, 0.98)
Bilayer roughness, \AA	3.12 (3.09, 3.14)	3.19 (3.14, 3.25)
Lipid APM, \AA^2	70.08 (69.64, 70.48)	56.98 (56.68, 57.29)
Inner HG thickness, \AA	11	15
Outer HG thickness, \AA	15	59
Tail region thickness, \AA	21	20
Bilayer coverage 2, %		59 (58, 60)
Bilayer roughness 2, \AA		0.19 (0.18, 0.19)
Bilayer coverage 3, %		29 (28, 29)
Bilayer roughness 3, \AA		8.17 (7.89, 8.44)
Bilayer coverage 4, %		14 (14, 14)
Bilayer roughness 4, \AA		12.69 (12.48, 12.96)
Tannin proximal thickness / \AA		0.00 (0.00, 0.00)
Tannin proximal hydration, %		52.00 (50.54, 53.60)
Tannin medial thickness / \AA		0.53 (0.52, 0.55)
Tannin medial hydration, %		30.58 (29.66, 31.53)
Tannin distal thickness / \AA		82.91 (81.09, 85.16)
Tannin distal hydration, %		93.93 (93.18, 94.66)
Tel-II volume fraction, %		4 (4, 4)

to *ca.* 57 \AA^2 per molecule. This is attributed to the intercalation of Tel-II into the membrane tail core. The ability of Tel-II to intercalate into the membrane is also responsible, at least in part, for the formation of multilamellar structures after the interaction. Addition of a substance to the high coverage membrane (99% before Tel-II is added) and insertion into the membrane layer in a closed system leaves no space in the plane of the membrane for lipids to move into. Because of this, lipids are forced into the area towards the bulk solution, likely on the grounds of less energy required to move into free space.

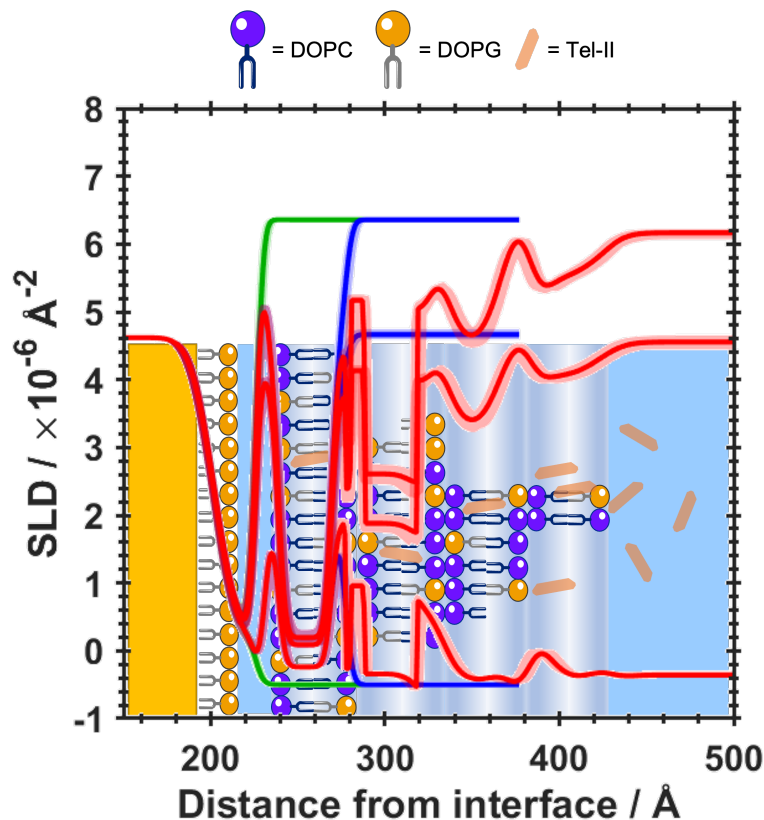


Figure 4.25: Neutron SLD profile overlaid on a diagrammatic representation of the 4 membrane regions of decreasing coverage. Tel-II is depicted both in the membrane regions and in the solution layers moving towards and in the bulk solution. Consecutive membranes show decreasing bilayer coverage moving away from the Si interface. Values output from the fitting are shown in table 4.10. SLD profile has been cropped to the membrane region of interest leaving out the underlayers.

4.7 Summary

The aim of this chapter, building on chapter 3, is to investigate the effects of polyphenol interactions on bacterial membrane models. The effects of polyphenols on these membranes were studied using a variety of techniques to provide a wide range of information. Model bacterial membranes are a useful and suitable tool given the promise that polyphenolic compounds of this type have shown as antibacterial and antimicrobial agents, as well as medicinal and agricultural properties. This is covered in more depth in chapter 1. If these polyphenols do interact with model bacterial membranes then the question shifts to what information can be gained about the interactions using the selected techniques.

It should be understood that the research findings presented in this chapter contain largely positive experimental results. In reality, more membrane compositions and sample conditions were tested to verify experimental setups and to progress membrane composition and accuracy. Table A.1 shows a more

complete list of samples and conditions that for whatever reason were not suitable or require optimisation, before neutron experiments are performed.

The interactions of EGCg and Tel-II with bacterial model membranes that have been characterised with FTIR, QCM-D, and neutron measurements reported in this chapter represent new findings in the field. Measurements of this kind of interaction with these kinds of compounds have not been shown before, and stand as front line results that demonstrate the nature of the interactions of polyphenol compounds on a molecular level.

Calorimetric experiments showed that the trends for the polyphenols that moved the T_m for the lipid peaks the most show that increasing both molecular area of the polyphenol and the number of free galloyl functional groups both increase the ability of the polyphenol to interact. EGCg does not appear to follow this trend, in the sense that it induced a large temperature shift at lower molecule area than the other three polyphenols studied. EGCg seems to be small enough that sterics do not inhibit the interaction with the DPPE/DPPG (3:2) model. Above a molecular area of 500 \AA^2 the main predictor of interaction is the number of free galloyl groups on the compound, evidenced by Tel-II displaying more interactivity than Tel-I. PGG provides an edge case in that it has the greatest number of free galloyl groups, but because of the conformation of the molecule, all of 5 galloyl groups are not accessible to the bilayer surface simultaneously, so PGG likely behaves as a polyphenol with fewer free galloyl groups. The preference of the polyphenols for DPPG was clear, from table 4.7, based on the shifting of the DPPG associated peak to higher temperatures. Higher transition temperatures are related to a more stable gel phase.

EGCg shows only a positive temperature shift in the ideally mixed lipid sample, indicating that it is able to interact with the membrane in a way that stabilises the pre-transition phase of the membrane. In the ideally mixed sample, an induced phase separation of the lipids is apparent, especially at the highest EGCg concentration. The ability to induce lateral non-homogeneity points towards preference towards DPPG, thereby altering only the DPPG lipid transition temperature and shifting in to lower temperatures and resolving it from the lipid mixture. The non-ideal samples in show both peaks of the individual lipid components before any interactions are measured. Upon interaction both lipid peaks are affected according to the factors and extents as outlined above.

Moving from vesicle based samples to planar supported lipid bilayers (SLBS), the tails of the lipids were shortened and contained some unsaturation to reduce the phase transition temperature and improve the fluidity of the lipids. This compelled to form a bilayer at the temperature of the sample environment. Further, DPPE was replaced by DOPC, as DPPE resists the formation bilayer phases, reducing its effectiveness and the validity of the model membrane system.

Interactions of EGCg and Tellimagrandins I and II were investigated at the membrane interface of SLBs using both ATR-FTIR and QCM-D. FTIR is a

powerful technique for detecting the presence of functional groups present at the Si-water interface. The lipid peaks remain unaffected by the presence of polyphenol injection into the liquid flow cell, but in all cases a peak appears in the FTIR at around 1600 cm^{-1} . Analysis of the rate of change of the 1600 cm^{-1} FTIR peak shows that the Tel-II interaction at the surface is prolonged compared to both Tel-I and EGCg.

QCM-D allowed mass detection at the interface after polyphenol interaction. The mass changes after injection into the liquid flow cell for EGCg and Tel-II showed clear persistent changes (-20 Hz and -25 Hz respectively) for both interactions with a DOPC/DOPG (7:3) membrane. Tel-I also shows a sustained interaction (*ca.* 10 Hz) but reduced in magnitude compared with for Tel-II.

Both FTIR and QCM-D analyses show that the interactions at the planar membrane surface are persistent under flow. Even with prolonged rinsing of the bilayer the FTIR and QCM-D data show that each polyphenol remains in or around the membrane. This is an important distinction from the DSC data where, although lipid polyphenol interaction is clear, this cannot be attributed to pre-mixing with the lipid sample before membrane formation.

Neutron reflectometry was used to structurally characterise the interactions of EGCg and Tel-II with the DOPC/DOPG (7:3) model membrane based on the promise shown in SLB experiments. NR studies used floating lipid bilayers and model fits and error estimates are used to describe and validate the experimental data.

The best fits for EGCg and Tel-II were very different in terms of the model. Both models shared three layers of polyphenol outside the leaflet of the membrane distal to the Si interface, though the EGCg interaction fits (from figure 4.20 showed 3 layers moving into the bulk solution becoming thinner and more hydrated. EGCg was able to cross the membrane, evidence by the non-zero value of the inner thickness parameter (0.16 \AA) but it seems clear that the preference for EGCg was outside the headgroup region adjacent to the bulk solution. After interaction with EGCg, there seem to be no major alterations to the tail region both in the SLD profile or the derived output parameters. Pre-mixing (doping) EGCg into the lipid sample before deposition of the membrane, in order to mirror the DSC samples, showed similar results with EGCg appearing only in the distal membrane leaflet. Whether this is because the EGCg doped layer is too bulky or rough to deposit in the inner leaflet, or does not interact favourably with the SAM on charge grounds, is difficult to identify. In addition, the coverage of the doped bilayer dropped to *ca.* 50% compared to the lipid only membrane (95%). It is likely the case that a number of factors need addressing if a full coverage membrane doped with polyphenol is required to be deposited, perhaps with some of the lessons learned in section 3.3.2 being appropriate for application here.

In contrast, Tel-II interaction with the model membrane (from figure 4.24) showed changes to the membrane as lamellar membranes formed where the

volume fraction of Tel-II was 4% within each membrane. The 3 layers for Tel-II were not thickest at the membrane surface, but rather increase both in terms of their hydration and polyphenol thickness as the layers progress towards the bulk solution. Each external layer of Tel-II resides between the lamellar membranes, and can be understood schematically from figure 4.25. The formation of the lamellar layers likely comes from the intercalation of Tel-II into the membrane, which causes expansion and faults at the bilayer margin leading the bilayer to shear and form a new layer.

After addition of both EGCg and Tel-II into the membrane environment the effects of each can also be noticed in the lipid area per molecule (APM). Interaction of EGCg shifted the available area from 73.95 to 74.3 Å² per molecule while Tel-II resulted in a change from 70 to 57 Å². The EGCg induced change has fit values with error bounds that overlap one another, and so the change is not significant. On the other hand, the results of Tel-II show the impact of the size difference of the two polyphenols on the membrane lipids surrounding them.

In seeking to understand whether the polyphenols EGCg, PGG, Tellimagrandins I and II would interact with model bacterial membranes this chapter has shown a variety of techniques that lipid-polyphenol interactions do take place. On the nature of the interactions it has been shown that the different properties (number of free galloyl groups, logP, molecular area *etc.*) are all relevant. Neutron reflectometry highlighted structural differences between interactions of a small polyphenol with a low number of free galloyl groups and a larger polyphenol with more free galloyl groups. In both cases interactions were successfully detected and verified perturbations modelled at the membrane-water interface.

References

- [1] M. M. Fernandes, A. Francesko, J. Torrent-Burgués and T. Tzanov, *Reactive and Functional Polymers*, 2013, **73**, 1384–1390.
- [2] R. T. Coones, R. Green and R. A. Frazier, *Soft Matter*, 2021, **17**, 6773–6786.
- [3] H. Zhu, R. Sun, T. Zhang, C. Hao, P. Zhang, J. Wang and S. Li, *J. Nanomater.*, 2015, **2015**, 7–16.
- [4] C. Schwieger and A. Blume, *European Biophysics Journal*, 2007, **36**, 437–450.
- [5] N. Caturla, E. Vera-Samper, J. Villalaín, C. R. Mateo and V. Micol, *Free Radical Biology and Medicine*, 2003, **34**, 648–662.
- [6] K. Kajiya, S. Kumazawa, A. Naito and T. Nakayama, *Magnetic Resonance in Chemistry*, 2008, **46**, 174–177.
- [7] T. Hashimoto, S. Kumazawa, F. Nanjo, Y. Hara and T. Nakayama, *Bioscience, Biotechnology and Biochemistry*, 1999, **63**, 2252–2255.
- [8] B. Liu, Z. Kang and W. Yan, *Molecules*, 2021, **26**, year.
- [9] M. Karonen and V. Virtanen, *Molecules*, 2020, **25**, 3691.
- [10] V. Virtanen, S. Räikkönen, E. Puljula and M. Karonen, *Molecules (Basel, Switzerland)*, 2021, **26**, year.
- [11] T. W. Sirk, E. F. Brown, A. K. Sum and M. Friedman, *Journal of Agricultural and Food Chemistry*, 2008, **56**, 7750–7758.
- [12] M. Stasiuk and A. Kozubek, *Cellular and Molecular Life Sciences*, 2010, **67**, 841–860.
- [13] H. T. Phan, T. Yoda, B. Chahal, M. Morita, M. Takagi and M. C. Vestergaard, *Biochimica et Biophysica Acta - Biomembranes*, 2014, **1838**, 2670–2677.
- [14] L. A. Clifton, R. A. Campbell, F. Sebastiani, J. Campos-Terán, J. F. Gonzalez-Martinez, S. Björklund, J. Sotres and M. Cárdenas, *Adv. Colloid Interface Sci.*, 2020, **277**, 102118.
- [15] T. K. Lind and M. Cárdenas, *Biointerphases*, 2016, **11**, 020801.
- [16] M. C. Dixon, *J. Biomol. Tech.*, 2008, **19**, 151–158.

- [17] N. J. Cho, C. W. Frank, B. Kasemo and F. Höök, *Nat. Protoc.*, 2010, **5**, 1096–1106.
- [18] C. A. Keller and B. Kasemo, *Biophys. J.*, 1998, **75**, 1397–1402.
- [19] T. H. Anderson, Y. Min, K. L. Weirich, H. Zeng, D. Fygenon and J. N. Israelachvili, *Langmuir*, 2009, **25**, 6997–7005.
- [20] A. Åkesson, T. Lind, N. Ehrlich, D. Stamou, H. Wacklin and M. Cárdenas, *Soft Matter*, 2012, **8**, 5658–5665.
- [21] T. K. Lind, H. Wacklin, J. Schiller, M. Moulin, M. Haertlein, T. G. Pomorski and M. Cárdenas, *PLoS ONE*, 2015, **10**, year.
- [22] J. Kurniawan, J. F. V. D. Souza, A. T. Dang, G. Y. Liu and T. L. Kuhl, *Langmuir*, 2018, **34**, 15622–15639.
- [23] J. Pre-proofs, S. E. Ayscough, L. A. Clifton and M. W. A. Skoda, *Journal of Colloid And Interface Science*, 2022.
- [24] W. Pohle, C. Selle, H. Fritzschea and M. Bohlb, *Comparative FTIR spectroscopic study upon the hydration of lecithins and cephalins*, 1997.
- [25] A. Ricci, K. J. Olejar, G. P. Parpinello, P. A. Kilmartin and A. Versari, *Applied Spectroscopy Reviews*, 2015, **50**, 407–442.
- [26] M. Lucarini, A. Durazzo, J. Kiefer, A. Santini, G. Lombardi-Boccia, E. B. Souto, A. Romani, A. Lampe, S. F. Nicoli, P. Gabrielli, N. Bevilacqua, M. Campo, M. Morassut and F. Cecchini, *Foods*, 2020, **9**, year.
- [27] M. V. Voinova, M. Jonson and B. Kasemo, *Biosensors and Bioelectronics*, 2002, **17**, 835–841.
- [28] R. P. Richter and A. R. Brisson, *Biophysical Journal*, 2005, **88**, 3422–3433.
- [29] G. Fragneto, T. Charitat, E. Bellet-Amalric, R. Cubitt and F. Graner, *Langmuir*, 2003, **19**, 7695–7702.
- [30] G. Fragneto and M. Rheinstädter, *Comptes Rendus Phys.*, 2007, **8**, 865–883.
- [31] A. V. Hughes, J. R. Howse, A. Dabkowska, R. A. Jones, M. J. Lawrence and S. J. Roser, *Langmuir*, 2008, **24**, 1989–1999.
- [32] A. V. Hughes, S. A. Holt, E. Daulton, A. Soliakov, T. R. Charlton, S. J. Roser and J. H. Lakey, *Journal of The Royal Society Interface*, 2014, **11**, 20140447.
- [33] W. Helfrich, *Zeitschrift fur Naturforschung - Section C Journal of Biosciences*, 1973, **28**, 693–703.
- [34] S. Nouhi, L. Ahrens, H. C. Pereira, A. V. Hughes, M. Campana, P. Gutfreund, G. K. Palsson, A. Vorobiev and M. S. Hellsing, *Journal of Colloid and Interface Science*, 2018, **511**, 474–481.

- [35] J. Daillant and A. Gibaud, *X-ray and neutron reflectivity: principles and applications*, Springer, 2008, vol. 770.
- [36] J. Penfold and R. K. Thomas, *J. Phys. Condens. Matter*, 1990, **2**, 1369–1412.
- [37] D. S. Sivia and J. R. Webster, *Physica B: Condensed Matter*, 1998, **248**, 327–337.
- [38] L. A. Clifton, S. C. Hall, N. Mahmoudi, T. J. Knowles, F. Heinrich and J. H. Lakey, *Structural Investigations of Protein–Lipid Complexes Using Neutron Scattering*, Springer, 2019, vol. 1990, pp. 201–251.

—Life can only be
understood backwards;
but it must be lived forwards.

Søren Kierkegaard

5

Systematically Reviewing Lipid Head Group Composition within Biological Membranes

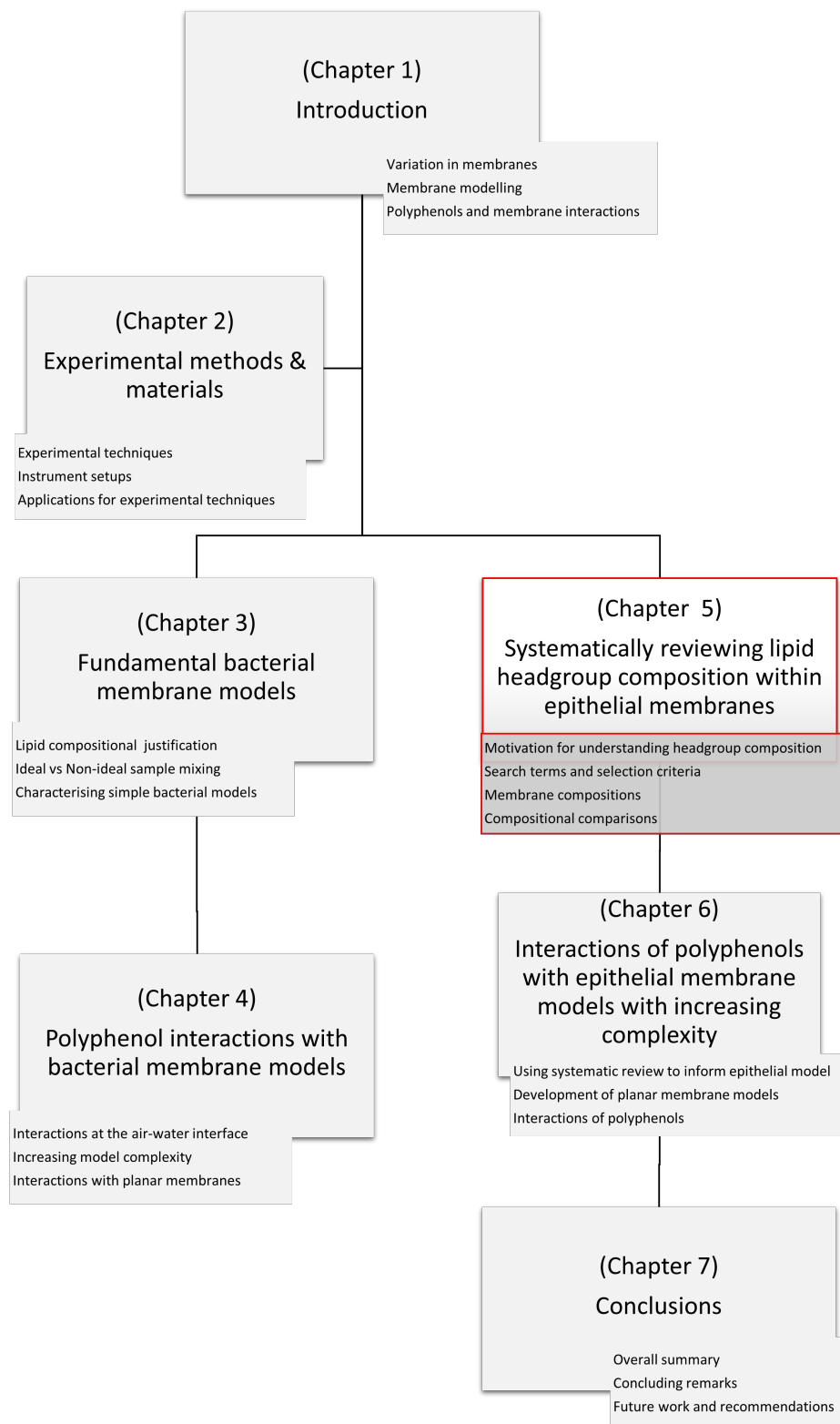
This chapter has been published in an open access format:

Coones, R. T., Green, R. J., Frazier, R. A., Investigating lipid headgroup composition within epithelial membranes: a systematic review. *Soft Matter*, 2021, **17**, 6773–6786., <https://doi.org/10.1039/d1sm00703c>

Contents

5.1	Motivation for Understanding Lipid Headgroup Composition of Membranes	136
5.2	Methodology	136
5.2.1	Systematically Reviewing Epithelial Cell Composition	136
5.2.2	Search Terms and Selection Criteria	137
5.3	Bacterial and Erythrocyte Membrane Search	141
5.3.1	Bacterial Outer Membrane Composition	141
5.3.2	Human Erythrocyte Membrane Composition	141
5.4	Publication Rate for ‘Lipid Composition’ Studies	142
5.5	Epithelial Membrane Compositional	143
5.6	Bacterial Outer Membrane Composition	147
5.7	Human Erythrocyte Membrane Composition	148
5.8	Membrane Composition Comparison	149
5.9	Outlier Search	151
5.10	Open Questions and Further Work	154
5.11	Summary	155

Disclaimer: This chapter is derived from a systematic review that was published May 2021[1]. Author contributions are listed as follows: RTC – conceptualization, data curation, formal analysis, investigation, methodology, software, validation, visualization, writing (original draft), writing (review and editing). RJG – conceptualization, methodology, project administration, supervision, validation, writing (review and editing). RAF – conceptualization, project administration, supervision, validation, writing (review and editing). Contributor role definitions taken from <https://casrai.org/credit/>.



5.1 Motivation for Understanding Lipid Headgroup Composition of Membranes

The fluid mosaic model of cellular membranes remains the foundation of our understanding of cell surfaces since its introduction in 1972 by Singer and Nicholson [2]. Given the complexity of cell membranes understanding every part of the membrane in detail is not trivial, and there are various techniques and strategies one can employ to study different aspects of the membrane. The background, scope, and challenges (and references therein) involved in membrane modelling are covered in depth in chapters 1, 2 and 3. Usually, more than one of these techniques are required to be used together in order to get a complete, more detailed, understanding on different facets of membrane behaviour.

Previous chapters of this work have focused on modelling bacterial membranes and interactions with polyphenolic compounds. The models used in those experiments are appropriate and powerful methods for examining the effects of polyphenols on bacterial membrane models. As well as showing promise as anti-microbial compounds, polyphenols are also important compounds both for humans and in agriculture as dietary compounds and pharmaceutical ingredients. This is covered in detail at the end of chapter 1. In order for polyphenols to be useful in a mammalian diet or medicine it is necessary for them to be absorbed by the relevant organism, which requires interaction and transport across a membrane. A critical part of this process is interaction with the epithelial layer of a membrane involved in adsorption and absorption of these compounds in, for example, the gastrointestinal tract (GIT).

5.2 Methodology

5.2.1 Systematically Reviewing Epithelial Cell Composition

The focal point of the work in this chapter is to systematically review the literature in an effort better understand the epithelial membrane in terms of lipid headgroup composition. That information can be used to design and build model membranes to investigate the effects of polyphenols on a model epithelium. The problem: Epithelial composition is not simple, and is not very well understood. The purpose of this chapter is to collect data from literature sources and to analyse them and condense it into something pragmatic and actionable to aid model membrane design. Particular emphasis here is put onto the lipid headgroup composition of the GIT environment, and more specifically, the human GIT. Searches for bacterial membrane composition and human erythrocyte membrane to act as points of comparison. These membranes were chosen because they are well characterised and understood, and the human erythrocyte membrane has the added advantage of offering insight into differences between human membrane types based on both physiological

location and function.

5.2.2 Search Terms and Selection Criteria

The literature was surveyed for articles that contained information about the lipid headgroup composition of epithelial cells using Web of Science. In Web of Science, all databases were searched and results were screened initially by the document type 'Articles'. Search terms were selected to generate a list of results that removed irrelevant hits, and then a second list of terms was added in order to focus the results to those containing relevant information. The search was not filtered by year, and contained articles from 1970 - February 2020 when writing of this article began. It should be noted that 1970 was not selected by the authors, but was the earliest year that was listed by Web of Science when conducting searches.

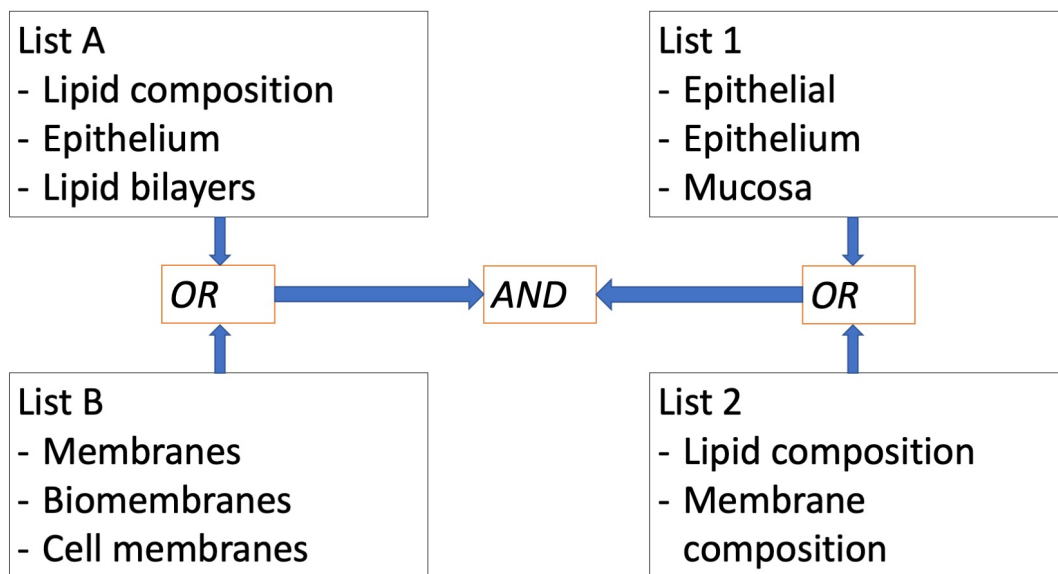
Articles were acquired using two separate searches with the results of both searches being combined. Each search was completed using two lists of search terms: either lists A & B, or lists 1 & 2. Sets A & B and 1 & 2 respectively were combined using the Boolean OR operator, with results from lists being combined using the Boolean AND. This way, only articles featuring in both searches would be output. In order to generate outputs every possible combining of searches within respective lists was used. The lists of search shown in figure 5.1a along with the flow chart showing the pathway from search terms input to the article extracted.

The literature search found articles that met the inclusion criteria set out before the search was conducted which included (a) lipid composition, (b) epithelial membranes, and (c) membrane structure for healthy cells [3–57]. Any studies that did not contain quantitative data were discarded from the list of search results. Two of the authors of this publication conducted the search independently (RTC and RJG) and the results were filtered and collated by a single author (RTC). At this point in the process the abstracts of the articles were screened with the inclusion criteria being applied.

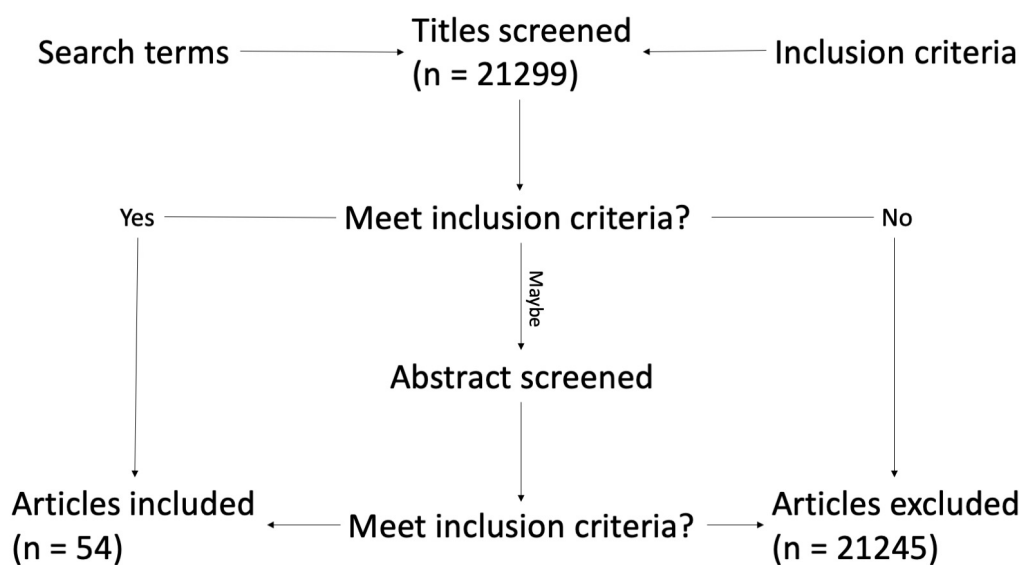
The systematic search gave articles (n=54) that contained 75 individual data sets corresponding to the lipid headgroup composition of a broad range of mammalian cell types. This range of cell types is broken down in more depth later on in the chapter during data processing and analysis. Data were differentiated based on cell type, physiological location, species *etc.* Figure 5.2 displays a breakdown of the search results based on the number of lipid species reported in the article. The number of lipids reported in any one sample ranged from 3 to 8 lipids, with 71% of publications reporting at least 5 lipids.

As has previously been discussed in chapters 1, 3, and 4 the effects of tail length and unsaturation are important. This is commented on again later on in this chapter, but the focus of this study remains the headgroup composition [58]. Further, this study does not examine variation in composition between

membrane leaflets, but it should be acknowledged that this phenomenon takes place in the majority of natural membranes [59].



(a)



(b)

Figure 5.1: (a) Flow diagram that summarising the method for the selection of relevant articles to be included in the data set collected for lipid headgroup composition of epithelial membranes. (b) Schematic showing how search terms were combined between lists using both AND and OR Boolean operators.

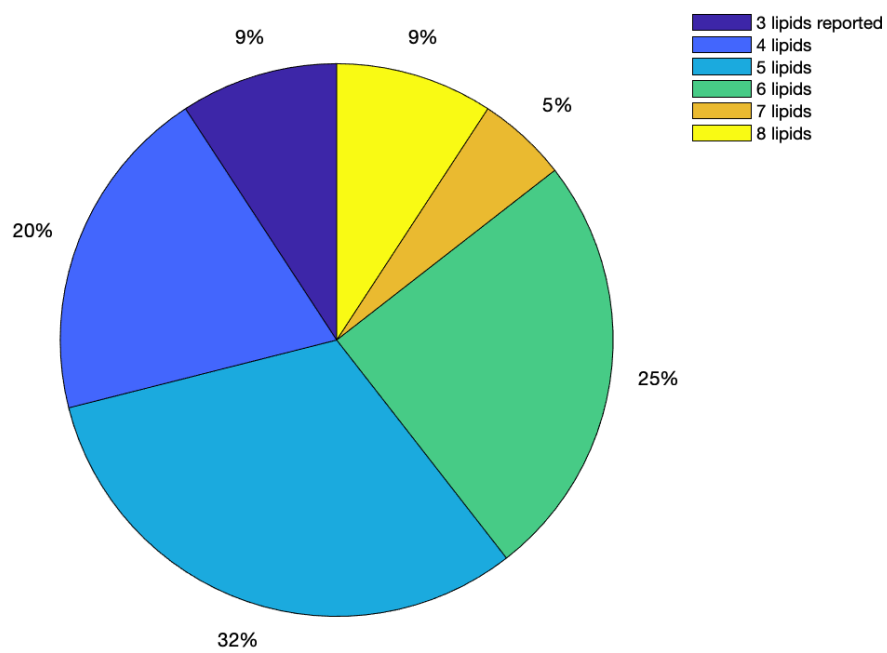


Figure 5.2: Chart displaying the number of lipids reported per publication as a percentage.

5.3 Bacterial and Erythrocyte Membrane Search

Following the search for epithelial membrane composition two other analogous searches were carried out in an effort to understand what makes a human epithelial layer unique, and how epithelial lipid composition might differ based on function. It should be understood that the searches for both the bacterial outer membrane (OM) and human erythrocyte membrane were not comprehensive systematic searches. Instead, they were intended to stand adjacent to the epithelial membrane search to act as points for comparison.

5.3.1 Bacterial Outer Membrane Composition

The bacterial OM lipid headgroup composition was highlighted using three distinct search terms, with the results being collated using the Boolean AND operator, and are listed below. The search was again conducted using Web of Science within “All Databases”. The date was once again not limited and spanned from 1970-2020. When evaluating the bacterial composition and comparing to the epithelial lipids there are differences in the presences of lipids that are common to both membrane types. Search terms results were narrowed down by only included studies that gave values for the outer membrane composition of bacterial membranes. This search yielded n=21 results [60–80].

- Bacterial
- Outer membrane
- Phosphatidylethanolamine

5.3.2 Human Erythrocyte Membrane Composition

In addition to the bacterial OM the human erythrocyte membrane was also included as a point of comparison. Being able to compare the prevalence of lipid headgroups across membrane types allows some insight into the role of different lipids of membrane function. This search was designed to only include erythrocyte membrane compositions that were human and contained several lipid classes in the analysis. Search terms were used in two pairs: (a) membrane composition OR phospholipid composition AND (b) human erythrocyte OR human red blood cell. Results within each pair were combined using the Boolean OR, and results between pairs being combined using the Boolean AND. This search came up with 23 results, of which 9 were appropriate for inclusion [81–89].

5.4 Publication Rate for ‘Lipid Composition’ Studies

An initial part of the study was concerned with how the phospholipid composition has appeared in the literature as a function of time. Figure 5.3 displays the number of publications over time that resulted from the search term “lipid composition” in the Web of Science database. In the early 1990s the volume of publications jumps 5-fold. Much of this is attributed to the analysis of lipids being able to enter the “-omics” realm behind genomics and proteomics, thanks to developments in mass spectrometry and liquid chromatography techniques along with tandem methodologies [90]. The blue bars in figure 6 represent the total number of publications. The coloured portions of the blue bars represent categories by which the total number of results can be sub-divided based on an applied filter. That is, the coloured bars are segments of the blue bars and should not be taken cumulatively.

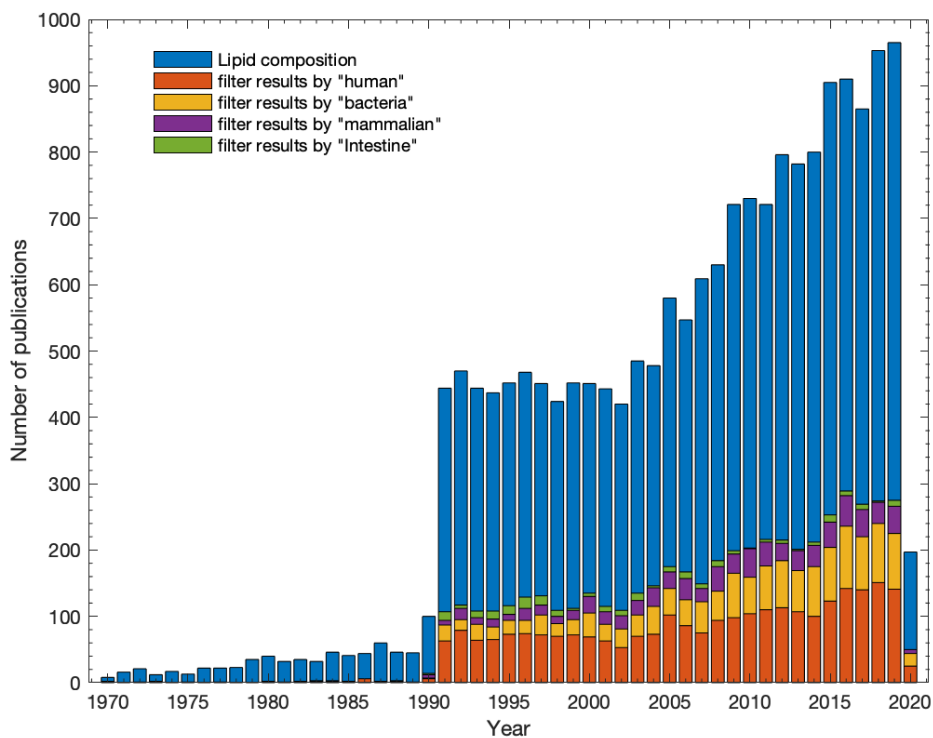


Figure 5.3: Stacked bar plot representing the number of publications for a given year as a result of the search term ‘lipid composition’. Colouring within the bars represents the total number of publications in a given filter term used to refine the overall ‘lipid composition’ search. The smaller coloured bars are included within the total count and form part of the blue bars. The date range for the publication rate spans from the earliest date allowed by the search engine, 1970, until writing of the manuscript started in Feb 2020. It is likely that publications after Feb 2020 would have contributed to a larger value for that particular bar.

5.5 Epithelial Membrane Compositional

It is to be expected that there is a lot of variability in the information contained when searching for lipid compositional data. This variability is explored in more detail later on in the chapter. The literature search provided a wide range of biological sources from which phospholipid composition could be determined. The search conducted in this study provided 54 articles that have defined the lipid composition, and these data are normalised to relative percentage (rel%) and visualised in figure 5.4. While this hides any distinct variability between cell types it does give a baseline idea for the types of lipid species present and, on average, in what quantities. Deviations from the mean amount can then be assessed and rationalised based on cell type, location, function *etc.*

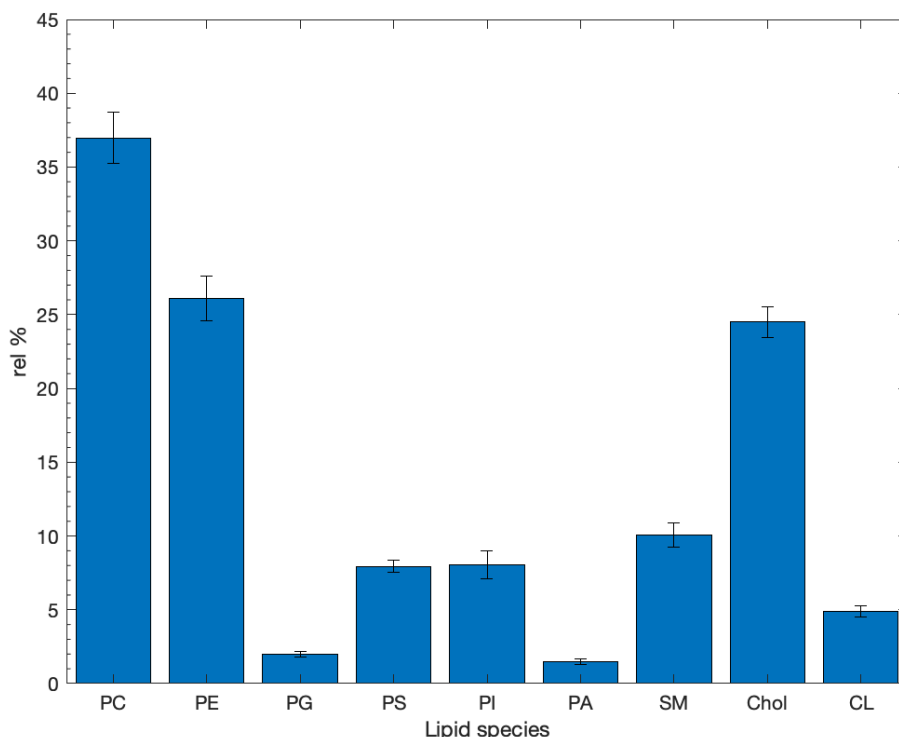


Figure 5.4: Values of overall mean lipid content taken from the studies found as a result of the initial literature search in Web of Science ($n = 54$). These percentages represent the proportion of lipids present in all membranes irrespective of origin or type. Numerical values for the mean are presented along with their standard deviation. Numerical values for the results shown here can be found in 5.1.

Across the 54 articles it is clear from figure 5.4 that PC and PE lipid types dominate, with cholesterol featuring as a major membrane component also, accounting for average amounts of 37, 26 and 25% respectively. It has been reported that PC can be present in amounts greater than 50% relative abundance in eukaryotes [4], although based on the search conducted here that may be an overestimate. No doubt, the variability of lipid composition is dependent on the origin of the tissue under investigation. While the information contained

in figure 5.4, along with the values in table 5.1, gives a broad idea of the abundance of lipid composition it does not by necessity take into consideration function of the different membrane samples. In order to assess composition differences in this way, the data must be separated and scrutinised using a more focused analysis. One limitation of the literature search was that not all articles contained data that pertained exclusively to cell membrane composition. Where the membrane was not isolated, these data may reflect more the whole cell lipid isolates. Because of this these data should be handled with care, and later are separated out into various surface types to reduce the effects of non-specific lipid extraction. Table 5.1 also gives values for the range of each lipid headgroup to help highlight the diversity and large variance in relative abundance of each lipid as well as the standard error of the mean (SEM).

Table 5.1: Values that accompany the plot shown in figure 5.4 for the overall mean lipid headgroup composition as averaged from all 54 articles that were output from the systematic search. Values are given as rel% and quoted alongside are the SEM and standard deviations of the mean.

Lipid	Mean rel%	SEM	Std. dev.	Range
PC	37.0	1.7	15.1	66.5
PE	26.1	1.5	13.2	61.8
PG	1.8	0.4	1.8	5.4
PS	7.9	0.5	3.6	18.3
PI	7.9	1.1	7.9	49.9
PA	1.4	0.4	1.6	5.9
SM	10.1	0.9	7.1	30.6
Chol	24.5	1.7	9.1	43.8
CL	4.9	0.8	3.0	10.1

Figure 5.5 shows data for cell membrane lipid headgroup composition that relate to intestinal (n=18), epithelial (n=22) and human GIT epithelial (n=10) samples. As for the mean values in figure 5.4 the most abundant lipid types in the 3 cellular environments in figure 5.5 remain the same, although not necessarily ranking the same most abundant lipids in the same order. For example, results filtered by intestinal (n=18) cell types show that PE is in fact the most abundant lipid ($32.9 \pm 2.9\%$) followed again by PC and cholesterol (29.5 ± 2.5 and $26.5 \pm 3.5\%$ respectively). This differs from either epithelial (n=22) or human GIT epithelial (n=10) samples where PC lipids are the most abundant. One point of interest is that the sphingomyelin (SM) composition of intestinal samples is *ca.* 3% lower than for the mean lipid data, where the decrease in SM is made up for by the presence of other minor membrane lipids such as PS, PI, and PA.

Intestinal lipids data also shows elevated amounts of anionic lipids compared to epithelial samples. This suggests that the role of anionic lipids is not as prevalent in the epithelium as it may be in basal or non-lumen facing portions of the intestinal tract. It should be noted that while intestinal data shown here are not all human-derived, they are still deemed important as they help to

give insight into the lipid composition given that they have the same function: acting as a barrier for nutrient exchange. In general the SM composition sits around 10%, which may be important for influencing cholesterol presence and location within the membrane. There is some evidence that cholesterol has shown to preferably associate with SM over other membrane species [91, 92]. The influence of SM and cholesterol both on each other and other membrane lipids is linked closely to the lateral membrane microdomain (raft) organisation within the bilayer, and this has been reviewed extensively elsewhere [93–95].

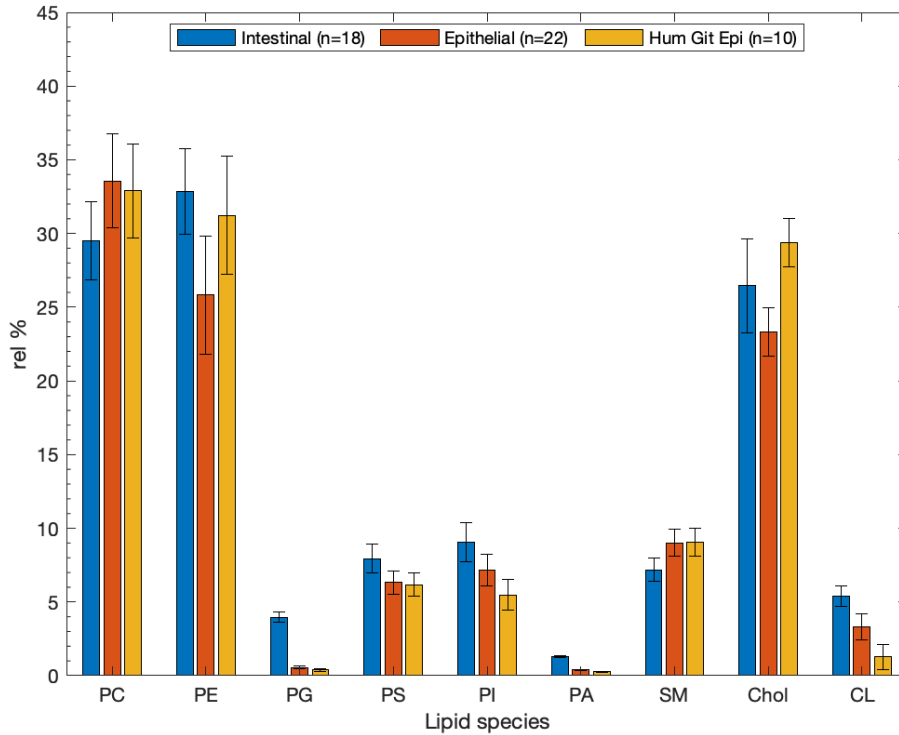


Figure 5.5: Plot displaying mean compositional data for intestinal studies obtained from the systematic review search for articles that pertained to intestinal tissues ($n = 18$), epithelial samples ($n = 22$), and samples that related to the human GIT epithelium ($n = 10$). Values are presented as relative means \pm SEM and can be found numerically in table 5.2.

In epithelial ($n=22$) membrane types, but not necessarily exclusive to the GIT), PC, PE, and cholesterol (33.6, 25.8, and 23.3% respectively) are still the lipid headgroups with the highest relative amounts. Conversely to intestinal samples though, PC is the most abundant lipid and the amount of cholesterol on average is lower. This is accounted for in relation to the function of epithelia which largely require the transfer of substances across the membrane. This likely requires a more fluid and less strictly ordered bilayer, hence lower cholesterol content. In all membrane types in figure 5.5 PS and PI make up a combined total of approximately 10% of the lipids. These lipids are useful in helping to regulate membrane charge, where balancing polarity/non-polarity of the membrane constituents is useful for helping only *desired* substances to cross

Table 5.2: Comparison of the lipid compositions of samples taken from the literature study conducted as outlined above. Data below is from the total 54 articles found, and divided into subsets related to intestinal (n = 18), epithelial (n = 22), and human GIT epithelial samples (n = 10) to accompany the plots show in figure5.5. Values are given as rel% and quoted alongside are the SEM and standard deviations of the mean.

Lipid	Epithelia	SEM	Std. dev.	Intestinal	SEM	Std. dev.	hum. GIT epi.	SEM	Std. dev.
PC	37.0	1.7	15.1	29.5	2.6	12.1	33.6	3.1	13.1
PE	26.1	1.5	13.2	32.9	2.9	13.4	25.8	3.9	16.5
PG	1.8	0.4	1.8	4.0	1.3	2.3	0.6	0.2	0.3
PS	7.9	0.5	3.6	7.9	0.9	4.0	6.3	0.9	3.2
PI	7.9	1.1	7.9	8.5	1.4	5.7	7.2	1.1	4.3
PA	1.4	0.4	1.6	1.3	0.0	0.0	0.4	0.1	0.1
SM	10.1	0.9	7.1	7.2	0.7	3.4	9.0	1.0	3.8
Chol	24.5	1.7	9.1	26.4	3.5	10.4	23.3	2.1	6.7
CL	4.9	0.8	3.0	5.4	1.1	3.1	3.3	1.4	3.4

the membrane.

5.6 Bacterial Outer Membrane Composition

The bacterial membrane is significantly different in terms of lipid composition compared to the epithelial membranes that have been highlighted up to this point. In the lipids that are common to both membrane types it can be seen that the amounts are very different. Bacterial membranes here have on average around 13% cardiolipin (CL) compared to the 3-5% average for human, intestinal, and epithelial membrane types. CL is reported to be involved in the solubilisation of proteins into the membrane along with some non-bilayer lipids such as PE [96–98]. This goes some way to explaining the difference that can be seen between the overall mean lipid values (figure 5.6) and the bacterial membrane values (figure 5.3). Rather than PC being the major lipid constituent in bacterial membranes, instead PE is the major zwitterionic component. The role of CL likely remains the same in terms of protein integration within the membrane.

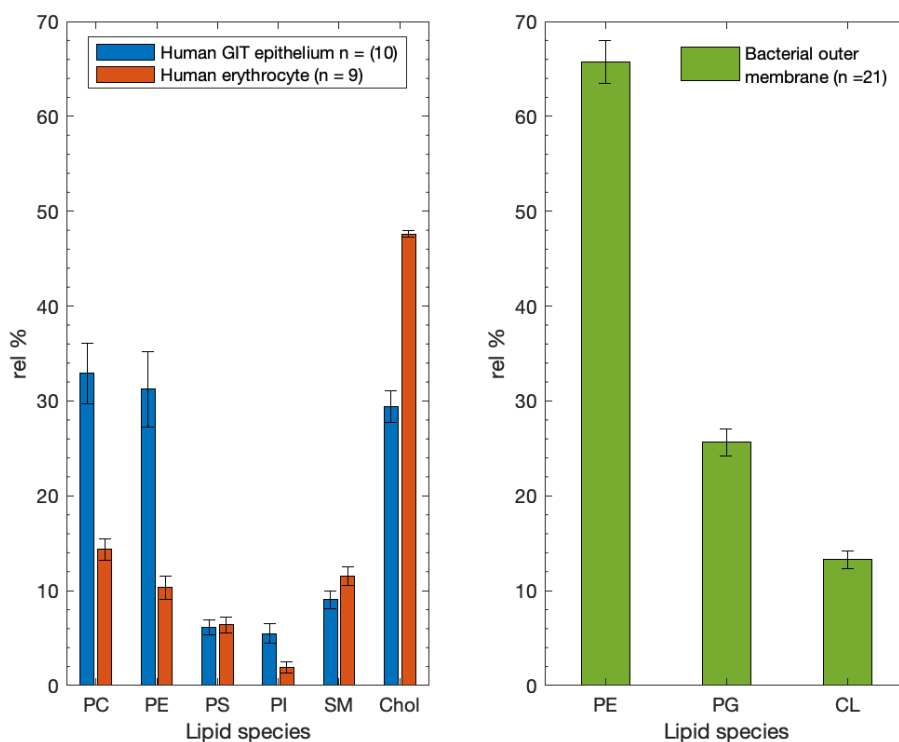


Figure 5.6: Figure showing the mean relative percentage lipid compositions of the human GIT epithelium (blue, n=10), the human erythrocyte membrane (orange, n=9), and a bacterial outer membrane (green, n=21). The GIT and erythrocyte membranes are compared according to the common lipid species that are contained within the respective membrane, while all the lipid species taken from the bacterial membrane search are shown. Numerical values for the data presented here can be found in tables 5.2, 5.3 and 5.4.

Bacterial membrane composition has been reviewed previously; with this in

Table 5.3: Lipid composition of the bacterial outer membrane (n=21), as shown in figure 5.6 to highlight how individual lipid abundance compares to both the human GIT epithelium and human erythrocyte membrane. Values are given as mean relative % \pm SEM, and shown with the standard deviations.

Lipid	Bacterial			Mammalian			Erythrocyte		
	Mean rel %	SEM	Std. dev.	Mean rel %	SEM	Std. dev.	Mean rel %	SEM	Std. dev.
PE	62.6	23.0	3.5	26.1	1.5	13.2	47.6	0.4	1.1
PG	25.6	19.9	2.8	1.8	0.4	1.8	-	-	-
CL	13.0	2.1	13.9	2.1	13.9	49.0	-	-	-

mind the minor lipids in bacterial compositions were omitted from this study in order to better highlight the fundamental differences between the membrane types [99]. The Sohlenkamp and Geiger (2015) review outlines changes in bacterial membrane composition and how *E. coli* has long served as a model organism. For a thorough breakdown of bacterial membrane composition the reader is referred to the Sohlenkamp *et.al.* review. Crucially, the Sohlenkamp review supports the findings from this mini search of the literature in terms of dominant bacterial headgroups. However, the questions surrounding variety and diversity remain largely unsolved.

5.7 Human Erythrocyte Membrane Composition

To further help develop the understanding of these kinds of membrane surfaces and help serve as another point of comparison, the human erythrocyte membrane composition was also used. Data for this membrane type is given above in figure 5.6 and numerically in table 5.4. One point of interest is that only 2 of the 9 articles collected from the search contained data points for the cholesterol content of the erythrocyte membrane, and as such it may not be strictly representative. The cholesterol content was corrected for as described in the methodology section of this chapter. While the average value defined here is consistent with the literature, the error bar for the human erythrocyte cholesterol content are artificially small. The other lipid values and errors are more representative due to their “sample size”.

The human GIT epithelial data remain higher with respect to PC and PE than in the erythrocyte membrane, however the proportion of cholesterol in the erythrocyte is far greater. The large amount of cholesterol within the human erythrocyte membrane has been understood for some time, so while only 2 articles quote a value, they should not be discarded. As both of these membrane types are human epithelia, the differences are markedly large in terms of their lipid composition. It follows that there is a “geographical” factor involved when membranes regulate lipid species [100, 101]. Further, the 3-dimensional shape of the erythrocyte is critical for gas exchange across the membrane, and so a

Table 5.4: Lipid composition of the human erythrocyte membrane (n=9), as shown in figure 5.6 to highlight how individual lipid abundance compares to both the human GIT epithelium and human erythrocyte membrane. Values are given as mean relative % \pm SEM, and shown with the standard deviations.

Lipid	mean	SEM	Std. dev.	Min. value	Max. value	range
PC	14.3	1.2	3.3	8.5	19.6	11.2
PE	10.3	1.3	3.7	4.5	14.6	10.1
PS	6.4	0.9	2.4	1.8	10.5	8.7
PI	1.9	0.7	1.8	0.3	5.5	5.1
LPC	1.0	0.3	0.7	0.4	2.2	1.8
LPE	3.1	1.2	1.8	1.3	4.8	3.5
SM	11.6	1.0	2.8	7.0	15.7	8.7
Chol	47.6	0.4	1.1	45.5	49.8	4.3

large amount of cholesterol-induced rigidity is not far fetched to help maintain the membrane geometry.

5.8 Membrane Composition Comparison

Comparing across all the membrane types gives some idea of the abundant variation in lipids. Differences in membrane function and geometry take some steps towards explaining how the lipid presence varies between samples. The role of cholesterol in maintaining the structural integrity of the membrane provides an explanation for the high relative amount within the human erythrocyte, where strict mediation of the cell geometry is vital for optimal function [102]. Conversely, the human GIT epithelium is a site for pharmaceutical and nutrient absorption and is required to allow the passage of substances across the bilayer. Because of this, the fluidity requirements of this kind of membrane are likely greater than other non-absorbing membranes and so would account for reduced cholesterol and more PC and PE type species[103–105].

The bacterial OM is reported to contain asymmetry between leaflets, with the outer leaflet enriched in lipopolysaccharide (LPS) and containing large amounts of PE [106]. The bacterial OM contains far more PE than human derived membrane samples, and it is thought that LPS forms mixed bilayers with phospholipids and proteins intercalated into the layer, with PG and cardiolipin also being abundant membrane components [107, 108]. The bacterial OM and human erythrocyte membrane compositions (figure 5.6) can be compared with mammalian sample types that are sorted according to their origin in figure 5.7. One point of note: an error bar is missing from the animal relative percentage for PG in figure 5.7 as only a single study quoted PG levels. As a standard deviation and standard error cannot be calculated for a single value, the SEM of this value is omitted.

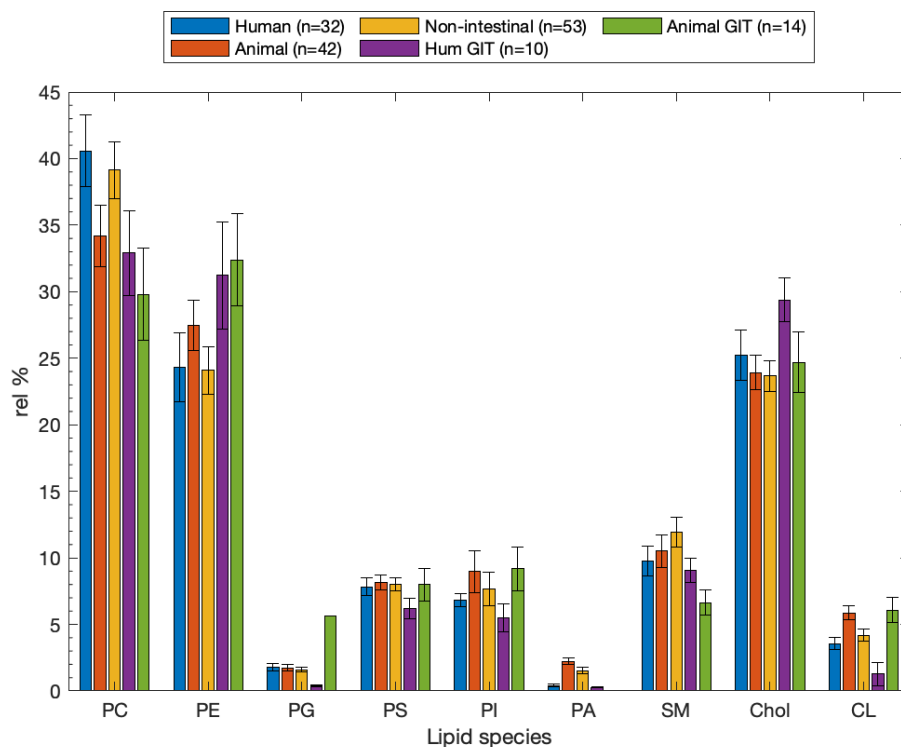


Figure 5.7: Grouped bar chart showing mean lipid composition that varies by sample environment as well as species. Lipid environments are compared according to common lipid types. It should be noted that the animal GIT value for PG has no error bar because there is only value reported. Values are given as mean relative percentage with their associated SEM values.

While the bacterial OM is dominated by PE and PG lipids figure 5.7 shows that mammalian cell types are on average dominated by PC, PE and cholesterol. Where sample types may lack PC, they seemingly make up for it with peripheral lipids such as PS or PI. In all cases for the animal type membrane environments SM and cardiolipin appear to play a supplementary role. Compared to the bacterial outer membranes the value for mammalian cell types have only roughly half the amount of cardiolipin. Further, PG and PA are present in only very small quantities (*ca.* 2%) in the mammalian membranes, although this is not surprising given that PG is a bacterial membrane lipid. Any charge requirements that PG might serve in the mammalian membrane are presumably taken on by PS and PI, both hovering at a mean relative percentage of 10%. The low abundance of PA in the membrane is explained on the basis that as the simplest membrane lipid, it is present only in amounts sufficient for being a mediator and intermediate species in lipid biosynthesis [109]. As the simplest membrane lipid it has roles as precursors for more derivatised lipids as well in the regulation of membrane dynamics and lipid signalling.

5.9 Outlier Search

During data acquisition, processing, and analysis it was noticed that the lipid values spanned a wide range of values. The spread of the relative amount of each lipid were compiled and visualised as box and whisker plots (figure 5.8) to help show a wide spread data set on a more digestible scale. Each lipid is given a separate box plot that shows the median value (horizontal red line) with the bottom and top edges of the box representing the 25th and 75th percentiles respectively. The whiskers show the spread of the most extreme non-outlier data points, with outliers themselves being represented by individual '+' marks. The boundary for a point being defined as an outlier or not was 1.5 x interquartile range.

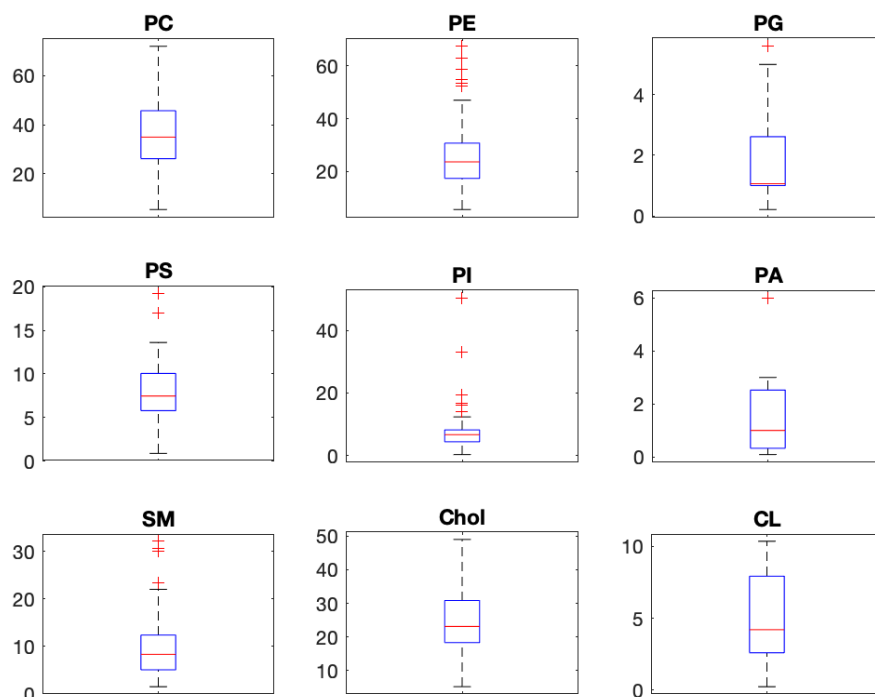


Figure 5.8: Box and whisker plots displaying the spread of data for each lipid available from the results of the literature search. The red line represents the median value with the edges of the box showing the 25th and 75th percentiles. Data points that are outliers are represented using the red '+' marker.

Scatter plots were also developed in order to try and unpack more patterns and trends within the lipid values and seek out the origin of the outlying data points. Using publication year as a crude marker of experimental precision the data were grouped to see if this had an effect on the trends seen for any of the outliers lipid percentages. Figure 5.9 shows data points for PC lipid values grouped by decade, starting at 1970 and proceeding in the groups 1970-79 (red), 80-89 (gold), 90-99 (green), 2000-2010 (cyan), 2010-19 (blue), and 2020 (black).

Within the plots, the black line represents the mean relative percentage for the given lipid the solid red lines show one standard deviation, while the dashed red lines show 1.5 standard deviations. There seem to be no obvious trends that point to any particular time period displayed more outliers than expected given the inherent variation within the results set.

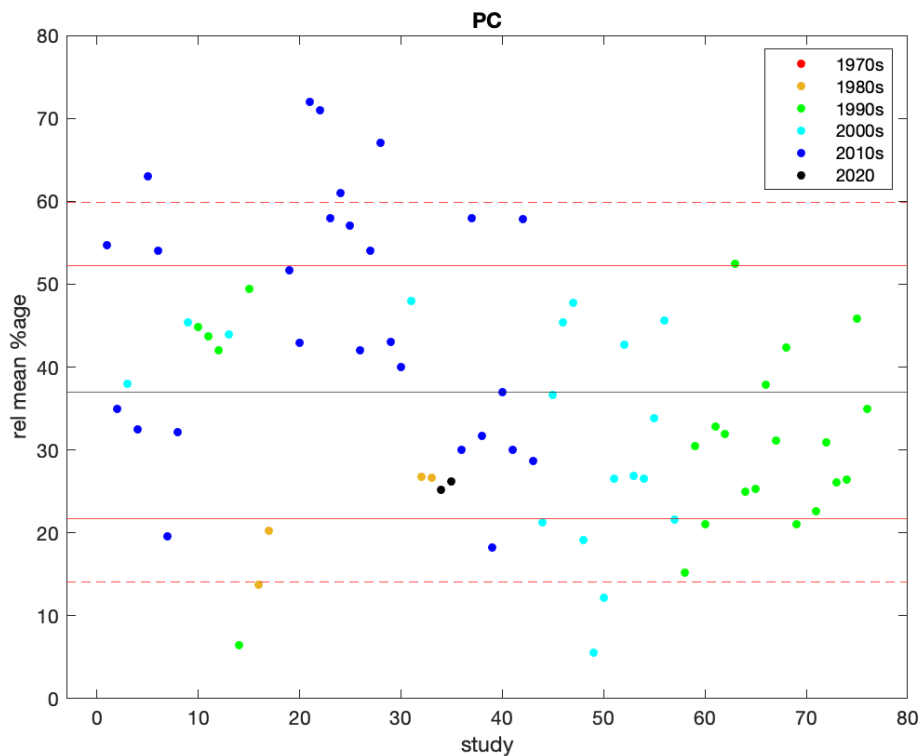


Figure 5.9: Scatter plot showing year of publication for lipid data relating to PC headgroup containing lipids. Mean value (black line), 1 and 1.5 x standard deviation (solid red and dashed red lines respectively) are shown for data points taken from the systematic literature search.

To complete a full analysis across all lipids, the same procedure was carried out for all the lipid species from the systematic search. The scatter plots show no real correlation with the year of publication leading to more outliers.

Within the results, any publications from the search that did not report a particular lipid were omitted from the scatter plots. As a result, not all plots contain the full amount of entries from the epithelial, bacterial, or erythrocyte values retrieved from the search. In a similar way, outliers within the results were sorted based on if they were from a human sample or not, and the results are given in figure 5.10. The plots show that there are a larger number of outliers that come from non-human samples. However, non-human samples make up 59% of all the samples recorded from the literature search and so the increased number of outliers is representative of the sample size. Again, any points here in the plot that were not contained in the literature results were omitted for the given lipid and as such some lipids contain fewer than 54 entries.

Overall, the most populated sub-plots of PC, PE, PS, and SM are all helpful in providing an insight into the large spread of the data.

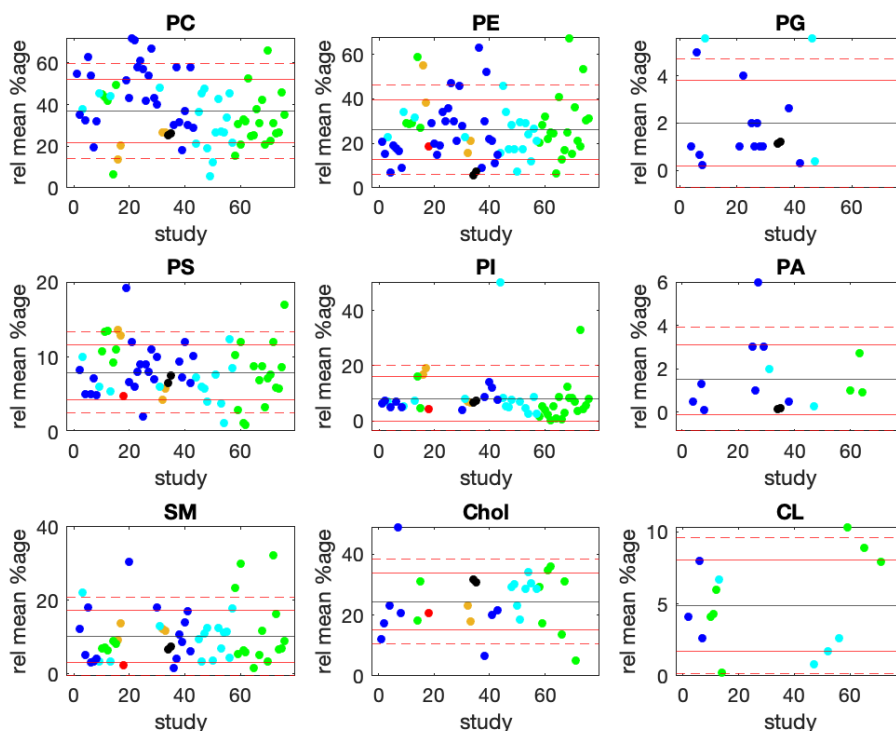


Figure 5.10: Scatter plots showing the spread of the relative percentages of lipid head groups taken from the systematic literature search. Mean value (black line), 1 and 1.5 x standard deviation (solid red and dashed red lines respectively) are shown and data points are grouped by their year of publication. The colour scheme for this figure is the same as for figure 5.9.

The influence of cholesterol and SM on each other in the membrane has been reported, especially in the formation of nanodomains, and the regulation of membrane fluidity and packing[110–113]. To see if the abundance of one was a predictor of the other could be observed in this work the mean relative percentages of each were plotted and a linear regression performed. SM and cholesterol were both plotted as the dependant variable (y axis) and independent variable (x-axis) to help visualise the effects of one another in terms of composition. These effects are plotted in figure 5.11.

The trend from the linear fit in 5.11 and the R^2 value (-0.023) for cholesterol’s impact on SM indicates that the the cholesterol relative abundance (independent, or “predictor”, variable) is a worse predictor of SM content (dependent variable) than a horizontal line that passes through the mean value. While at first glance this result is uninspiring, it still provides some information in that these data were taken from a wide range of samples, crossing membrane types from different species, membranes with different functions, and different anatomical locations.

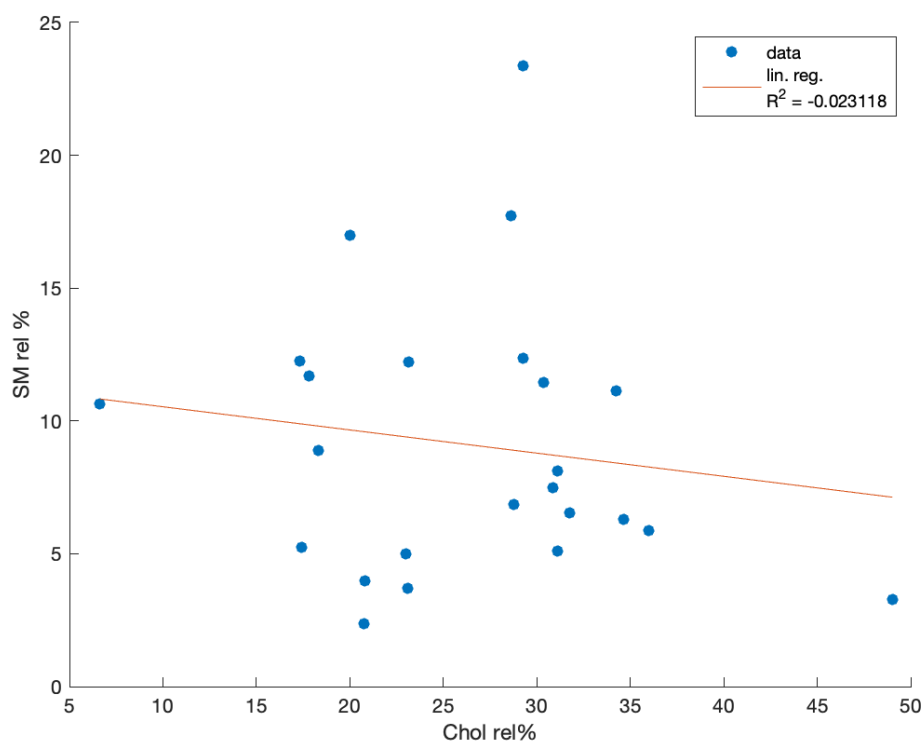


Figure 5.11: Scatter plot showing the relative percentages of cholesterol and sphingomyelin to understand if the presence of one membrane component can be used as a predictor of the other. A simple linear regression ($R^2=-0.023$) shows that cholesterol content cannot be used as a predictor of sphingomyelin amount within a membrane.

There is scope for a more in depth analysis that may reveal more statistically significant trends if data points were filtered by membrane type. For now, this remains beyond the scope of this body of work.

5.10 Open Questions and Further Work

One question that remains relatively unanswered is surrounding the need for lipid variability, particularly on a localised scale. Some insights have been offered elsewhere although no concrete insights have been reported [114]. For such niche questions it may be hard to pinpoint any answers, especially given the debate that surround lipid rafts [115, 116]. The dynamics of membranes, and the lipids within them, remain an ongoing area of investigation to help try and understand the asymmetry and roles of various lipids in membranes [117, 118].

There is a need for more accurate information on the compositions of various epithelial membranes which can be acquired through further lipidomic studies of epithelia in all their forms. While some data is stored in online databases such as the Lipid MAPS database, a more centralised set of information would be useful

[119]. One recommendation of the review is founded on the analysis conducted in this chapter is that an online tool be developed for these kinds of data sets. Similar tools have been established, one such as the genetic epidemiology of novel coronavirus samples, which could serve as inspiration [120]. This kind of tool would allow filtering, searching, visualising and processing of lipid data based on a whole host of criteria; for example cell type, cell function, species, physiological location, healthy tissues versus tumour tissue *etc.*

By making analyses of this kind more specific to cell function or location, one may be able to provide clarity on some patterns that may emerge for using a given selection criteria as a predictor for lipid composition. Further, as briefly outlined in figure 5.11 some lipids may be able to be used as predictors for the presence of other lipids. More in depth investigation is required on this front, and while selection criteria may need to be tightly controlled, the ability to use some lipid species as markers for other membrane components could be powerful. Data from model membrane experiments can be used in conjunction with this systematic analysis. Both by being guided by it, allowing a more accurate model to be designed using this kind of study as a framework, especially in the design and synthesis of multi-component model membrane architectures. Also by pairing together results from cell and model studies to understand differences and make attempts to fill any gaps.

A shortcoming of our review is that minor lipid components that likely have a vital role in cell membrane function may have either been excluded or have had amounts too small to measure. Some papers only mentioned three or four lipid components, potentially to only focusing on the major lipid components, or were not sensitive to or did not have significant resolving power in the techniques used to be able to identify the more peripheral membrane components. As a result, some errors may have been artificially inflated in cases where the values may be more spread out. Further, while the age of some publications included in this review may have had an effect on experimental capability, these do not have an obvious effect on the introduction of errors. The limitations of these kinds of studies were consistently observed and cases where the number of lipids reported is low is assumed to be a product of the time in which the work was conducted.

5.11 Summary

In this chapter it has been demonstrated how the phospholipid composition of human epithelial membranes is reflected in the scientific literature. These findings were compared to bacterial membranes and the human erythrocyte membrane to show how different membranes vary in terms of their composition. Considering specifically composition of the human GIT epithelium we have shown that the amount of data available when surveying the literature is small, with a gap in the current understanding highlighted. In order to address the reason for such lipid variability as well as the role of lipids in these environments more information is required. Recommendations have been made to address gaps in the literature, as well as how to make these kinds of data accessible through online tools. Coupling information from *in vivo* samples, as well as

model and computational data, will help provide further insight.

We have highlighted that the membranes in the human GIT are dominated by PC, PE and cholesterol. There is a large presence of zwitterionic lipids, with cholesterol showing greater abundances in membrane areas that require more strict geometric control. Peripheral lipids in more minor amounts are still present, and show responsibility for aspects of membrane function such as charge regulation, cell signalling, influencing membrane curvature, and protein solubilisation.

The development of model biological interfaces and their interactions is an area that is growing rapidly. Taking advantage of surface sensitive techniques to explore these interfaces are crucial in order to understand how they behave [121]. With membranes being so ubiquitous, it is hardly surprising that a huge number of drug targets are a membrane in some form or other [122]. Having an understanding of the both the structure and composition of biological membranes on a molecular scale is vital for being able to provide accurate, well informed models. These models are then viable for elucidating complex mechanisms and awareness about how interactions with biologically active compounds can be obtained.

References

- [1] R. T. Coones, R. Green and R. A. Frazier, *Soft Matter*, 2021, **17**, 6773–6786.
- [2] S. Singer, *The fluid mosaic model of membrane structure*, Springer, 1977, pp. 443–461.
- [3] D. Essaid, V. Rosilio, K. Daghighian, A. Solgadi, J. Vergnaud, A. Kasselouri and P. Chaminade, *Biochim. Biophys. Acta - Biomembr.*, 2016, **1858**, 2725–2736.
- [4] G. Van Meer, D. R. Voelker and G. W. Feigenson, *Nature Reviews Molecular Cell Biology*, 2008, **9**, 112–124.
- [5] J. L. Sampaio, M. J. Gerl, C. Klose, C. S. Ejsing, H. Beug, K. Simons and A. Shevchenko, *Proc. Natl. Acad. Sci. U. S. A.*, 2011, **108**, 1903–1907.
- [6] M. Jakubec, E. Bariás, F. Kryuchkov, L. V. Hjørnevik and Ø. Halskau, *ACS Omega*, 2019, **4**, 21596–21603.
- [7] G. W. Sewell, Y. A. Hannun, X. Han, G. Koster, J. Bielawski, V. Goss, P. J. Smith, F. Z. Rahman, R. Vega, S. L. Bloom, A. P. Walker, A. D. Postle and A. W. Segal, *Int. J. Biochem. Cell Biol.*, 2012, **44**, 1839–1846.
- [8] A. Stefanko, C. Thiede, G. Ehninger, K. Simons and M. Grzybek, *PLoS One*, 2017, **12**, 1–12.
- [9] R. Busche, B. Schröder, K. Huber, H. P. Sallmann and G. Breves, *J. Comp. Physiol. B Biochem. Syst. Environ. Physiol.*, 2007, **177**, 135–142.
- [10] M. G. Schmitz and W. Renooij, *Gastroenterology*, 1990, **99**, 1292–1296.
- [11] L. Mrnka, O. Nováková, F. Novák, E. Tvrzická and J. Pácha, *J. Steroid Biochem. Mol. Biol.*, 2000, **73**, 11–17.
- [12] K. Turnheim, J. Gruber, C. Wachter and V. Ruiz-Gutierrez, *Am. J. Physiol. - Cell Physiol.*, 1999, **277**, 83–90.
- [13] H. Weisser and M. Krieg, *Prostate*, 1997, **30**, 41–46.
- [14] S. M. Schwarz, H. E. Bostwick, M. D. Danziger, L. J. Newman and M. S. Medow, *American Journal of Physiology - Gastrointestinal and Liver Physiology*, 1989, **257**, 138–144.

- [15] T. Billington and P. R. Nayudu, *Australian Journal of Experimental Biology and Medical Science*, 1978, **56**, 25–29.
- [16] S. E. Hancock, M. G. Friedrich, T. W. Mitchell, R. J. Truscott and P. L. Else, *GeroScience*, 2017, **39**, 73–82.
- [17] C. Tessier, K. Sweers, A. Frajerman, H. Bergaoui, F. Ferreri, C. Delva, N. Lapidus, A. Lamaziere, J. P. Roiser, M. De Hert and P. Nuss, *Translational Psychiatry*, 2016, **6**, e906–e906.
- [18] C. H. Cortie, A. J. Hulbert, S. E. Hancock, T. W. Mitchell, D. McAndrew and P. L. Else, *Experimental Gerontology*, 2015, **70**, 135–143.
- [19] V. B. O'Donnell, R. C. Murphy and S. P. Watson, *Circulation Research*, 2014, **114**, 1185–1203.
- [20] R. Bartz, W. H. Li, B. Venables, J. K. Zehmer, M. R. Roth, R. Welti, R. G. Anderson, P. Liu and K. D. Chapman, *Journal of Lipid Research*, 2007, **48**, 837–847.
- [21] P. K. Dudeja, J. M. Harig, K. Ramaswamy and T. A. Brasitus, *American Journal of Physiology - Gastrointestinal and Liver Physiology*, 1989, **257**, G809–G817.
- [22] Y. Wang, S. Hinz, O. Uckermann, P. Hönscheid, W. von Schönfels, G. Burmeister, A. Hendricks, J. M. Ackerman, G. B. Baretton, J. Hampe, M. Brosch, C. Schafmayer, A. Shevchenko and S. Zeissig, *Biochimica et Biophysica Acta - Molecular and Cell Biology of Lipids*, 2020, **1865**, 158579.
- [23] Y. P. Kang, J. H. Yoon, N. P. Long, G. B. Koo, H. J. Noh, S. J. Oh, S. J. S. B. Lee, H. M. Kim, J. Y. Hong, W. J. Lee, S. J. S. B. Lee, S. S. Hong, S. W. Kwon and Y. S. Kim, *Frontiers in Oncology*, 2019, **1865**, 158579.
- [24] F. F. Eiriksson, O. Rolfsson, H. M. Ogmundsdottir, G. G. Haraldsson, M. Thorsteinsdottir and S. Halldorsson, *International Journal of Biochemistry and Cell Biology*, 2018, **103**, 99–104.
- [25] L. Macchioni, M. Petricciuolo, M. Davidescu, K. Fettucciari, P. Scarpelli, R. Vitale, L. Gatticchi, P. L. Orvietani, A. Marchegiani, P. Marconi, G. Bassotti, A. Corcelli and L. Corazzi, *Biochimica et Biophysica Acta - Molecular and Cell Biology of Lipids*, 2018, **1863**, 895–908.
- [26] E. Morel, S. Ghezzal, G. Lucchi, C. Truntzer, J. P. Pais de Barros, F. Simon-Plas, S. Demignot, C. Mineo, P. W. Shaul, A. Leturque, M. Rousset and V. Carrière, *Biochimica et Biophysica Acta - Molecular and Cell Biology of Lipids*, 2018, **1863**, 199–211.
- [27] K. Mida, A. Shamay and N. Argov-Argaman, *J. Agric. Food Chem.*, 2012, **60**, 10657–10665.
- [28] B. C. Cohen, A. Shamay and N. Argov-Argaman, *PLoS ONE*, 2015, **10**, 1–19.

- [29] R. Zarbock, M. Woischnik, C. Sparr, T. Thurm, S. Kern, E. Kaltenborn, A. Hector, D. Hartl, G. Liebisch, G. Schmitz and M. Griese, *BMC Pulm. Med.*, 2012, **12**, year.
- [30] M. G. Márquez, F. Leocata Nieto, M. C. Fernández-Tome, N. O. Favale and N. Sterin-Speziale, *Lipids*, 2008, **43**, 343–352.
- [31] M. G. Márquez, N. O. Favale, F. Leocata Nieto, L. G. Pescio and N. Sterin-Speziale, *Biochimica et Biophysica Acta - Biomembranes*, 2012, **1818**, 491–501.
- [32] Q. Li, Q. Zhang, M. Wang, S. Zhao, J. Ma, N. Luo, N. Li, Y. Li, G. Xu and J. Li, *Clinical Immunology*, 2008, **126**, 67–80.
- [33] L. Huang, R. Estrada, M. C. Yappert and D. Borchman, *Free Radical Biology and Medicine*, 2006, **41**, 1425–1432.
- [34] I. Diaz-Del Consuelo, Y. Jacques, G. P. Pizzolato, R. H. Guy and F. Falson, *Archives of Oral Biology*, 2005, **50**, 981–987.
- [35] G. A. Bongiovanni, A. R. Eynard and R. O. Calderón, *Molecular and Cellular Biochemistry*, 2005, **271**, 69–75.
- [36] R. Prabhu and K. A. Balasubramanian, *Journal of Gastroenterology and Hepatology (Australia)*, 2003, **18**, 809–814.
- [37] R. E. Olsen, B. T. Dragnes, R. Myklebust and E. Ringø, *Fish Physiology and Biochemistry*, 2003, **29**, 181–192.
- [38] M. Engelke, S. Tykhonova, M. Zorn-Kruppa and H. Diehl, *Pharmacology and Toxicology*, 2002, **91**, 13–21.
- [39] I. O. Thompson, P. Van der Bijl, C. W. Van Wyk and A. D. Van Eyk, *Archives of Oral Biology*, 2001, **46**, 1091–1098.
- [40] R. Prabhu and K. A. Balasubramanian, *Anal. Biochem.*, 2001, **289**, 157–161.
- [41] G. A. Fines, J. S. Ballantyne and P. A. Wright, *American Journal of Physiology - Regulatory Integrative and Comparative Physiology*, 2001, **280**, 16–24.
- [42] B. J. Tewes and H. J. Galla, *Endothelium: Journal of Endothelial Cell Research*, 2001, **8**, 207–220.
- [43] M. Madesh, R. Anup, O. Benard and K. A. Balasubramanian, *Free Radical Biology and Medicine*, 1999, **26**, 836–843.
- [44] V. Calderón, A. Lázaro, R. G. Contreras, L. Shoshani, C. Flores-Maldonado, L. González-Mariscal, G. Zampighi and M. Cerejido, *Journal of Membrane Biology*, 1998, **164**, 59–69.
- [45] J. M. Lopez-Pedrosa, M. I. Torres, M. I. Fernández, A. Ríos and A. Gil, *The Journal of Nutrition*, 1998, **128**, 224–233.

- [46] G. Griffiths, H. E. Jones, C. L. Eaton and A. K. Stobart, *Prostate*, 1997, **31**, 29–36.
- [47] V. Ruiz-Gutierrez and C. W. Vasquez, *International Journal of Gastroenterology*, 1997, **58**, 161–67.
- [48] G. S. Schuster, J. F. Erbland, C. A. Lefebvre, G. B. Caughman and K. L. Knoernschild, *J. Biomater. Sci. Polym. Ed.*, 1997, **8**, 363–375.
- [49] H. Weisser and M. Krieg, *Prostate*, 1998, **36**, 235–243.
- [50] R. Acierno, M. Maffia, P. Sicuro, L. Fiammata, M. Rollo, L. Ronzini and C. Storelli, *Comparative Biochemistry and Physiology - A Physiology*, 1996, **115**, 303–307.
- [51] H. G. Gulcan, R. A. Alvarez, M. B. Maude and R. E. Anderson, *Investigative Ophthalmology and Visual Science*, 1993, **34**, 3187–3193.
- [52] E. Levy, L. Thibault and D. Menard, *J. Lipid Res.*, 1992, **33**, 1607–1617.
- [53] V. Ruiz-Gutierrez, A. Cert and J. J. Rios, *Journal of Chromatography B: Biomedical Sciences and Applications*, 1992, **575**, 1–6.
- [54] M. A. Pérez-Albarsanz, P. López-Aparicio, S. Senar and M. N. Recio, *BBA - Biomembranes*, 1991, **1066**, 124–130.
- [55] M. E. Turini, A. B. Thomson and M. T. Clandinin, *Lipids*, 1991, **26**, 431–440.
- [56] V. Duranthon, L. Frémont and C. L. Léger, *Lipids*, 1991, **26**, 175–181.
- [57] R. Christon, J. C. Meslin, J. Thévenoux, A. Linard, C. L. Léger and S. Delpal, *Reproduction, nutrition, development*, 1991, **31**, 691–701.
- [58] K. Simons and W. Vaz, *Annual Review of Biophysics and Biomolecular Structure*, 2004, **33**, 269–295.
- [59] M. A. Kiselev and D. Lombardo, *Biochimica et Biophysica Acta - General Subjects*, 2017, **1861**, 3700–3717.
- [60] R. Schmidt, D. Yonghong and R. Hoffmann, *Diagnostic Microbiology and Infectious Disease*, 2018, **90**, 316–323.
- [61] L. Zheng, Y. Lin, S. Lu, J. Zhang and M. Bogdanov, *Biochimica et Biophysica Acta - Molecular and Cell Biology of Lipids*, 2017, **1862**, 1404–1413.
- [62] V. W. Rowlett, V. K. P. S. Mallampalli, A. Karlstaedt, W. Dowhan, H. Taegtmeier, W. Margolin and H. Vitrac, *Journal of Bacteriology*, 2017, **199**, 1–22.
- [63] L. Davydova, S. Bakholdina, M. Barkina, P. Velansky, M. Bogdanov and N. Sanina, *Biochimie*, 2016, **123**, 103–109.

- [64] H. Benamara, C. Rihouey, I. Abbes, M. A. B. Mlouka, J. Hardouin, T. Jouenne and S. Alexandre, *PLoS ONE*, 2014, **9**, e108478.
- [65] N. N. Mishra, A. S. Bayer, T. T. Tran, Y. Shamoo, E. Mileykovskaya, W. Dowhan, Z. Guan and C. A. Arias, *PLoS ONE*, 2012, **7**, 1–10.
- [66] D. K. Giles, J. V. Hankins, Z. Guan and M. S. Trent, *Molecular Microbiology*, 2011, **79**, 716–728.
- [67] R. F. Epand, P. B. Savage and R. M. Epand, *Biochimica et Biophysica Acta - Biomembranes*, 2007, **1768**, 2500–2509.
- [68] S. Laurinavičius, R. Käkälä, P. Somerharju and D. H. Bamford, *Virology*, 2004, **322**, 328–336.
- [69] F. R. Rana, C. M. Sultany and J. Blazyk, *Journal of Microbiological Methods*, 1991, **14**, 41–51.
- [70]
- [71] I. Contreras, L. Shapiro and S. Henry, *Journal of Bacteriology*, 1978, **135**, 1130–1136.
- [72] G. Barrett, M. Horiuchi, M. Paul, R. E. Pratt, N. Nakamura and V. J. Dzau, *Proceedings of the National Academy of Sciences of the United States of America*, 1992, **89**, 885–889.
- [73] W. Yuqian, W. Jianli, L. Ye, W. Biwen, G. Tao and W. Xiaoyuan, *European Journal of Mass Spectrometry*, 2015, **21**, 739–746.
- [74] R. F. Epand, J. E. Pollard, J. O. Wright, P. B. Savage and R. M. Epand, *Antimicrobial Agents and Chemotherapy*, 2010, **54**, 3708–3713.
- [75] S. Laurinavičius, D. H. Bamford and P. Somerharju, *Biochimica et Biophysica Acta - Biomembranes*, 2007, **1768**, 2568–2577.
- [76] G. M. LLoyd and N. J. Russell, *Canadian Journal of Microbiology*, 1984, **30**, 1357–1366.
- [77] H. Anwar, M. R. Brown, R. M. Cozens and P. A. Lambert, *Journal of General Microbiology*, 1983, **129**, 499–507.
- [78] R. Masilamani, M. B. Cian and Z. D. Dalebroux, *Infection and Immunity*, 2018, **86**, 1–15.
- [79] A. Aloui, M. Mihoub, M. M. Sethom, A. Chatti, M. Feki, N. Kaabachi and A. Landoulsi, *Foodborne Pathogens and Disease*, 2010, **7**, 573–583.
- [80] R. M. Epand and R. F. Epand, *Biochim. Biophys. Acta - Biomembr.*, 2009, **1788**, 289–294.
- [81] H. G. Patel, R. V. Aras, S. S. Katyare and K. R. Dave, *Zeitschrift fur Naturforschung - Section C Journal of Biosciences*, 2000, **55**, 770–777.

- [82] *Molecular Biology Reports*, 1978, **4**, 25–28.
- [83] L. Li and W. Reserve, *Biochemical Journal*, 1991, **274**, 121–132.
- [84] Y. Kurumi, Y. Adachi, T. Itoh, H. Kobayashi, T. Nanno and T. Yamamoto, *Gastroenterologia Japonica*, 1991, **26**, 628–632.
- [85] J. Bramham and F. G. Riddell, *Journal of Inorganic Biochemistry*, 1995, **57**, 23–32.
- [86] J. A. Virtanen, K. H. Cheng and P. Somerharju, *Proceedings of the National Academy of Sciences of the United States of America*, 1998, **95**, 4964–4969.
- [87] E. Faloià, G. G. Garrapa, D. Martarelli, M. A. Camilloni, G. Lucarelli, R. Staffolani, F. Mantero, G. Curatola and L. Mazzanti, *European Journal of Clinical Investigation*, 1999, **29**, 432–437.
- [88] K. G. Karageuzyan, *Neurochemical Research*, 1999, **24**, 1161–1167.
- [89] V. V. Revin, N. V. Gromova, E. S. Revina, I. P. Grunuyshkin, A. Y. Tyckov, A. Y. Samonova, A. N. Kukina, A. A. Moskovkin, J. C. Bourdon and N. Zhelev, *Biotechnology and Biotechnological Equipment*, 2018, **32**, 1236–1250.
- [90] A. Triebel, J. Hartler, M. Trötz Müller and H. C. Köfeler, *Biochimica et Biophysica Acta - Molecular and Cell Biology of Lipids*, 2017, **1862**, 740–746.
- [91] J. P. Slotte, *Chemistry and Physics of Lipids*, 1999, **102**, 13–27.
- [92] M. Pörn, M. Ares and J. Slotte, *Journal of lipid research*, 1993, **34**, 1385–1392.
- [93] D. A. Brown and E. London, *J. Biol. Chem.*, 2000, **275**, 17221–17224.
- [94] K. Simons and E. Ikonen, *Nature*, 1997, **387**, 569–572.
- [95] D. A. Brown and E. London, *Biochemical and biophysical research communications*, 1997, **240**, 1–7.
- [96] D. Marsh, *Biophysical journal*, 2007, **93**, 3884–3899.
- [97] W. Dowhan, M. Bogdanov and E. Mileykovskaya, in *Biochemistry of lipids, lipoproteins and membranes*, Elsevier, 2008, pp. 1–37.
- [98] W. Dowhan and M. Bogdanov, in *Biochemistry of Lipids: Lipoproteins and Membranes*, ed. D. E. Vance and J. E. Vance, Elsevier Science, 4th edn., 2002, vol. 36, pp. 1–35.
- [99] C. Sohlenkamp and O. Geiger, *FEMS Microbiology Reviews*, 2015, **40**, 133–159.

- [100] Y. Zhong, H. Tang, Q. Zeng, X. Wang, G. Yi, K. Meng, Y. Mao and X. Mao, *Uppsala journal of medical sciences*, 2012, **117**, 390–398.
- [101] F. D. Kolodgie, H. K. Gold, A. P. Burke, D. R. Fowler, H. S. Kruth, D. K. Weber, A. Farb, L. Guerrero, M. Hayase, R. Kutys *et al.*, *New England Journal of Medicine*, 2003, **349**, 2316–2325.
- [102] M. Girasole, G. Pompeo, A. Cricenti, A. Congiu-Castellano, F. Andreola, A. Serafino, B. Frazer, G. Boumis and G. Amiconi, *Biochimica et Biophysica Acta - Biomembranes*, 2007, **1768**, 1268–1276.
- [103] F. De Meyer and B. Smit, *Proceedings of the National Academy of Sciences of the United States of America*, 2009, **106**, 3654–3658.
- [104] E. J. Fernández-Pérez, F. J. Sepúlveda, C. Peters, D. Bascuñán, N. O. Rifo-Lepe, J. González-Sanmiguel, S. A. Sánchez, R. W. Peoples, B. Vicente and L. G. Aguayo, *Frontiers in Aging Neuroscience*, 2018, **10**, 1–14.
- [105] J. Lee, S.-t. Yang, V. Kiessling and L. K. Tamm, *Biophysical Journal*, 2017, **112**, 9a.
- [106] N. Ruiz, D. Kahne and T. J. Silhavy, *Nature Reviews Microbiology*, 2006, **4**, 57–66.
- [107] Y. Kamio and H. Nikaido, *Biochemistry*, 1976, **15**, 2561–2570.
- [108] M. Ishinaga, R. Kanamoto and M. Kito, *Journal of Biochemistry*, 1979, **86**, 161–165.
- [109] R. Thakur, A. Naik, A. Panda and P. Raghu, *Frontiers in Cell and Developmental Biology*, 2019, **7**, 1–14.
- [110] M. Lokar, D. Kabaso, N. Resnik, K. Sepčić, V. Kralj-Iglič, P. Veranič, R. Zorec and A. Iglič, *International journal of nanomedicine*, 2012, 1891–1902.
- [111] A. V. Samsonov, I. Mihalyov and F. S. Cohen, *Biophysical journal*, 2001, **81**, 1486–1500.
- [112] A. B. García-Arribas, A. Alonso and F. M. Goñi, *Chemistry and physics of lipids*, 2016, **199**, 26–34.
- [113] C. Dahley, E. D. G. Garessus, A. Ebert and K.-U. Goss, *Biochimica et Biophysica Acta (BBA)-Biomembranes*, 2022, **1864**, 183953.
- [114] L. A. Bagatolli, J. H. Ipsen, A. C. Simonsen and O. G. Mouritsen, *Prog. Lipid Res.*, 2010, **49**, 378–389.
- [115] K. Simons and G. Van Meer, *Biochemistry*, 1988, **27**, 6197–6202.
- [116] I. Levental, K. R. Levental and F. A. Heberle, *Trends Cell Biol.*, 2020, **30**, 341–353.

- [117] H. P. Wacklin, *Langmuir*, 2011, **27**, 7698–7707.
- [118] M. Chabanon, J. C. Stachowiak and P. Rangamani, *Wiley Interdiscip. Rev. Syst. Biol. Med.*, 2017, **9**, 20–22.
- [119] V. B. O’Donnell, E. A. Dennis, M. J. Wakelam and S. Subramaniam, *Science signaling*, 2019, **12**, eaaw2964.
- [120] J. Hadfield, C. Megill, S. M. Bell, J. Huddleston, B. Potter, C. Callender, P. Sagulenko, T. Bedford and R. A. Neher, *Bioinformatics*, 2018, **34**, 4121–4123.
- [121] L. A. Clifton, R. A. Campbell, F. Sebastiani, J. Campos-Terán, J. F. Gonzalez-Martinez, S. Björklund, J. Sotres and M. Cárdenas, *Adv. Colloid Interface Sci.*, 2020, **277**, 102118.
- [122] J. P. Overington, B. Al-Lazikani and A. L. Hopkins, *Nature reviews Drug discovery*, 2006, **5**, 993–996.

—*The greatest challenge to any thinker is stating the problem in a way that will allow a solution.*

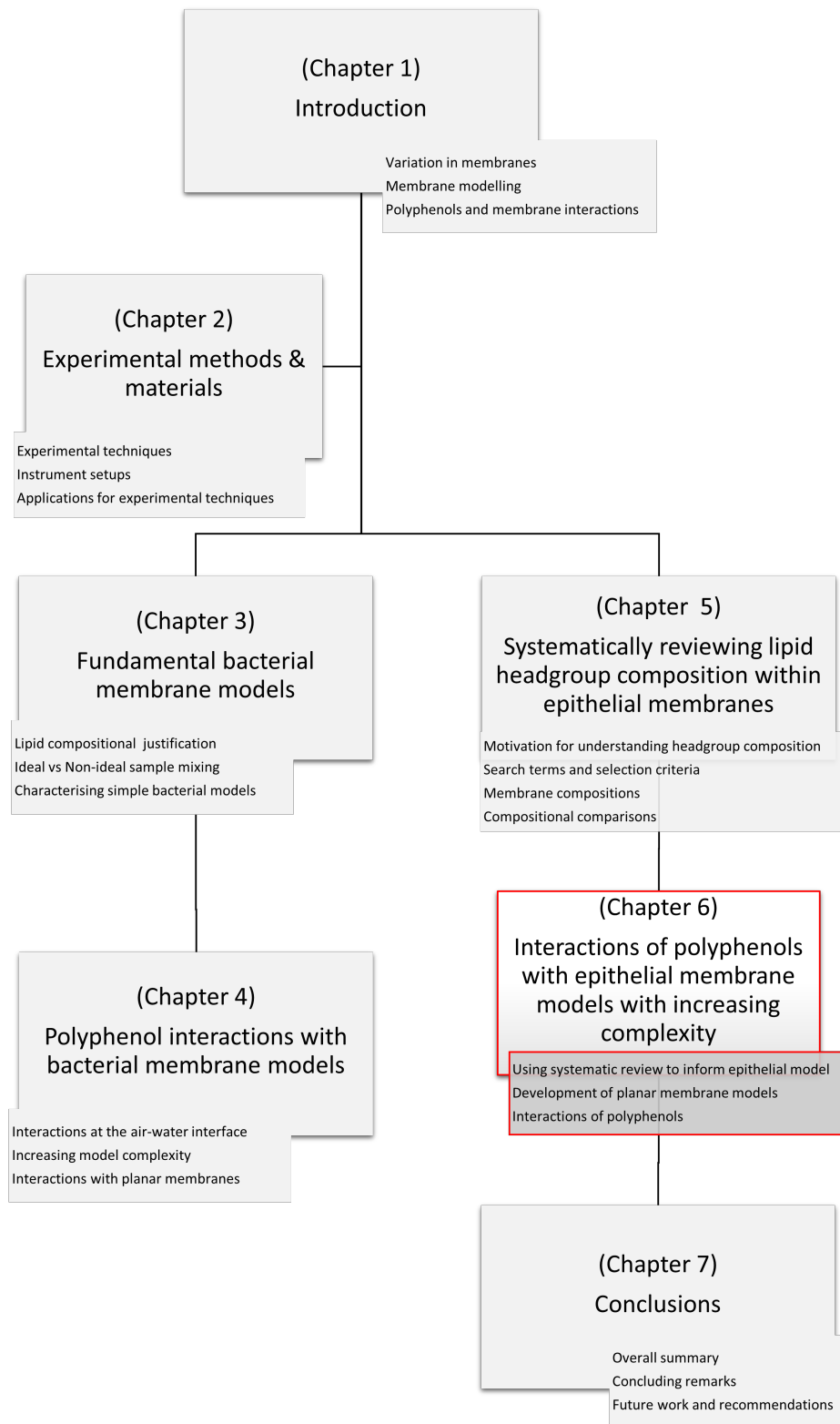
Bertrand Russell

6

Model Epithelial Membranes and Interactions with Polyphenols

Contents

6.1	Epithelial Membrane Architecture	167
6.1.1	Motivation for Epithelial Membrane Modelling	167
6.2	Results	168
6.2.1	Developing the Complexity of the Model Lipid Membrane	168
6.2.2	Determination of Model Epithelial Membrane Interactions Using Supported Lipid Bilayers	169
6.2.3	Characterising Model Epithelial Membrane Interactions with Neutron Reflectometry	172
6.2.4	Refining the Model Membrane Composition	181
6.3	Summary	187



6.1 Epithelial Membrane Architecture

Every tissue is composed of many cell types, which each help contribute to the form and function to optimise its physiological role. Establishment and maintenance of biological tissues remains an important avenue of research [1]. Epithelia can be considered layers of cells that separate a tissue from the outside world, covering both the outside of the organism as well as lining organs. In general, epithelial surfaces contain at least 3 surface types: an apical lumen adjacent surface, an adherent surface to neighbouring cells, and a basal surface that adheres to the extracellular matrix [2]. Further, the apical and basolateral portions of the membrane tend to be distinct from one another in their lipid and protein composition as a result of their differing functions [3, 4].

From the work carried out and published in chapter 5, it is clear among the literature that epithelia are rich in PC and PE lipids [5, 6]. Figures 5.7 and 5.5 show that epithelial membranes contain around 10% each of PS and PI lipids as well as sphingomyelin (SM), with this trend also being reflected in the human gastro-intestinal tract (GIT). Cholesterol also features as a prevalent membrane component at approx 25%. It is believed that the apical epithelial membranes are enriched in their lipid and cholesterol content, with one way of this being achieved is through coupling of protein and lipid sorting and delivery to the epithelial surface [7]. For this to occur in nature, there must be a need for a variety of lipids at the membrane surface, or cells would not expend the energy and resources putting them there. To help understand the roles of these membrane lipids, multi-component models can be used to investigate epithelial membranes of this kind and to use them to understand their interactions.

6.1.1 Motivation for Epithelial Membrane Modelling

The GIT epithelium is a critical interface for substance exchange into an organism. Modelling these kinds of biological surfaces so that they can be used to understand how substances interact with and cross the membrane. In the context of these experiments, the focus will be on the lipid composition of the membrane and how the composition relates to interactions with polyphenols, which are relevant pharmaceutical and nutritional compounds. The polyphenols used in this chapter are the same as those from chapter 4. In this way, direct comparison is allowed between the effects on both bacterial model and epithelial model membranes. The composition of membranes has been shown to be an important factor in influencing interaction and penetration of polyphenols into the bilayer [8, 9]. Constructing a model membrane with as much accuracy as possible whilst evading practical issues is important for obtaining genuine insight into the ways in which polyphenols interact with epithelia. The focus of the models being developed and used for polyphenol interaction studies in this chapter are based on the human GIT membrane composition found in the systematic review of chapter 5. General motivations for membrane modelling are covered in more detail in chapter 1. With the human GIT in mind, having a model whose composition is accurate is essential for getting access to detailed

data for the behaviour of these kinds of membranes in isolation and during biological interactions. Polyphenols are of interest in terms of their interactions with these kinds of membranes because they are (a) bioavailable to humans through diet and (b) have pharmaceutical and physiological benefits [6, 10]. For an in depth introduction to polyphenols and their biological effects the reader is directed back to section 1.4.

The data presented in this chapter, both in terms of the complexity of the model membranes themselves, and of their interactions with EGCg, Tel-I, and Tel-II, are novel experimental results that have not before been shown.

6.2 Results

6.2.1 Developing the Complexity of the Model Lipid Membrane

The starting point for this section of investigation picks up from where chapter 4 left off in terms of complexity of composition. The model bacterial membranes and their interactions used 2 components membranes, where some accuracy of the membrane composition was sacrificed in order to be able to use a model membrane with high confidence of deposition to cast a spotlight on their interactions with various polyphenols. The desire for the work involving model epithelial membranes was to increase complexity in terms of the number of lipid components. The basis for lipid component selection was our systematic review, covered in chapter 5 [5].

The first step for progression from the model membranes developed and used in chapters 3 and 4 is to consider adjusting the membrane composition from lipids relevant to the bacterial membrane model to those needed for a human GIT epithelial membrane model. An overview of the human GIT epithelial composition is shown in figure 5.7 which shows that the majority of lipids from samples of this kind are rich in PC and PE headgroups. Further, sphingomyelin (SM) forms a significant portion of the membrane at around 10-15% on average. The structure of sphingomyelin is shown in figure 6.1, and the structures of the other lipids used in the experimental samples going forwards are given back in figure 1.2.

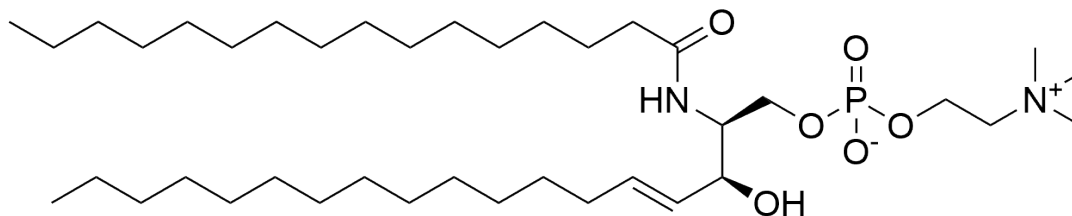


Figure 6.1: Skeletal structure of egg sphingomyelin as used for the epithelial model membrane samples.

As with chapter 4, the ultimate goal of the epithelial model line of inquiry is to be able to use neutron reflectometry to structurally resolve and characterise interactions with polyphenols. An initial step of making sure that membranes containing these three components, PC, PE, and SM, were suitable for bilayer formation was carried out.

Figure 6.2 shows FTIR spectra with regions of interest for a supported lipid bilayer (SLB) formed from DOPC/DOPE/SM (6:3:1). DOPC was selected as the majority component both because of its prevalence in the human GIT (see figure 5.7), and also due to fluidity considerations as discussed previously in chapters 3.3.2 and 4.3. Comparison of the FTIR region for the lipid tails for the DOPC/DOPE/SM (6:3:1) sample shows a small additional feature compared to previous FTIR spectra around 1660 cm^{-1} . This feature is assigned to the amide I peak that corresponds to the amide functional group in SM [11]. As for the interaction studies carried out on model bacterial membranes (see chapter 4 there is a clear change to the spectrum in the $1600\text{-}1700\text{ cm}^{-1}$ region with increased area under the curve after the addition of (-)-EGCg ($100\text{ }\mu\text{M}$) to the membrane. There position and intensity of the peaks relating to the lipid tails' CH_3 and CH_2 symmetric and asymmetric stretching is unchanged by the addition of (-)-EGCg.

Using small amounts of lipids containing a PE headgroup in processes aimed at generating fluid lipid membranes has been shown to result in incomplete bilayer formation, especially in instances where PC lipids are present [12]. Because of the tendency of PE lipids to form hexagonal phases. Coupled with the fact that there is a significant amount of PC in the membrane mixture, PE lipids are not appropriate for selection as membrane components in these model bilayers for neutron reflectometry studies where the method of membrane formation is vesicle fusion. [13]. The PC component in the model epithelial membranes is both a genuine membrane component and a fluid, lamellar phase forming lipid. The increase in the PC lipid amounts for the membrane composition was used in place of using PE lipids, particularly for NR experiments where PE lipids were not used at all.

6.2.2 Determination of Model Epithelial Membrane Interactions Using Supported Lipid Bilayers

The sample analysed in figure 6.2 does not account for the cholesterol contents of the membrane. Chapter 5 showed that cholesterol is a major bilayer constituent in mammalian membranes in general, as well as in the human GIT. Following the FTIR data showing that DOPC/DOPE/SM (6:3:1) model membranes displayed interactions with (-)-EGCg, progress on two counts was sought. Firstly to increase the complexity of the model membrane by adding another component, namely, cholesterol. Secondly, along with the addition of a more minor membrane component, namely a phosphatidylserine (PS), added to the cholesterol we increased the accuracy of the model [14]. As mentioned at the end of section 6.2.1 the PE portion of the membrane will need to be replaced with DOPC instead [15, 16]. From figure 5.7 PC and PE combine for around

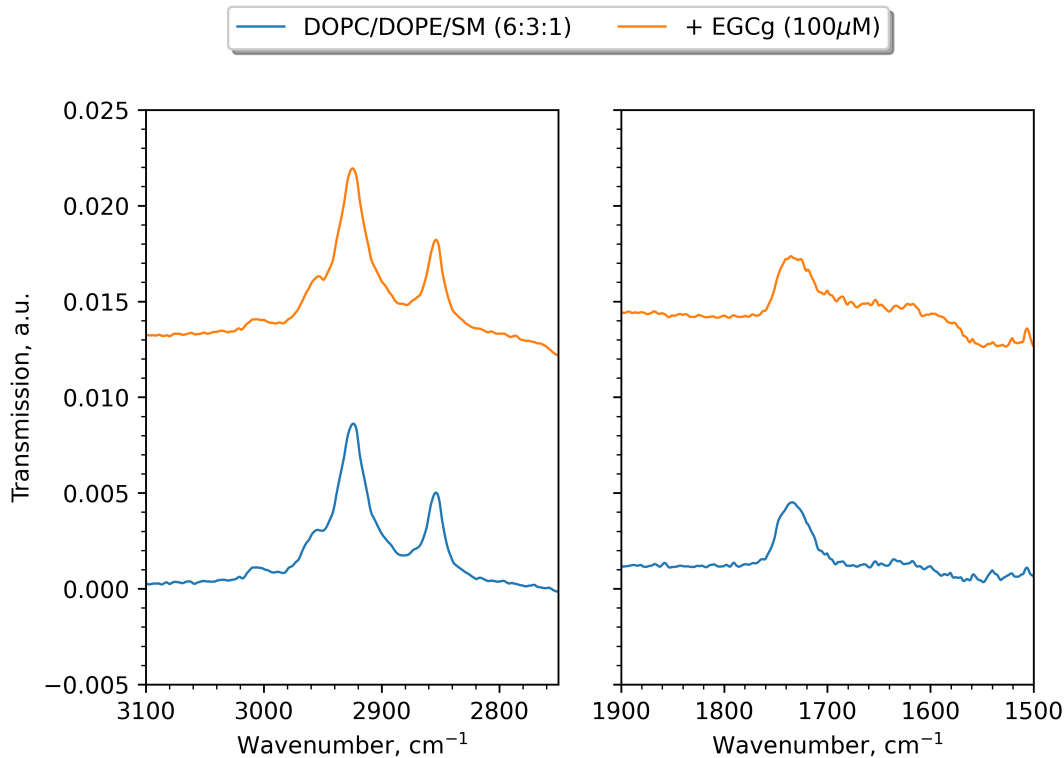


Figure 6.2: FTIR spectrum for a DOPC/DOPE/SM (6:3:1) SLB before (blue) and after (orange) addition of (-)-EGCg (100 μM), showing regions of interest highlighting the asymmetric (2920 cm^{-1}) and symmetric (*ca.* 2840 cm^{-1}) C–H stretching modes as well as the C=O stretching mode (*ca.* 1720 cm^{-1}), as well as a peak assigned to the amide moiety from the sphingomyelin headgroup at 1620 cm^{-1} . With the addition of (-)-EGCg there is an increase in the area under the broad feature between 1550 at 1740 cm^{-1} showing the interaction with the model membrane is persistent under solution flow.

60% of the membrane components, cholesterol and while PS accounts for 10%, on average, of the bilayer lipids. To ensure fluidity, and therefore confidence in the formation of the membrane, DOPC amount was set at 50%, and was used to represent both PC and PE lipid types. Depositing membranes with high amounts of cholesterol using vesicle rupture can also be a challenge due to the rigidity that high cholesterol content brings, therefore we kept cholesterol content at a maximum of 20% [17].

In a similar way to PC being used as a proxy for PE, PS was used as a proxy in place of all the minor lipid components. Anionic lipids, such as phosphatidylserine and phosphatidylinositol (PI, from figure 5.7), are challenging in the way they are deposited due to non-favourable interactions with the substrate interface in neutron experiments. For this reason, PS lipids were used to model all the anionic minor lipid constituents. Note that only very low concentrations of ionic lipids exist on the outer leaflet of the membrane, predominantly residing in the inner [18–20].

Figure 6.3 shows the FTIR spectra for formation of a DOPC/DOPS/Chol/SM (5:2:2:1) model membrane (blue) using vesicle rupture methods, along with the interaction of the membrane with (-)-EGCg (100 μ M, orange). The lipid tail group features are largely similar to those from previous model membrane interaction studies. The FTIR spectrum is cropped to the regions of interest, showing both the asymmetric (2930 cm^{-1}) and symmetric (*ca.* 2850 cm^{-1}) C–H stretching modes from the lipid tails. The C=O from the lipid headgroups and the amide feature from SM are shown in the right hand panel at 1720 cm^{-1}) and 1610 cm^{-1} respectively. Interaction of (-)-EGCg with the membrane is confirmed by the increase in area under the curve in the 1550-175 cm^{-1} region. This change was persistent even after copious washing of the membrane surface with buffer solution, and falls in the region corresponding to the aromatic C–H and C–C stretching modes.

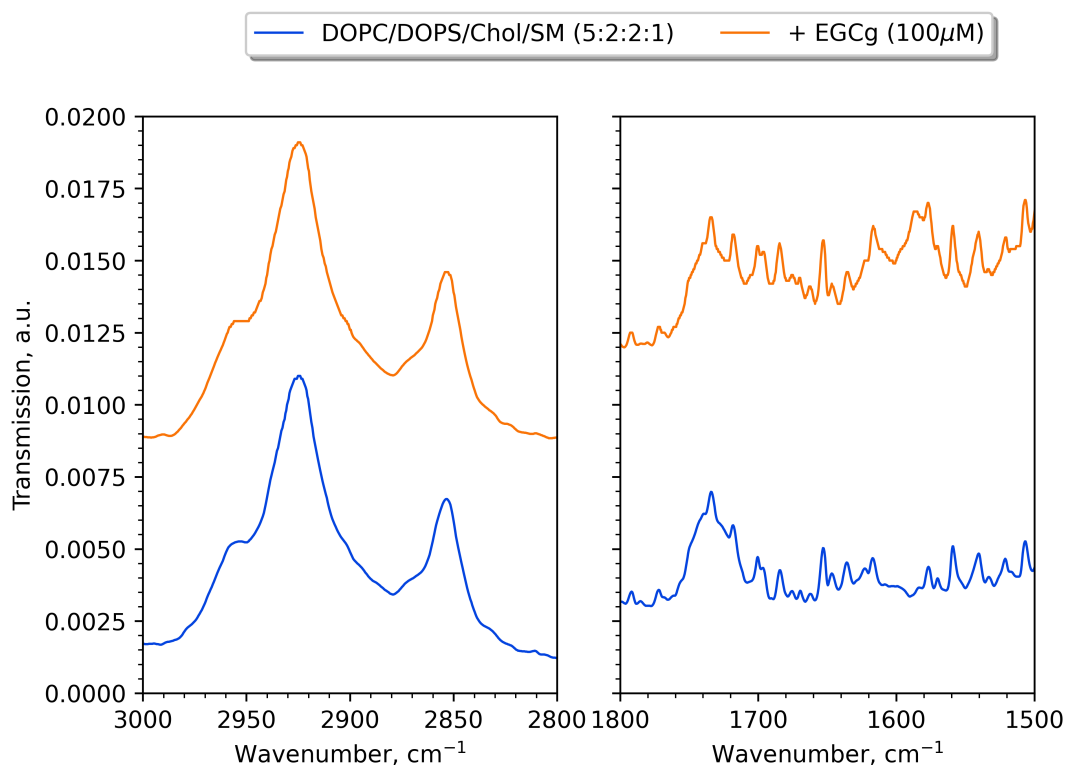


Figure 6.3: FTIR spectrum for a DOPC/DOPS/Chol/SM (5:2:2:1) SLB before (blue) and after (orange) addition of (-)-EGCg (100 μ M), showing regions of interest highlighting the asymmetric (2930 cm^{-1}) and symmetric (*ca.* 2850 cm^{-1}) C–H stretching modes as well as the C=O stretching mode (*ca.* 1720 cm^{-1}), as well as a peak assigned to the amide moiety from the sphingomyelin headgroup at 1610 cm^{-1} . With the addition of (-)-EGCg there is an increase in the area under the broad feature between 1550 at 1730 cm^{-1} showing the interaction with the model membrane is persistent after substantial washing of the membrane surface.

Interaction of the DOPC/DOPS/Chol/SM (5:2:2:1) model membrane with (-)-EGCg was also confirmed by QCM-D, and the data shown in figure 6.4.

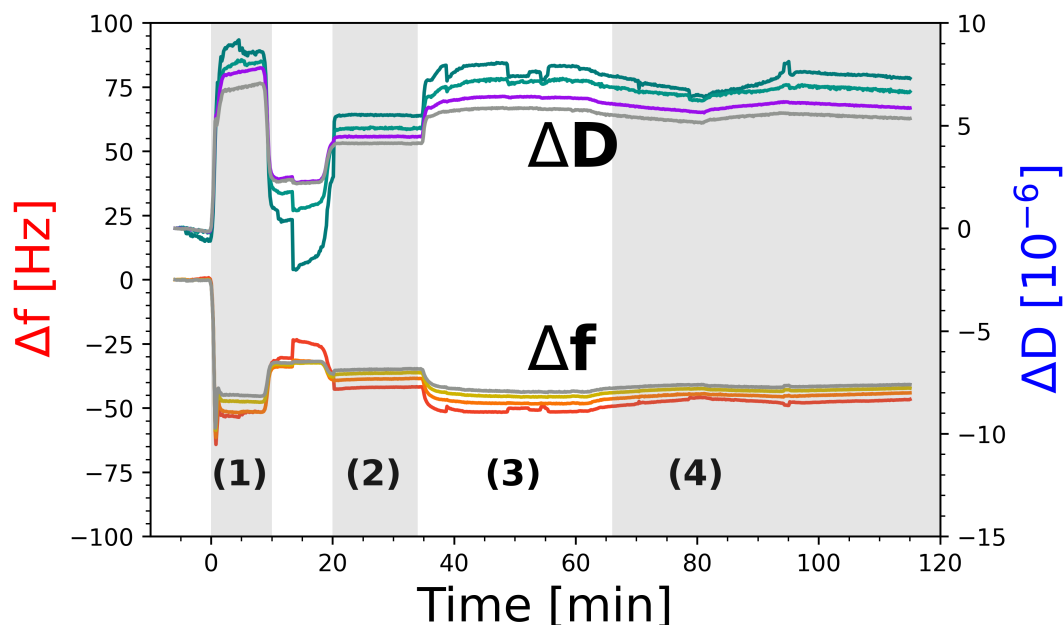


Figure 6.4: QCM-D plots showing changes to both frequency and dissipation (ΔF , Δd respectively) in the 3rd (red, green) 5th (orange, teal), 7th (yellow, purple), and 9th (grey, grey) overtones for formation of a DOPC/DOPS/Chol/SM (5:2:2:1) SLB followed by interaction with (-)-EGCg ($100 \mu\text{M}$). Bilayer formation was ensured through osmotic shock after vesicle adsorption (stage 2). The change in ΔF shows that the interaction at the bilayer surface was strong enough such that the (-)-EGCg remained bound at the membrane surface under constant flow of buffer solution (stage 4).

The numbers inset in the figure describe the various stages of the membrane formation and interaction: (1) vesicle injection and adsorption and osmotic shock, (2) membrane formation and buffer washing, (3) injection of (-)-EGCg ($100 \mu\text{M}$) and (4) washing of the lipid-polyphenol membrane with buffer solution. The frequency changes for the formation of the bilayer are consistent with those outlined for (-)-EGCg interactions in chapter 4. The dissipation changes show the formation of a suitably thin and rigid layer after vesicle rupture (figure 6.4, stage 2) followed by becoming more diffuse and viscous upon (-)-EGCg addition. These changes to the dissipation values were stable during and after washing of the surface with buffer solution.

6.2.3 Characterising Model Epithelial Membrane Interactions with Neutron Reflectometry

The epithelial model membrane systems described above, which are shown to interact with (-)-EGCg, were used as the basis for neutron reflectometry (NR) studies. In the design of the experiment there were some risks that were taken. Despite not having tested the interactions of Tel-I and Tel-II on the epithelial membrane model, we knew from chapter 4 that they showed interactions

with bacterial model membranes. Because of the precious nature of neutron experiment time, each model membrane system would be interacted first with one of the two Tellimagrandins before (-)-EGCg. If neither of these interactions showed changes after the interaction of Tellimagrandin addition, there was an opportunity to add (-)-EGCg to the membrane system as an alternative. Since less work has been done on the interactions of Tellimagrandins with epithelial membranes, a structural characterisation of their interactions was sought as a priority. Another point of note is that Tellimagrandins I and II are difficult to extract and purify in large quantities. Due to limitation of the available quantities of the Tellimagrandins, (-)-EGCg was used in FTIR and QCM-D experiments in place of Tel-I and Tel-II.

Interaction with Tellimagrandin II

The interaction for Tel-II (100 μM) with a model epithelial membrane composed of DOPC/DOPS/Chol/SM (5:2:2:1) as measured by NR is shown in figure 6.5. Membranes were formed, as for the floating bacterial model membranes, using vesicle adsorption and rupture methods. For experimental detail in depth, the reader is referred to chapter 2.7.2 and the appropriate sections in chapters 3 and 4.

The reflectivity profiles for the DOPC/DOPS/Chol/SM (5:2:2:1) bilayer before (blue) and after (red) the interaction are shown in panels A-C for both the data (points) and model fits (lines). The underlayers, Silicon-Chromium-Gold-Terminally carboxylated SAM (Si-Cr-Au-SAM-COOH) are shown in green. The changes to the bilayer before and after are more intuitively shown in panel D of figure 6.5 in the scattering length density (SLD) profile. Key parameters from the fitting of the membrane before and after interaction with Tel-II are given in table 6.1. For a full list of fit parameters the reader is referred to table A.4. The fits for the bilayer before the addition of Tel-II (blue) shows a high coverage (93.2%) membrane. The inner and outer headgroup thicknesses are symmetrical at 9 Å each with a 24 Å for the tail groups on both leaflets. These values are in line with DOPC membranes found in other studies [21, 22]. The roughness of the surface after the formation of the floating membrane is relatively low (3.65 Å) indicating a relatively homogeneous membrane was achieved, with lipid area per molecule values that are commensurate with findings from computational studies [22].

After the interaction of Tel-II (red) the inner and outer headgroup layers became slightly thicker (10 Å), as did the tail region (27 Å). This is likely due to the presence of Tel-II associating at the headgroups of the membrane, through intercalation into the bilayer. The best fit values were obtained through modelling the bilayer and the interaction as three external Tel-II layers from the outer leaflet, away from the silicon substrate, moving into the bulk solution. Further, these fits were obtained when there was no inner layer of Tel-II allowed between the silicon substrate and the membrane. The thickness and hydration values for the proximal (11.9 Å, 77.9%), medial (19.1 Å, 74.4%), and distal (6.95

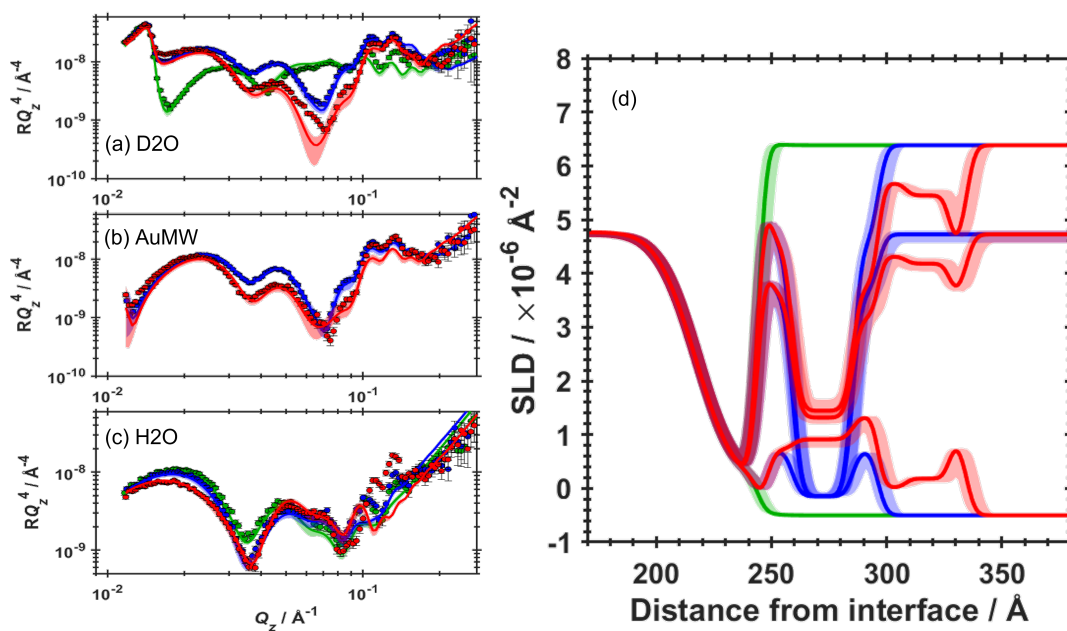


Figure 6.5: Panels (A-C) showing neutron reflectivity profiles for data (points) and model fits (lines) for a COOH-SAM/Gold/Chromium coated silicon substrate (green) with DOPC/DOPS/Chol/SM (5:2:2:1) model membrane before (blue) and after (red) interaction with Tel-II (100 μM) in various solution contrasts. (D) Neutron SLD profiles showing the Si-Cr-Au-SAM-COOH underlayers (green) with DOPC/DOPS/Chol/SM (5:2:2:1) bilayer both before (blue) and after (red) interaction with Tel-II (100 μM) solution in H₂O, gold matched water (AuMW), and D₂O contrasts. The SLD profile has been cropped to show membrane regions more clearly, leaving out the underlayers.

\AA , 45%) show that the regions nearest the membrane show higher thickness and Tel-II density, while moving into the bulk solution shows a Tel-II region, not quite adjacent to the membrane, that is thinner and more hydrated. This suggests an aggregation of Tel-II at the membrane surface, as well as into the tail region.

The Tel-II was shown to enter into the tail region, where volume fraction of Tel-II in the tail region is 0.49 (see table 6.1), and this large amount of Tel-II was reflected in the SLD profile through increased SLD values of the tail region after the interaction (red) compared to before (blue). The planar nature of Tel-II (see figure 4.8a) likely allowed Tel-II to intercalate into the tail regions in a similar way to cholesterol. This is pictorially shown in figure 4.25 where a schematic of the polyphenol and membrane interaction is set underneath the SLD profile from figure 6.5. The galloyl groups' insertion into the headgroup region of the membrane likely removed free space for the individual lipids to move around in the membrane, and so a decrease in the area per molecule was observed from approximately 65 to 63 \AA^2 [23, 24].

Table 6.1: Table of values for some key parameters from fits for DOPC/DOPS/Chol/SM (5:2:2:1) model membrane before and after interaction with Tel-II. Errors are taken from Bayesian error estimation routines as an output of the fitting of the experimental data. Parameters with no associated error bounds have been derived from the appropriate SLD profiles.

Parameter	Before Tel-II	After Tel-II
Central water thickness, Å	9.17 (8.87, 9.53)	3.78 (3.73, 3.84)
Bilayer coverage, %	93.2 (91.7, 94.8)	99.2 (98.8, 99.5)
Bilayer roughness, Å	3.65 (3.50, 3.88)	3.09 (3.06, 3.12)
Lipid APM, Å ²	65.57 (64.32, 66.83)	63.35 (62.48, 64.10)
Inner HG thickness, Å	9	10
Outer HG thickness, Å	9	10
Tail region thickness, Å	24	27
Tannin outer roughness, Å	-	2.47 (2.45, 2.50)
Tannin proximal thickness / Å	-	11.86 (11.60, 12.01)
Tannin proximal hydration, %	-	77.86 (77.06, 78.74)
Tannin medial thickness / Å	-	19.10 (18.91, 19.34)
Tannin medial hydration, %	-	74.40 (73.44, 75.64)
Tannin distal thickness / Å	-	6.95 (6.51, 7.25)
Tannin distal hydration, %	-	45.27 (44.41, 45.63)
Tel-II volume fraction	-	0.49 (0.47, 0.50)

After the interaction of Tel-II there was a small increase in bilayer coverage from 93 to 99%. This likely came from the addition of Tel-II into any defects in the lipid bilayer or to indicate an increase in the packing of the layer due to the incorporation of Tel-II. Thus, coverage may have come from intercalation of Tel-II into the tail region, causing the membrane to expand to fill any empty space in the liquid-flow cell. Compared to the bacterial membrane model and its interaction with Tel-II in chapter 4, the addition of Tel-II into the membrane did not result in the formation of multi-lamellar structures. The extent of the effects of Tel-II on the tail region thickness may be artificially reduced when the bilayer coverage increase is considered. If the bilayer coverage were not able to increase to accommodate Tel-II in the tail region, more thickening of the tail region of the membrane may be observed as opposed to filling any bilayer defects.

Interaction with Tellimagrandin I

Following the success of the interaction of the DOPC/DOPS/Chol/SM (5:2:2:1) model epithelial membrane with Tel-II, the interaction with Tel-I was also investigated. Like Tel-II, the attraction of Tel-I to a model bacterial membrane was shown back in chapter 4. It should be noted that due to limited amounts of Tel-I material, there was a constraint on how much could be used for membrane interactions. Given that Tel-I showed promise during interactions with model bacterial membranes, and coupled with the fact that polyphenols

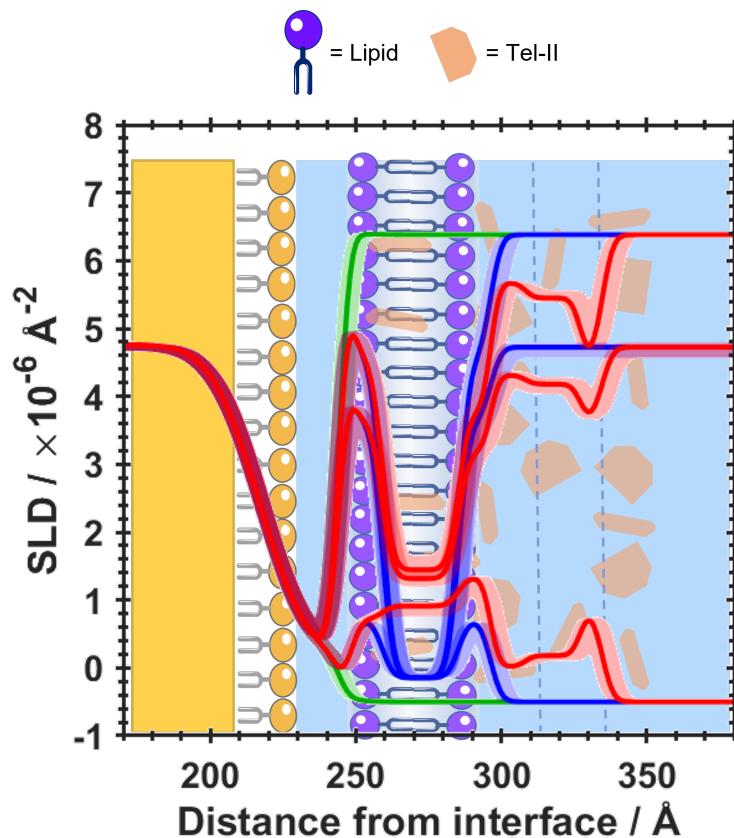


Figure 6.6: Neutron SLD profile overlaid on a cartoon of the model epithelial membrane composed of DOPC/DOPS/Chol/SM (5:2:2:1). The schematic shows the variable regions of Tel-II thickness external to the bilayer along with the large amount of intercalation within the membrane. Values output from the fitting are shown in table 6.1. SLD profile has been cropped to the membrane region of interest leaving out the underlayers.

showed an affinity for interactions with epithelial model membranes, Tel-I would be used for floating bilayer interaction in NR studies rather than for FTIR and QCM-D studies. The strong nature of the interaction with Tel-II provided some confidence given the similarity in the structures of the two molecules. For the structure of Tel-I the reader is referred back to figure 4.9a.

Figure 6.7 shows data (points) and model fits (lines) in the reflectivity profiles in panels A-C. Underlayers (green), the bilayer before (blue) and after interaction (red) with Tel-I (100 μ M) display changes to the membrane as a result of the interaction. A list of key values obtained from the fitting of the model to the reflectometry data can be found in table 6.2. A full parameter list for the Tel-I interaction with a model DOPC/DOPS/Chol/SM (5:2:2:1) can be found in table A.5. In contrast to the interaction of Tel-II, the fits for the impact of Tel-I on the model epithelial membrane were improved by an inner polyphenol layer (1×10^{-3} \AA), with Tel-I showing overall thicker outer combined layers than Tel-II. The best fits from the model were obtained from having

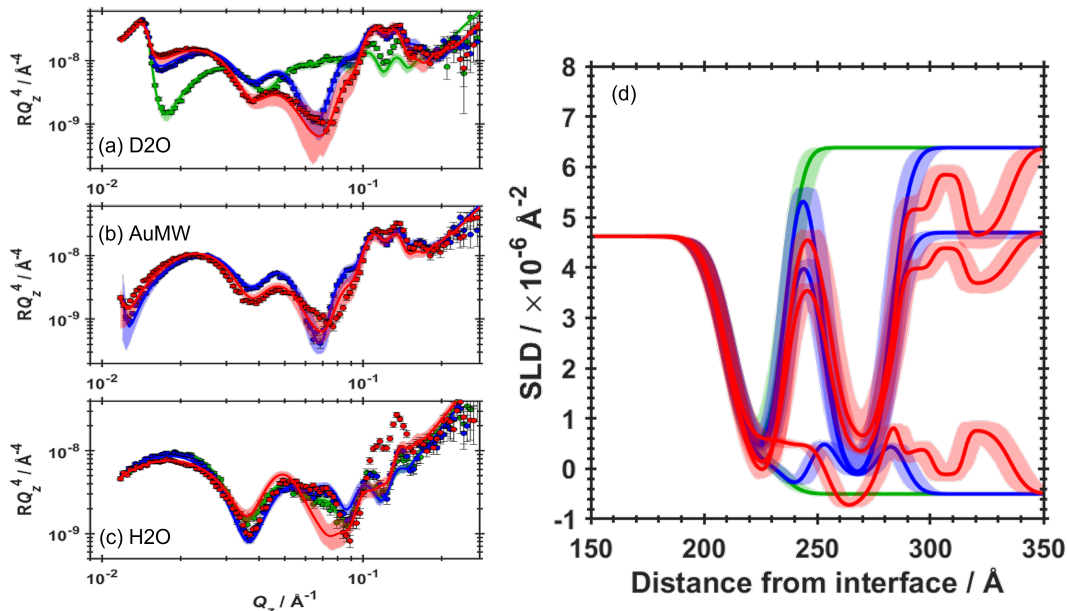


Figure 6.7: Panels (A-C) showing neutron reflectivity profiles for data (points) and model fits (lines) for a COOH-SAM/Gold/Chromium coated silicon substrate (green) with DOPC/DOPS/Chol/SM (5:2:2:1) model membrane before (blue) and after (red) interaction with Tel-I (100 μM) in various solution contrasts. (D) Neutron SLD profiles showing the Si-Cr-Au-SAM-COOH underlayers (green) with DOPC/DOPS/Chol/SM (5:2:2:1) bilayer both before (blue) and after (red) interaction with Tel-I (100 μM) solution in H₂O, gold matched water (AuMW), and D₂O contrasts. The SLD profile has been cropped to show membrane regions more clearly, leaving out the underlayers.

three outer Tel-I layers, as seen for Tel-II. The outer proximal (14.2 Å), medial (13.9 Å), and distal (20.7 Å) showed variation in the same manner as for Tel-II with the middle layer being the thinnest.

In contrast to Tel-II, the volume fraction of Tel-I in the membrane region of the model is far lower (2.97×10^{-4}), which is reflected in the SLD profile (figure 6.7, panel D) where the tail region has an SLD value much closer to that of the tails before the interaction than compared to that seen for the Tel-II epithelial (DOPC/DOPS/Chol/SM (5:2:2:1)) interaction. From the model fits, it is apparent that the affinity for Tel-I and Tel-II being attracted to the membrane are similar given the three layers of polyphenol external to the bilayer. However, the very thin inner layer of Tel-I providing the best fit and the lower volume fraction within the lipid layer compared to Tel-II suggests that Tel-I prefers not to reside inside the membrane. The differences observed here are rationalised in terms of the respective logP values of the two Tellimagrandins (see table 4.7) as well as differences in molecular structure. The extra galloyl group that Tel-II contains allows for more favourable interactions within the bilayer core compared to Tel-I. The planarity of both polyphenols is similar given that they both contain similar skeletal structures in the form of

an (S)- hexahydroxydiphenoyl (HHDP) group.

Table 6.2: Table of values for some key parameters from fits for DOPC/DOPS/Chol/SM (5:2:2:1) model membrane before and after interaction with Tel-I. Error values are from Bayesian error estimation routines as an output of the fitting of the experimental data. Parameters with no associated error bounds have been derived from the appropriate SLD profiles.

Parameter	Before Tel-I	After Tel-I
Central water thickness, Å	9.37 (8.98, 9.88)	13.02 (12.69, 13.39)
Bilayer coverage, %	94.53 (92.84, 96.12)	96.68 (95.42, 97.82)
Bilayer roughness, Å	4.90 (4.75, 5.08)	5.55 (5.41, 5.71)
Lipid APM, Å ²	74.02 (72.73, 75.41)	69.12 (67.73, 70.49)
Inner HG thickness, Å	13	13
Outer HG thickness, Å	12	10
Tail region thickness, Å	17	23
Tannin outer roughness, Å	-	2.16 (2.10, 2.22)
Tannin proximal thickness / Å	-	14.23 (13.87, 14.49)
Tannin proximal hydration, %	-	64.86 (61.77, 68.00)
Tannin medial thickness / Å	-	13.92 (13.55, 14.34)
Tannin medial hydration, %	-	82.78 (80.03, 84.95)
Tannin distal thickness / Å	-	20.72 (19.72, 21.71)
Tannin distal hydration, %	-	49.56 (47.74, 52.44)
Tannin Inner Roughness	-	23.59 (22.57, 24.54)
Tannin Inner Thickness, Å	-	1e-3 (9.8e-4, 1.03e-3)
Tannin Inner Hydration / %	-	0.32 (0.31, 0.34)
Tel-I volume fraction	-	2.97x10 ⁻⁴ (2.88x10 ⁻⁴ , 3.04x10 ⁻⁴)

As a result of having Tel-I cross the bilayer to form an inner layer between the floating membrane and the underlayers, the thickness of the central water gap increases (from around 9 to 13 Å) in order to accommodate the polyphenol. The insertion of the galloyl moiety on Tel-I into the headgroup region of the bilayer results in less space available per molecule to freely move around the membrane, as suggested by the decrease in lipid area per molecule from 74 to 69 Å² [23, 24]. In essence, any wiggle room of the lipid molecules is removed once the rigid galloyl group is inserted into the bilayer, and so the space available for a given lipid is reduced. From the output of the fitting routines it is also observed that there is a small increase in the thickness of the tail region. It is possible that this can be accounted for by the insertion of Tel-I into the membrane from both sides as well as a small amount of polyphenol residing within the membrane, although given the very small volume fraction of Tel-I this is unlikely. The interaction of the model epithelial membrane is shown schematically in figure 6.8 aligned to the SLD profile of the model fits.

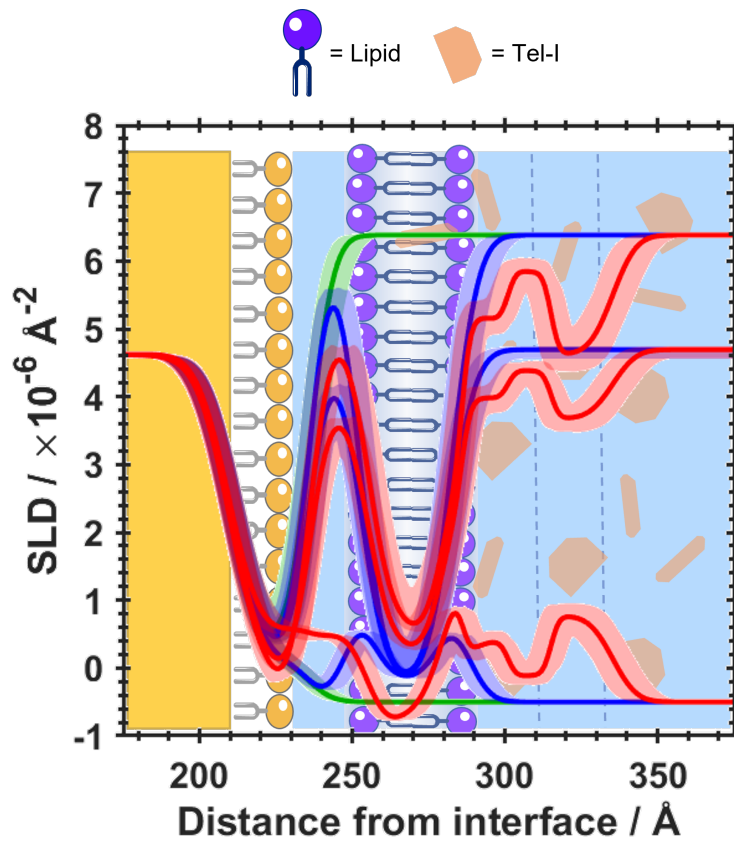


Figure 6.8: Neutron SLD profile overlaid on a cartoon of the model epithelial membrane composed of DOPC/DOPS/Chol/SM (5:2:2:1). The schematic shows the variable regions of Tel-I thickness moving from the outside of the membrane towards the bulk solution. Values output from the fitting are shown in table 6.2. SLD profile has been cropped to the membrane region of interest leaving out the underlayers.

Table 6.3: Values for some key structural properties for Tel-I and Tel-II. These values are linked to their membrane interaction results from NR and SLB data. ^a Molecular area estimated using the Chemdraw Professional (v20.0.0.41) molecular area tool; ^b Interaction with DOPC/DOPS/Chol/SM (5:2:2:1) model; ^c Interaction with DOPC/DOPS/Chol/SM (5:1:2:2) model

Polyphenol	mol wt, g/mol	logP	mol area ^a , Å ²	Free galloyl groups	H-bond donors	H-bond acceptors	NR total thickness, Å	Membrane Vol. Frac.	QCM-D ΔF, Hz
Tel-I	786.56	-0.5	582.839	4	13	18	48.87	x10 ⁻⁴	-13
Tel-II ^b	938.66	0.75	688.767	5	15	21	37.91	0.49	-20
Tel-II ^c	938.66	0.75	688.767	5	15	21	105.98	0.06	-

Table 6.3 draws together some data for key structural properties of Tel-I and Tel-II for their interactions with epithelial membranes. For a DOPC/DOPS/Chol/SM (5:2:2:1) model epithelial membrane Tel-I shows a thicker layer at the membrane surface than for Tel-II. Given the logP values, the amount of Tel-I outside the membrane is rationalised by its partition coefficient, showing a preference for aqueous phases. This finding is corroborated by the membrane volume fraction for Tel-I (2.97×10^{-4}) which is substantially lower than for Tel-II (0.49). It is apparent that the affinity to interact with the membrane and intercalate into the tail region increases with logP, as well as increases to the number of free galloyl groups, the number of H-bond donors and acceptors, and the molecular area available for interaction. The QCM-D data showing the change in frequency (i.e. mass) also suggests Tel-II has a stronger interaction with the membrane. If the difference in frequency were only a product of Tel-II having a greater molecular weight then it would be expected that the difference in frequency would be proportional to the ratio of the two molecular weights of the Tellimagrandins:

$$\text{predicted } \Delta F = -13 \cdot \frac{938.66}{786.56} = -15.5\text{Hz} \quad (6.1)$$

As the mass change for the addition for Tel-II is -20 it is assumed that the 5 Hz difference is due to increased interaction with the membrane than compared to Tel-I. The comparison of Tel-II interaction between different epithelial model membranes will be discussed in due course.

6.2.4 Refining the Model Membrane Composition

Following the observations for the interaction of the DOPC/DOPS/Chol/SM (5:2:2:1) model membrane with Tellimagrandins I and II, the composition of the model epithelial membrane was refined in order to better represent the amount of dominant lipids present in real epithelial surfaces. At this stage no further complexity was introduced, instead a reorganising of the amounts each membrane component. It was mentioned in the previous section that PS is mainly an inner leaflet lipid, and SM is known to be present in high proportions in the outer leaflet [25]. In order to address the overcompensation for the PS abundance from the previous set of experiments, the DOPS amount was dropped to 10%, and the sphingomyelin amount raised to 20%. Assuming that over long timescales the lipids would equilibrate across both leaflets this would bring the lipid composition of the membrane closer to the amounts found in figure 5.7. Although it should be noted that the rate of exchange of lipids between membranes in the absence of proteins is reduced [26].

In the design of the new model membrane system, it was posited that the changing of the component amounts in this way may lead to a decrease in fluidity, and therefore possible decreases in surface coverage also. Because of this, FTIR experiments with both (-)-EGCg and Tel-II were conducted in order to give insight into not only if an interaction would take place, but also if even a membrane could be deposited. One reason for not having added additional

components and increasing the model complexity was to maintain the relatively large DOPC content to best aid fluidity of the bilayer.

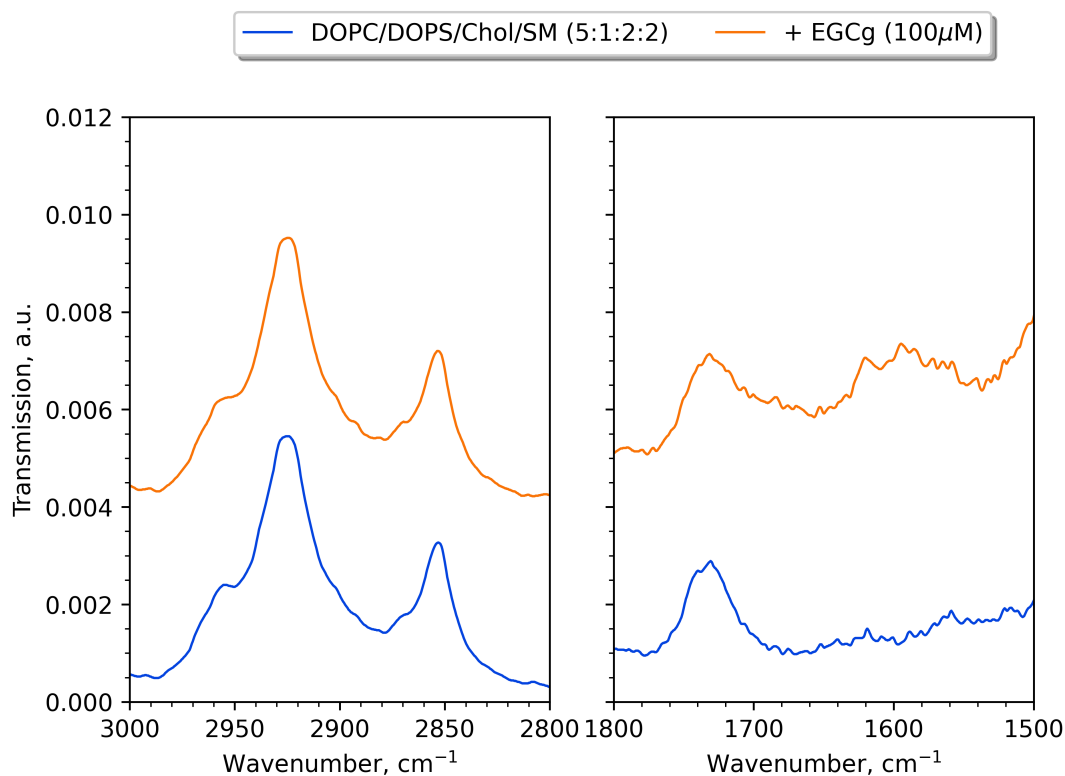


Figure 6.9: ATR-FTIR spectrum for model DOPC/DOPS/Chol/SM (5:1:2:2) membrane before (blue) and after (orange) interaction with (-)-EGCg (100 μM). Symmetric and asymmetric C–H stretching modes, at 2850 and 2930 cm^{-1} respectively, remain unchanged after the interaction. Area under the features at 1580-1620 cm^{-1} increase in intensity after the interaction due to the presence of aromatic C–O and C–C stretching at the interface.

Figures 6.9 and 6.10 show FTIR spectra for the DOPC/DOPS/Chol/SM (5:1:2:2) model membranes before (blue) and after interaction with (-)-EGCg and Tel-II (orange) respectively. In both cases, as for previous FTIR studies, the effects of the addition of polyphenol has no impact on the position or intensity of the symmetric and asymmetric C–H stretching modes. Further, it can be seen that there is an increase in the area under the peak around 1715 cm^{-1} for both spectra, corresponding to the C=O stretch. The peak that was assigned to the amide of the SM headgroup is present in both of these cases also, at around 1610 cm^{-1} in both cases. Upon polyphenol addition the area under the region 1580-1620 cm^{-1} also likely due to the presence of aromatic C–O and C–C stretching [27].

In light of Tel-II showing interaction by FTIR characterisation using neutron reflectometry could be performed. Characterisation at the molecular level for this system, and allowing comparison to the previous model epithelial membrane

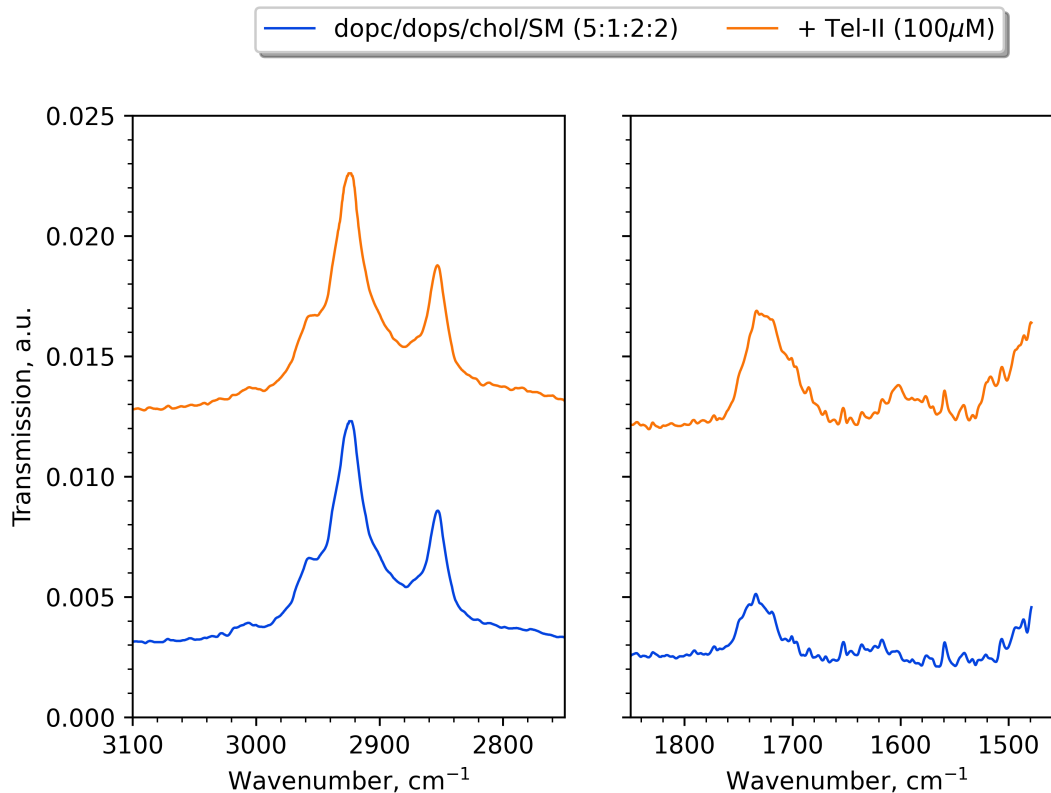


Figure 6.10: ATR-FTIR spectrum for model DOPC/DOPS/Chol/SM (5:1:2:2) membrane before (blue) and after (orange) interaction with Tel-II (100 μM). Symmetric and asymmetric C–H stretching modes, at 2825 and 2910 cm^{-1} respectively are unaffected by the addition of Tel-II. Area under the features at 1560-1650 cm^{-1} increase in intensity after the interaction due to the presence of aromatic C–O and C–C stretching at the membrane surface.

studied (see figure 6.5), allows for the possibility of understanding the role of SM and PS in polyphenol-lipid interactions.

Figure 6.11 shows changes to the floating model epithelial bilayer (DOPC/DOPS/Chol/SM (5:1:2:2)) before (blue) and after (red) the addition of Tel-II (100 μM) membrane. Underlayers are shown in green. Panels A-C of figure 6.11 show the reflectivity profiles for the data (points) and model fits (lines), with (d) showing the SLD profile. Values and associated errors of some key fitting parameters are listed in table 6.4. The full list of parameters is shown in table A.6.

Again, high coverage floating membranes were formed using vesicle rupture methods, and were comparable in coverage to the model DOPC/DOPS/Chol/SM (5:2:2:1) membrane. The best fits were once more obtained allowing Tel-II into the core tail region of the bilayer as well as three connected external layers. Allowing Tel-II to cross the membrane, however, led to worse fits in all cases. The thickness of the three layers external to the bilayer in the bulk solution shows the thickest layer (62.1 \AA) in this case as the medial

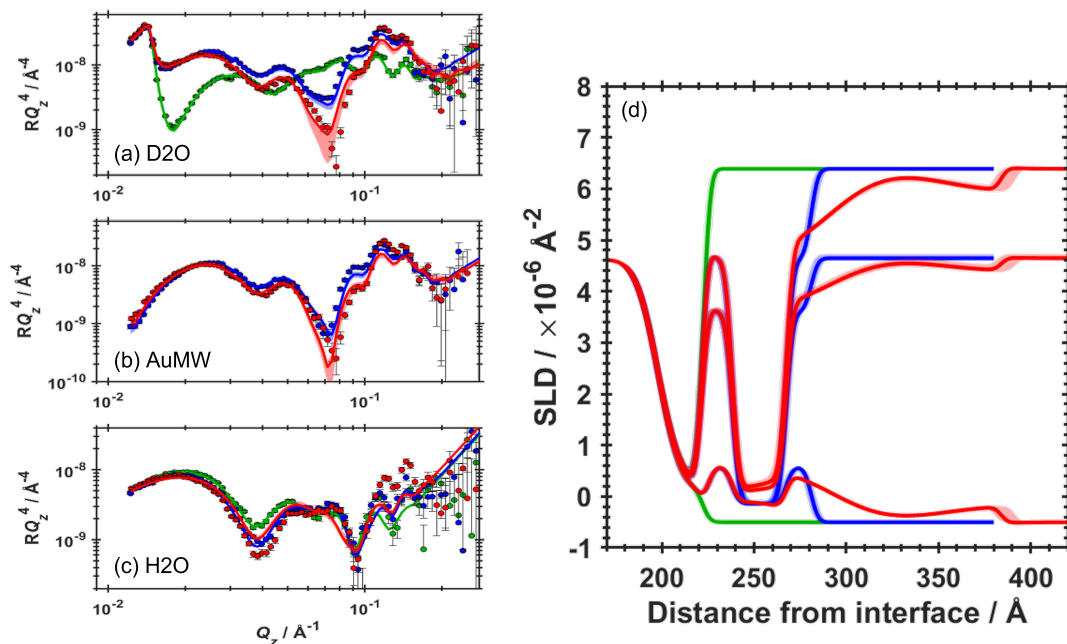


Figure 6.11: Panels (A-C) showing neutron reflectivity profiles for data (points) and model fits (lines) for a COOH-SAM/Gold/Chromium coated silicon substrate (green) with DOPC/DOPS/Chol/SM (5:1:2:2) model membrane before (blue) and after (red) interaction with Tel-II (100 μ M) in various solution contrasts. (D) Neutron SLD profiles showing the Si-Cr-Au-SAM-COOH underlayers (green) with DOPC/DOPS/Chol/SM (5:1:2:2) bilayer both before (blue) and after (red) interaction with Tel-II (100 μ M) solution in H₂O, gold matched water (AuMW), and D₂O contrasts. The SLD profile has been cropped to show membrane regions more clearly, leaving out the underlayers.

layer, although this layer is also very hydrated (98.9%) compared to the layer most closely located to the membrane (9.58 \AA , 46.76%). This suggests that the proximal layer of Tel-II shows higher polyphenol density compared to the other two layers in the bulk solution, and is largely saturated at the membrane surface with Tel-II. This finding is echoed in the outer headgroup thickness which goes up from 13 to 25 \AA where the outer headgroup and polyphenol become embroiled, and both being hydrogenous, are not easily resolved with the solution contrasts available.

From a comparison of the interaction of Tel-II between two varying epithelial membrane models of differing lipid composition, it is observed that changes to the composition of the membrane have an impact on the nature of the interaction. Referring back to table 6.3 it can be seen that there are some large differences in both the membrane volume fraction and the thickness of the external Tel-II layers. Following the interaction of Tel-II with the DOPC/DOPS/Chol/SM (5:1:2:2) the volume fraction of Tel-II in the membrane region is much lower at 6%, which is in stark contrast to compared to 49% during the interaction with the DOPC/DOPS/Chol/SM (5:2:2:1) model membrane.

Table 6.4: Table of values and error bounds (lower bound, upper bound) for some key parameters from fits for DOPC/DOPS/Chol/SM (5:1:2:2) model membrane before and after interaction with Tel-II. Error values are from Bayesian error estimation routines as an output of the fitting of the experimental data. Parameters with no associated error bounds have been derived from the appropriate SLD profiles.

Parameter	Before Tel-II	After Tel-II
Central water thickness, Å	9.02 (8.81, 9.29)	2.11 (2.07, 2.15)
Bilayer coverage, %	98.44 (97.76, 98.94)	99.33 (99.00, 99.57)
Bilayer roughness, Å	3.18 (3.10, 3.28)	3.07 (3.04, 3.11)
Lipid APM, Å ²	67.14 (66.40, 67.92)	57.79 (57.51, 58.02)
Inner HG thickness, Å	11	11
Outer HG thickness, Å	13	25
Tail region thickness, Å	27	29
Tannin proximal thickness / Å	-	9.58 (9.49, 9.73)
Tannin proximal hydration, %	-	46.76 (45.98, 47.47)
Tannin medial thickness / Å	-	62.10 (60.08, 63.56)
Tannin medial hydration, %	-	98.93 (98.48, 99.29)
Tannin distal thickness / Å	-	34.30 (33.43, 34.93)
Tannin distal hydration, %	-	87.19 (86.55, 87.70)
Tel-II volume fraction	-	0.06 (0.06, 0.06)

Coupled with the increase in the outer headgroup thickness and the minimal change in tail thickness, it follows that the Tel-II is inserting galloyl moieties into the membrane because of the decreasing area available to the lipids as shown by the lipid area per molecule. However, Tel-II is much less able to intercalate into the membrane. There is a high chance that this is because of the increased rigidity of the membrane from the altered composition. Reducing the DOPS content in favour of increased SM, and therefore reducing the fluidity of the bilayer, means that the membrane is much less able to adopt Tel-II into its tail region. The tails of SM are largely saturated, unlike DOPS, and so there is less scope for adopting a conformation that allows polyphenol to insert fully into the membrane. The interaction of Tel-II with the bilayer is shown schematically in figure 6.12.

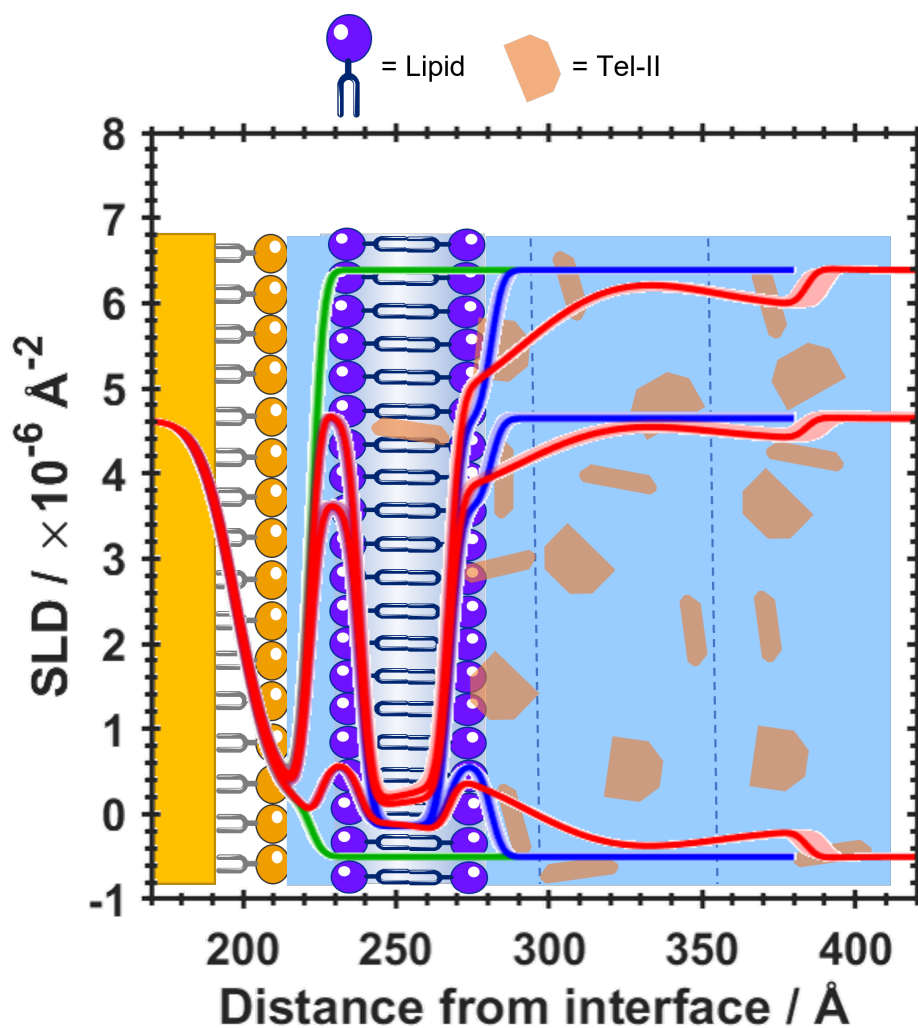


Figure 6.12: Neutron SLD profile overlaid on a cartoon of the model epithelial membrane composed of DOPC/DOPS/Chol/SM (5:1:2:2). The schematic shows the variable regions of Tel-II thickness moving from the outer leaflet of the membrane towards the bulk solution. Values output from the fitting are shown in table 6.2. SLD profile has been cropped to the membrane region of interest leaving out the underlayers.

6.3 Summary

This chapter has shown how, using the data analysis method from chapter 5, a novel model membrane to mimic the human gastrointestinal tract (GIT) was developed and can be optimised. The interactions of the polyphenols that were conducted stand as the first interactions with polyphenols to be characterised using these kind of surface sensitive methods. Early versions of this model contained only three components, DOPC/DOPE/SM (6:3:1), and it was demonstrated that these membranes were suitable for study using supported lipid bilayers (SLBs). FTIR allowed detection of (-)-EGCg at the membrane surface and showed that the interaction was strong enough to withstand laminar flow of the solution above.

It should be understood that the research findings presented in this chapter contain largely positive experimental results. In reality, more membrane compositions and sample conditions were tested to verify experimental setups and to progress membrane composition and accuracy. Table A.2 shows a more complete list of samples and conditions that for whatever reason were not suitable, or require optimisation before neutron experiments are performed.

The composition of the model epithelial membranes was increased in complexity to include more components that are germane to the human GIT. Much of the decision making process for the development of the model membranes regarding an increase in the number of lipid components was informed by the work surrounding figure 5.7. Model membranes of this kind, both in terms of type and complexity, are largely unstudied, especially using techniques with the available resolution of neutron reflectometry (NR).

Increasing from three to four components allowed the inclusion of cholesterol, a critical structural component in membranes. Further, as for the bacterial membranes, DOPE was removed from the model when tuning the membranes for NR experiments due to phase challenges that are discussed. In brief, PE lipids are non-bilayer forming and prefer hexagonal phases rather than lamellar phases as a result of the curvature of the individual lipid molecules. A DOPC/DOPS/Chol/SM (5:2:2:1) membrane showed interactions in FTIR experiments with (-)-EGCg, and using NR the interactions with Tellimagrandins I and II were recorded.

In both cases high coverage floating membranes were formed, and the best model fits to the data were obtained by allowing three connected polyphenol layers external to the membrane. In the case of Tel-II a large membrane volume fraction was observed, indicating that the polyphenol was able to penetrate and intercalate into the bilayer, presumably in a manner similar to cholesterol, given the planar nature of the molecule. Further, the area per molecule decreased in both Tel-I and Tel-II interactions along with an increase in the outer headgroup thickness, likely as a result of the insertion of the galloyl groups into the headgroup region. However, while Tel-II did not show any inner polyphenol layers, Tel-I did. In addition, the volume fraction of Tel-I in the membrane was

markedly lower than for Tel-II (2.94×10^{-4} compared to 0.49). This difference is accounted for in the logP values of the two Tellimagrandins (Tel-II: 0.75; Tel-I: -0.45) where Tel-I is far more opposed to residing in an organic environment. As a result, it forces itself through the bilayer to end up in the water gap between the membrane and the underlayers.

The effects of altering membrane fluidity on the interactions with Tel-II can also be observed. Upon refining the membrane composition to more precisely represent that of a human GIT epithelium, SM was increased from 10% to 20% composition, and DOPS was reduced from 20% to 10%. Because of this, it is likely that the reduction of the unsaturation of the tail region by 10% resulted in a more rigid, less fluid bilayer. FTIR studies showed that DOPC/DOPS/Chol/SM (5:1:2:2) interacted with both (-)-EGCg and Tel-II. Upon transferring to NR experiments, the membrane characteristics of the bilayer before interaction with Tel-II were very similar to its closely related DOPC/DOPS/Chol/SM (5:2:2:1) counterpart. After interaction with Tel-II however, fitting the data showed a much reduced bilayer volume fraction of Tel-II (down from 0.49 to 0.06). It seems that the more rigid tail region of the membrane is less willing to accommodate the intercalation of Tel-II than it was for the membrane with higher DOPS contents. The outer headgroup thickness increase is larger for the DOPC/DOPS/Chol/SM (5:1:2:2) sample, perhaps because interaction at the outer headgroup is preferred to interaction inside the bilayer. In contrast to Tel-II interacting with bacterial samples, no multilamellar phase formation is observed.

References

- [1] M. J. Bissell, A. Lochter and C. Hagios, *Philosophical Transactions of the Royal Society of London. Series B: Biological Sciences*, 1998, **353**, 857–870.
- [2] L. E. O'Brien, M. M. Zegers and K. E. Mostov, *Nature Reviews Molecular Cell Biology*, 2002, **3**, 531–537.
- [3] K. Mostov, T. Su and M. Beest, *Nature Cell Biology*, 2003, **5**, 287–93.
- [4] K. Koichi, F. Michiya and N. Makoto, *Biochimica et Biophysica Acta (BBA)/Lipids and Lipid Metabolism*, 1974, **369**, 222–233.
- [5] R. T. Coones, R. Green and R. A. Frazier, *Soft Matter*, 2021, **17**, 6773–6786.
- [6] A. Reis, J. P. Teixeira, A. M. Silva, M. Ferreira, P. Gameiro and V. de Freitas, *Biomolecules*, 2022, **12**, year.
- [7] S. C. van IJzendoorn, J. Agnetti and A. Gassama-Diagne, *Biochimica et Biophysica Acta - Biomembranes*, 2020, **1862**, 183145.
- [8] H. A. Filipe, C. Sousa, J. T. Marquês, D. Vila-Viçosa, A. de Granada-Flor, A. S. Viana, M. S. C. Santos, M. Machuqueiro and R. F. de Almeida, *Free Radical Biology and Medicine*, 2018, **115**, 232–245.
- [9] N. B. Leite, D. B. Martins, V. E. Fazani, M. R. Vieira and M. P. dos Santos Cabrera, *Biochimica et Biophysica Acta - Biomembranes*, 2018, **1860**, 2320–2328.
- [10] A. N. Li, S. Li, Y. J. Zhang, X. R. Xu, Y. M. Chen and H. B. Li, *Nutrients*, 2014, **6**, 6020–6047.
- [11] T. Matsubara, H. Yasumori, K. Ito, T. Shimoaka, T. Hasegawa and T. Sato, *Journal of Biological Chemistry*, 2018, **293**, 14146–14154.
- [12] C. Hamai, T. Yang, S. Kataoka, P. S. Cremer and S. M. Musser, *Biophysical Journal*, 2006, **90**, 1241–1248.
- [13] A. M. Sendecky, M. F. Poyton, A. J. Baxter, T. Yang and P. S. Cremer, *Langmuir*, 2017, **33**, 13423–13429.
- [14] A. Reis and V. de Freitas, *Food Chemistry*, 2020, **333**, 127509.
- [15] S. L. Keller, S. M. Bezrukov, S. M. Gruner, M. W. Tate, I. Vodyanoy and V. A. Parsegian, *Biophysical Journal*, 1993, **65**, 23–27.

- [16] H. I. Petrache, S. W. Dodd and M. F. Brown, *Biophysical Journal*, 2000, **79**, 3172–3192.
- [17] W. K. Subczynski, M. Pasenkiewicz-Gierula, J. Widomska, L. Mainali and M. Raguz, *Cell Biochemistry and Biophysics*, 2017, **75**, 369–385.
- [18] J. A. F. Op den Kamp, *Annual Review of Biochemistry*, 1979, **48**, 47–71.
- [19] J. C. Holthuis and T. P. Levine, *Nature Reviews Molecular Cell Biology*, 2005, **6**, 209–220.
- [20] M. A. Kiselev and D. Lombardo, *Biochimica et Biophysica Acta - General Subjects*, 2017, **1861**, 3700–3717.
- [21] W. Ding, M. Palaiokostas, W. Wang and M. Orsi, *The Journal of Physical Chemistry B*, 2015, **119**, 15263–15274.
- [22] R. D. Hills Jr and N. McGlinchey, *Journal of computational chemistry*, 2016, **37**, 1112–1118.
- [23] M. Karonen, *Plants*, 2022, **11**, 1809.
- [24] N. Caturla, E. Vera-Samper, J. Villalaín, C. R. Mateo and V. Micol, *Free Radical Biology and Medicine*, 2003, **34**, 648–662.
- [25] Q. Lin and E. London, *Biophysical journal*, 2015, **108**, 2212–2222.
- [26] J. S. Allhusen and J. C. Conboy, *Accounts of chemical research*, 2017, **50**, 58–65.
- [27] Y.-H. Lee, *Journal of applied polymer science*, 2007, **103**, 251–257.

*—How could it be anything
but hard! It was more than
the human heart could bear:
to fall beneath the beloved
ax – then have to justify its
wisdom.*

Aleksandr Solzhenitsyn

7

Epilogue

Contents

7.1	Concluding Remarks	191
7.2	Recommendations for Further Work	196

7.1 Concluding Remarks

This thesis at its outset was concerned with developing accurate methods of modelling membranes from a bottom up perspective, and then using those models in order to better understand polyphenol interactions. The development of model membranes took the work in two parallel streams that covered a bacterial and an epithelial membrane model. The bottom up approach to modelling in both strands of research refers to the use of initially basic systems that are understood, with additional complexity introduced on top of the parts of the model that came before. Ultimately, this bottom up approach begins at the molecular level with individual membrane lipids and is progressed in complexity with the acquisition of data and optimisation of the model. Both the bacterial and epithelial work streams began by choosing an appropriate, relatively simplistic, membrane model then adapting and iterating it so that structural characterisation could be achieved, most notably using neutron reflectometry (NR). The experimental approaches used for the supported lipid bilayer work contained in chapters 3, 4, and 6 were not novel, but were appropriate for planar membrane formation and biophysical interaction studies. Novelty was contained in both the epithelial lipid composition for the SLB studies as well as in the interactions studies contained with all polyphenols for all of the SLB and floating bilayer studies. Biophysical studies using these particular membrane and polyphenol combinations are, at the time of writing, unreported in the scientific literature.

The techniques used in this body of work are both empirical and computational in nature. Model membranes in their increasing complexity were analysed using a variety of physio-chemical, calorimetric, and surface sensitive techniques. This allowed an understanding across a range of the properties of model membranes. Monolayers of relevant lipid components were studied at the air-water interface to get a sense of the effect of additional components on the compressibility and rigidity of a bilayer leaflet. Calorimetry revealed how multi-component mixtures behave in terms of their phase transitions, and how differences in the sample preparation methods altered the mixing of the lipid components. Addition of polyphenols to lipid vesicles for calorimetric study showed how the transition behaviour of the lipids was altered by the presence of lipids, as well as how the mixing of individual lipid components with one another was impacted.

Surface sensitive methods were powerful in a number of ways. Largely they acted as screening methods for neutron reflectometry experiments by highlighting model membranes and their interactions with different polyphenols. Investigations using methods such as quartz crystal microbalance with dissipation monitoring (QCM-D) and attenuated total reflection Fourier transform infrared (ATR-FTIR) spectroscopy were able to demonstrate that a particular lipid mixture was a suitable candidate for biological interaction studies through the formation of a supported lipid bilayer (SLB). QCM-D allowed the measurement of mass changes on a sensor surface, both for the formation of a lipid bilayer and for the interaction of the membrane with a polyphenol, for nanogram scale changes. In both cases the formation of an SLB could be used as a basis for polyphenolic interaction, with both methods being able to show that interactions take place and that they were persistent enough to withstand copious washing of the bilayer surface with buffer solution.

The biological interactions of polyphenols are of interest because of their various pharmaceutical, nutritional, and agricultural benefits [1]. The literature was reviewed with respect to these properties towards the end of chapter 1. Agriculturally they show importance with their ability to increase protein digestion and absorption, useful for optimising the growth of livestock. Further, as an additive in livestock feed there is scope for the inclusion of polyphenols to treat and prevent digestive stress as well as nematode infection. Polyphenol and polyphenolic extracts have shown to provide some anti-carcinogenic effects including being able to limit the growth of unwanted vasculature, as well as inhibiting cell proliferation and being able to induce cell apoptosis. As antimicrobial agents polyphenols are able to inhibit bacterial growth where one viable mode of action is to disrupt the bacterial membrane. Being able to disrupt the bacterial membrane is a result that is observed using the neutron studies at the end of chapter 4 where lamellar phases are observed and modelled after the addition of a polyphenol to a model bacterial membrane. This finding is significant for a number of reasons, most notably because it is the first evidence for interactions using membranes of this type and these particular polyphenols being structurally characterised. Further, implications of this work may relate to disruption of the cellular membrane being a potential factor

involved in limiting the proliferation of cancer cells.

The literature was reviewed in chapter 1 to address a number of areas. At the outset to get a fundamental understanding of membrane architecture for both epithelial and bacterial membranes, moving on to understand the state of surface measurement methods and techniques suitable for detecting and characterising interactions with model biological membranes. A rationale for the use of polyphenols as biological targets for membranes was given, with the effects of polyphenols and how they are currently thought to interact with membrane also being reviewed. The technical detail of the experimental setup for each given technique was given in chapter 2 as well as some of the advantages and drawbacks of a given technique. Throughout, the use of all the experimental methods were able to be combined as the information gained from each technique is complementary to many of the other methods, allowing a full picture to be gained in terms of behaviour of model membranes and interactions.

Initial characterisation methods are outlined in chapter 3 along with a more practical introduction into the data obtained from each kind of experimental technique. Aspects such as lipid phase and geometry are discussed using both monolayer and DSC studies. DSC experiments show the link between the transition temperatures of both individual bacterial membrane components and the relevant mixtures for bacterial membrane modelling. Sample preparation methods differ in that either *ideal* or *non-ideal* lipid mixing could be induced during the vesicle synthesis steps. The differences between the two methods of vesicle preparation are discussed, eventually with *non-ideal* lipid mixing being used and taken forward as the appropriate sample preparation method. Reasons for this rest largely on the understanding of lateral heterogeneities in real world membranes, and that replication of the *non-ideal* biological membranes would add another dimension of accuracy to the models. Development of the suitable bacterial model membranes from vesicles and monolayers to planar membrane formation was carried out. The challenges of forming floating lipid membranes and practical aspects of the model are addressed. By the end of the chapter a full analysis of a model membrane was completed before a biological interaction was undertaken, setting the scene for the biological interaction studies that follow.

Building on the foundations of the model membrane formation laid down in the previous chapter, chapter 4 sets out to begin to measure changes to model bacterial membranes upon the addition of polyphenolic compounds. The polyphenols studied here are (-)-epigallocatechin gallate ((-)-EGCg), 1,2,3,4,6-penta-O-galloyl-d-glucose (PGG), and Tellimagrandins I and II (Tel-I and Tel-II). The addition of polyphenols to the vesicle model membrane lipid mixtures that were introduced in chapter 3 showed different effects depending on the method of vesicle preparation. However, the impact of the polyphenol on making the model membrane either more or less stable was detected. In the calorimetric measurements, (-)-EGCg shows slightly different effects on the membrane compared to the other polyphenols listed with the deviation from the trend being explained by (-)-EGCg being physically smaller. FTIR and

QCM-D were both critical in showing that for planar membrane models were capable of interacting from solution rather than having been prepared with the lipids. Using these surface sensitive techniques the presence of the polyphenolic functional groups at the interface was possible along with mass changes during membrane adsorption. This provided not only justification for analysis of these particular bacterial model membranes using neutron reflectometry, but also confidence that a floating membrane could be formed and that an interaction could be observed. In an effort to structurally understand the impact of having pre-mixed (doped) lipid-polyphenol mixtures that were used for DSC, a sample that contained pre-mixed (-)-EGCg in the membrane was also analysed using NR. The impact of each polyphenol on the bacterial membrane model was discussed and differences are rationalised using some of the polyphenols' physical properties. This strand of work culminates in the induction of lamellar phase formation after polyphenol addition to bacterial model membranes, showing apparent membrane lysis. This is explored and characterised through the NR experimental work, and corroborates some of the antimicrobial effects of the polyphenols that have been previously discussed.

Chapter 5 details a published systematic meta-analysis of the literature of the lipid headgroup composition of epithelial membranes [2]. The composition of epithelial membranes was compared to bacterial membranes and the human erythrocyte to understand the roles of different lipid in different membrane environments. It was concluded that epithelia, in particular the human gastrointestinal (GIT) epithelium, is dominated by PC, PE and cholesterol. Overwhelmingly, the lipid headgroups present are zwitterionic with increases in cholesterol amounts where stricter geometric control of the membrane surface is required. The presence of other minor lipid components was noted, often with roles in cell signalling or protein integration within the membrane. The effect of lipids on the membrane curvature was also addressed, and this is something that needed to be considered during the model epithelial membrane synthesis as it was for the complex bacterial model membranes and their interactions in chapter 4. Chapter 5 served as the bridge between the bacterial model membrane studies that preceded it and the epithelial model membrane studies that follow in chapter 6. The meta-analysis was the main influence for determining the composition of the model epithelial membranes.

Chapter 6 saw the move from two lipid component model membranes to the inclusion of a third and fourth component. The composition of the membranes was developed, optimised, and in the case of NR experiments, compromised to account for the practical barriers faced. This chapter demonstrates novel floating membrane formation of membrane complexity never before seen for human GIT model membranes. Similarly, the interaction of EGCg, Tel-I, and Tel-II with this kind of membrane are, to the knowledge of the author, as yet unreported. Using models with composition characterised and tested using FTIR and QCM-D high coverage floating bilayers were formed that are more complex than any other epithelial models that have been previously reported to the knowledge of the author. Iteration of components closer to that of the corresponding real world membranes allowed an accurate analysis on the effects

of polyphenols on epithelial membrane models, showing stark differences to their effects of bacterial membranes. Instead of inducing lamellar phases the epithelial membrane sees polyphenolic aggregation at the membrane surface. Knowing that polyphenol activity in humans (from chapter 1 and references therein) requires adsorption in the gut, their aggregation at the membrane surface in preparation for transport across the membrane can be rationalised. The effects of different lipid components in the membrane are explored along with the effects of some physical parameters of the different polyphenols being used to explain the extent of interactions. This chapter sees the ability to compare the interactions of a polyphenol, Tellimagrandin II, between two model membrane types.

From chapter 4 the interaction of Tel-II with a model bacterial membrane displayed lamellar phase formation, with lower coverage membranes being moved towards the bulk solution stacking atop one another. As mentioned above this indicates apparent membrane lysis which backs up the reported ability of polyphenols to act as antimicrobial compounds. For this data, the reader is referred back to figure 4.25. In chapter 6 however, the data from the neutron studies suggest instead that there is an aggregation of Tel-II at the membrane surface. As the layers of Tel-II extend into solution the layers become increasingly hydrated and less polyphenol dense. The interaction is given pictorially in figure 6.12. Aggregation at the surface in this way may be showing signs that polyphenols are attracted to the membrane surfaces where dietary absorption and transport occurs, and here they wait for other more active processes to occur to cross the membrane rather than diffusion.

One limitation of this stream of research is the nature of exploring exclusively lipid-polyphenol interactions. In reality, there are many more membrane components present in the membrane, such as surface and integral membrane proteins, carbohydrates protruding from the membrane surface, and in the case of the human GIT, a protective mucin layer. The effects of these non-lipid membrane components was not investigated here, but cannot be ruled out as contributing important aspects in polyphenol-membrane interactions.

As is the nature of research, more time to carry out more experiments to increase accuracy or optimisation is always desired. The vast array of subjects, and the study of increasing complexity of any area of interest is imitated only by time. More time to carry out “just one more” experiment seems appealing. In the context of this work, three further limitations are apparent. Most notably is the impact of the SARS-CoV-2 pandemic. In the United Kingdom, the lockdowns and the lack of access to laboratories meant that 6 months of time carrying out experiments and data acquisition was lost. The loss of access to the DSC instrument at the University of Reading while it was being serviced and fixed meant the calorimetric studies for the epithelial models and their interactions could not be performed. Similarly, QCM-D data for the final epithelial membrane model and interaction with (-)-EGCg and Tel-II were not possible. Inclusion of these data would have helped provide a more “complete” picture. While concordant conclusions can be drawn from the data that were

collected, a gap remains.

7.2 Recommendations for Further Work

Areas for future development also made themselves apparent. For the work conducted in the first part of this thesis a more accurate model of the bacterial surface would be a logical next step for investigating interactions with the polyphenols that were carried out in chapter 4. Interesting comparisons between the two models would allow for (i) a more accurate representation of the interaction to be understood and (ii) determining the efficacy of the relatively simple model used in this work.

The systematic review focused on the lipid headgroup composition of epithelia. Extending this understanding to the nature of the lipid tails in terms of length and (un)saturation would provide a host of complementary information regarding the nature of epithelial membranes. As commented upon in the summary section of the review itself there is scope for a whole portion of analysis on the effects of membrane sphingomyelin and cholesterol on one another. The extent of missing data from some literature sources lends this area a potential undiscovered gem and could help to provide critical insight into bilayer behaviour. This kind of understanding can then be fed into model membrane systems to investigate their effects in all manner of biological interaction studies as well as providing a more accurate model membrane basis. Further, the development of the work from chapter 6 to include lipid-bound carbohydrates or membrane proteins is a logical development. The use of a model membrane containing lipid bound gangliosides was attempted during a neutron beamtime, although sufficient coverage bilayers could not be formed and some development is needed.

This body of work has taken advantage of complementary surface sensitive techniques to investigate lipid-polyphenol interactions using two kinds of membrane models: bacterial and epithelial. The motivation for this lies in the application of polyphenols as pharmaceutical and nutraceutical target compounds, and the modes of interaction between the two membrane types are compared and contrasted. Novel epithelial membrane models were developed and the results reported along with bacterial model membrane interactions that have been investigated in a way that has never before been reported. The model membranes themselves serve as foundation that can be applied for other kinds of biological investigations where epithelial membrane models are needed, yet whose geometry and composition can be tightly controlled.

Interactions of polyphenolic compounds have been studied previously largely using Langmuir trough, calorimetry, and nuclear magnetic resonance (NMR) methods, among others. For the most part these methods did not allow or account for the affinity of the polyphenols for the model membrane from solution. This is particularly true of some NMR type experiments where analysis took place in the solid state. To address this the use of supported lipid

bilayers and floating bilayers allowed a flow of polyphenol containing solution over the membrane and could assess the viability of polyphenol interactions from the bulk solution in real time. FTIR and QCM-D were successful in showing that lipid-polyphenol interactions took place at the water-membrane interface. Selection of a substrate other than SiO_2 would allow detection of changes to the phosphate esters in the lipid headgroups. NR studies enabled structural determination as well as the measurement and derivation of some quantitative information for both the model membrane and the series of interactions. Selective deuteration of membrane or polyphenolic components could shed further light on the dynamics of the interactions of polyphenols at bacterial and epithelial membrane surfaces.

To address any areas that lacked understanding, the use of lipid bilayer samples were developed for studying polyphenols in a way that had not before been completed. The publication of a meta-analysis was useful as a reference tool for determining lipid composition in future model membrane studies that could be adapted depending on the required membrane. Using NR we were able to show the difference in the mode of interaction between model bacterial (DOPC/DOPG (7:3)) and model epithelial membranes (DOPC/DOPS/Chol/SM (5:1:2:2)). Moving forward development of these models to better represent specific lipid composition, as informed by our systematic review, or addition of membrane carbohydrates or proteins as mentioned above, is both appropriate and of interest. The use of these model membranes as a platform for other kinds of biological interaction studies is suitable as the composition can be easily revised and customised. In this way, the techniques and the membrane models developed here lay foundations for the advancement of cellular membrane science for many alternative areas of study or application.

References

- [1] M. Karonen, *Plants*, 2022, **11**, 1809.
- [2] R. T. Coones, R. Green and R. A. Frazier, *Soft Matter*, 2021, **17**, 6773–6786.



Appendix 1

A.1 Fitting Parameters for Model Bacterial Membrane + EGCg

A.1.1 Interaction from Solution

Table A.1: Full list of parameters for the fitting of the DOPC/DOPG (7:3) model bacterial membrane with addition of EGCg (100 μM) as shown in figure 4.21. Values are given with their associated limits beyond which the model was not permitted to step when finding best fits parameters.

Parameter	Value	Lower limit	Upper limit
Substrate Roughness	5.212322346	3	8
SiO ₂ Thickness	24.53101412	5	70
SiO ₂ SLD	3.76196E-06	0.000002	0.000008
SiO ₂ Roughness	6.923785614	2	10
Py Thickness	170.3379159	100	300
Py SLD	9.57639E-06	0.000005	0.00001
Py Roughness	9.911410332	2	20
Gold Thickness	147.3133728	80	200
Gold Roughness	6.767646198	2	15
Thiol APM	22.14460584	10	300
Thiol WPH	0.045314698	0	30
Thiol Coverage	0.97383111	0	1
Thiol Roughness	2.45162656	0	10
Central Water Thickness	7.046864218	0	70
Central Water Roughness	2.260937047	2	8
Lipid APM	74.42424313	55	80
Head bound waters	9.708279966	2	10

Bilayer Coverage	0.986528539	0	1
Bilayer Roughness	5.285709353	5	10
Not Lipid Membrane	0.243269227	0	1
Lipid Membrane	0.94767425	0	1
Tannin Inner Thickness	0.161194786	0	10
Tannin Inner Hydration	76.33619087	50	100
Tannin Inner Roughness	9.591120804	6	10
Tannin Outer Roughness	37.36361331	0	50
Tannin Outer Proximal Thickness	0.023800166	0	10
Tannin Outer Proximal Hydration	19.87814239	0	30
Tannin Outer Medial Thickness	0.475264822	0	20
Tannin Outer Medial Hydration	23.37716088	0	50
Tannin Outer Distal Thickness	14.20651439	5	20
Tannin Outer Distal Hydration	98.12896726	0	100
Gold SLD	4.35767E-06	0.0000043	0.0000047
Background 1	3.82003E-06	0.000001	0.00001
Background 2	8.81099E-06	0.000001	0.00007
Background 3	3.65981E-06	0.000001	0.00003
Background 4	5.11646E-06	0.000001	0.00003
Background 5	7.5411E-06	0.000001	0.00003
Background 6	8.20077E-06	0.000001	0.00003
Background 7	3.85894E-06	0.000001	0.00003
Background 8	3.94033E-06	0.000001	0.00003
Background 9	6.65209E-06	0.000001	0.00003
Background Ten	7.63515E-06	0.000001	0.00003
Scalefactor 1	0.834964314	0.01	1
Qz Shifts 1	0.000519201	-0.03	0.001
D2O	6.36127E-06	0.0000063	0.0000064
H2O	-2.29977E-07	-5.0E-7	-1.0E-6
AuMW	4.68626E-06	0.000004	0.000005
SiMW	2.28907E-06	0	0.000003
Resolution 1	0.052911239	0.01	0.08

A.1.2 Interaction from Doped Bilayer

Table A.2: Full list of parameters for the fitting of the DOPC/DOPG (7:3) model bacterial membrane with addition of EGCg (100 μ M) as shown in figure 4.23. Values are given with their associated limits beyond which the model was not permitted to step when finding best fits parameters.

Parameter	Value	Lower limit	Upper limit
Substrate Roughness	4.890680732	3	8
SiO2 Thickness	25.94670789	5	70
SiO2 SLD	5.23411E-06	0.000002	0.000008
SiO2 Roughness	7.325637208	2	10
Py Thickness	164.6174614	100	300

Py SLD	9.41112E-06	0.000005	0.00001
Py Roughness	10.41490997	2	20
Gold Thickness	146.6213608	80	200
Gold Roughness	5.08071073	2	15
Thiol APM	23.41804032	10	300
Thiol WPH	0.157611286	0	30
Thiol Coverage	0.944936801	0	1
Thiol Roughness	5.230861396	0	10
Central Water Thickness	5.704480978	0	70
Central Water Roughness	2.323766654	2	8
Lipid APM	75.79874442	30	80
Head bound waters	2.788033912	2	50
Bilayer Coverage	0.493513552	0	1
Bilayer Roughness	5.703712633	5	30
Gold SLD	4.35098E-06	0.0000043	0.0000047
Tannin Inner Thickness	8.741480935	0	10
Tannin Inner Hydration	39.34044235	0	100
Tannin Proximal Outer Thickness	27.62694138	0	30
Tannin Proximal Outer Hydration	71.3517646	0	100
Tannin Distal Outer Thickness	8.645025133	0	20
Tannin Distal Outer Hydration	20.45054183	0	100
Background 1	3.00386E-06	0.000001	0.00001
Background 2	6.31198E-06	0.000001	0.00007
Background 3	4.17299E-06	0.000001	0.00003
Background 4	4.87241E-06	0.000001	0.00003
Background 5	7.35312E-06	0.000001	0.00003
Background 6	4.42585E-06	0.000001	0.00003
Scalefactor 1	0.877709346	0.01	1
Qz Shifts 1	0.00068466	-0.03	0.001
D2O	6.35957E-06	0.0000063	0.0000064
H2O	-2.18503E-07	-0.00000056	-0.0000002
AuMW	4.33413E-06	0.000004	0.000005
SiMW	2.47338E-06	0	0.000003
Resolution 1	0.046010102	0.01	0.08

A.2 Fitting Parameters for Model Bacterial Membrane + Tel-II

Table A.3: Full list of parameters for the fitting of the DOPC/DOPS/Chol/SM (5:2:2:1) model epithelial membrane with addition of Tel-II (100 μ M) as shown in figure 4.25. Values are given with their associated limits beyond which the model was not permitted to step when finding best fits parameters.

Parameter	Value	Lower limit	Upper Limit
Substrate Roughness	3.337037827	3	8

Cr thickness	52.71736947	0	80
Cr SLD	3.27026E-06	0.000003	0.000004
Cr roughness	0.946504797	0	15
Gold thickness	148.8533497	0	200
Gold roughness	10.56128017	5	15
Thiol APM	21.86543199	0	40
Thiol coverage	0.977061033	0	1
Thiol roughness	4.623603856	0	10
Central water thickness	4.873199773	4	20
Central water roughness	5.244103657	2	8
Lipid APM	56.95310559	50	80
Head bound waters	4.702844065	2	30
Bilayer coverage	0.975974717	0	1
Bilayer roughness	3.214654588	3	30
Gold SLD	4.57538E-06	0.000004	0.000005
Tannin outer roughness	6.268560456	0	50
Tannin outer proximal thickness	0.000104401	0	75
Tannin outer proximal hydration	52.47422014	0	100
Tannin outer medial thickness	0.536170904	0	150
Tannin outer medial hydration	30.55269702	0	100
Tannin outer distal thickness	82.66101446	0	150
Tannin outer distal hydration	93.85490394	0	100
Tannin tails	1.8438E-05	0	1
Bilayer coverage 2	0.592432332	0	1
Bilayer coverage 3	0.286367759	0	1
Bilayer coverage 4	0.140578929	0	1
Not Lipid VF	0.043878736	0	1
Bilayer_roughness 2	0.187115884	0	15
Bilayer_roughness 3	8.105289318	0	15
Bilayer_roughness 4	12.80430848	0	15
Central water thickness 2	2.849792095	0	15
Central water thickness 3	0.056859484	0	15
Central water thickness 4	8.740288711	0	10
Background 1	3.65958E-06	0.00000005	0.000007
Background 2	4.92148E-06	0.000001	0.00003
Background 3	1.11516E-06	0.000001	0.00003
Background 4	1.43534E-06	0.000001	0.00003
Background 5	1.09448E-06	0.000001	0.00003
Background 6	1.07716E-06	0.000001	0.00003
Background 7	1.11375E-06	0.000001	0.00009
Background 8	3.24502E-06	0.000001	0.00009
Scalefactor 1	0.888948142	0.01	1.5
Scalefactor 2	0.944720486	0.01	1.5
Scalefactor 3	0.816052719	-0.01	1.5
Qz Shifts 1	-2.01676E-05	-0.03	0.03
Qz shift 2	0.000176064	-0.03	0.03
Qz shift 3	0.000132768	-0.03	0.03
D2O	6.36112E-06	0.0000063	0.0000064

H2O	-5E-07	-5.105E-07	-1E-6
AuWW	4.65727E-06	0.000004	0.000005
Resolution 1	0.033597705	0.01	0.05

A.3 Fitting Parameters for Model Epithelial Membrane + Tel-II

Table A.4: Full list of parameters for the fitting of the DOPC/DOPS/Chol/SM (5:2:2:1) model epithelial membrane with addition of Tel-II (100 μ M) as shown in figure 6.6. Values are given with their associated limits beyond which the model was not permitted to step when finding best fits parameters.

Parameter	Value	Lower limit	Upper limit
Substrate Roughness	3.04738214	3	8
Cr thickness	50.2081211	0	80
Cr SLD	3.11215E-06	0.000003	0.000004
Cr roughness	3.799863175	0	15
Gold thickness	168.2819296	0	200
Gold roughness	13.08247747	5	15
Thiol APM	20.00212506	0	40
Thiol coverage	0.986616547	0	1
Thiol roughness	7.448331622	0	10
Central water thickness	3.744579173	0	20
Central water roughness	3.029753275	2	8
Lipid APM	62.9125895	50	80
Head bound waters	12.96850033	2	30
Bilayer coverage	0.988077256	0	1
Bilayer roughness	3.095246713	3	30
Gold SLD	4.76732E-06	0.000004	0.000005
Tannin outer roughness	2.475980269	0	30
Tannin outer proximal thickness	11.69095684	0	30
Tannin outer proximal hydration	77.65535242	0	100
Tannin outer medial thickness	19.20575924	0	30
Tannin outer medial hydration	75.04264204	0	100
Tannin outer distal thickness	6.609826875	0	30
Tannin outer distal hydration	45.07512763	0	100
Tannin tails	0.946187649	0	1
Tel-II Vol. Frac.	0.479116815	0	1
Background 1	3.27367E-06	0.00000005	0.000007
Background 2	1.27799E-05	0.000001	0.00003
Background 3	1.42293E-06	0.000001	0.00003
Background 4	5.52005E-06	0.000001	0.00003
Background 5	1.36597E-05	0.000001	0.00003
Background 6	6.70613E-06	0.000001	0.00003
Background 7	8.79631E-06	0.000001	0.00003

Background 8	8.85773E-06	0.000001	0.00003
Scalefactor 1	0.771298307	0.01	1.5
Scalefactor 2	0.768659219	0.01	1.5
Scalefactor 3	0.814648005	-0.01	1.5
Qz Shifts 1	0.000135057	-0.03	0.03
Qz shift 2	0.000348604	-0.03	0.03
Qz shift 3	0.00025948	-0.03	0.03
D2O	6.37378E-06	0.0000063	0.0000064
H2O	-5.005E-07	-5.E-07	-1.0E-6
AuWW	4.57697E-06	0.000004	0.000005
Resolution 1	0.032836632	0.01	0.05

A.4 Fitting Parameters for Model Epithelial Membrane + Tel-I

Table A.5: Full list of parameters for the fitting of the DOPC/DOPS/Chol/SM (5:2:2:1) model epithelial membrane with addition of Tel-II (100 μ M) as shown in figure 6.8. Values are given with their associated limits beyond which the model was not permitted to step when finding best fits parameters.

Parameter	Value	Lower limit	Upper limit
Substrate Roughness	5.627436123	3	8
Cr thickness	49.43381502	0	80
Cr SLD	3.13406E-06	0.000003	0.0000039
Cr roughness	0.020330631	0	10
Gold thickness	160.4096692	0	200
Gold roughness	8.420978414	0	20
Thiol APM	20.22274834	0	40
Thiol coverage	0.966764385	0	1
Thiol roughness	11.85271383	0	20
Central water thickness	13.01626231	8	20
Central water roughness	10.26636538	0	20
Lipid APM	69.06928958	50	150
Head bound waters	3.27284698	3	20
Bilayer coverage	0.962466953	0	1
Bilayer roughness	5.600873726	3	20
Gold SLD	4.66901E-06	0.000004	0.000005
Tannin outer roughness	2.206482452	2	15
Tannin outer proximal thickness	14.07885784	3	15
Tannin outer proximal hydration	65.99300094	0	100
Tannin outer medial thickness	13.84037196	3	30
Tannin outer medial hydration	81.88202971	0	100
Tannin outer distal thickness	21.05310232	0	40
Tannin outer distal hydration	51.5586191	0	100
Tel-I Vol. Frac	0.000293074	0	1

Tannin inner roughness	23.51790429	0	30
Tannin inner proximal thickness	0.001016056	0	30
Tannin inner proximal hydration	0.332493256	0	100
Tannin Tails	0.23439045	0	1
Background 1	8.86592E-06	0.00000005	0.00001
Background 2	1.16727E-05	0.000001	0.00003
Background 3	5.7483E-06	0.000001	0.00003
Background 4	1.01366E-05	0.000001	0.00003
Background 5	1.21008E-05	0.000001	0.00003
Background 6	5.813E-06	0.000001	0.00003
Background 7	9.48354E-06	0.000001	0.00003
Background 8	1.4124E-05	0.000001	0.00003
Scalefactor 1	0.807996079	0.01	1.5
Scalefactor 2	0.780518848	0.01	1.5
Scalefactor 3	0.753295672	0.01	1.5
Qz Shifts 1	0.000439749	-0.03	0.03
Qz shift 2	3.71143E-05	-0.03	0.03
Qz shift 3	0.000233748	-0.03	0.03
D2O	6.3701E-06	0.0000063	0.0000064
H2O	-5E-07	-5.63E-7	-1E-06
AuMW	4.56832E-06	0.000004	0.000005
Resolution 1	0.038852718	0.01	0.05

A.5 Fitting Parameters for Optimised Model Epithelial Membrane + Tel-II

Table A.6: Full list of parameters for the fitting of the DOPC/DOPS/Chol/SM (5:1:2:2) model epithelial membrane with addition of Tel-II (100 μ M) as shown in figure 6.12. Values are given with their associated limits beyond which the model was not permitted to step when finding best fits parameters.

Parameter	Value	Lower limit	Upper limit
Substrate Roughness	3.207356913	3	8
Cr thickness	50.72763263	0	80
Cr SLD	3.27468E-06	0.000003	0.000004
Cr roughness	5.957139897	0	15
Gold thickness	147.2892502	0	200
Gold roughness	9.569947344	5	15
Thiol APM	21.93739102	0	40
Thiol coverage	0.976966746	0	1
Thiol roughness	5.276856554	0	10
Central water thickness	2.086597836	0	20
Central water roughness	4.318987124	2	8
Lipid APM	57.79680521	50	80
Head bound waters	15.57429619	2	30

Bilayer coverage	0.990997853	0	1
Bilayer roughness	3.094951538	3	30
Gold SLD	4.67181E-06	0.000004	0.000005
Tannin outer roughness	23.30772551	0	30
Tannin outer proximal thickness	9.608038769	0	30
Tannin outer proximal hydration	46.95430648	0	100
Tannin outer medial thickness	62.09880337	0	80
Tannin outer medial hydration	98.63556582	0	100
Tannin outer distal thickness	33.82944169	0	80
Tannin outer distal hydration	87.02332054	0	100
Tel-II Vol. Frac.	0.059539923	0	1
Tannin tails	0.513271194	0	1
Background 1	1.43322E-06	0.00000005	0.000007
Background 2	5.20684E-06	0.000001	0.00003
Background 3	2.44431E-06	0.000001	0.00003
Background 4	1.84127E-06	0.000001	0.00003
Background 5	5.66768E-06	0.000001	0.00003
Background 6	1.15687E-06	0.000001	0.00003
Background 7	1.60877E-06	0.000001	0.00003
Background 8	6.59817E-06	0.000001	0.00003
Scalefactor 1	0.879291944	0.01	1.5
Scalefactor 2	0.945101002	0.01	1.5
Scalefactor 3	0.838125522	-0.01	1.5
Qz Shifts 1	-3.73399E-06	-0.03	0.03
Qz shift 2	-3.02068E-06	-0.03	0.03
Qz shift 3	0.000108785	-0.03	0.03
D2O	6.38208E-06	0.0000063	0.0000064
H2O	-5.0E-07	-5.017E-7	-1.0E-6
AuWW	4.6389E-06	0.000004	0.000005
Resolution 1	0.028315364	0.01	0.05

A

Appendix2

Tables A.1 and A.2, for bacterial model membranes and epithelial model membranes respectively, show the extent of samples and their conditions that either showed use as stepping stones when moving towards more complex and accurate samples. In addition, samples that showed no promise or did not yield positive results are included. This information is provided to add transparency and awareness that some mixtures and preparation methods did not result in stable bilayer models. In some cases, the models lacked complexity and accuracy in their compositions and were used to beta-test a technique and were stepping stones in method development. Some models simply did not make it to the neutron experiments, either due to foreseeable sample issues, or did not. yield positive results. In these cases, optimisation to the samples themselves, the membrane formation conditions, or both are required.

Table A.1: Table summarising experimental conditions for some bacterial membrane interaction studies that showed non-optimal conditions or results, and that ultimately were deemed not suitable for neutron reflectometry samples.

Sample	Technique	Sample conditions	Shortcoming
DPPC + BSA	ATR-FTIR	20 mM HEPES, 2 mM Ca ²⁺ , 100 mM NaCl, pH 7.2, 38°C	Membrane lacked complexity and accuracy
DOPC/DOPG (7:3) + PGG	SANS	20 mM HEPES, 2 mM Ca ²⁺ , 100 mM NaCl, pH 7.2, 38°C	No change detected after drug addition
DOPE/DOPG (3:2)	ATR-FTIR, QCM-D	20 mM HEPES, 2 mM Ca ²⁺ , 100 mM NaCl, pH 7.2, 38°C	Showed use in SLB studies, not suitable for carrying on to neutron experiments, DOPE phase issues
DOPC/DOPG (7:3)	NR	20 mM HEPES, 2 mM Ca ²⁺ , 100 mM NaCl, pH 7.2, 38°C	No viable deposition in pH 7 solution - Very low coverage bilayer
DOPC/DOPG (7:3) + Vescalagin	ATR-FTIR, QCM-D	20 mM HEPES, 2 mM Ca ²⁺ , 100 mM NaCl, pH 7.2, 38°C	Not taken to neutron studies, showed less strong interaction than compounds chosen
DOPC/DOPG (7:3) + Genistein	ATR-FTIR, QCM-D	20 mM HEPES, 2 mM Ca ²⁺ , 100 mM NaCl, pH 7.2, 38°C	Not taken to neutron studies, showed less strong interaction than compounds chosen

Table A.2: Table summarising experimental conditions for some epithelial membranes and interaction studies that showed non-optimal conditions or results, and that ultimately were deemed not suitable for neutron reflectometry samples.

Sample	Technique	Sample conditions	Shortcoming
DOPC/DOPS/Chol (5:3:2) +EGCg	ATR-FTIR	20 mM HEPES, 2 mM Ca ²⁺ , 100 mM NaCl, pH 7.2, 38°C	Composition lacks complexity and accuracy
DOPC/DOPS/Chol/SM (5:2:2:1) +Vescalagin	ATR-FTIR, QCM-D	20 mM HEPES, 2 mM Ca ²⁺ , 100 mM NaCl, pH 7.2, 38°C	Not taken to neutron studies, showed less strong interaction than compounds chosen
DOPC/DOPS/Chol (5:1:2:2) + EGCg	ATR-FTIR, QCM-D	20 mM HEPES, 2 mM Ca ²⁺ , 100 mM NaCl, pH 7.2, 38°C	Limited neutron time, chose to explore interaction with more interesting polyphenol
DOPC/GM3 (7:3)	NR	20 mM HEPES, 2 mM Ca ²⁺ , 100 mM NaCl, pH 7.2, 38°C	Very low bilayer coverage. Likely both sample and deposition conditions need optimising

